Anton Kulyakhtin

Numerical Modelling and Experiments on Sea Spray Icing

Thesis for the degree of Philosophiae Doctor

Trondheim, December 2014

Norwegian University of Science and Technology
Faculty of Engineering Science and Technology
Department of Civil and Transport Engineering

NTNU – Trondheim
Norwegian University of
Science and Technology

UNIS
The University Centre in Svalbard

NTNU
Norwegian University of Science and Technology

Thesis for the degree of Philosophiae Doctor

Faculty of Engineering Science and Technology
Department of Civil and Transport Engineering

ISBN 978-82-326-0588-0 (printed ver.)
ISBN 978-82-326-0589-7 (electronic ver.)
ISSN 1503-8181

Doctoral theses at NTNU, 2014:338

Printed by NTNU-trykk

to my family

Abstract

Oil and gas activities in the cold seas are endangered by icing. Icing may occur when water spray or moisture is deposited on a vessel or offshore structure above sea level and the air temperatures is below the freezing temperature of water. Ice accumulation can block rescue equipment and doors, and clog ventilation systems, which may increase the risk of explosion as result of volatile gas accumulation. Icing can be caused by supercooled fog, freezing rain, falling snow and freezing sea spray. The freezing sea spray caused 80 – 90% of all offshore icing incidents and is the focus of this study.

To take precautions against icing, it is important to understand the physics of icing and to model it. The rate of ice accretion is mainly defined by the spray flux and heat transfer, and both must be accurately predicted. Existing icing models, e.g., ICEMOD and RIGICE04, simplify the structure, subdividing it into cylindrical and flat components. In these models, airflow around a component is assumed to be unaffected by other parts of the structure, and the heat transfer is approximated using empirical relations. In reality, however, the airflow field is complex. Upwind components can create wind shadow regions or regions of accelerated flow in front of downwind components; this changes both the spray flux and the heat transfer, thus making ICEMOD and RIGICE04 inadequate.

A research subject of this PhD study was the heat transfer and spray flow around a structure in a real airflow. The full-scale measurements in the literature are limited and it is expensive to perform them. Therefore, for a preliminary answer the question was addressed using computational fluid dynamics (CFD), which is capable of predicting the spray flow and heat transfer around a structure with any shape; however, the accuracy of CFD is uncertain.

Existing models of sea spray icing, e.g., ICEMOD and RIGICE04, neglect heat flux into the accreted ice and assume that air cooling is directly spent to freeze the water film on the ice surface. This assumption is good for steady ice growth. However, it is also used in modelling icing caused by periodic sea spray. This study proves numerically and experimentally that the heat flux into the accreted ice generated by freezing must not be neglected.

The main contributions of this work are as follows:

- The study develops the marine icing model, MARICE, which uses CFD to calculate spray flux and heat transfer, and models water film motion on any arbitrary surface.
- The study shows that Reynolds-averaged Navier-Stokes (RANS) models should be used with care in icing simulations: the collision efficiency is well predicted upstream flow separation point by any RANS turbulence model; however, the wake and separation of the flow is modelled poorly.
- The study develops and validates a new model of ice growth caused by periodic sea spray, which accounts for the heat conduction inside the accreted ice.

Preface

This thesis is submitted to the Norwegian University of Science and Technology (NTNU) for partial fulfilment of the requirements for the degree of philosophiae doctor.

This doctoral work has been performed at the Department of Civil and Transport Engineering, NTNU, Trondheim and the Department of Arctic Technology of the University Centre in Svalbard (UNIS) with Professor Sveinung Løset as main supervisor and with co-supervisors Professor Aleksey Marchenko and Doctor Olga Shipilova.

The PhD position was financed through NTNU and the MARICE project, which is a joint industry project between Det Norske Veritas, Statoil, the Norwegian University of Science and Technology and the Research Council of Norway.

Acknowledgements

Many people contributed to my work. I try here to thank at least some of them. First, I would like to thank Aleksey Marchenko who was my Master thesis supervisor; I would not have started this PhD journey without visiting Svalbard and working with him. Sveinung Løset gave me precious practical knowledge on how to plan, develop and present my research.

I would like to thank my University colleagues, participants of the MARICE project and the Department of Technical and Logistical services in UNIS for their help and advising, especially Andrei Tsarau, Kåre Johansen, Laszlo Kollar, Olga Shipilova, Ole-Christian Ekeberg, and Per Asbjørn Østensen. Part of this research included field experiments and I'm grateful to the people who did experiments with me during cold Svalbard nights: Sergey Kulyakhtin, Anna Pustogvar, Nikita Onishchenko, Alexey Prusakov, Jurii Dobrynets and Peter Likutov. I'm also grateful to Lucie Strub-Klein, Louis Delmas and Dmitry Brazhnikov, who reviewed my papers before the submission.

Thanks also to the rest of the "basement gang" and Svalbard folks who were not mentioned before but who I had fun with and scientific support from: Alexey Shestov, Anatoly Sinitsyn, Alex Klein-Paste, Ekaterina Kim, Ivan Metrikin, Johan Wåhlin, Felix Breitschädel, Kenneth Eik, Marion Beentjes, Maria Azucena Gutierrez Gonzalez, Marat Kashafutdinov, Sergiy Sukhorukov, Renat Yulmetov, Raed Lubbad, Torodd Nord, Wenjun Lu, and Wolfgang Kampel.

In its final stage, my research and completion of this thesis was affected by Lasse Makkonen, Kathleen Jones and Eirik Schrøder Hansen. Lasse explained what my attitude should be and motivated me to continue to dig into the problem in addition to the valuable knowledge about icing. Kathleen criticized my work and it motivated me to improve my writings. Eirik showed me that the heat transfer at high Reynolds numbers is not properly modelled by the existing icing models.

I want to finish this by thanking my family: my ex-wife, Natalia Iakymenko; my parents, Olga and Alexey, my sister, Alena, and Sofie Gradmann for supporting me during this challenging time. Most of all, I am grateful to my brother, Sergey Kulyakhtin, who supported me mentally and scientifically, and took a lead in part of the experiments in Spitsbergen instead of me and doing even more than I would ask.
Thank you all!

Contents

List of Publications

Selected papers:

1. Kulyakhtin A., Løset S., 2011. Sea spray icing: In-cloud evaporation. Semi-analytical and numerical investigation. International Workshop on Atmospheric Icing (IWAIS2011), Chong-Chin, China

2. Kulyakhtin, A., Kollar, L, Løset, S., Farzaneh, M., 2012. Numerical simulation of 3D spray flow in a wind tunnel with application of O'Rourke's interaction algorithm and its validation. Proceedings of the 21st IAHR International Symposium on Ice (IAHR2012).

3. Kulyakhtin, A., Shipilova, O., Libby, B. and Løset, S., 2012. Full-scale 3D CFD simulation of spray impingement on a vessel produced by ship-wave interaction. Proceedings of the 21st IAHR International Symposium on Ice (IAHR2012).

4. Kulyakhtin A., Kulyakhtin S., Løset S. Measurements of Thermodynamic Properties of Ice Created by Frozen Sea Spray, 2013. The 23rd International Ocean and Polar Engineering Conference (ISOPE), Anchorage, USA, June 30 - July 5 2013.

5. Kulyakhtin, A., Shipilova, O. and Muskulus, M., 2014. Numerical simulation of droplet impingement and flow around a cylinder using RANS and LES models. Journal of Fluid and Structures, Vol. 48, pp. 280-294.

6. Kulyakhtin, A., Tsarau, A., 2014. A time-dependent model of marine icing with application of computational fluid dynamics, Journal of Cold Regions Science and Technology, Vol. 104-105, pp. 33-44.

7. Kulyakhtin, A., Kulyakhtin, S. and Løset, S, 2014. The role of the ice heat conduction in the ice growth caused by periodic sea spray. Journal of Cold Regions Science and Technology (submitted).

Secondary papers:

8. Kulyakhtin, A., Løset, S. and Kollar, L. Small scale simulation of sea water icing in natural field conditions. Proceedings of the 21st IAHR International Symposium on Ice (IAHR2012).
9. Shipilova O., Kulyakhtin, A., Tsarau, A., Libby, B., Moslet, P. O., and Løset, S. Mechanism and Dynamics of Marine Ice Accretion on Vessel Archetypes. Arctic Technology Conference in Houston, USA, 3-5 December 2012.

List of Symbols and Abbreviations

Abbreviations

CFD	computational fluid dynamics
DNS	direct numerical simulation
LES	large eddy simulation
LWC	liquid water content
MARICE	name of the developed icing model
METOCEAN	a contraction of the words 'meteorology' and 'oceanography' referring to the waves, winds and currents conditions
RANS	Reynolds-averaged Navier-Stokes

Roman symbols

A_c	area of the structure projection on the plane perpendicular to the free stream airflow velocity
a	diameter of the structure or one of the columns for a multicolumn structure at the water line
b	thickness of accreted ice
$\frac{db_M}{dt}$	heat flux to the air
$\frac{db_{WL}}{dt}$	ice accretion
C_d	droplet drag coefficient
c_{pw}	specific heat capacity of the water
d	droplet diameter
D_{sw}	diffusion coefficient of the salt in the water
E_c	collision efficiency of water droplets
F_{sp}	mass flux of incoming spray
$\mathbf{g}$	gravity vector
H_s	significant height of sea wave
k	turbulence kinetic energy
k_R	sea wave number
k_w	thermal conductivity of water
L_f	latent heat of fusion of pure ice

m_d	droplet mass
Nu	Nusselt number, non-dimensional heat transfer coefficient
P	pressure
P_a	static air pressure
Q_c	convective heat flux from the air to the water film surface
Q_e	evaporative heat flux from the air to the water film surface
Q_d	heat capacity of the spray impinging to the surface of accreted ice
Q_r	radiant heat flux from the air to the water film surface
Q_{dc}	convective heat flux from the air to the water droplet
Q_{de}	evaporative heat flux from the air to the water droplet
Q_{dr}	radiant heat flux from the air to the water droplet
Re	Reynolds number, $Re = UL\nu^{-1}$, where U and L are the characteristic velocity and length, respectively
S_w	salinity of water film on the surface of the accreted ice
S_{sp}	salinity of sea spray
S_{ac}	salinity of accreted ice
T_d	average temperature of single droplet
T_f	freezing temperature of the water film
T_w	water-film temperature at the air/water interface
U_c	free stream airflow velocity relative to the obstacle
$\mathbf{U}$	air velocity vector
U_i	velocity component in i-direction
U_{10}	wind speed at the 10 m height
$\mathbf{V}_d$	droplet velocity vector
w	liquid water content (LWC), i.e., the total mass of water droplets per unit volume of air

Greek symbols

δ	thickness of the diffusion-limited boundary layer
ε	turbulent dissipation
η	water film thickness

ν	kinematic viscosity
Π	production of turbulence kinetic energy
ρ	air density
ρ_w	water density
ρ_i	density of the accreted ice
σ_M	ratio of entrapped liquid water mass to the mass of ice accretion if the heat release is mainly to the air
σ_{WL}	ratio of entrapped liquid water mass to the mass of ice accretion if the heat release is mainly to the ice
$\boldsymbol{\tau}_a$	wind stress applied to the free surface of the film

1. Introduction

1.1. Background

Significant navigation in the northern seas started with whale and seal hunting (Jørgensen, 1982). In those waters, ships were exposed to cold storms that resulted in ice accumulation onboard; this phenomenon is called icing. Hundreds of vessels and a British battle ship (during the Second World War) are claimed to have sunk due to icing (Jørgensen, 1982; Stallabrass, 1980). Icing is still a problem for fishing vessels and oil and gas activities today. Ice accumulation can block rescue equipment and doors, and clog ventilation systems, which may increase the risk of explosion as a result of gas accumulation. Slippery decks caused 22% of crew injuries (Jørgensen, 1982). "Semisubmersibles are also sensitive to overloading due to the low ratio between rig water surface area and displacement" (Nauman, 1984). Ice accretion on offshore rigs with a mass of less than 20 tonnes is frequent (Brown and Mitten, 1988). However, in only three events (Treasure Seeker, Ocean Bounty, SEDNETH I), the total ice load exceeded 100 tonnes and drilling operations were interrupted (Brown and Mitten, 1988; Ryerson, 2008). The mean duration of icing events is 15 hours with a standard deviation of 13 hours (Brown and Agnew, 1985). The longest reported event lasted 84 hours over the period of 26-30 March, 1978 by the GCGS HUDSON in the Labrador Sea (Brown and Agnew, 1985).

Icing occurs when water spray or moisture is deposited on a vessel or structure surface above sea level and the air temperatures is below freezing temperature of water. The water can be supplied by (Stallabrass, 1980):

a) Supercooled fog;
b) Freezing rain or freezing drizzle;
c) Falling snow, in particular wet snow;
d) Freezing sea spray (vessel and/or wind generated).

Freezing sea spray caused 80 – 90% of all offshore icing incidents (Brown and Mitten, 1988; Jørgensen, 1982; Makkonen, 1988). Ryerson (2011) reviewed the impacts of different sources of icing and concluded that the ice caused by sea spray is the main threat to offshore structures, causing a risk for stability, integrity, fire and rescue equipment, helicopter deck, and air vents issues and etc.

There are two sources of sea spray: (1) splashing, which is created by wave interaction with a structure wall or by a vessel slamming waves; and (2) water droplets blown off wave crests. When wind exceeds 9 m/s, it is able to carry and deliver droplets to the walls of a structure (Horjen and Vefsnmo, 1985). Storms in freezing temperatures that last for more than 3 days happen on average 3 times per year in Norwegian arctic seas (Smirnov in Nauman (1984)). The daily expectation of moderate or greater icing (>1.5 mm hr^{-1}) is 25.1% and of heavy or greater icing (>2.8 mm hr^{-1}) is 9% from the 1st of December to the 31st of March in the region between 42°N and 60°N and between 45°W and the east coast of North America (Stallabrass, 1980).

The understanding of physics and numerical modelling is widely used to take precautions against icing. The model of Overland et al. (1986) is commonly applied to forecast dangerous sea areas. This model is based on the icing statistics of fishing vessels and, therefore, cannot be used for larger vessels or offshore oilrigs. Also, Makkonen et al. (1991) found a mistake in the physical analysis performed by Overland et al. (1986). In contrast to model by Overland et al. (1986), the vessel size and spray flux are taken into account by the model of Blackmore and Lozowski (1994), which, however, is not used widely because it requires the description of the spray flux.

Most models of marine icing use an empirical equation of spray flux for vessels (Horjen, 1990; Zakrzewski, 1986) and offshore structures (Brørs et al., 2009; Forest et al., 2005; Jones and Andreas, 2012). ICEMOD prescribes the vertical distribution of the spray flux on the structure surface (Brørs et al., 2009). Other models track droplets after generation in a constant uniform wind field (Lozowski et al., 2000) or in the airflow around single cylindrical components calculated using potential flow theory (Finstad et al., 1988a; Jones and Andreas, 2012). In both approaches, the spray flux on the structure surface is defined by the number of droplets that interact with the structure.

Numerical modelling can also be used to improve structure designs with the aim to reduce icing. The rate of ice accretion is mainly defined by the spray flux and heat transfer (Lozowski et al., 2000), and both must be accurately predicted. Existing icing models, e.g., ICEMOD (Horjen, 1990; Horjen, 2013) and RIGICE04 (Forest et al., 2005), calculate icing in a transient mode, which takes the periodicity of the interaction-generated spray and the water film dynamics into account. However, both models simplify the structure by subdividing it into independent cylindrical and flat components. The airflow around a component is assumed to be unaffected by other parts of the structure, and the heat transfer is approximated using empirical relations (Horjen, 2013; Lozowski et al., 2000). In reality, the airflow field is complex and cannot

be split into parts: the upwind components create wind shadow regions or regions of accelerated flow in front of the downwind components.

1.2. Objectives and scope

This PhD study focuses on the development of a new sea spray icing model that applies modern techniques, such as CFD, to predict icing. Icing includes many physical processes and even though icing models have been developed over decades, many of these processes are still not well described.

When spray flux is high, the factor limiting ice accretion growth is heat transfer. As mentioned above, all existing icing models split a given structure into simple geometries (cylinders and plates) and the heat transfer from their surface to airflow is predicted by relations obtained in the lab. For example, those relations for the cylinders were measured for subcritical and critical flow regimes (i.e., Reynolds numbers from 2.2×10^4 to 4×10^6); however, a part of a structure with a width of 10 m in 20 m s^{-1} wind corresponds to a substantially higher Reynolds number of 1.2×10^7. In addition, ICEMOD and RIGICE suffer from inconsistencies because the airflow around different components is interrelated and structures have many corners which cause flow separations.

All existing models also use empirical equations to represent spray flux which maybe inaccurate. The validity of these models and spray generation process is beyond the scope of this study; thus, existing empirical equations were used in this work. However, when water droplets fly around a structure, they are deflected by airflow; only a portion of the spray interacts with the structure. Therefore, the spray flux measured on a surface of a certain structure cannot be directly applied to other structures. For example, Brørs et al. (2009) assumed that the spray flux to the back of the cylindrical structure was 10%, based on observations made on a multicolumn semisubmersible. For a cylindrical structure, substantial wave splashing occurs only on the front; and it is unknown whether they can be transferred to the cylinder back by the air vortexes, or by the waves splashing behind the structure, or by the complex airflow around the semisubmersible. The first and last options are investigated in this study.

A research question in this PhD study was the heat transfer and spray flow around a structure in a real airflow (RQ1). The full-scale measurements in the literature are limited and it is expensive to perform them. Therefore, for a preliminary answer, RQ1 was addressed using CFD, which is capable of predicting the spray flow and heat transfer around a structure with any shape; however, the accuracy of CFD is not well

understood. The study investigated how CFD can improve icing prediction. The CFD results were compared with ICEMOD and RIGICE04 and analysed based on the knowledge about general behaviour of heat transfer caused by airflow.

To complete the model, a computation of freezing was developed based on existing models. Several approaches to model fluid film and ice growth processes exist in the literature: the steady model of Makkonen (1987), and the transient models applied in ICEMOD (Horjen, 1990) and RIGICE04 (Forest et al., 2005). All these models neglect the heat flux into the accreted ice and assume that air cooling is directly spent to freeze the water film on the ice surface. This assumption is true for steady ice growth. However, it is also used in modelling icing caused by periodic spray. This study investigates numerically and experimentally if the ice accretion caused by the periodic spray is similar to the ice accretion caused by continuous spray (RQ2).

1.3. Research approach

Many icing aspects are well understood and are calculated in existing icing models, so the new icing model is based on the current knowledge (Paper 6). In addition to that, some aspects of spray flow and freezing were further investigated (Figure 1). The respective numerical and field studies were conducted in parallel (Table 1) primarily because field measurements were only possible during the winter season in Spitsbergen.

In previous studies, the spray flow was modelled as a flow of independent droplets in an air stream (Lozowski et al., 2000). Therefore, the question was how the droplets affect each other thermodynamically (Paper 1) and mechanically via interactions and coalescence (Paper 2). Paper 2 established the numerical setup for the droplet flow around full-scale structures (Paper 3) and indicated that future work should analyse how well CFD and RANS turbulent models represent real airflow. This resulted in the work published in Paper 5. In particular, Paper 5 showed the limitations of the CFD modelling and resulted in abandoning modelling of spray coalescence. Results of the studies were also implemented in the MARICE icing model which was developed and is described in Paper 6.

Initially, field experiments were started to validate the spray flow and thermodynamics. Spray dynamics had already been studied and verified for the case of scarce small droplets (less than 200 μm) (Kollar, 2009; Kollar et al., 2006; Makkonen and Stallabrass, 1987; Stallabrass, 1980). In our experiments, a dense spray was used with large droplets with a diameter of 1 – 2 mm which is typically created by wave-structure

interaction (Ryerson, 1995). Experiments showed that existing techniques were not applicable to measure droplet diameter distribution inside of a dense spray. However, experiments yielded knowledge about the properties of ice accretion (Paper 4) and natural conditions (Paper 8) and showed that existing models of ice growth should be reviewed. As result, a new ice growth model was developed (Paper 7).

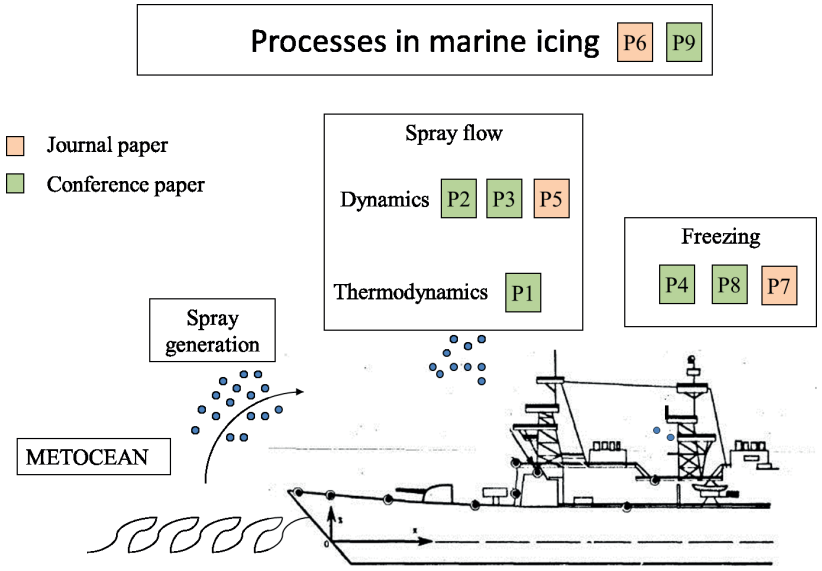

Figure 1. Contribution of papers collected in this thesis to the investigation of the icing process.

Table 1. Timelines of work on different topics.

Research topic		2010					2011				2012				2013				2014			
		4	1	2	3	4	1	2	3	4	1	2	3	4	1	2	3	4	1	2	3	4
Spray flow	a) Fundamental	■	■	■		■																
	b) Thermodynamics				■	■	■															
	c) Interactions							■	■	■		■										
	d) Airflow													■	■	■						
	e) Large scale									■	■											
Experiments						■	■	■		■	■	■		■	■							
MARICE model development									■			■			■							
Case studies															■	■	■					
Thesis writing																	■				■	
New model of ice growth																	■	■	■			

1.4. Main contributions

C1. Creation of the marine icing model, MARICE, which uses CFD to calculate spray flux and heat transfer by airflow (Paper 6)

C2. Realisation of a semi-3D numerical model of freezing of a saline water film applicable to surfaces with complex geometries (Paper 6)

C3. Comparison of existing marine icing models with MARICE (Paper 6)

C4. It was shown that the heat transfer coefficient of the full-scale structure should be measured and that the coefficient measured for a small cylinder is not applicable, yielding an underestimation of icing (Paper 6)

C5. In the case of large structures, collision efficiency of big droplets with a diameter of 1 mm is less than 1. This also means that the spray flux measured on vessels is affected by the geometry of a superstructure, i.e., the measured spray flux to a certain structure cannot be directly applied to another structure for modelling icing (Paper 3)

C6. Existing CFD techniques and turbulence models are unreliable for modelling the interaction of droplets inside of a dense spray cloud (Paper 2)

C7. RANS turbulence models should be used with care in icing simulations. Collision efficiency before separation is well predicted by any RANS turbulence model; however, the wake and separation of the flow is modelled poorly (Paper 5).

C8. Increase of the humidity inside the spray cloud is a minor effect (Paper 1)

C9. This study developed and validated a new model of ice growth caused by periodic sea spray, which accounts for the heat conduction inside the accreted ice (Paper 7).

1.5. Thesis structure

The physics of the icing process is described briefly in Chapter 2. Sections 3.1 and 3.2 present field experiments and numerical models, respectively. A brief summary of the research is given in Chapter 4, which is followed by conclusions and recommendation for future research. The detailed description of the research and results are compiled in main papers in Appendix A. Abstracts of the secondary papers are given in Appendix B. In addition, some useful and unpublished material is collected in this thesis: comparison of spray flux functions used by ICEMOD and RIGICE (Appendix F), a summary of the experimental setups of previous icing experiments (Appendix C), a detailed description of the experimental setup on Spitsbergen (Appendix D), and a complete list of ice accretion measurements performed on Spitsbergen (Appendix E).

2. Overview of Marine Icing Physics

2.1. Marine icing examples

Marine icing is an accumulation of ice on an offshore structure or vessel. To illustrate the icing process, some examples are given below. Figure 2 shows the ice accretion on K/V Nordkapp formed during a storm at an air temperature of -15°C. The ice clogged the windows on the bridge and blocked access to equipment installed on the deck and disarmed the battleship by covering a gun. In addition, the icing made the use of rescue boats impossible in the case of any accident, which would require the crew to abandon the vessel (Figure 3). The icing of the K/V Nordkapp is an example of a severe accident; however, the icing of railings and minor icing of the equipment is more common and always occurs when the air temperature drops below the freezing temperature of seawater (Figure 4). Some other examples of icing events are given by Ryerson (2011).

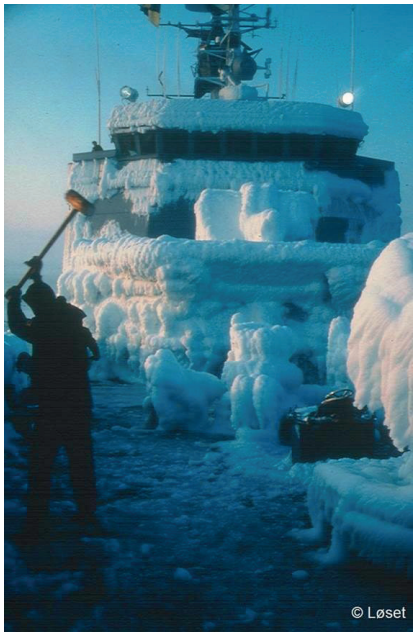

Figure 2. Icing on the K/V Nordkapp on the 27th of February 1987. More than 110 tons of ice accreted in 17 hrs in storm conditions at an air temperature of -15°C. Ice on the bridge window was already removed. Photo by Prof. Sveinung Løset.

Figure 3. Icing on the starboard side (left) and on the rescue boats (right) of the K/V Nordkapp on the 27th of February 1987. Photos by Prof. Sveinung Løset.

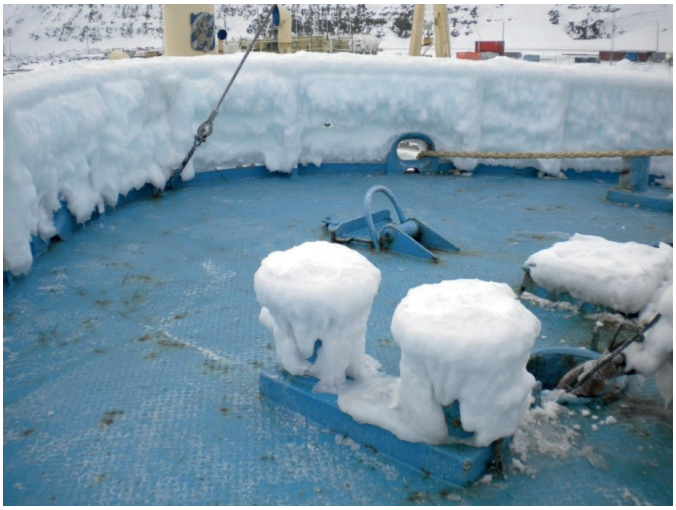

Figure 4. Ice accretion on the bow of the R/V Lance in May 2009. Photo by Prof. Sveinung Løset.

2.2. Overview of processes

The main processes and stages that water passes through before freezing on a structure surface are shown in Figure 5. The wave interaction with the structure breaks the wave and creates bursts of water droplets moving upwards. The water droplets are further carried by wind until they hit the structure. After the impingement, the water freezes due to the cooling caused by the air flow passing the structure.

The airflow plays an important role in the process: it brings droplets to the structure surface, cools droplets during the flight, and cools the water film on the structure surface. The airflow is affected by the structure motion, the wave surface, and the momentum of the water droplets. Even a flat sea surface creates turbulence by means of surface friction. The effect is stronger during a storm; high waves continuously change the geometry in which the air moves. The air flow is affected up to several tens of meters above the mean sea level by waves.

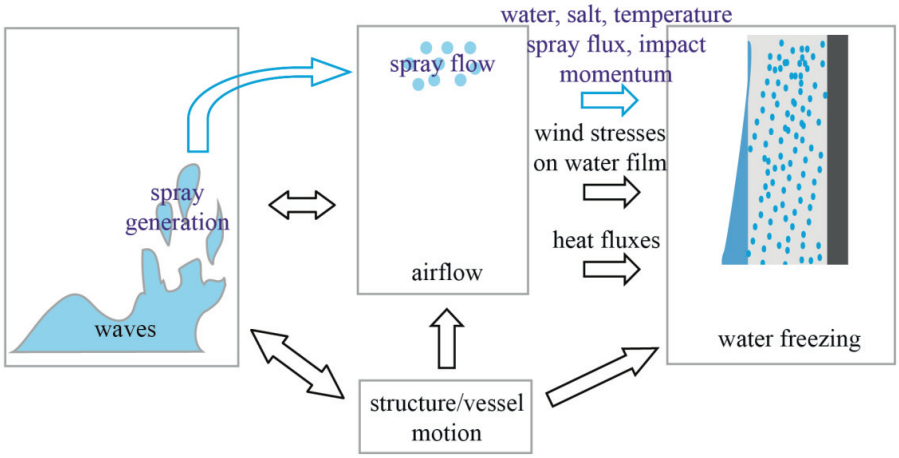

Figure 5. Overview of icing processes. Arrows show connection between different processes.

In the final stage before freezing, the rate of ice accretion is defined by the spray flux and heat transfer at the structure surface (Lozowski et al., 2000). The following sections describe the details and challenges related to modelling each of the processes shown in Figure 5.

2.3. Spray generation

Investigation of the spray generation (Figure 6) is beyond the scope of this PhD study; however, a small overview is given here as an introduction to the problem.

Sea spray is caused by wave interactions with the structure wall. The wave energy is dissipated by moving water upwards and separating water into small droplets. In addition, some spray is created by wind ripping seawater from the crests of waves, as described by Jones and Andreas (2012).

The wave-structure interaction causes violent eruptions of the water film that are not well described by existing theories. The linear wave theory and potential flow, which were applied to predict spray generation in RIGICE_N (Lozowski et al., 2000) do not describe the behaviour of real waves. Linear wave theory requires that the ratio of the wave height to the wave length be significantly small, resulting in the assumption of a fixed position of the free surface (Sarpkaya and Isaacson, 1981). This assumption contradicts the main interest which is to describe the wave height increase and breaking of the wave close to the structure.

Numerical modelling of the wave breaking is an area of active research and widely used in coastal research and ship hydrodynamics. Extensive experimental data and modelling results are available in the literature (Fairall et al., 2009; Marrone et al., 2011; Muzik and Kirby, 1992; Taylor and Wu, 1997; Waniewski Sur and Chevalier, 2006; Waniewski et al., 2000). The main focus of those models is the wave load on the structure. One of the main challenges of the models is the simulation of air entrapment into the waves and the interaction between the air and water, requiring a high mesh resolution. To describe the created spray and droplet-diameter distribution, more detailed physics of the water film disruption is required. This physics is described and modelled in problems of spray atomisation (Basha and Raja, 2009; Chigier and Farago, 1992; Faeth et al., 1995). However, knowledge from the coastal and atomisation studies has not yet been applied to solve icing problems; this should be done in the future.

Instead of physical modelling of the spray source, most models of marine icing use empirical equations of spray flux for vessels (Horjen, 1990; Zakrzewski, 1986) and offshore structures (Brørs et al., 2009; Forest et al., 2005; Jones and Andreas, 2012). These empirical equations describe the resulting spray flux on the structures after generation, which was empirically measured. The number of measurements is limited,

and the measurements were made on particular structures and in particular conditions. Therefore, it is impossible to make any preferable choice among the existing equations.

The equation of Zakrzewski (1986), which is based on the measurements done on fishing vessels and its application with CFD, is described in detail in Paper 3. Horjen and Vefsnmo (1985) made another empirical equation based on the measurements done on the multicolumn structure called Treasure Scout. This equation was used to simulate the icing on a similar offshore rig called West Hercules in Paper 6. The same equation was used by Brørs et al. (2009) to estimate the icing on the 90-m-diameter structure, and the calculations were repeated using MARICE with the same spray generation function to compare the models in Paper 6. However, wave interactions with such a large structure are different and can be considered similar to wave interactions with a vertical wall.

Figure 6. Spray generation by the R/V Lance in a relatively calm sea. Photo by Renat Yulmetov.

The spray generation function used in RIGICE04 (Forest et al., 2005) should be more suitable to predict the icing on the 90-m-diameter structure. The equation used in RIGICE04 is based on measurements performed on an artificial island (Forest et al., 2005) that is bigger than the columns of the semi-submersible; however, the island does

not move in response to waves, which contrasts to the structure considered by Brørs et al. (2009). The application of the function used in RIGICE04 was left out of the scope of this study. The equations of Horjen and Vefsnmo (1985) and Forest et al. (2005) are compared in Appendix F; however, both equations make several assumptions about droplet aerodynamics and spray period which may make them inaccurate. Those existing empirical equations were used due to lack of better options.

2.4. Wave washing

Spray generation is closely related to the water run-up on the walls of a structure. Ice does not accrete in places where it is destroyed or melted by an excessive amount of seawater. The maximal height without ice is defined by the maximal wave run-up defined by the sea state and structure geometry. In the case of a multicolumn structure, the process is also complicated by the wave diffraction on the columns. In ICEMOD (Brørs et al., 2009), a simplified approach was used that assumed that a wave does not run-up on the structure, and ice does not accrete below the wave height. RIGICE04 used data from laboratory experiments (Mitten, 1994) and linear wave theory (Sarpkaya and Isaacson, 1981) for a circular cylinder, which predicts the maximal wave run-up relative to mean sea level, R_M, on the cylinder front as follows:

$$R_M = \begin{cases} 0.5H_s\left(2.0589 + 2.3292k_R a - 1.3194\left(k_R a\right)^2\right) - 0.5H_s, \text{ for } k_R a < 0.9 \\ H_s, \text{ for } k_R a \geq 0.9 \end{cases} \quad (1)$$

where H_s is the significant wave height, k_R is the wave number and a is the representative diameter of the structure or one of the columns of a multicolumn structure at the water line.

As was mentioned before, the linear wave theory is not applicable to wave generation; however, it is the best available estimation, and Eq. (1) was used in the current work to predict wave run-up.

2.5. Spray flow

The spray flux on the structure wall is defined by the spray flow in the air and by the number of droplets interacting with the structure. A common way to describe the portion of droplets interacting with the structure is the collision efficiency. According to Stallabrass (1980), the water flux is described as:

$$M_c = E_c U_c w A_c \quad (2)$$

where U_c is the free stream airflow velocity relative to the obstacle, w is the liquid water content (LWC), i.e., the total mass of water droplets per unit volume of air, E_c is

the collision efficiency, and A_c is the area of the structure projection onto a plane perpendicular to the free stream airflow velocity. The collision efficiency represents the ratio of droplets that interact with the object compared with the total concentration in the undisturbed air. The common way to obtain E_c or M_c is to numerically calculate droplets trajectories in the airflow (Finstad et al., 1988a; Lozowski et al., 2000). The theory presented here assumes that the spray after generation is a collection of droplets that can be considered as mass points moving in the air.

2.5.1. Spray dynamics

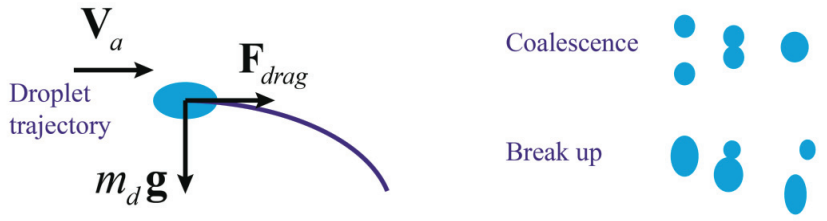

Figure 7. Overview of the processes and forces affecting droplet trajectory.

The droplet is moved in the air due to the air drag force and gravity (Lozowski et al., 2000) (Figure 7):

$$m_d \frac{d\mathbf{V}_d}{dt} = C_d \frac{\pi d^2}{4} \rho |\mathbf{V}_d - \mathbf{U}| (\mathbf{V}_d - \mathbf{U}) - \mathbf{g} m_d \qquad (3)$$

where m_d is the droplet mass, $\mathbf{V}_d$ and $\mathbf{U}$ are the droplet and air velocity vector, respectively, C_d is the droplet drag coefficient, d is the droplet diameter, ρ is the air density, and $\mathbf{g}$ is the gravity vector. C_d depends on the Reynolds number as described by the empirical formulas of the drag on a spherical particle (Lozowski et al., 2000; Morsi and Alexander, 1972). Yoon and Ettema (1993) estimated a possible effect from the non-sphericity of droplets. They tested ellipsoidal droplets with a ratio of their principal axes equal to 2. This resulted in a change in drag coefficient by 35%, whereas the resulting collision efficiency was changed by less than 1%. Thus, for the purpose of the calculation of collision efficiency and the spray flux on the surface, the effect of non-sphericity can be neglected.

In contrast with Eq. (3), the complete expression for the unsteady droplet drag force contains two additional terms: the added mass and historical term (Odar, 1966; Odar and Hamilton, 1964). The added mass is negligible because the air density is 1000 times

less than the water density. The historic term is high in the case of high droplet accelerations (Finstad et al., 1988a). The droplet acceleration usually becomes high close to the structure surface where the air changes direction and flows around the structure. If the droplets are small compared to the structure size, they follow the air streamlines and are exposed to high accelerations. In many icing problems, the historical term can be neglected. It only becomes important when less than 5-10% of the droplets in the cloud interact with the structure (Finstad et al., 1988a; Makkonen and Oleskiw, 1997). Introduction of the historical term increases the number of droplets interacting with the structure. The results of Finstad et al. (1988a) and Makkonen and Oleskiw (1997) are based on the potential theory, which neglects the air viscosity and the boundary layer close to the structure. In the boundary layer, significant flow deceleration occurs and it may have an additional effect, however, it was left out of the thesis scope.

It is complicated to separate the spray generation process and the spray flow and to define when the water can be considered as separate droplets. When the spray is dense, a collection of droplets can affect the airflow around them, and thus, will not fly in the free stream air, but in air-water mixture. In addition, droplets interact with each other and it can lead to an increase in droplet diameter (Kollár et al., 2005). A big droplet created from two smaller ones will have a different trajectory and, therefore, will change the spray flux on the surface.

Droplets interactions leading to coalescence can be modelled according to a probabilistic theory developed by O'Rourke (1981). The outcome of droplet coalescence is also reviewed by Orme (1997). Kollár and Farzaneh (2007) extended the theory of O'Rourke (1981) to include different results of the interaction product and compared modelled spray properties with the spray properties measured in an icing tunnel. The probability of droplet collisions depends on the relative velocity of the droplets and the airflow, and therefore, is enhanced by turbulence. Kollár and Farzaneh (2007) reviewed the effect of droplets on the airflow turbulence. However, the capability of models of the airflow turbulence was not covered and is discussed in Section 4.4.

The reverse process called droplet break-up occurs when the air shear stress elongates a droplet and causes it to break up into smaller ones. The break-up depends on the droplet size and velocity, viscosity of the fluid and the criteria for droplet stability (i.e., a Webber number < 13), which is given by Faeth et al. (1995). This criteria was applied to water droplets to show the maximal size of a stable droplet against the relative velocity of the droplet to the airflow (Figure 8). The air speed around a droplet can suddenly

change due to turbulence only; however, in offshore conditions, the level of turbulence intensity is not more than 12% for air speeds above 5 m/s (Türk and Emeis, 2010), and thus, cannot cause droplet break-up. The droplet falls in the air with a speed that depends on its mass, which can cause the droplet to break up if the droplet has a diameter greater than 5 mm (Figure 8). This result is in good agreement with the maximum diameter of 8 mm measured offshore on board of a vessel by Ryerson (1995). Also, droplet diameters in a spray are typically 1-2 mm; this indicates that the break-up process can be neglected in icing modelling.

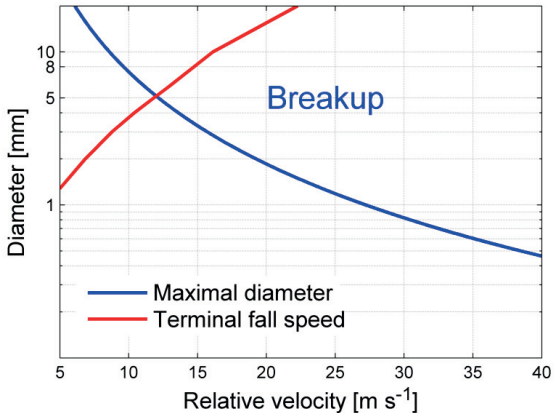

Figure 8. Droplet diameter against the relative velocity of the droplet in the airflow.

2.5.2. Spray impact

Spray impact can break accreted ice and reduce the total mass of ice accretion. This can be an important issue; however, it is not covered in the current work due to its complexity. The spray impact likely has less effect than processes considered in the thesis except in the region of the direct washing of the ice by sea waves.

2.5.3. Spray thermodynamics

During flight, the droplet temperature changes due to the convective, Q_{dc}, evaporative, Q_{de}, and radiant, Q_{dr}, heat fluxes (Horjen, 1990; Lozowski et al., 2000; Zarling, 1980):

$$m_d c_{pw} \frac{dT_d}{dt} = \pi d^2 \left(Q_{dc} + Q_{de} + Q_{dr} \right) \tag{4}$$

where c_{pw} is the specific heat capacity of the water, and T_d is the average droplet temperature. It is assumed that the main heat flux resistance happens at the surface of the droplet in the air. The temperature inside the droplet is assumed to be uniform due to water mixing inside the droplet and due to the high thermal conductivity of the water

compared with the air (Zarling, 1980). The heat transfer coefficient is described by the empirical formula of Ranz and Marshall (1952), which depends on the droplet's Reynolds number.

Evaporation decreases the mass of the droplet and can change the droplet's trajectory. However, the mass decrease due to evaporation is negligible for droplets with diameters larger than 200 μm (Andreas, 1990). For practical applications, mass decrease due to evaporation can be neglected for sea spray created by the wave-structure interaction (Lozowski et al., 2000). However, the heat flux created by evaporation is substantial and is comparable to the convective heat flux. In the case of small droplets, as in wind-generated sea spray, evaporation leads to a substantial increase of water salinity inside the droplets, which can be 8 times higher than the salinity of the seawater when the air relative humidity is 80% (Andreas, 1990).

In the case of a dense spray, it can be expected that the thermal energy released by the droplets will increase the air temperature inside the cloud. The rate of heat transfer therefore will decrease and will decrease the rate of the droplet temperature change. The same process is related to water vapour release and air humidity. Spray cloud evaporation and heat transfer inside the cloud were investigated for different spray concentrations and different droplet sizes; these results are presented in Section 4.1.

Radiant heat flux consists of long and short wave radiations. Long wave radiation is described by the Stefan-Boltzmann law and accounts for only a small portion of the total heat flux (Jones, 1996). Short wave radiation was neglected in all previous icing models (Horjen, 1990; Lozowski et al., 2000; Myers and Charpin, 2004). However, sunlight can reduce the rate of droplet temperature decrease during the day. The clouds reduce solar radiation by a maximum of 33% (Wang et al., 2007). The detailed description of the heat exchange of sea spray is widely available in the literature (Horjen, 1990; Lozowski et al., 2000; Makkonen, 1985).

Spray can supercool below the freezing temperature of water (Gao et al., 2000). However, it usually does not turn into ice before hitting the structure. Homogenous nucleation of droplet (i.e., instantaneous freezing of a whole droplet) happens for pure water at a temperature of approximately -35° C (Pruppacher, 1995; Zarling, 1980). The temperature of homogenous nucleation decreases with the droplet diameter (Pruppacher, 1995) and the salinity of the water (Koop, 2004; Koop et al., 2000). The seawater contains dust and plankton, which can create centres of crystallisation. These centres create conditions for heterogeneous nucleation, which happens at higher temperatures

than heterogeneous (Koop and Zobrist, 2009). Stallabrass and Hearty (1967) indicated that sea spray turns into ice particles at temperatures below -18°C which do not adhere to structures. Also, rain droplets freeze at a temperature of approximately -20° C (Zarling, 1980); the same can be expected for seawater that droplets do not tend to freeze during flight at temperatures exceeding -20°C. However, Gao et al. (2000) measured the freezing time of freely falling droplets of industrial waste-water with sizes of 2.8 and 4.3 mm to be near 20-30 sec and 5-10 sec at temperatures of -5.5 and -17.7°C, respectively. Waste-water contains nuclei, as does seawater, and can therefore be used as a good reference for seawater. In addition, for even more reliable results, the experiments by Gao et al. (2000) can be repeated with real seawater.

2.6. Airflow

As was shown before, airflow defines: (1) the droplet flow (i.e., the spray flux to the surface of the structure); (2) the shear stress on the water film; and (3) the heat transfer from the structure surface. According to Lozowski et al. (2000), (1) and (3) are the main factors defining the ice accretion rate. Therefore, accurate modelling of the airflow is crucial.

In numerical methods, the airflow, which is a description of the air velocity in space and time, $\mathbf{U}(\mathbf{x},t)$, is solved from the combination of continuity and momentum equations. The continuity equation is (Pope, 2000):

$$\frac{\partial \rho}{\partial t} + \nabla \cdot (\rho \mathbf{U}) = 0 \tag{5}$$

where ρ is the air density, $\nabla \cdot (\ )$ is the divergence operator, and $\mathbf{U}$ is the fluid velocity. When the air is incompressible and its density and viscosity are assumed constant, the momentum equation yields the following form of the Navier-Stokes equations (Pope, 2000):

$$\frac{\partial \mathbf{U}}{\partial t} + (\mathbf{U} \cdot \nabla)\mathbf{U} = -\frac{1}{\rho}\nabla P + \nu \nabla^2 \mathbf{U} \tag{6}$$

where P is the pressure, and ν is the kinematic viscosity. The direct approach to solve the Navier-Stokes equations (Eq. (6)) for turbulent flows is called direct numerical simulation (DNS), which resolves the airflow down to micrometres where the viscosity becomes dominant (Kolmogorov scale, time scale $\sim Re^{-0.5}$ and length scale $\sim Re^{-0.75}$ of the largest scales of the flow, Pope (2000)). Thus, DNS is intractable for the high-Reynolds-number flows of practical interest (Pope, 2000).

The practical approaches solve Eq. (6) in combination with additional algebraic or partial differential equations used to model turbulence. The key word is "to model", meaning that certain processes are modelled based on empirical knowledge to obtain, for example, the correct values of the mean airflow. Among those approaches, the two most common are the large eddy simulation (LES) and the Reynolds-averaged Navier-Stokes (RANS) modelling. In LES, equations are solved for a "filtered" velocity field, which represents the larger-scale turbulent motions, and the influence of the smaller-scale motions is modelled. RANS determines the mean velocity field $\bar{\mathbf{U}}$. In general, both LES and RANS types of modelling are incomplete compared with DNS, because they require a certain semi-empirical knowledge of the flow–dependent specifications. Thus, each model and its parameters are applicable only for the flow and purpose for which it was designed. Even a simple flow around a circular cylinder is a challenge for the RANS and LES models (Benim et al., 2008; Ong et al., 2009). In detail, RANS models decompose the velocity component in the i-direction, U_i, into the mean, $\bar{U}_i$, and the fluctuating, u_i, parts:

$$U_i = \bar{U}_i + u_i \tag{7}$$

The same is done for pressure and energy. Thus, Eq. (6) is rewritten in the form:

$$\frac{\partial \bar{U}_i}{\partial t} + \bar{\mathbf{U}} \cdot \nabla \bar{U}_i = -\frac{1}{\rho}\frac{\partial \bar{P}}{\partial x_i} + \nu \nabla^2 \bar{U}_i - \frac{\partial}{\partial x_i}\left(\overline{u_j u_i}\right) \tag{8}$$

The last term in Eq. (8) is the Reynolds stresses, which represent the energy dissipation in the turbulent eddies and are obtained from a turbulent or turbulent-viscosity model. The turbulent viscosity can be obtained from an algebraic relation, such as in the mixing-length model, or from turbulence quantities, such as the turbulent kinetic energy, k, and the turbulent dissipation, ε, for which the transport equations are solved (Pope, 2000). An example of such equations is the widely used k-ε model:

$$\frac{\partial k}{\partial t} + \bar{\mathbf{U}} \cdot \nabla k = \nabla \cdot \left(\frac{\nu_T}{\sigma_k} \nabla k \right) + \Pi - \varepsilon \tag{9}$$

$$\frac{\partial \varepsilon}{\partial t} + \bar{\mathbf{U}} \cdot \nabla \varepsilon = \nabla \cdot \left(\frac{\nu_T}{\sigma_\varepsilon} \nabla \varepsilon \right) + C_{\varepsilon 1} \frac{\Pi \varepsilon}{k} - C_{\varepsilon 2} \frac{\varepsilon^2}{k} \tag{10}$$

where $\nu_T = C_\mu k^2 \varepsilon^{-1}$ is the turbulent viscosity, Π is the turbulence kinetic energy production, and C_μ, $C_{\varepsilon 1}$, $C_{\varepsilon 2}$, σ_k, and σ_e are constants obtained to match a given experiment.

The complete relation between Eqs. (8), (9), and (10) is not shown for brevity. An example of the k-ε model shows the basic principle behind RANS models, which try to

mimic experimental results without capturing details of the physical processes. The model uses a substantial number of constants obtained empirically for certain flows, and those constants are not universal. This is also true for modern models, for example, the k-ω SST model (Menter, 1994) and the Transitional SST model (Menter et al., 2006).

The models described above were mainly designed for turbo-machinery, aerodynamics and hydrodynamics. As a result, turbulent fluctuations and dissipation were used as a parameter to fit experimental data of the drag and lift forces on objects, and the correct turbulent fluctuations of velocities were not required. However, turbulent fluctuations affect droplet flow and their interactions (Kollár and Farzaneh, 2007). Lad et al. (2010), Yoon et al. (2006), and Kollár and Farzaneh (2007) erroneously used a RANS k-ε model to simulate droplet flow, which was not designed for this purpose. Thus, analysis of the turbulent models for droplet flow simulations was performed in Paper 5 to find the most suitable model.

The modelling of the heat transfer from the structure surface by CFD is done in a similar manner by adding additional terms into the energy equation that also includes a number of empirical coefficients. Thus, CFD modelling should be validated against real measurements. However, the measurements of heat transfer on a large scale are not common. It should also be considered that the heat transfer coefficient is independent of the temperature in the case of forced convection (Kays et al., 2005) but varies with the wind speed and structure geometry. Thus, validation data need to be collected at different wind speeds while temperatures are not important and can be different from those typical for icing.

2.7. Freezing of saline water film

Many scientists studied icing caused by continuous supercooled sea and fresh water spray (Blackmore et al., 2002; Makkonen, 1987; Makkonen, 2010). The sea spray, which arrived at the surface of the accreted ice, freezes due to four main heat fluxes at the air-water interface (Figure 9): convection, Q_c; evaporation, Q_e; heat capacity of the impinging spray, Q_d; and radiant heat flux, Q_r. The aerodynamic heating and kinematic energy of droplets are typically neglected (Lozowski et al., 2000).

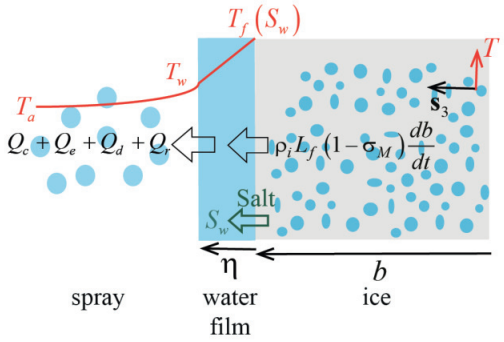

Figure 9. Ice growth due to supercooled water and cooling from air.

According to previous research, the ice thickness, b, increases due the absorption of the heat flux released from freezing by the air and spray. The conduction is the main heat transfer mechanism in the water film, and the temperature gradient is linear when the water film thickness, η, is less than 3 mm (Myers and Charpin, 2004). The heat balance at the ice/water interface is:

$$\rho_i L_f (1-\sigma_M) \frac{db}{dt} = -k_w \frac{T_w - T_f(S_w)}{\eta} = Q_c + Q_e + Q_d + Q_r \tag{11}$$

where ρ_i is the density of the accreted ice, L_f is the latent heat of fusion of pure ice, $L_f(1-\sigma_M)$ is the latent heat of fusion of the saline ice accretion (Makkonen, 1987), k_w is the thermal conductivity of water, η is the water film thickness, T_w is the temperature at the water surface, and T_f is the freezing temperature, which is a function of the water film salinity, S_w. When the water film is colder than the freezing temperature (Figure 9 and Eq. (11)), the ice entraps liquid water between its dendrites. The ratio of entrapped liquid water mass to the mass of ice accretion is σ_M = 0.3 (Makkonen, 2010). The salinity of the water film changes over time, increasing between spray events and decreasing when the new spray comes. This causes a change of the freezing temperature. The freezing model, Eq. (11), is used in MARICE, and a similar model is used in RIGICE04 and ICEMOD. All of these freezing models assume that the accreted ice is thermally non-conductive. However, this is not true, mainly because the saline ice does not have a distinct melting temperature. The enthalpy of saline ice changes with temperature smoothly in contrast to the step change of the fresh water ice at 0°C.

Let's analyse the ice growth caused by periodic sea spray. Imaging that a spray first arrives in a discrete event on a non-conductive ice surface and begins to freeze because

of heat fluxes from the air (1) (Figure 10). When the spray ends (2), as described above, the salinity of the water film, S_w, will rise above the initial value of the spray salinity, S_{sp}. For freezing to continue, the temperature of the film must decrease. This is accomplished by air cooling (i.e., part of the cooling is spent to decrease the internal energy of the water film).

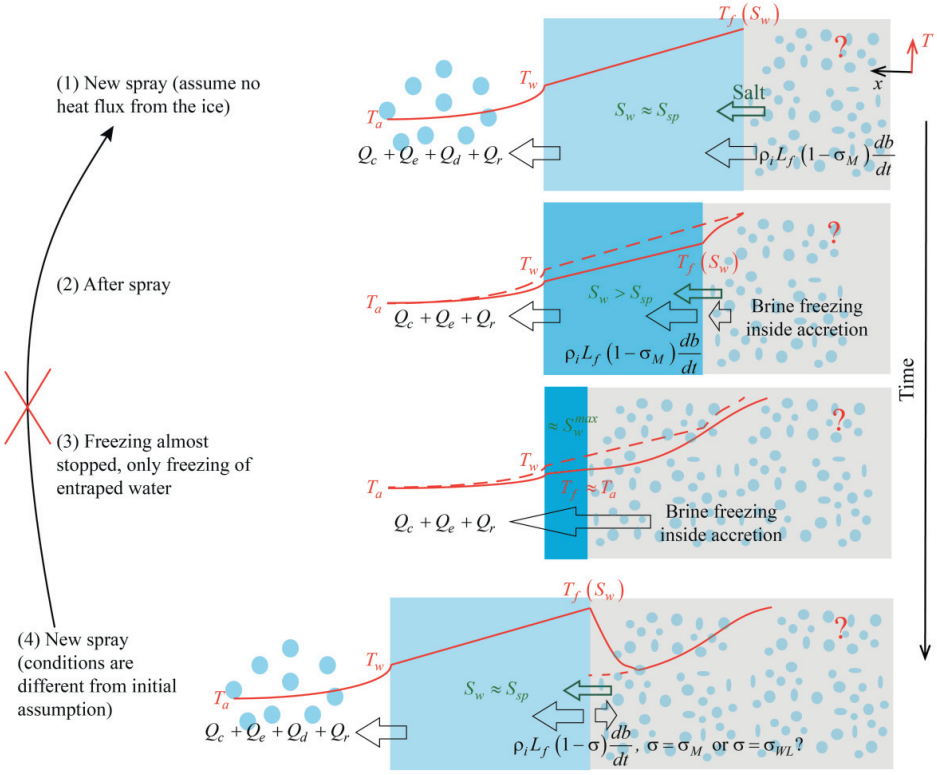

Figure 10. Scheme of the ice growth caused by periodic sea spray. The black arrows represent the directions of the heat fluxes. The solid red line represents the temperature profile in the water and ice accretion. The dashed red line represents the temperature profile in the previous step.

Once the water film has become colder than it was during step (1), freezing continues; however, the temperature of the ice created during step (2) is lower than the temperature of the ice produced during step (1). This difference creates a temperature gradient in the formed ice. Therefore, air cooling must both create new ice and cool the ice accreted during the previous step. This process continues until step (3) when the freezing

temperature of the water film approaches the air temperature; then, the heat flux from the air is mainly used to freeze the saline, liquid water, called brine, inside the accreted ice; the heat flux from air is not used to form new ice.

When a new spray event happens in step (4), the temperature of the ice accretion is lower than the freezing temperature of the spray. "New" ice will form not only because of the heat released to the air but primarily because of the heat absorption by the "old" ice accretion. This situation contradicts the initial assumption that the accreted ice is thermally non-conductive. Thus, one of the research goals of this study was to develop a new model of icing that accounts for the heat conduction inside the ice; this model is described in Section 4.6 and Paper 7.

2.8. Water film motion

On the surface of the ice, the water film is moved by gravity and tensile stresses from the air and it should be modelled to achieve the correct spatial distribution of accreted ice on the surface. The conservation of mass per unit area on the ice surface can be written as follows:

$$\rho_w \frac{\partial \eta}{\partial t} + \rho_w \nabla_s \cdot (\mathbf{Q}\eta) = -\rho_i \frac{db}{dt} + F_{sp} \tag{12}$$

where ρ_w is the water density, ∇_s is the gradient along surface principal directions, and F_{sp} is the mass flux of the incoming spray. On the left hand side of Eq. (12), the two terms are the change in water film mass per unit area and the convective fluxes. In addition to its movement, the water film mass is reduced due to freezing, and is increased by the spray flux. These source terms are on the right hand side of Eq. (12).

The same conservation equation can be written for the salt mass:

$$\rho_w \frac{\partial (\eta S_w)}{\partial t} + \rho_w \nabla_s \cdot (\mathbf{Q}\eta S_w) = -\rho_i \frac{db}{dt}(\sigma S_w) + F_{sp} S_{sp} \tag{13}$$

Salt diffusion is neglected because the aspect ratio (i.e., ratio of the water film thickness to the characteristic length of the structure surface) is very small, thus, the variation of spray flux and ice growth along the ice surface is too small to cause strong salt concentration gradient.

The water is moved by gravity, $(\rho_w \mathbf{g}\cdot\mathbf{s}_1, \rho_w \mathbf{g}\cdot\mathbf{s}_2)$; the hydrostatic pressure of the water column, $\eta \mathbf{g}\cdot\mathbf{s}_3$; the wind stress applied to the free surface of the film, $\boldsymbol{\tau}_a$; the static air pressure P_a; and the momentum of the spray impact (Figure 11). To describe the water

film, the lubrication theory for a thin water film's motion was used (Horjen, 1990; Horjen, 2013; Myers, 1998; Myers and Charpin, 2004). This theory is reasonable for a spray flux of 0.08 – 0.16 mm min^{-1} measured on the deck level of the Ocean Bounty rig, which was 10 - 15 m above mean sea level, according to (Forest et al. (2005)). It is also reasonable for a maximal spray flux of 0.4 mm min^{-1} measured on the Treasure Scout rig at 1-2 m above the maximal wave run-up at 20-25 m s^{-1} wind (Jørgensen, 1985). The lubrication theory yields the following solution for the water film velocity:

$$\mathbf{Q} = \begin{bmatrix} -\frac{\eta^2}{3\nu_w}\left(\mathbf{g}\cdot\mathbf{s}_1 + \left(\frac{\partial\eta}{\partial s_1} + \frac{1}{\rho_w}\frac{\partial P_a}{\partial s_1}\right)\mathbf{g}\cdot\mathbf{s}_3\right) + \frac{\eta}{2\nu_w}\frac{\boldsymbol{\tau}_a\cdot\mathbf{s}_1}{\rho_w} \\ -\frac{\eta^2}{3\nu_w}\left(\mathbf{g}\cdot\mathbf{s}_2 + \left(\frac{\partial\eta}{\partial s_2} + \frac{1}{\rho_w}\frac{\partial P_a}{\partial s_2}\right)\mathbf{g}\cdot\mathbf{s}_3\right) + \frac{\eta}{2\nu_w}\frac{\boldsymbol{\tau}_a\cdot\mathbf{s}_2}{\rho_w} \end{bmatrix} \tag{14}$$

Eq. (14) lacks the contribution of the spray momentum; however, the large droplets destroy the film flow and may even cause erosion of the accreted ice, as was observed during the experiments on Spitsbergen. This all leads to inapplicability of the lubrication theory. At this stage, this process was not included into the model.

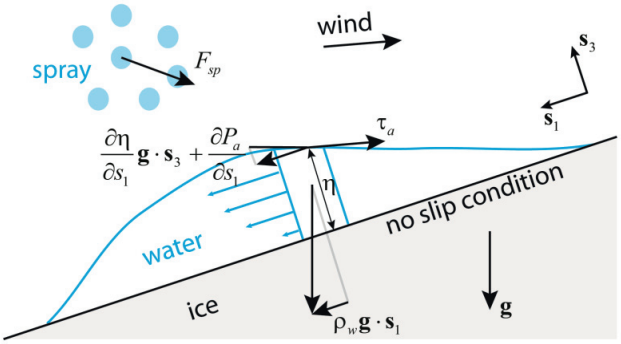

Figure 11. Illustration of the forces acting on the water film on the inclined plane.

A better way to model the green water and higher spray fluxes for the case of vessels may be the approach by Blackmore and Lozowski (1998), which models both the laminar and turbulent flows of the film. The lubrication theory only roughly approximates the behaviour of green water, which in principle destroys the ice. The water freezing happens only when the water layers become as thin as required for the lubrication theory to be valid. In any way the models applied here and by Horjen (2013), and Blackmore and Lozowski (1998) are approximate. Eq. (14) neglects the roughness of the ice surface, the change of the ice geometry, and the air/water surface tension. The last two processes are described by the model of Myers and Charpin

(2004), which requires a few orders finer mesh. The details of the real processes are complex and computationally expensive. Fortunately, the ice accretion rate is mainly defined by the spray flux and the heat transfer (Lozowski et al., 2000) and less by the movement of the water film, which can be resolved approximatelly in practical applications.

3. Methods

3.1. Field experimentation

Numerous icing experiments studied the icing caused by continuous sprays of fresh and saline water in indoor and outdoor wind tunnels. Icing caused by periodic salt water spray was studied only in Alberta (Lozowski and Zakrewski, 1992) and in Trondheim (Horjen and Vefsnmo, 1986). The differences in the conditions and setups are summarised in Appendix C.

To extend the knowledge of icing caused by periodic seawater spray, we performed experiments in the natural conditions of Spitsbergen. The goal was to measure the ice mass in real time to see how the ice accretion rate develops with time and what happens between sequential spray events. The first experiments were conducted in the harbour area of Longyearbyen from the end of February until the end of March in 2011. The equipment consisted of three main parts: a weather station, a spraying rig and icing objects (i.e., horizontal cylinders) (Figure 12). Seawater was pumped directly from the fjord and sprayed 5.2 m upwind from the cylinder in pulses with a duration of 2.5 s and periods of 33 s (see Paper 8, for details). The main finding of these experiments was a better understanding of the natural wind conditions, problems related to the freezing of the system, and requirements to improve the real-time mass measurements. The salinity and internal structure of the ice accreted during these studies were analysed in Paper 4. Another challenge was that a "stable" wind in nature has typically a turbulence intensity of 12-30% and has both long term and short term fluctuations directing the spray off the cylinder. In the long term (i.e., 1 - 4 hours), the wind direction changes ± 10° from the mean, but it varies within 2-3° in the short term (i.e., 15 min).

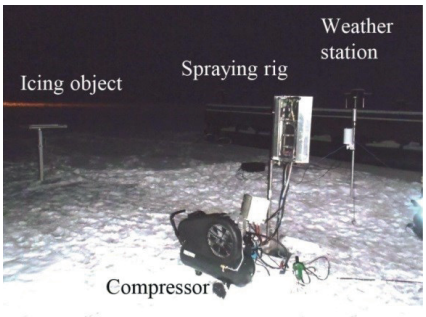

Figure 12. Experimental setup in the winter season of 2011.

Therefore, the setup for the later experiments was redesigned and rebuilt to enable the cylinder to follow the change of the wind direction (Figure 13 and Figure 14). A new location in the Adventdalen valley was chosen based on weather analysis. There, the wind is one directional (± 30°) for 74% of the time (Appendix D).

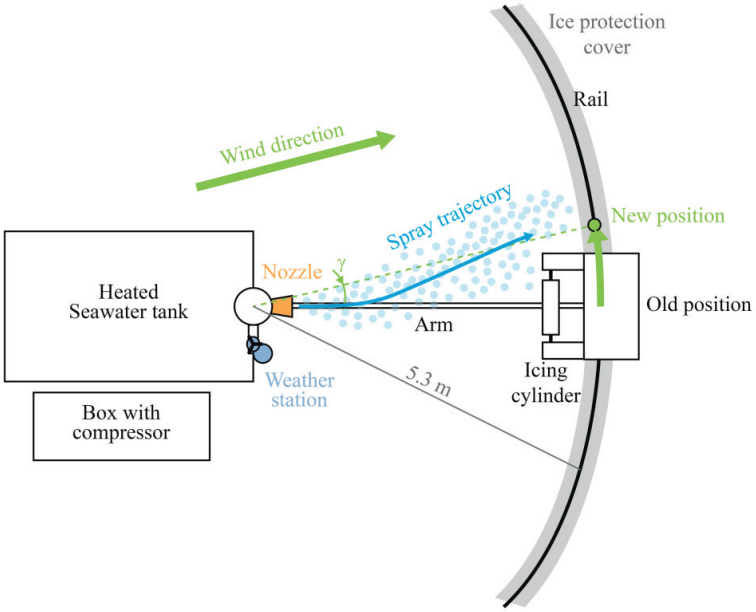

Figure 13. Scheme of the experimental setup and control of the position of the icing object (elevated view). The icing cylinder is moved along the rail to follow changing wind direction. The arm between the icing cylinder and nozzle turns the spray nozzle and the weather station, which measures wind direction relative to its position.

The mass measurements were also improved. The new equipment measured mass of the accreted ice up to 2 kg with a 20 Hz frequency and an accuracy of 0.7 g. Therefore, it was possible to observe the exact time of the spray arrival and how the mass changes while the water sheds off the cylinder. The duration of each test was 20-30 minutes, which allowed several tests with different spray periods and/or cylinders with different diameters to be run in similar wind conditions. In addition, photos, salinity and density of the final ice accretion were collected.

In 2012, ice accretion was measured on horizontally-oriented cylinders with diameters of 20, 40, and 100 mm. In experiments, the spray pulses with a flux of approximately

220 g $m^{-2}s^{-1}$ had a duration of 1.9 s. The time between spray pulses was 31.7 s in 31 tests and 49.8 s in 13 tests.

In 2013, 275 tests were conducted with spray periods of 22, 32, 49, 76, 79 and 149 s, and a duration of 1 s. The wind speed ranged from 1 m s^{-1} to 12 m s^{-1} and the air temperature ranged from -25°C to -4°C.

Many challenges were encountered, including measuring the size of big droplets, wind fluctuations, etc. Those challenges together with the detailed description of the experimental setup and results are presented in several reports (Kulyakhtin, 2013; Kulyakhtin et al., 2013a; Kulyakhtin et al., 2013b). In addition, the detailed description of the experimental setup is in Appendix D and the list of all performed experiments is in Appendix E.

The most important outcome of these experiments was that the observed ice growth provoked development and gave input for a new model of the ice growth caused by periodic sea spray that is described in Section 4.6 and the development and validation are in Paper 7.

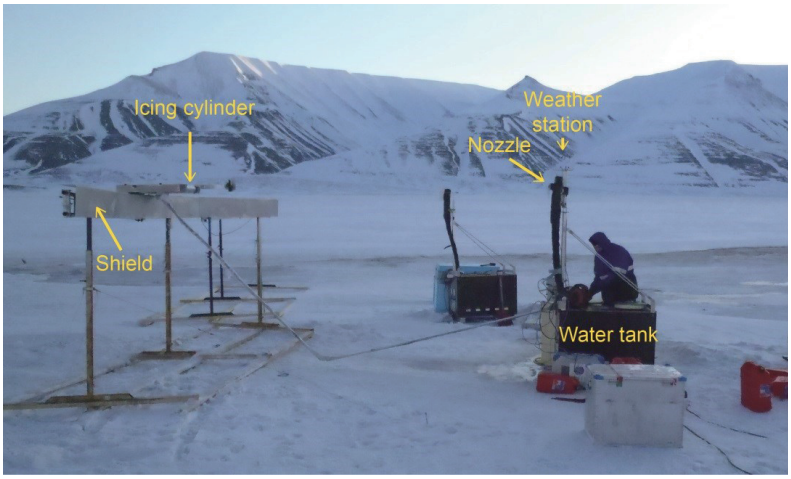

Figure 14. Experimental setup in the winter-spring seasons of 2012-2013

3.2. MARICE model

The main goal of this PhD study was to develop a numerical icing model that uses the advantages of modern computational fluid dynamics (CDF) solvers to predict the air

flow. The air flow controls the heat transfer from the structure surface and the spray flow and therefore plays a key role in the icing process.

The model input parameters are the structure geometry, meteorological and oceanographic data (Figure 15). The developed model called MARICE uses empirical relations to describe the spray generation as previous models do. However, MARICE uses a finite volume CFD solver FLUENT (ANSYS, 2009) to calculate the airflow, heat transfer from the structure and the droplet flow for a given spray generation function. The airflow modelling consists of choosing a turbulent model and mesh construction. The user can choose from several turbulence models that are available in FLUENT, including the Reynolds-averaged Navier-Stokes (RANS) model and the Large Eddy Simulation. Airflow is then calculated in the reference frame of the structure, and the sea surface is modelled as a flat frictionless wall. The structure motion and the effect of the sea waves on the airflow are neglected. The change of the structure geometry caused by the ice growth, which may affect the air flow, is also neglected.

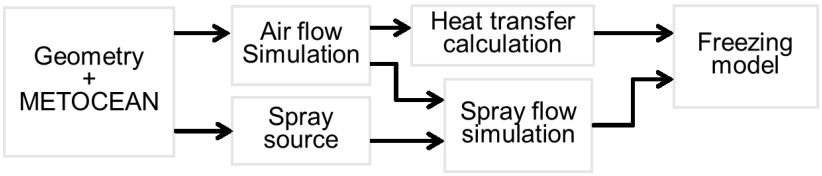

Figure 15. Structure of the MARICE icing model.

Once the airflow is obtained for certain wind conditions, the distribution of the heat transfer coefficient on the structure surface is calculated from the energy balance equation. The heat transfer and spray flux on the structure surface are used as an input for the freezing module, which was implemented using User Defined Functions in FLUENT (ANSYS, 2009). The freezing module was kept relatively simple and is a core, which can be extended in the future. The model solves the system of Eqs. (11), (12), (13) completed by an equation describing the change of the freezing temperature. Note that the heat capacity of the ice was not yet included, and Eq. (14) describes the water film velocity in which only the gravity forces are considered. The model details are described in Paper 6.

The main physical processes and their importance are given in Figure 16, which also shows processes that are already included in MARICE. The details of spray generation are not given because they were not included in the study; the available empirical relations (Forest et al., 2005; Horjen and Vefsnmo, 1985; Jones and Andreas, 2012)

were used. The thermodynamics of droplets were excluded because most of the spray generation relations describe the spray flux on the surface of the structure and the path of the droplets before interaction with the structure is unknown. The advantage of MARICE compared to previous icing models (e.g., ICEMOD and RIGICE04) is the application of CFD to calculate the turbulent airflow and the heat transfer around the complete geometry of the structure. In addition, the model of the water film dynamics and freezing was designed so that it is connected to the CFD solver and is applicable to any arbitrary surface. The air flow and water film motion can be modelled on any surfaces with any curvature or sharp corners. The spreading of the water film on the horizontal surface due to hydrostatic pressure is also included.

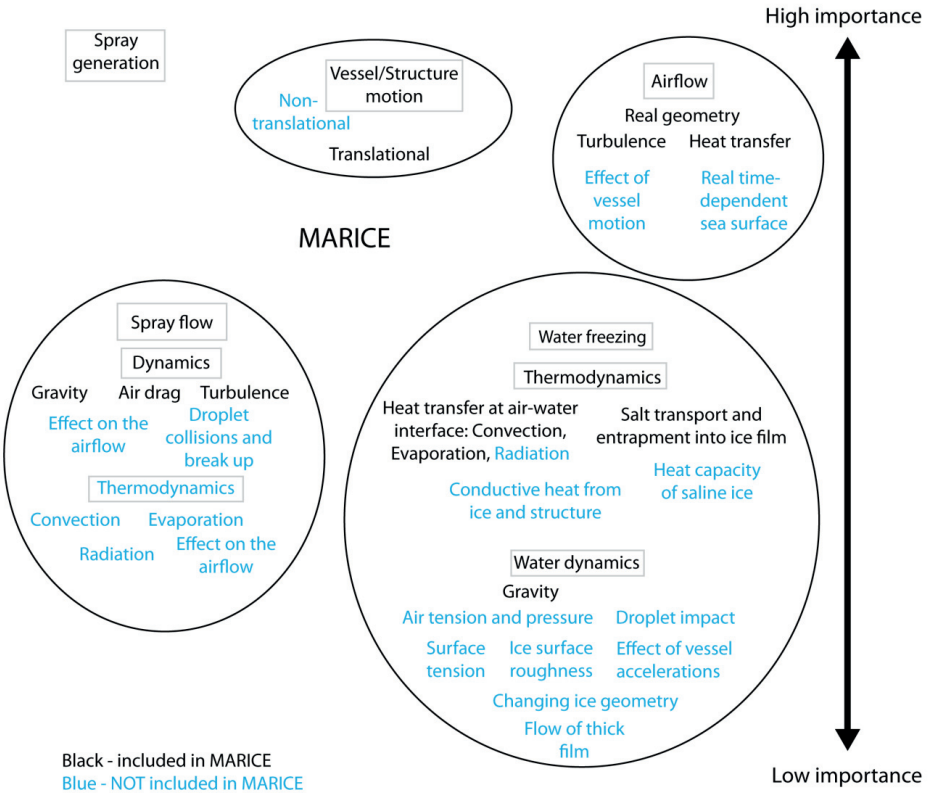

Figure 16. Outline of processes included and not included into MARICE. An attempt is made to sort processes by importance: the most important are on top and the least are shown lower.

4. Summary of Results and Discussions

In this chapter, results are presented in the order that they were obtained. It also briefly describes the insight gained during different parts of the study and thereby provides reasoning for the subsequent steps. Here, only summaries from the papers are given and details are in Appendix A.

4.1. Spray evaporation

The results presented here are published in Paper 1.

4.1.1. Background and goal

In many studies (e.g., Chung and Lozowski (1998) and Forest et al. (2005)) the relative air humidity is considered constant for the spray simulations. Inside the spray, the humidity can increase due to droplets evaporation and, as a result, decreases the rate of droplet temperature change. In the case of marine icing, the spray is dense with a liquid water content (LWC) up to several 100 g m^{-3} (Ryerson, 1995). Therefore, droplets contribution to the air humidity may be significant. The goal of this work was to investigate when the increase in air humidity must be considered for typical conditions of icing on a vessel.

4.1.2. Assumptions and Methods

Simulations were done in ANSYS FLUENT with an air velocity of 10 m s^{-1}. The effect of droplets on the air temperature and speed was neglected. The droplet diameter spectrum applied in the simulations followed the measurements of Ryerson (1995), and the initial spray temperature was set to -1°C. Several cases were considered in which the LWC was 1, 20 or 100 g m^{-3}, the air temperature was -5 or -15°C, and the initial relative humidity was 70, 80 and 90%.

4.1.3. Results

In the simulations, the air becomes saturated or nearly saturated (>90%) with water vapour in 1-3 s, even when the initial relative humidity was 70%. Therefore, it is better to assume from the beginning that droplets fly in air saturated with water vapour instead of using the humidity of the air outside the spray. The humidity increase in the cloud resulted in a droplet temperature change of less than 1°C for the wide range of the droplet diameters (i.e., from 83 μm to 920 μm), even when the LWC was 100 g m^{-3}. The

error in the droplet temperature of 1°C is only 1.3% of the energy necessary to freeze this droplet and can therefore be neglected.

4.2. Droplet interactions

The results presented here are published in Paper 2.

4.2.1. Background and goals

The ice accretion rate is proportional to the amount of spray that hits a cold surface. The spray trajectory and the amount and temperature of the droplets hitting the surface depend on the droplet-diameter distribution, which can change during the spray flow due to droplets coalescence. This effect is both important for the full-scale structures and for the small-scale experiments designed for the validation of icing models.

The number of droplets in the spray is too high to model each droplet and each interaction. One of the computationally efficient approaches to simulate droplets interactions is the O'Rourke's algorithm (O'Rourke, 1981), which is, however, mesh- and discretisation-dependent (Schmidt and Rutland, 2004). To find the correct mesh and discretisation requirements, the model results were validated against measurements done in the CIGELE icing wind tunnel of the University of Quebec at Chicoutimi in Canada (Kollár and Farzaneh, 2007).

4.2.2. Methods

Simulations were done in ANSYS FLUENT (ANSYS, 2009). The steady-state airflow in the wind tunnel was calculated using the RANS RNG k-ε model. The input parameters for the model included the tunnel geometry, the airspeed and the turbulence intensity measured at the inlet before the entrance of the test section. The droplets interactions were simulated using O'Rourke's algorithm. The droplets were injected at a distance of 0.4 m from the model with the properties measured by Kollar et al. (2006). The simulated LWC and DSD were compared with measurements by Kollár and Farzaneh (2007) in the test section 4.35 m from the nozzle.

4.2.3. Results

The requirements for the droplet simulations were obtained and were used in later droplet simulations (Papers 3, 5, and 6). These requirements included: the distance between the droplets parcels, the time step for the droplet flow simulations, the discretisation of the droplet-diameter spectrum, and certain aspects of the mesh requirements for the airflow.

Calculations showed that the spatial distribution of the LWC depend on air velocity non-uniformities, turbulence and spray pattern (i.e., the spatial distribution of the LWC inside spray cone) (Figure 17). The few percents of variation in the turbulence intensity resulted in a change in LWC by a factor of 5. The turbulence intensity calculated in the test section was dependent on the turbulence dissipation in the inlet.

The median volume diameter (MVD) measured in the test strongly depended on the spray pattern, because most of the interactions happened within 1 m from the nozzle. Both the dissipation and the spray pattern at a distance of 0.4 m from the nozzle were not measured and had to be assumed. Their variation gave a wide range of MVD and LWC in the test section. Certain combinations of the dissipation and pattern gave good agreement with measurements. However, the amount of collected data was not sufficient for the model validation.

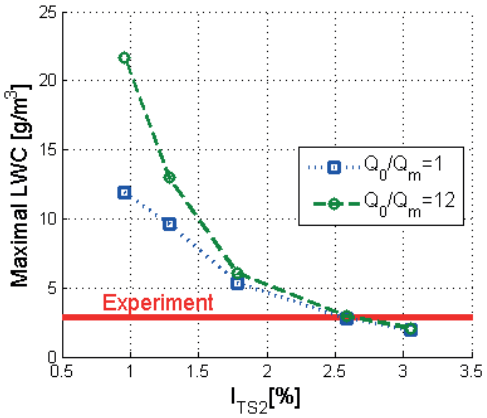

Figure 17. The effect of turbulence intensity in the test section on the LWC peak value. The spray pattern at a distance of 0.4 m from the nozzle, Q_0/Q_m is the ratio of the LWC in the centre of the cloud to the mean LWC of the cross-section.

Not only the turbulence intensity and airflow must be measured, but also the turbulence dissipation (i.e., the size of the turbulence eddies) and the spray pattern. The results also show that the experiments performed on Spitsbergen could not be used for the validation of the spray flow, because too many airflow and spray injection parameters would have needed to be measured and controlled properly.

The RANS k-ε model predicted the average airflow in the tunnel well; however, the turbulence predicted by the model was questionable, because the RANS models are

designed to model the average flow properties, while the turbulence model is used to complete the averaged Navier-Stokes equation. This insight was only gained during the simulations of the droplets interaction for this paper. Therefore, this result showed that before continuing to analyse droplet interactions, the air turbulence models for the modelling of the spray flow must be validated; this is presented in Section 4.4.

4.3. Spray flow around real structure

The results presented here are published in Paper 3.

4.3.1. Background and goals

The main objective was to demonstrate an improved prediction of the icing rates using accurate spray flow calculations in a "real airflow field", which can potentially be predicted using CFD. An additional objective was to determine the primary physical phenomena of the spray flow by testing different conditions, such as wind speed, droplet size and different droplets distributions. Another goal was to compare the CFD results to an approach by Lozowski et al. (2000), which assumes a uniform wind speed that is not disturbed by the structure. This approach assumes that airflow can be neglected for large droplets (i.e., 1-2 mm in diameter), and only the effect of gravity and the mean free stream speed are important.

It is computationally cheaper to simulate the droplet flow in the averaged airflow. This study investigates how strong the small fluctuations in the air velocity caused by turbulence affect the droplet flow. METOCEAN data do not contain information related to the free-stream turbulence of the airflow. However, the turbulence intensity in the real conditions is at a level of 10-20% (Türk and Emeis, 2010), and thus, its importance should be investigated.

4.3.2. Methods

The airflow was modelled for one particular vessel using a steady RNG k-ε turbulence model. The droplets flow was modelled using the discrete particle model (DPM). Simulations were done for illustrative purposes using a coarse mesh in ANSYS FLUENT. Droplets were injected 5 m ahead of the vessel bow, and the local collision efficiency of the droplets was calculated as the ratio of the average spray inflow rate per unit area on each surface to the initial mass flow rate per unit area of the spray cloud. Simulations included the following cases:

1. Comparison of the approaches: (a) by Lozowski; (b) CFD, which excluded the effect of airflow fluctuations on the spray; and (c) CFD, which included turbulent effects.

2. Comparison of the collision efficiency of droplets with diameters of 250, 500, 2000 and 5000 μm with vessels in a wind with a speed of 15 and 25 m s^{-1}.
3. Different droplet spectra were simulated to verify whether the MVD could be used instead of the droplet spectrum, as proposed by Finstad et al. (1988b).

4.3.3. Results

The major finding of this part of the thesis is that collision efficiency of even large droplets (0.25 – 2 mm) is less than 1. Thus, the approach by Lozowski et al. (2000) (Figure 18a) is incorrect, and the flux of spray measured on board vessels was affected by the vessel's superstructure, i.e., this spray flux cannot be directly extended to other vessels.

It was shown that turbulence plays an important role, a wind with a turbulent intensity of 15% lifts droplets in the air and brings them higher up and on the leeside of the structure, increasing spray flux (Figure 18c). Turbulent airflow predicts a spray flux to the port and starboard sides of the vessels, which was observed in reality (Figure 3), in contrast to approaches (a) and (b).

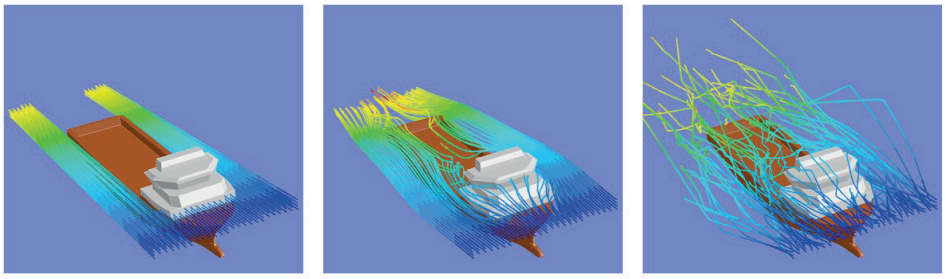

Figure 18. Effect of droplet flow modelling: (a) droplets in constant velocity field as by Lozowski et al. (2000); (b) turbulent air flow with non-stochastic droplet tracking; (c) turbulent air flow with stochastic droplet tracking.

These simulations also showed that that lower wind speeds cause higher collision efficiency. Thus, higher ice accretion can occur at lower wind speeds if spray generation is similar.

The droplet spectrum is also shown to be important. On the lower windward side of the structure, the effect of the droplet size distribution was minor (i.e., change of collision efficiency by less than 10% compared to simulations using MVD). It was significant (i.e., 25-100%) on the upper windward side and aft of the vessel because of the gravity

effect on the droplets with different mass. Also, small droplets (i.e., 250 and 500 μm) should not be neglected, because they are the primary reason for the spray flux at the aft, port and starboard sides of the vessel, where rescue boats are usually placed.

4.4. Choice of turbulence model for the simulations of spray flow

The results presented here are published in Paper 5.

4.4.1. Background and goals

The results presented in Sections 4.2 and 4.3 raised an important question: "How well do we mimic real airflows using CFD?" To answer this question we examined different turbulence models in Paper 5. As mentioned above, all existing turbulence models were designed for special purposes. Most of the models were created to predict an airflow separation point and drag coefficient. Therefore, we examined their ability to model droplet flow, their impingement to the cylinder and the flow of the droplets in the wake of the structure which is representative for the case of multicolumn semisubmersibles and complex superstructures. In addition, we investigated the possibility of droplet impingement on the cylinder sides and back which was observed in the results for a vessel (Section 4.3).

4.4.2. Method

For validation, we studied a particular case of droplets (diameters of 13, 17, 45 μm) impingement to a circular cylinder with a diameter of 10.24 m in 20 m s^{-1} wind speed, which corresponds to a Reynolds number of 1.6×10^4, chosen due to existence of experimental data. Three different RANS models were considered, namely, the renormalisation group (RNG) k–ε model with both the standard wall function and the enhanced wall treatment, the transition shear-stress transport (SST) model, and the Reynolds-stress model (RSM) with a stress-omega submodel. There are no published measurements of the droplet flow in the wake of the cylinders; thus, the RANS models were compared with a LES turbulent model.

4.4.3. Results

All turbulence models and the potential theory predicts similar airflows upstream the cylinder (Figure 19). Even though the separation point predicted by different models was in the range of 80-150° from the stagnation line, approximately 90% of the droplets interact with the cylinder before 50°. Thus, both total and local collision efficiency on the windward side of the cylinder is predicted with accuracy better than 10% by any of the models investigated.

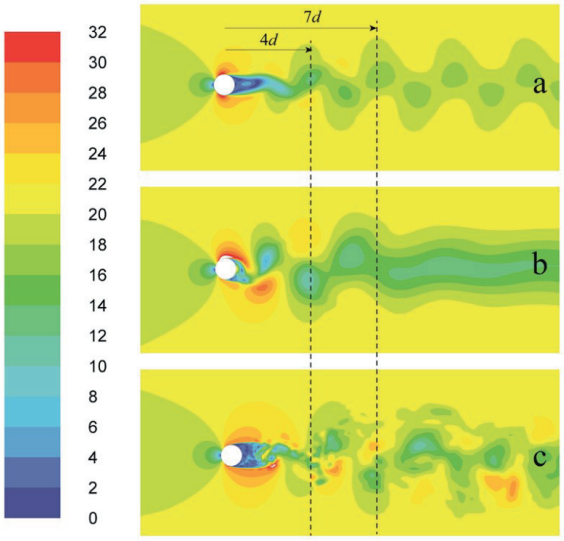

Figure 19. Instant velocity magnitude: (a) RNG k-ε with EWT; (b) RSM; (c) LES.

The angle at which flow separation occurs is always above 75° in the Reynolds number range from 1.0×10^4 to 5.0×10^6 with its lowest value near Re = 1.0×10^5, depending on the turbulence intensity and surface roughness (Achenbach, 1968; Zdravkovich, 1997). This means that potential theory can also be used for flow regimes other than those considered here. The only condition that could possibly affect the results is a transition from a laminar to a turbulent boundary layer. Therefore, it would be interesting to investigate the droplet interaction with a cylinder at higher Reynolds numbers for which the transition point is located at less than 50°.

It was shown that flow separation moves the non-interacting droplets even further away from the cylinder surface. Because the flow does not attach to the surface after separation, thus, droplets did not impinge on the sides or on the back of the cylinder. This also shows that vortexes shed from the cylinder cannot bring droplets to the back of the cylinder. The calculated ice accretion on the sides described in Kulyakhtin et al. (2012) may however be explained by the flow field around rectangular corners (see, for example, Okajima (1982), and Shimada and Ishihara (2012)), at which the flow separates at the leading edge and later reattaches. Another reason may be the interaction between the wake behind structural elements and the boundary layer along the walls; see, for example, He et al. (2013).

The investigated models predicted significantly different behaviours of the airflow and droplet flow in the wake of the cylinder (Figure 19). Both the RNG *k-ε* model with the standard wall function and potential theory predict a shadow-region free of droplets behind the cylinder along the flow direction for a distance greater than at least 16 diameters. The transition SST and RSM models predict large vortices, which droplets follow with only small deviations due to their inertia. These two models also predicted that the droplet-free region extends less than one diameter behind the cylinder (Figure 20).

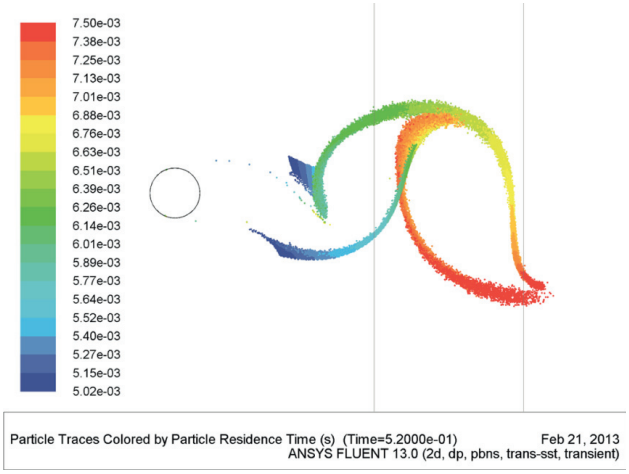

Figure 20. 17.1 µm droplet flow in the cylinder wake predicted by 2-D SST. The colour represents the time the droplet spent in the domain after injection. Surfaces at $4d$ and $7d$ distances behind the cylinder are marked by grey lines.

The LES simulations resulted in the most reasonable behaviour, such as a shadow region free of droplets that extends to a distance of approximately $7\,d$ for the given combination of cylinder and droplet diameters (Figure 21). Only the 2-D RNG *k-ε* model with the enhanced wall treatment is able to exhibit droplet distributions similar to the ones predicted by LES, even though 2-D RNG *k-ε* model and LES predicted different separation points, vortex shedding frequencies, and drag coefficients, i.e., none of the typical non-dimensional number used in hydrodynamics can be used to characterize the applicability of a certain model for the prediction of the droplet flow. Also, the agreement between of RNG *k-ε* model with the enhanced wall treatment and LES can be worse for the higher Reynolds numbers or different droplet sizes, and therefore, requires additional validation.

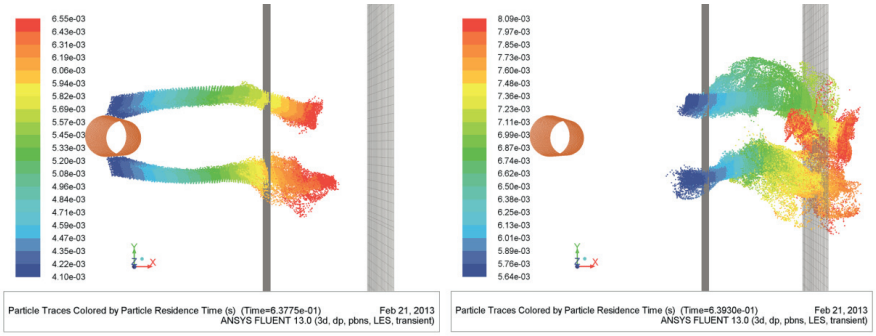

Figure 21. 17.1 μm droplet flow in the cylinder wake predicted by 3-D LES at two moments of time. The colour represents the time the droplet spent in the domain after injection. Surfaces at $4\,d$ and $7\,d$ distances behind the cylinder are marked by grey lines.

4.5. MARICE icing model

One of the main outcomes of this work is the MARICE icing model, which was described in Section 3.2 and in Paper 6. MARICE incorporates all the knowledge described in Chapter 2 and Chapter 4.

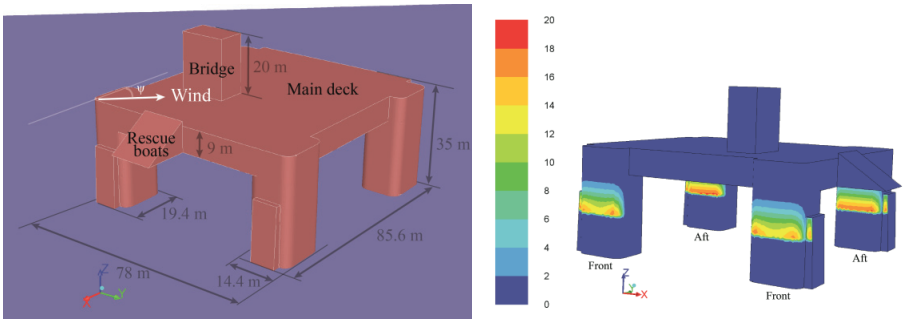

Figure 22. Geometry of the West Hercules drilling rig – (left); ice accretion rate [mm hr^{-1}] on West Hercules at T_a = -17°C, ψ = 90° and U_{10} = 33 m s^{-1} – (right).

MARICE predicts the spatial distribution of the ice accretion on an offshore structure with any complex geometry, and one example is shown in Figure 22, where the ice accretion is predicted on a semisubmersible. MARICE can be used for the design of a structure to either hide or protect rescue equipment or working areas from icing in the most efficient way. In addition, there is a need to have a tool to forecast regions with icing danger. Such a tool created by Overland et al. (1986) exists for small fishing vessels and is widely used due to the lack of an alternative model even though

Makkonen et al. (1991) found significant errors in it. The definition of a dangerous ice load depends on the vessel size. MARICE can, for example, be used to calculate icing on the vessel archetypes, and the results can be stored in a database. The data can be further used together with a weather forecast to warn each particular vessel, depending on its characteristics.

The application of MARICE and its comparison to other sea spray icing models gave the following additional knowledge:

- Both RIGICE04 and ICEMOD underestimate the heat transfer coefficient on the structure surface in airflows with Reynolds numbers greater than 10^7. These models based their empirical equations for the heat transfer on the small-scale experiments which cannot be extended to the full-scale structures. MARICE applies CFD and its predictions agree well with existing measurements of the heat transfer from buildings.
- Wind-generated spray is unlikely to create a significant contribution to icing. The portion of spray that settles on structures as big as a drilling rig is negligible compared to the spray concentration in the air due to the low inertia of small droplets (diameter less than 100 μm), which easily follow the airstreams around the structure. Additionally, the salinity of the wind-generated spray is high, and therefore, wind-generated spray has a significantly lower freezing temperature than seawater.
- The choice of spray flux functions is essential for icing predictions. However, the function used in ICEMOD predicts 10 – 1000 times less spray flux than the function used in RIGICE04. Thus, study of the spray fluxes should be the main priority for further icing research.
- Furthermore, the effect of heat conduction from the structure surface to the water/ice interface and the heat capacity of the ice and water should be included in models of icing caused by periodic sea spray.

4.6. A new model of periodic sea spray icing

The results presented here are from Paper 7.

The last question in the previous section (Paper 6) and observations during the experiments on Spitsbergen (Paper 4, Kulyakhtin et al. (2013a), and Kulyakhtin (2013)) motivated the development of a new icing model that would account for the heat conduction inside of accreted ice.

The developed model states that ice growth is caused by heat flux to the air, $\frac{db_M}{dt}$, and to the ice accretion, $\frac{db_{WL}}{dt}$:

$$\frac{db}{dt} = \frac{db_{WL}}{dt} + \frac{db_M}{dt} \tag{15}$$

It is important to note that the salt entrapment into the ice accretion, S_{ac}, depends on the direction of the heat flux and is determined as follows:

$$S_{ac} = \frac{\sigma_{WL}\frac{db_{WL}}{dt} + \sigma_M\frac{db_M}{dt}}{\frac{db_{WL}}{dt} + \frac{db_M}{dt}} S_w \tag{16}$$

where σ_M is equal to 0.3 (Makkonen, 1987; Makkonen, 2010), and σ_{WL} is determined by the growth rate of ice dendrites (Weeks, 2010; Weeks and Lofgren, 1967):

$$\sigma_{WL} = \frac{\sigma_0}{\sigma_0 + (1-\sigma_0)exp\left(-\delta D_{sw}^{-1}\frac{db_{WL}}{dt}\right)} \tag{17}$$

where σ_0 = 0.26, δ is the thickness of the diffusion-limited boundary layer, and D_{sw} is the diffusion coefficient of the salt in the water. Combining the model with our experiments, we determined δD_{sw}^{-1} roughly equal to 36.2 s mm^{-1} but further studies are required to obtain more precise value.

Primary ice growth is caused by the heat release into the ice accretion and it causes significant salt entrapment (20 ppt and greater); this agrees with salinities measured in our experiments. The ice grows only in short-time bursts of up to 2 s, which are comparable to the duration of the spray event (i.e., 1.1 s) (Figure 23). Between spray events, the airflow cools the accreted ice and causes negligible freezing of the water film. It also means that the modelling of water film dynamics has only a minor effect on the accuracy of the ice growth.

The developed model was validated against experiments which showed that existing marine icing models, e.g., ICEMOD (Horjen, 1990; Horjen, 2013), RIGICE04 (Forest et al., 2005) and MARICE (Kulyakhtin and Tsarau, 2014), which neglect heat conductivity and heat capacity of the accreted ice, underestimate the ice accretion rate by more than 50%. Thus, the new model presented in this section should be used to model icing caused by periodic sea spray.

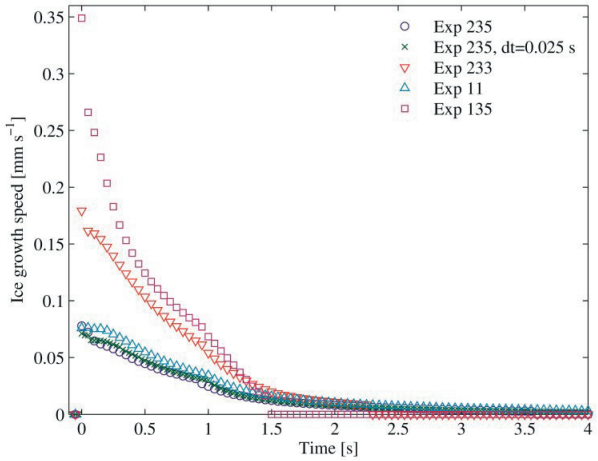

Figure 23. Examples of calculated ice growth rate after spray arrival. See Paper 7 for the thermodynamic conditions of the experiment.

The sensitivity study of the model gave the following additional conclusions:

- The heat released during water film freezing is rapidly absorbed by the accreted ice. The amount of absorbed heat is defined by the heat flux to the air between spray events and by the heat capacity of the accreted ice. Thus, the exact method of modelling the heat conductivity of the accreted ice is not important.
- The heat flux from the surface on which the ice accretes affects the ice accretion when the ice thickness is less than approximately 2 cm. Neglecting this heat flux predicts approximately 0.5 cm less ice during the initial growth.

5. Conclusions

This thesis briefly presented an overview of marine icing processes, followed by methods and main results. Details are compiled in Appendix A and the main results summarised in Chapter 4 are concluded below.

MARICE model

A major achievement of this PhD study is the development of the MARICE icing model. MARICE is the first marine icing model that applies CFD modelling. The model was built in ANSYS FLUENT and uses CFD to model the main physical processes: spray inflow, heat transfer, water film motion and the ice growth on a structure with any arbitrary geometry using, as input, weather conditions and a spray generation function.

Development and application of the model gave the following additional results:

Spray flow

- Any RANS model can predict the spray flux with an accuracy better than 10% on the windward side of the structure.
- In general, RANS models poorly predict poorly the spray flow in the wake behind the structure or after separation of the airflow. For the subcritical flow regime, the k-ε model with the enhanced wall function agrees with the results of LES while other more sophisticated models such as the transition shear-stress transport model and the Reynolds-stress model fails to give physically reasonable results. However, RANS models are expected to perform better for flows around full-scale offshore structures, i.e., at higher Reynolds numbers.
- The collision efficiency of even large droplets (with diameters exceeding 1 mm) is less than unity for full-scale structures.
- To use a Median Volume Diameter instead of complete droplet diameter spectrum is only adequate for small droplets, such as in wind generated spray. When the effect of gravity compared to the wind drag is significant, as in the case of interaction-generated spray, the complete droplet size distribution should be used to model the droplet trajectories.

Heat transfer by airflow

- MARICE models the heat transfer for any flow regime and around any structure.
- MARICE predicts heat transfer better than ICEMOD and RIGICE04 for high Reynolds number flows according to available measurements of the heat transfer

from buildings. ICEMOD and RIGICE04 can underestimate the heat transfer coefficient for the full-scale structure by 100% or more because they are using results of small-scale measurements.

A new ice growth model

MARICE and all other existing marine icing models assume no heat release from freezing into the accreted ice. Our study proved numerically and experimentally that this assumption is wrong for the ice growth caused by periodic sea spray. Neglecting of the heat conduction inside the accreted ice results in a wrong prediction of the ice salinity and underestimation of the accretion rate (may exceed 50% depending on the spray period), and the error increases with an increase in the interval between spray events. A new physical model was developed. However, the model was developed during the latest stage of the PhD study and is not yet implemented in MARICE.

Some other minor contributions to the spray flow modelling

Using CFD modelling, this study proved that neglecting the increase of the air humidity due to droplet evaporation causes an error in a droplet temperature of only 1 °C even when the liquid water content is as high as 100 g m^{-3}.

This study showed that droplet coalescence and interaction cannot be modelled properly for the marine icing problems before improving knowledge and modelling of spray generation and turbulent properties of the airflow.

6. Recommendations for future work

Ice accretion is primarily defined by freezing processes, spray flux, and heat transfer. In the field of marine icing, the modelling of freezing, salt entrapment and water film motion is on a relatively accurate, considering Contribution C9. The ice growth model developed as a part of this PhD study should be implemented in the models of sea spray icing. Before applying the developed ice growth model, additional research is required to make this model computationally efficient. In addition, in the proposed equation describing salt entrapment, the precision of its coefficients should be improved. This can be done using the remaining experiments done on Spitsbergen (Appendix E) and not used in Paper 7.

The main uncertainty of the icing prediction comes from a lack of spray flux measurements, which should be a goal of further icing research. The spray flux is used as an input to the icing models. The input spray flux of ICEMOD is 10-1000 times less than the spray flux of RIGICE04. However, it is unknown which of them is better. It may be different for different structures: the one used in ICEMOD is the spray generated by waves interacting with the semisubmersible and the one used in RIGICE04 was measured after interaction of waves with an island. However, the difference in the structure geometry could not likely cause this difference of 10-1000 times. Therefore, this question should be investigated more deeply.

It is unknown how the spray properties, which include density, droplet size distribution, and cloud geometry, depend on the structure geometry and weather conditions (waves, wind). The study of wave properties should include both modelling and measurements. Initial modelling should start from the simple considerations of the maximal height that the seawater can reach, caused by impulse from wave interaction with the structure. Modern CFD techniques are believed to be accurate, but require substantial computational resources and time. Therefore, simpler approaches must first be applied to study the physics of the phenomena. Knowledge can be obtained from the field of coastal research, where wave forces have been studied for decades. These studies yielded substantial experimental data and knowledge of the physical processes. These data can also be used for model validations. In addition, coastal engineering studies should be used to improve the prediction of maximal wave run-up on the structure that defines a zone free of icing.

The droplet size distribution depends on small-scale effects that are related to disintegration of the water stream or film, which was studied in spray atomisation, e.g.,

for firefighting. In this sense, it is important to understand the acceleration of the water volume, which depends on the impulse of the wave interaction with the structure.

The heat transfer is mainly defined by the airflow, which can be modelled using CFD. CFD, as any model, should be validated. In the case of airflow, the Reynolds number defines the properties of the flow. The airflow around an offshore rig typically has a high Reynolds number and is different from the airflow that can be measured in a wind tunnel. There is a small number of full-scale airflow measurements, especially those that are suitable for the validation of CFD. Thus, according experimetnal data should be collected. It is easier and cheaper to collect data onshore in regions with high wind speeds by measuring the heat transfer coefficients from buildings and the airflow around them. The scientific value of those data is equal to the data collected offshore.

The main difference between onshore and offshore measurements is the surface roughness of the ground and sea. Sea waves likely affect the airflow. In the first attempt, the magnitude of this effect can be estimated using CFD. Comparison of simulated airflow around a structure with a predefined static profile of sea waves can give an estimation of the effect of the waves on the airflow.

The MARICE icing model that was developed as a part of this PhD study is a powerful tool, but definitely requires improvements. The most important improvements were explained above. Other effects that are not included in MARICE are described in Figure 16. Among these, it is important to incorporate ice breakage by mechanical interaction with the “green water”. The effect of vessel motion on the modelling of water film flow can also be included in the model as a change of the gravity direction and does not require re-meshing. However, as mentioned in this study, the water film modelling has a rather small effect on the prediction of the ice growth rate.

The modelling in this work was deterministic. Air temperature and humidity change rather slowly, however, the wind and wave exhibit fluctuations. Thus, uncertainty in the deterministic model should be studied in the future.

7. References

Achenbach, E., 1968. Distribution of local pressure and skin friction around a circular cylinder in cross-flow up to Re= 5× 106. Journal of Fluid Mechanics, 34(4): 625-639.

Andreas, E.L., 1990. Time constants for the evolution of sea spray droplets. Tellus B, 42(5): 481-497.

ANSYS, 2009. FLUENT 12.0 Theory Guide. Ansys Inc, 5, Cannonsburg.

Basha, S.A. and Raja, G.K., 2009. In-cylinder fluid flow, turbulence and spray models—a review. Renewable and Sustainable Energy Reviews, 13(6): 1620-1627.

Benim, A., Pasqualotto, E. and Suh, S., 2008. Modelling turbulent flow past a circular cylinder by RANS, URANS, LES and DES. Progress in Computational Fluid Dynamics, 8(5): 299-307.

Blackmore, R. and Lozowski, E., 1994. An heuristic freezing spray model of vessel icing. International Journal of Offshore and Polar Engineering, 4(2): 119-126.

Blackmore, R. and Lozowski, E., 1998. A theoretical spongy spray icing model with surficial structure. Atmospheric research, 49(4): 267-288.

Blackmore, R., Makkonen, L. and Lozowski, E., 2002. A new model of spongy icing from first principles. Journal of Geophysical Research: Atmospheres (1984–2012), 107(D21): AAC 9-1-AAC 9-15.

Brown, R.D. and Agnew, T.A., 1985. Characteristic of marine icing in Canadian waters, International Workshop on Offshore Winds and Icing, Halifax, Nova Scotia, Canada, pp. 78-94.

Brown, R.D. and Mitten, P., 1988. Ice Accretion on Drilling Platforms Off the East Coast of Canada. In: A.H.a.J.F. Storm (Editor), International Conference on Technology for Polar Areas. Trondheim, Norway, Tapir Publishers, Trondheim, Norway, pp. 409–421.

Brørs, B., Løset, S., Iden, K., Reistad, M., Harstveit, K., Nygård, B. and Engedahl, H., 2009. Goliat Environmental/Icing Evaluation Study. 25/08, Norwegian Meteorological Institute.

Chigier, N. and Farago, Z., 1992. Morphological classification of disintegration of round liquid jets in a coaxial air stream. Atomization and Sprays, 2(2): 137-153.

Chung, K. and Lozowski, E., 1998. A three-dimensional time-dependent icing model for a stern trawler. Journal of ship research, 42(4): 266-273.

Faeth, G., Hsiang, L.-P. and Wu, P.-K., 1995. Structure and breakup properties of sprays. International Journal of Multiphase Flow, 21: 99-127.

Fairall, C., Banner, M., Peirson, W., Asher, W. and Morison, R., 2009. Investigation of the physical scaling of sea spray spume droplet production. Journal of Geophysical Research: Oceans (1978–2012), 114(C10): 19.

Finstad, K.J., Lozowski, E.P. and Gates, E.M., 1988a. A computational investigation of water droplet trajectories. Journal of Atmospheric and Oceanic Technology, 5(1): 160-170.

Finstad, K.J., Lozowski, E.P. and Makkonen, L., 1988b. On the median volume diameter approximation for droplet collision efficiency. Journal of the Atmospheric Sciences, 45(24): 4008-4012.

Forest, T., Lozowski, E. and Gagnon, R., 2005. Estimating marine icing on offshore structures using RIGICE04, International Workshop on Atmospheric Icing on Structures (IWAIS), Monreal.

Gao, W., Smith, D. and Sego, D., 2000. Freezing temperatures of freely falling industrial wastewater droplets. Journal of cold regions engineering, 14(3): 101-118.

He, G., Pan, C. and Wang, J., 2013. Dynamics of vortical structures in cylinder/wall interaction with moderate gap ratio. Journal of Fluids and Structures, 43: 100-109.

Horjen, I., 1990. Numerical modeling of time-dependent marine icing, anti-icing and deicing, Norwegian University of Science and Technology, Trondheim, Norway, 175 pp.

Horjen, I., 2013. Numerical modeling of two-dimensional sea spray icing on vessel-mounted cylinders. Cold Regions Science and Technology, 93(0): 20-35.

Horjen, I. and Vefsnmo, S., 1985. A kinematic and thermodynamic analysis of sea spray (in Norwegian), Offshore Icing – Phase II. STF60 F85014, Norwegian Hydrodynamic Laboratory (NHL), Norway.

Horjen, I. and Vefsnmo, S., 1986. Calibration of ICEMOD – extension to a time dependent model, SINTEF.

Jones, K.F., 1996. Ice accretion in freezing rain. 96-2, U.S. Army Cold Regions Research and Engineering Laboratory, Hanover, NH.

Jones, K.F. and Andreas, E.L., 2012. Sea spray concentrations and the icing of fixed offshore structures. Quarterly Journal of the Royal Meteorological Society, 138(662): 131-144.

Jørgensen, T.S., 1982. Influence of ice accretion on activity in the northern part of the Norwegian Continental Shelf. STF88 F82016, Offshore Testing and Research Group.

Jørgensen, T.S., 1985. Sea spray characteristics on a semi-submersible drilling rig. STF60 F 85015, Norwegian Hydrodynamic Laboratory (NHL), Trondheim.

Kays, W., Crawford, M. and Weigand, B., 2005. Convective Heat and Mass Transfer. McGraw-Hill, New York, 546 pp.

Kollar, L.E., 2009. Spray characteristics of artificial aerosol clouds in a low-speed icing wind tunnel. Atomization and Sprays, 19(4).

Kollár, L.E. and Farzaneh, M., 2007. Modeling the evolution of droplet size distribution in two-phase flows. International Journal of Multiphase Flow, 33(11): 1255-1270.

Kollar, L.E., Farzaneh, M. and Karev, A.R., 2006. Modeling droplet size distribution near a nozzle outlet in an icing wind tunnel. Atomization and Sprays, 16(6).

Kollár, L.E., Farzaneh, M. and Karev, A.R., 2005. Modeling droplet collision and coalescence in an icing wind tunnel and the influence of these processes on droplet size distribution. International journal of multiphase flow, 31(1): 69-92.

Koop, T., 2004. Homogeneous ice nucleation in water and aqueous solutions. Zeitschrift für Physikalische Chemie/International journal of research in physical chemistry and chemical physics, 218(11/2004): 1231-1258.

Koop, T., Kapilashrami, A., Molina, L.T. and Molina, M.J., 2000. Phase transitions of sea-salt/water mixtures at low temperatures: Implications for ozone chemistry in

the polar marine boundary layer. Journal of Geophysical Research: Atmospheres (1984–2012), 105(D21): 26393-26402.
Koop, T. and Zobrist, B., 2009. Parameterizations for ice nucleation in biological and atmospheric systems. Physical Chemistry Chemical Physics, 11(46): 10839-10850.
Kulyakhtin, A., 2013. Field experiment 2012-2013: sensitivity of icing on spray period and weather conditions. 2013-1778, Det Norske Veritas.
Kulyakhtin, A., Kulyakhtin, S. and Løset, S., 2013a. Marine Icing Field Experiment 2012. 2013-1776, Det Norske Veritas.
Kulyakhtin, A., Løset, S. and Kollar, L.E., 2013b. Marine icing field experiments, 2011. 2013-1775, DNV.
Kulyakhtin, A., Shipilova, O., Libby, B. and Løset, S., 2012. Full-scale 3D CFD simulation of spray impingement on a vessel produced by ship-wave interaction, the 21st IAHR International Symposium on Ice, Dalian, China, pp. 1129-1141.
Kulyakhtin, A. and Tsarau, A., 2014. A time-dependent model of marine icing with application of computational fluid dynamics. Cold regions science and technology, 104-105: 33-44.
Lad, N., Muhamad Said, M., Aroussi, A. and Adebayo, D., 2010. Experimental and computational characterisation of atomised spray flow around a circular cylinder. Progress in Computational Fluid Dynamics, 10(4): 232-238.
Lozowski, E.P., Szilder, K. and Makkonen, L., 2000. Computer simulation of marine ice accretion. Philosophical Transactions of the Royal Society of London, Series A, 358(1776): 2811-2845.
Lozowski, E.P. and Zakrewski, W.P., 1992. Marine icing laboratory and numerical experiments, Compusult Ltd.
Makkonen, L., 1985. Heat transfer and icing of a rough cylinder. Cold Regions Science and Technology, 10(2): 105-116.
Makkonen, L., 1987. Salinity and growth rate of ice formed by sea spray. Cold Regions Science and Technology, 14(2): 163-171.
Makkonen, L., 1988. Formation of spray ice on offshore structures, 9th IAHR Ice Symposium, Sapporo, Japan, pp. 708-739.
Makkonen, L., 2010. Solid fraction in dendritic solidification of a liquid. Applied Physics Letters, 96(9): 091910.
Makkonen, L., Brown, R.D. and Mitten, P.T., 1991. Comments on “Prediction of Vessel Icing for Near-Freezing Sea Temperatures”. Weather and forecasting, 6(4): 565-567.
Makkonen, L. and Oleskiw, M.M., 1997. Small-scale experiments on rime icing. Cold regions science and technology, 25(3): 173-182.
Makkonen, L. and Stallabrass, J., 1987. Experiments on the cloud droplet collision efficiency of cylinders. Journal of Climate and Applied Meteorology, 26(10): 1406-1411.
Marrone, S., Colagrossi, A., Antuono, M., Lugni, C. and Tulin, M.P., 2011. A 2D+t SPH model to study the breaking wave pattern generated by fast ships. Journal of Fluids and Structures, 27(8): 1199-1215.
Menter, F., Langtry, R., Likki, S., Suzen, Y., Huang, P. and Völker, S., 2006. A correlation-based transition model using local variables-Part I: model formulation. Journal of Turbomachinery, 128(3): 413-422.

Menter, F.R., 1994. Two-equation eddy-viscosity turbulence models for engineering applications. AIAA journal, 32(8): 1598-1605.
Morsi, S. and Alexander, A., 1972. An investigation of particle trajectories in two-phase flow systems. Journal of Fluid Mechanics, 55(2): 193-208.
Muzik, I. and Kirby, A., 1992. Spray overtopping rates for Tarsiut Island: model and field study results. Canadian Journal of Civil Engineering, 19(3): 469-477.
Myers, T., 1998. Thin films with high surface tension. Siam Review, 40(3): 441-462.
Myers, T.G. and Charpin, J.P., 2004. A mathematical model for atmospheric ice accretion and water flow on a cold surface. International Journal of Heat and Mass Transfer, 47(25): 5483-5500.
Nauman, J., 1984. Superstructure icing on the semi-submersible Ocean Bounty in Lower Cook Inlet, Alaska, the 2nd International Workshop on Atmospheric Icing of Structures, Trondheim, Norway, pp. 71–79.
O'Rourke, P.J., 1981. Collective drop effects on vaporizing liquid sprays, Los Alamos National Lab., NM (USA).
Odar, F., 1966. Verification of the proposed equation for calculation of the forces on a sphere accelerating in a viscous fluid. Journal of Fluid Mechanics, 25(03): 591-592.
Odar, F. and Hamilton, W.S., 1964. Forces on a sphere accelerating in a viscous fluid. Journal of Fluid Mechanics, 18(02): 302-314.
Okajima, A., 1982. Strouhal numbers of rectangular cylinders. Journal of Fluid Mechanics, 123: 379-398.
Ong, M.C., Utnes, T., Holmedal, L.E., Myrhaug, D. and Pettersen, B., 2009. Numerical simulation of flow around a smooth circular cylinder at very high Reynolds numbers. Marine Structures, 22(2): 142-153.
Orme, M., 1997. Experiments on droplet collisions, bounce, coalescence and disruption. Progress in Energy and Combustion Science, 23(1): 65-79.
Overland, J., Pease, C., Preisendorfer, R. and Comiskey, A., 1986. Prediction of vessel icing. Journal of climate and applied meteorology, 25(12): 1793-1806.
Pope, S.B., 2000. Turbulent flows. Cambridge University Press, Cambridge.
Pruppacher, H., 1995. A new look at homogeneous ice nucleation in supercooled water drops. Journal of the atmospheric sciences, 52(11): 1924-1933.
Ranz, W. and Marshall, W., 1952. Evaporation from drops. Chem. Eng. Prog, 48(3): 141-146.
Ryerson, C., 1995. Superstructure spray and ice accretion on a large US Coast Guard cutter. Atmospheric research, 36(3): 321-337.
Ryerson, C.C., 2008. Assessment of superstructure ice protection as applied to offshore oil operations safety. ERDC/CRREL TR-08-14, U.S. Army Cold Regions Research and Engineering Laboratory, Hanover, NH.
Ryerson, C.C., 2011. Ice protection of offshore platforms. Cold Regions Science and Technology, 65(1): 97-110.
Sarpkaya, T. and Isaacson, M., 1981. Mechanics of wave forces on offshore structures, 96. Van Nostrand Reinhold Company New York, New York, 651 pp.
Schmidt, D.P. and Rutland, C.J., 2004. Reducing grid dependency in droplet collision modeling. Journal of Engineering for gas turbines and power, 126(2): 227-233.

Shimada, K. and Ishihara, T., 2012. Predictability of unsteady two-dimensional k-ε model on the aerodynamic instabilities of some rectangular prisms. Journal of Fluids and Structures, 28: 20-39.
Stallabrass, J., 1980. Trawler icing: a compilation of work done at NRC, National Research Council Canada.
Stallabrass, J. and Hearty, P., 1967. The icing of cylinders in conditions of simulated freezing sea spray. National Research Council of Canada.
Taylor, E. and Wu, G., 1997. Interaction of steep waves with offshore structures. Philosophical Transactions of the Royal Society of London. Series A: Mathematical, Physical and Engineering Sciences, 355(1724): 593-605.
Türk, M. and Emeis, S., 2010. The dependence of offshore turbulence intensity on wind speed. Journal of Wind Engineering and Industrial Aerodynamics, 98(8): 466-471.
Wang, X., Key, J., Fowler, C. and Maslanik, J., 2007. Diurnal cycles in Arctic surface radiative fluxes in a blended satellite-climate reanalysis data set. Journal of Applied Remote Sensing, 1(1): 013535-013535-17.
Waniewski Sur, T. and Chevalier, K., 2006. Semi-Empirical Bow Spray Modeling, 26th Symposium on Naval Hydrodynamics, Rome, Italy.
Waniewski, T.A., Brennen, C.E. and Raichlen, F., 2000. Measurements of Air Entrainment by Bow Waves. Journal of Fluids Engineering, 123(1): 57-63.
Weeks, W., 2010. On sea ice. University of Alaska Press, Fairbanks, AK, 664 pp.
Weeks, W. and Lofgren, G., 1967. The effective solute distribution coefficient during the freezing of NaCl solutions. In: H. Oura (Editor), Physics of Snow and Ice. Institute of Low Temperature Science, Hokkaido University, Sapporo, Japan, pp. 579-597.
Yoon, B. and Ettema, R., 1993. Droplet trajectories and icing-collision efficiencies for cylinders determined using LDV. Cold Regions Science and Technology, 21(4): 381-397.
Yoon, S., DesJardin, P., Presser, C., Hewson, J. and Avedisian, C., 2006. Numerical modeling and experimental measurements of water spray impact and transport over a cylinder. International Journal of Multiphase Flow, 32(1): 132-157.
Zakrzewski, W.P., 1986. Icing of fishing vessles part I: splashing a ship with spray, 8th IAHR Symposium on Ice, Iowa City.
Zarling, J.P., 1980. Heat and mass transfer from freely falling drops at low temperatures. NASA STI/Recon Technical Report N, 81: 13311.
Zdravkovich, M., 1997. Flow around circular cylinders, volume 1: fundamentals, 19. Oxford University Press, Oxford, 185 pp.

Appendix A. Selected papers

SEA SPRAY ICING: IN-CLOUD EVAPORATION. SEMI-ANALYTICAL AND NUMERICAL INVESTIGATIONS.

Anton Kulyakhtin*, Sveinung Løset
Department of Civil and Transport Engineering, NTNU, Trondheim, Norway
*Email: anton.kulyakhtin@ntnu.no

Abstract: Interactions between waves and a ship produce sprays of seawater that may freeze on the surfaces of the ship. Simulations of water spray flow in the air are important for the understanding and assessment of ice accretion on offshore structures and ships. During the spray flow, the spray evaporates, and the humidity of the surrounding air may increase. The increased humidity may affect the evaporation process and the thermodynamics of the spray. This study numerically investigated the influence of increased humidity on the in-flight spray temperature and mass change. Using ANSYS Fluent and semi-analytical calculations, the process was studied for the conditions of constant wind speed and likely temperatures and humidity levels for offshore conditions. The input properties of the sea spray cloud were based on field measurements. When disregarding the air humidity change, the error of the spray temperature is approximately 0.5°C for a cloud with a concentration of 50 g/m^3 if we assume no diffusion of water vapour out of the cloud. This work is part of the MARICE project conducted by Det Norske Veritas (DNV).

1. INTRODUCTION

Sea spray is created by the interaction of a ship with waves. In many studies (e.g., [1]), the air humidity for the spray simulations is considered constant and is assumed to be in the range of 75%–90%. In the case of marine icing, the spray liquid water content (LWC) may reach values up to several hundreds of g/m³. For example, the mean value of the LWC of the sea spray measured by Ryerson [2] was 64 g/m³. An increase in the relative humidity (RH) inside the spray cloud can decrease the evaporative heat exchange and the rate of droplet temperature change.

The goals of this work were to investigate droplet behaviour inside the spray cloud and to indicate when it is necessary to take into account a change in the air humidity based on the values of the LWC.

2. RESULTS AND DISCUSSION

The temperature evolution of droplets was investigated numerically in clouds with different LWCs. Figure 1 shows an example of the humidity change inside the spray cloud due to the evaporation of droplets; the humidity changes by several per cent.

Figure 2 shows that the change in humidity does not substantially affect the calculated droplet temperature. The calculated temperature difference in the case of the lower LWC was directly associated with the humidity of the air. In most cases, the biggest difference was reached when the droplets were in heat flux equilibrium between convection and evaporation.

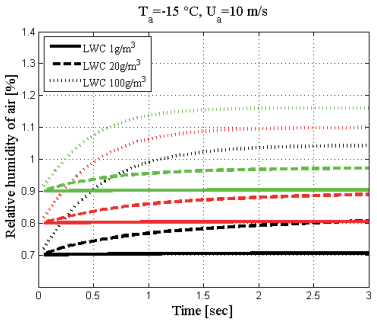

Figure 1: Change in humidity due to spray cloud cooling and evaporation for different LWCs of clouds at a temperature of -5°C and an initial humidity of 70%, 80% or 90%.

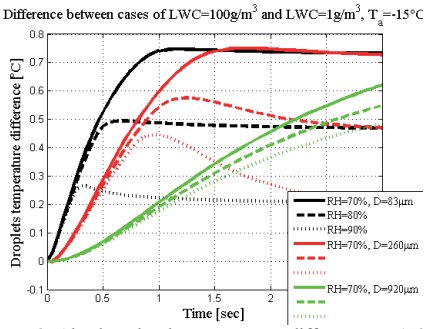

Figure 2: Absolute droplet temperature difference at -15°C between clouds with an LWC of 100 g/m³ and those with an LWC of 1 g/m³. The results are shown for different levels of initial humidity and for three droplet diameters.

3. CONCLUSIONS

The difference in the droplet temperature strongly depends on the initial humidity, the LWC of the cloud and the temperature of the ambient air. A humidity increase in the cloud cannot produce a change in the droplet temperature of more than 1°C, even for an LWC of 100 g/m³. Thus, in many problems, humidity can be neglected because there are many other sources that can result in much greater errors in the calculated mass accretion.

4. REFERENCES

[1] K.K. Chung, E.P. Lozowski, “A three-dimensional time-dependent icing model for a stern trawler”, J. of Ship Research, vol. 42, pp. 266-273, 1998.

[2] C.C. Ryerson, “Superstructure spray and ice accretion on a large U.S. Coast Guard cutter”, Atmospheric Research, vol. 36, pp. 321-337, 1995.

Sea spray icing: in-cloud evaporation. Semi-analytical and numerical investigations.

Anton Kulyakhtin
Department of Civil and Transport Engineering
NTNU
Trondheim, Norway
anton.kulyakhtin@ntnu.no

Sveinung Løset
Department of Civil and Transport Engineering
NTNU
Trondheim, Norway
sveinung.loset@ntnu.no

Abstract—**Interactions between waves and a ship produce sprays of seawater that may freeze on the surfaces of the ship. Simulations of water spray flow in the air are important for the understanding and assessment of ice accretion on offshore structures and ships. During the spray flow, the spray evaporates, and the humidity of the surrounding air may increase. The increased humidity may affect the evaporation process and the thermodynamics of the spray. This study numerically investigated the influence of increased humidity on the in-flight spray temperature and mass change. Using ANSYS Fluent and semi-analytical calculations, the process was studied for the conditions of constant wind speed and likely temperatures and humidity levels for offshore conditions. The input properties of the sea spray cloud were based on field measurements. When disregarding the air humidity change, the error of the spray temperature is approximately 0.5°C for a cloud with a concentration of 50 g/m^3 if we assume no diffusion of water vapour out of the cloud. This work is part of the MARICE project conducted by Det Norske Veritas (DNV).**

Keywords: Sea spray, icing, air humidity

I. INTRODUCTION

Sea spray is created by the interaction of a ship with waves. An example of sea spray generation is shown in Figure 1. In many studies (e.g., [1,2]) the air humidity for the spray simulations is considered constant and is assumed to be in the range of 75%–90% In the case of marine icing, the spray liquid water content (LWC) can reach values up to several hundreds of g/m³. For example, the mean value of the LWC of the sea spray measured by Ryerson [3] was 64 g/m³. When dealing with marine spray while it is warm, it evaporates quite readily. Water vapour has a relatively low molecular diffusivity, and therefore, it is expected that the water concentration inside the spray cloud will increase if it is not reduced much by convection. An increase in the relative humidity (RH) inside the cloud can decrease the evaporative heat exchange and the rate of droplet temperature change.

The goals of this work were to investigate the droplet behaviour inside the spray cloud and to indicate when it is necessary to take into account a change in air humidity based on the values of the LWC.

Figure 1. Example of sea spray. HMCS Fredericton, taken by Provincial Airlines and published at http://www.navy.forces.gc.ca/fredericton/.

II. ANALYSIS OF DROPLET HEAT EXCHANGE

First, the amount of heat transfer corresponding to evaporation is estimated. Equations describing evaporation and convection are given in [4]:

$$mc_p dT_d/dt=\pi D^2(Q_c+Q_e) \quad (1)$$

where m, T_d and D are the mass, the temperature and the diameter of the water droplet, respectively; c_p is the specific heat capacity of water at constant pressure; and Q_c and Q_e are the convective and the evaporative heat fluxes, respectively. In contrast to the equation presented in [4], the radiative heat flux is neglected because it is small and this exclusion simplifies the calculations. The convective heat transfer per unit area is described by the following equations:

$$Q_c=h_c(T_d-T_a) \quad (2)$$

$$h_c=k_a/D\cdot(2.0+0.6Pr^{0.33}Re^{0.5}) \quad (3)$$

where h_c is the convective heat transfer coefficient, T_a is the temperature of the ambient air, k_a is the thermal conductivity of air, Pr is the Prandtl number and Re is the Reynolds number.

The evaporative heat flux per unit area is as follows:

$$Q_e=h_e\rho_a l_e(C_d-C_a) \quad (4)$$

$$h_e=D_{wa}/D\cdot(2.0+0.6Sc^{0.33}Re^{0.5}) \quad (5)$$

where h_e is the mass transfer coefficient, ρ_a is the air density, l_e is the specific latent heat of vaporisation, C_d and C_a are the specific humidities at the droplet surface and in the air, respectively, D_{wa} is the diffusivity of water vapour in the air and Sc is the Schmidt number.

Thus, the ratio of the evaporative heat flux to the convective heat flux can be written in the following form:

$$Q_e/Q_c=\mu_a l_e/(\rho_a k_a Sc)\cdot\Theta(Re)\cdot(C_d-C_a)/(T_d-T_a) \qquad (6)$$

where μ_a is the viscosity of air. The *Sc* and *Pr* numbers can be considered constant in this case, and the term $\Theta(Re)$ has a weak dependence on the temperature. A change in the Reynolds number changes this function by up to 6% for values of *Re* between 0 and 8000. $\Theta(Re)$ will be further assumed to equal 1. Thus, the ratio of heat fluxes does not significantly depend on the droplet diameter or the velocity of the droplet relative to the air stream velocity.

Using the equation for the ideal gas state and determination of the relative humidity, we can rewrite (6):

$$\frac{Q_e}{Q_c} = K\frac{RH\cdot p_{sat}(T_a)/T_a - p_{sat}(T_d)/T_d}{T_a - T_d} \qquad (7)$$

where *RH* is the relative humidity, and p_{sat} is the saturated pressure by Bolton's equation [4]. Figure 2 shows the ratio of the evaporative heat flux to the sum of the absolute values of the evaporative and the convective heat fluxes.

In the study by Zarling [5], as an example, it was demonstrated that the evaporative heat transfer was 30% in the case of droplets at 0°C in saturated air at a temperature of -18°C. This result is in agreement with the estimations presented here. In the case of saturated air, the evaporative heat flux is always lower than the convective heat flux and is in the range of 10% to 50% of the total heat flux. However, Figure 2 shows that, in the case of unsaturated air, the evaporative heat flux can correspond to values higher than 50% of the total heat flux. In this case, at temperatures close to the ambient air temperature, the evaporative heat flux is close to 100% of the total heat flux, which means that the evaporation is much stronger than the convection. It should be noted that the equilibrium temperature of the droplets in the ambient unsaturated air is lower than the air temperature. The droplet temperature is approximately equal to -6°C and -7°C in the case of 80% and 60% RH, respectively. These values correspond to the point at which evaporative heat flux is equal to 50% of the total heat flux.

In addition, Figure 2 shows how strongly the droplet heat exchange depends on the RH. Thus, it is of interest to estimate the influence of the humidity change on the heat transfer in the spray.

III. Numerical Simulation of Sea Spray Cloud

For a realistic flow simulation, a high volume of air should be investigated. This requires high CPU expenses, thus a periodic mesh was used instead, making it possible to take into account gravity and the real motion of the droplets. However, the use of a periodic mesh creates some difficulties. In real conditions, the thermal diffusivity is much higher than the molecular diffusivity, and the droplets will not significantly affect the temperature of the domain. The heat will probably leave the cloud. In the case of the calculations, the domain was closed and a special energy

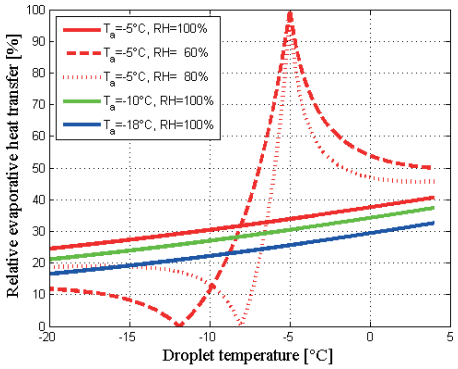

Figure 2. Ratio of evaporative heat flux to the sum of absolute values of convective and evaporative fluxes.

source was included to avoid heating the air. The goal of this heat source was to keep the air temperature constant:

$$S_E=-A_E\cdot(T_a-T_{a0}) \qquad (8)$$

where T_{a0} is the initial air temperature. The flow properties can change because the droplets fall in the flow field. If there is no momentum sink in the periodic domain, the air starts to move in the vertical direction, making the droplet falling velocity even greater. This velocity effect did not have a significant influence on the temperature of the droplets. However it was removed to make the simulation more realistic. The additional momentum source in the vertical direction is expressed by the following:

$$S_{Ym}=-A_{Ym}\cdot|V_y|V_y \qquad (9)$$

where V_y is the vertical component of the air velocity in a cell of the calculation domain, and A_E=100000 and A_{Ym}=10000 are coefficients to keep the temperature and the velocity of the domain constant.

Equations for droplet motion can be found in [4]. The standard ANSYS Fluent drag coefficient for a spherical particle was used. Equations describing the droplet heat-mass exchange have been previously described [4, 6]. In contrast to [4], the mass decrease due to evaporation was taken into account, and the radiation heat source was neglected. The calculations were performed for a seawater spray with a salinity of 35 ppt. The salinity correction factor was used for the saturated water pressure at the surface of the droplets. The relations can be found in [7] and lead to a correction factor of 0.981 in the present case. The fresh water saturation pressure was calculated by the equation given in [8].

IV. Numerical Set Up

Calculations were performed in ANSYS Fluent using the discrete particle model (DPM), the species transport model and the two-way coupling. The volume (2 by 1 by 0.5 m) was used with cubic cells with 0.25 m edge lengths. Offshore conditions vary within a wide range, and only a

few datasets were used here to show several possible conditions and the results of droplet evaporation. The results of the calculations are shown for a seawater salinity of 35 ppt and an initial spray temperature of -1°C. The number 31 droplet size distribution (DSD) was used from [3] because it was the closest to the mean DSD. The normal distribution function was used with the following parameters: D_{min}=63 µm, D_{max}=2650 µm, D_{mean}=251 µm and D_{std}=180.78 µm. One hundred bins of droplets were used for the calculations with the logarithmic separation. The boundaries of the bins were calculated with the formula:

$$D_i=D_{min}(D_{max}/D_{min})^{i/N},\ i=0...100 \qquad (10)$$

Droplets with the mean volume diameter were used as representative of each bin.

For the same DSD, the spray concentration was changed to increase the LWC and to analyse the results of this change. Calculations were performed for LWCs of 1, 20 and 100 g/m³. The initial velocities of the spray created by the ship/wave interaction are not well known and thus were set equal to an air stream velocity of 10 m/s. Calculations were performed for RHs of 70%, 80% and 90% and air temperatures of -5°C and -15°C. The results of a 3 sec cloud evolution are presented in accordance with [9].

The domain flow recalculation time step was 0.01, and the droplet time step was 0.001. Twenty inside domain iterations were performed per iteration of the DPM. The results of these calculations were compared for the set of RH 70%, LWC 100 g/m³ and temperature -5°C using the same calculation in which the mesh size and the time step were set 10 times smaller, and the number of bins was set to 1000. The difference between those two results was less than 0.1%, demonstrating that the result does not depend on the domain parameters of the model.

In summary, these calculations neglected the change in the air temperature and the speed due to droplets. The increase in the water vapour concentration in the air and its influence on the droplet temperature were investigated.

V. Results of the Numerical Simulations

Figures 3 and 4 show the change in humidity inside the cloud due to the water evaporation from the surface of the warm droplets. Even in the case of a cloud with an LWC of 20 g/m³, the humidity can increase by approximately 5% depending on the air temperature and the air humidity. In the case of a 100 g/m³ LWC, the cloud humidity changes by more than 10% in absolute value.

This result is more significant in the case of lower temperatures because the air becomes oversaturated and in less than 1.5 seconds reaches the maximal level of humidity because of the high temperature of the droplets relative to the air temperature. Figures 5 shows an example of the droplet temperature change.

For the case of T_a=-15 C, LWC=100 g/m³ and RH=70%, differences in the droplet temperature can be more than 0.7°C, as can be seen in Figure 6. The difference in temperature decreases with an increase in the initial RH.

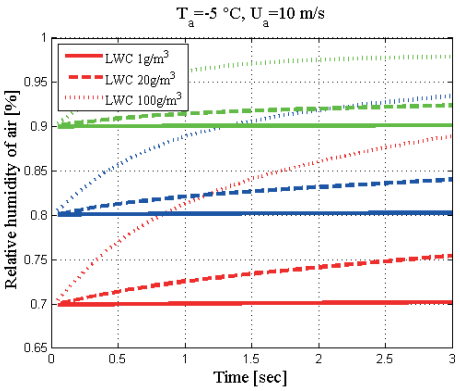

Figure 3. Change in humidity due to spray cloud cooling and evaporation for different LWCs of clouds at a temperature of -5°C and initial relative humidities of 70%, 80% and 90%.

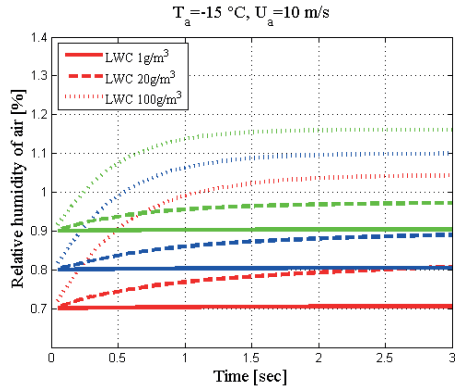

Figure 4. Change in humidity due to spray cloud cooling and evaporation for different LWCs of clouds at a temperature of -15°C and initial humidities 70%, 80% and 90%.

In fact, when a certain level of saturation is reached, the evaporation does not play an important role. As can be seen in Figure 2, the evaporative heat partition in cases of droplet temperatures close to the temperature of the ambient air strongly depends on the air saturation with water vapour. The ratio decreases with increasing air humidity.

A similar temperature difference was obtained at a temperature of -5°C (Figure 7), but the level of maximum humidity and the maximum difference in temperature were not reached as quickly as in the previous simulation. The air capacity for water vapour is higher at higher temperatures; consequently, the temperature difference can reach higher values.

Simulations were also conducted for an LWC of 20 g/m³. In this case, the temperature difference from an LWC of 1 g/m³ was less than 0.25°C at both air temperatures. The temperature difference obtained from the case with a lower LWC is directly associated with the air humidity.

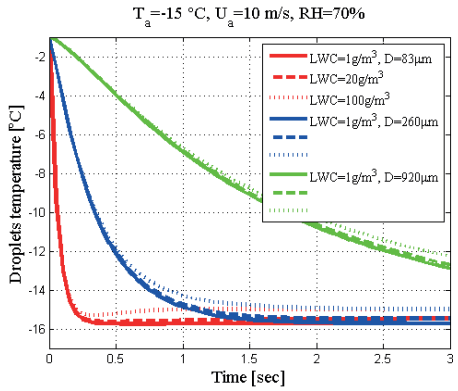

Figure 5. Droplet temperature evolution at -15 °C and a humidity of 70%. The results are shown for three different droplet diameters.

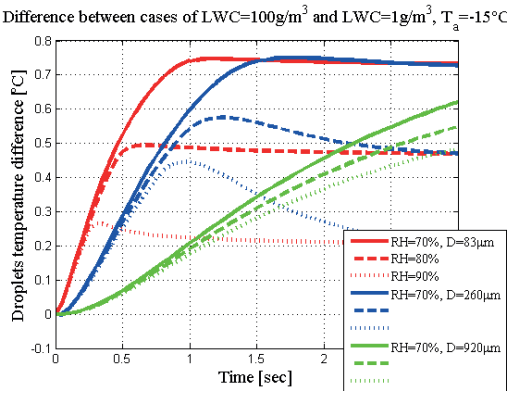

Figure 6. Absolute droplet temperature difference at -15°C between clouds with an LWC of 100 g/m³ and those with an LWC of 1 g/m³. The results are shown for different levels of initial humidity and for three different droplet diameters.

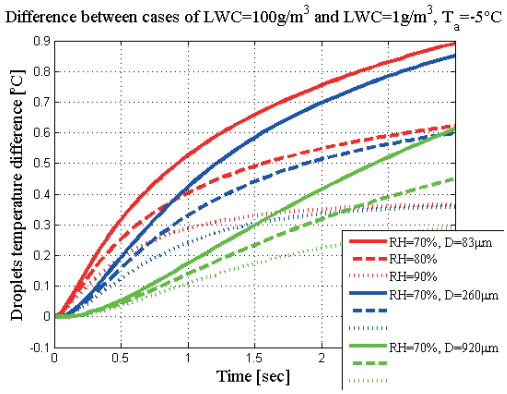

Figure 7. Absolute droplet temperature difference at -5°C between clouds with an LWC of 100 g/m³ and those with an LWC of 1 g/m³. The results are shown for different levels of initial humidity and for three different droplet diameters.

In most of the cases, the maximum difference is reached when the droplets are in equilibrium between convective heat flux and evaporative heat flux.

VI. Conclusions

The difference in the droplet temperature depends strongly on the initial humidity, the LWC of the cloud and the ambient air temperature. It should be noted that for the case of a warmer air temperature, this difference can be greater because the air capacity for the water vapour is higher when the air is warmer. In addition, the equilibrium is reached later.

The effect of the increase in the cloud humidity cannot produce changes in the droplet temperature exceeding 1°C, even at an LWC of 100 g/m³. Thus, many simulations can neglect the cloud humidity change because there are many other terms that can produce much higher errors in the calculated mass of accretion. We conclude that some errors in in-flight cooling do not have a strong influence on sea spray icing. The ratio of the specific heat capacity to the latent heat of water is approximately 0.013/°C. Thus, a change in the input energy due to a change in temperature of 1°C is only 1.3% of the energy necessary to freeze this amount of water. This amount of energy is much less than the accuracy of most simulations.

VII. Acknowledgements

This work is part of the MARICE project conducted by Det Norske Veritas (DNV). The authors would like to thank the Research Council of Norway, Statoil and Det Norske Veritas for the financial support of the project.

VIII. References

[1] K.K. Chung, E.P. Lozowski, "A three-dimensional time-dependent icing model for a stern trawler", J. of Ship Research, vol. 42, pp. 266-273, 1998

[2] T.W. Forest, E.P. Lozowski, R.E. Gagnon, "Estimating marine icing on offshore structures using RIGICE04" IWAIS XI, Montréal, June 2005

[3] C.C. Ryerson, "Superstructure spray and ice accretion on a large U.S. Coast Guard cutter", Atmospheric Research, vol. 36, pp. 321-337, 1995

[4] E.P. Lozowski, K. Szilder, L. Makkonen, "Computer simulation of marine ice accretion" Phil. Trans. R. Soc. Lond. Vol. A 358, pp. 2811-2845, 2000

[5] J.P. Zarling, "Heat and mass transfer from freely falling drops at low temperature", CRREL Report 80-18, November 1980

[6] J.P. Hindmarsh, A.B. Russell, X.D. Chen, "Experimental and numerical analysis of the temperature transition of a suspended freezing water droplet", International Journal of Heat and Mass Transfer, Vol. 46(7), pp. 1199-1213, 2003

[7] E.L. Andreas, "Handbook of physical constants and functions for use in atmospheric boundary layer studies", ERDC/CRREL M-05-1, October 2005

[8] W.C. Reynolds, "Thermodynamics properties in SI: graphs, tables, and computational equations for 40 substances", Department of mechanical engineering, Stanford University, 1979

[9] E.P. Lozowski, W.P. Zakrewski, "Simulating marine icing conditions in the refrigerated marine icing wind tunnel", NRC Institute for Ocean Technology, CR-1991-05

21st IAHR International Symposium on Ice
"Ice Research for a Sustainable Environment"
Dalian, China, June 11 to 15, 2012

Numerical Simulations of 3D Spray Flow in a Wind Tunnel with Application of O'Rourke's Interaction Algorithm and Its Validation

Anton Kulyakhtin[1,4*], Laszlo Kollar[2], Sveinung Løset[1,3], Masoud Farzaneh[2]
[1]*Norwegian University of Science and Technology (NTNU), Trondheim, Norway*
[2]*University of Quebec at Chicoutimi (UQAC), Chicoutimi, Canada*
[3]*Sustainable Arctic Marine and Coastal Technology (SAMCoT), Centre for Research-based Innovation (CRI), Norwegian University of Science and Technology, Trondheim, Norway*
[4]*The University Centre in Svalbard (UNIS), Longyearbyen, Norway*
Anton Kulyakhtin, NTNU, Høgskoleringen 7a, 7491, Trondheim, Norway
**anton.kulyakhtin@ntnu.no*

This paper presents a 3D air-dispersed water flow model developed to simulate the spray flow that is responsible for ice accretion when water reaches a cold surface. Modelling the spray dynamics and the processes inside the cloud to determine such spray characteristics as the droplet size distribution (DSD) and liquid water content (LWC), is essential for predicting ice accretion in nature and in laboratory. The model used in this study is constructed in ANSYS FLUENT using built-in tools. It includes airflow field simulation using the Eulerian approach and the Lagrangian simulation of droplet flow. The applied model neglects the thermodynamics of the spray but considers the influence of the flow field on the spray and the interdroplet interactions based on O'Rourke's algorithm. O'Rourke's algorithm is a stochastic computationally efficient, but mesh- and discretisation-dependent, approach. The model is applied to simulate spray flows produced in the CIGELE atmospheric icing research wind tunnel of the University of Quebec at Chicoutimi, Canada. The application of O'Rourke's algorithm is discussed for the particular case of droplet flow in this wind tunnel. The modelled spray had a median volume diameter (MVD) of approximately 30 μm and an LWC of approximately 1 g/m³ in the test section of the tunnel. The modelled processes also include spray focusing in the tunnel contraction. The simulation results are compared with available experimental data that include the DSD and the LWC of the spray in a few points in the same tunnel. Sensitivity studies are also carried out to investigate the influence of the flow field properties, initial spray conditions and their uncertainty on the spray DSD and LWC. The investigation focuses on the variation of initial spray patterns and the accuracy of the velocity and turbulence simulations.

1. Introduction

A simulation of spray flow is important in many applications. Importance of spray properties is different for different processes. In the icing process, one of the most important spray properties is the liquid water content (LWC). The ice accretion rate is directly proportional to the amount of spray that hits the cold surface. The amount of spray that reaches the surface can be estimated using empirical relationships for collection efficiency (Stallabrass, 1980); however, empirical relationships cannot be applied to complex flows or structures. In this case, a CFD tool that is able to model the spray evolution of real flows is necessary.

Several papers have presented models of spray flow. Lozowski et al. (2000) developed a spray model that can be applied to complex structures; however, this model assumes uniform airflow. Marek and Olsen (1986) simulated the fine spray flow in a wind tunnel. Kollar and Farzaneh (2007) derived a 2D model of spray flow in a wind tunnel with a more concentrated spray and larger droplets, illustrating the importance of the interdroplet interactions. Droplet coalescence can change the droplet size and thus droplet dynamics. This paper presents the development of a CFD model capable of predicting spray movement in a complex airflow field. Here, the droplet size distribution (DSD) modelling is only a means to an end, namely, the precise prediction of an LWC spatial distribution. The model showed good qualitative agreement with the experiment. However, additional experimental data were required to give solid quantitative conclusions. Therefore, several input parameters were varied, yielding a sensitivity study of the model.

2. Experimental Setup

Experimental data were recorded in the CIGELE atmospheric icing research wind tunnel of the University of Quebec in Chicoutimi, Canada. Fig. 1a shows a sketch of the tunnel reproduced for the simulation with the coordinate system. The tunnel has a contraction in which airflow is accelerated and turbulence is suppressed. The ratios of the distances between the walls before and after the contraction are approximately 3.75:1 in the vertical direction and 1.25:1 in horizontal direction. The droplets are injected prior to the contraction; thus, the cloud is compressed during the flow. The spray was produced by three nozzles manufactured by Spraying Systems Co. (2050 water cap and 67147 air cap) located in the plane of the inlet.

3. Simulation of Airflow in the Tunnel

3.1 Airflow Boundary Conditions

A turbulent airflow field was simulated in the wind tunnel prior to the spray flow simulation. The inlet boundary conditions were based on the available experimental data and are described below.

Velocity profiles measured in the inlet plane in the vertical and horizontal directions are given in Fig. 1b, along with a fitting curve used in the simulation. The spray bar section follows a corner connected to a vertical duct, causing the velocity magnitude to decrease near the top of the tunnel. Only the vertical velocity profile was used in the simulation as a boundary condition; the horizontal velocity profile was assumed to be uniform. To determine an accurate mean velocity in the test section, the fitted curve was corrected by a factor of 0.93 to account for the assumption

of a uniform horizontal velocity profile and the inaccuracy in the boundary conditions. This factor is the ratio of the mean airflow in the test section to that in the spray bar section.

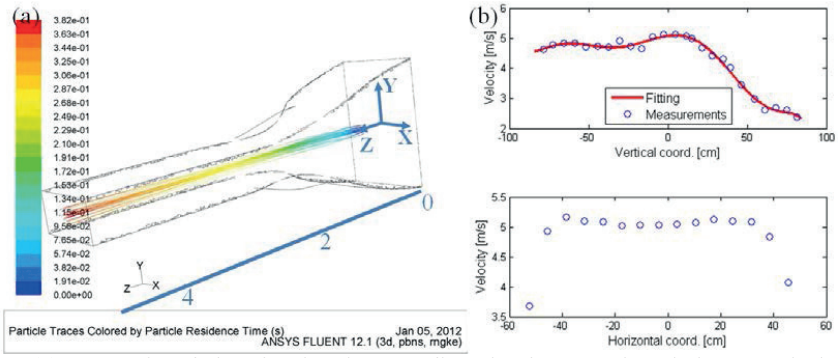

Figure 1. (a) Example of the simulated spray flow in the tunnel and the tunnel sketch. (b) Velocity profile in the inlet and a fitting curve used in the simulations as a boundary condition in the plane z=0.

The turbulence intensity, I_T, of the air measured in the spray bar section (SB) with no spray ranged from 4% to 16%. The mean value of 8% was used as the boundary condition in the simulation. This value is related to the airflow properties by the following equation:

$$I_T = \left(2k/3\right)^{0.5} \Big/ U_{avg} \qquad [1]$$

where k is the turbulent kinetic energy and U_{avg} is the average velocity.

Another parameter required for boundary conditions is the turbulence dissipation, ε, which is related to the turbulence length scale, L_T, by the equation in the FLUENT User's Guide (FUG):

$$\varepsilon = \left(0.09\right)^{3/4} k^{3/2} \Big/ L_T \qquad [2]$$

The size of the honeycomb cell installed before the nozzles is 6 mm. Thus, the estimated size of the turbulent eddy is between several millimetres and several centimetres. However, turbulence can be substantially changed by the injected spray. To obtain information about the effects of the spray on the air velocity and turbulence intensity, the airflow rate from the nozzle was determined. According to the formula given by Kollar et al. (2006), this airflow rate is 7.1e-4 m³/s for the conditions given in Section 4.2. This value is 4 orders of magnitude lower than the total airflow rate in the tunnel; therefore, the spray injection should not significantly affect the average velocity in the tunnel. At the nozzle exit, the spray velocity is approximately 600 m/s, based on the nozzle diameter and the airflow rate. Marek and Olsen (1986) revealed the importance of the interaction between droplets and the air jet, finding a several-percent increase of the turbulence level 5.6 m downstream of the nozzles due to the atomisation of the airflow and the negligible effect on the mean air speed when the air speed in the tunnel was approximately 16 m/s. Abramovich (1963) presented data demonstrating 20% turbulence intensity inside the

turbulent jet relative to the spray velocity in the spray centre. Thus, the spray can substantially change the turbulent properties of the flow.
Therefore, to investigate the effect of the turbulence uncertainty, the calculations were performed using values ranging from 6 to 120 mm for L_T in the SB. The effects of the intensity and length scale are almost interchangeable. Thus, to limit the number of calculations, the turbulence intensity in the SB was set as 8%.

3.2. Flow Field Simulation.

Calculations were performed on a mesh containing prism layers near the wall and tetrahedral elements inside the domain with an edge length of 3 cm. These small elements inside the tunnel were used for the proper modelling of the spray flow, especially the interdroplet interactions. This mesh gave a very good resolution of the flow field; all y+ values (see the FLUENT Theory Guide (FTG) for details) in the wall-adjacent elements were below 20. The total number of elements was 2.6 million. The steady-state flow field in the tunnel was simulated using the steady RANS RNG k-ε model. A non-slip smooth wall condition was assumed for the tunnel walls, and the standard wall function was used.

Fig. 2 and Table 1 show results from the flow field simulation for different initial values of L_T. The dissipation of the turbulence does not affect the average flow field. In all cases, the mean velocities in the test section and the velocity profiles are almost identical. However, the turbulence in the middle of the test section (TS2) varies substantially. Because the average flow field is independent of the velocity fluctuation, their affects can be studied separately.

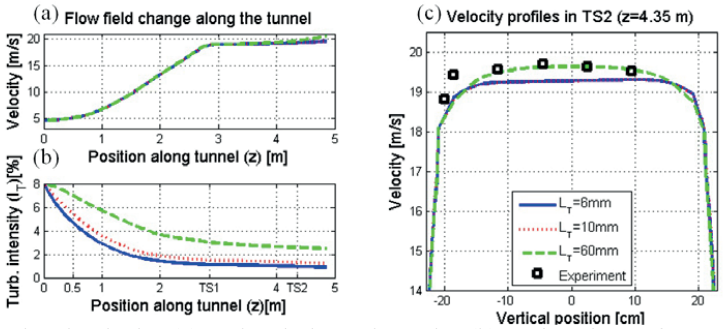

Figure 2. Simulated velocity (a) and turbulence intensity (b) as functions of tunnel position for different inlet turbulence lengths; TS1 is an entrance of the test section (at the end of the contraction). (c) Velocity profiles in the TS2.

Table 1. The dependence of the turbulence intensity in the TS2 on the inlet value for L_T.

L_T [mm]	6	10	20	60	120
I_T [%], TS2	1.0	1.3	1.8	2.6	3.1

4. Droplet Flow Simulation

4.1. Spray Flow Simulation

Droplets were combined into parcels to minimise the computational cost. Each parcel represents several droplets of equal diameter and was tracked individually using the Lagrangian approach in transient mode. The following equation of droplet motion can be found in the FTG:

$$\frac{d\mathbf{V}_d}{dt} = -\frac{3}{4}\frac{C_d}{D}\frac{\rho_a}{\rho_w}\left|\mathbf{V}_d - \left(\mathbf{U}+\mathbf{u}'\right)\right|\left(\mathbf{V}_d - \left(\mathbf{U}+\mathbf{u}'\right)\right) - \mathbf{g}\left(\rho_a/\rho_w - 1\right) \quad [3]$$

where $\mathbf{V}_d$ is the droplet velocity; C_d is the drag coefficient (this paper used the coefficient for a spherical particle); ρ_a and ρ_w are the densities of air and water, respectively; $\mathbf{g}$ is the gravitational acceleration; D is the droplet diameter; $\mathbf{U}$ is the mean air velocity and $\mathbf{u}'$ is the fluctuating velocity due to turbulence.

The turbulent dispersion was taken into account using the stochastic tracking model in FLUENT. Details for this model can be found in the FTG, but a simplified explanation is that the random fluctuation of the flow field velocity, $\mathbf{u}'$, is introduced when the motion of each parcel is calculated. The magnitude of the fluctuations is constrained by the turbulence intensity of the flow field. Their random values are kept constant over an interval of time needed to cross the turbulent eddy or equal to the eddy characteristic lifetime, T_e:

$$T_e = C\,k/\varepsilon \quad [4]$$

where C is a constant. Per the FTG's recommendations for the k-ε model, a value of 0.15 was used for C. Note that Marek and Olsen (1986) used the coefficient 0.2 in their work.

The droplet thermodynamics were not taken into account in this work because a main goal of this work was to test the O'Rourke's algorithm for droplet interactions. The possibility of droplet break-up was also excluded because the droplets are very small. See Faeth et al. (1995) for the details of the conditions needed for droplet break-up. The O'Rourke algorithm does not track collisions explicitly. Only droplets located within the same mesh cell can interact. The interaction probability of two droplets from two different parcels is calculated based on the ratio of a collision volume to the volume of the mesh cell, V_{cell}. The collision volume is estimated based on the droplets' relative velocity, V_{rel}, the calculation time step, Δt, and the droplets' radii, r_1 and r_2. The collector, the largest droplet of the two parcels (radius r_1, amount in parcel n_1), is exposed to the following mean number of expected collisions (FTG):

$$k = n_2\pi\left(r_1 + r_2\right)^2 V_{rel}\Delta t / V_{cell} \quad [5]$$

The probability distribution for the number of collisions follows the Poisson distribution:

$$P(M) = e^{-k}\,M^k / M! \quad [6]$$

where M is the number of collisions between a collector and the other droplets. Details on the O'Rourke method and the collision outcome can be found in the FTG or in O'Rourke (1981).

4.2. Spray Initial Conditions

The nozzles were supplied with a water pressure of 4.5 bar, and the air pressure was 4.8 bar. These nozzles sprayed water at a flow rate of 1.9 g/s. In the simulation, droplets were injected at a distance z_0=0.4 m from where the DSD was measured (Kollar et al., 2006). No spatial variation of the DSD was assumed in this plane. Only spray from one nozzle was simulated; it was assumed that the use of two side nozzles does not affect vertical distribution of the DSD and the LWC in the centre of the TS2. Droplets were injected from the surface on the z_0 plane with a certain radius, R_c, and discrete time step, Δt_{inj}. The radius was taken from Kollar et al. (2005), where the radius was calculated based on the assumption of a known spray angle and a distance from the nozzle of 0.5 m. Here, the same cloud radius was assumed at a distance of 0.4 m because the spray pattern (the variation of the spray flow density in a radial direction perpendicular to the spray flow direction) was unknown and the spray radius is rather uncertain in this case.

Some examples of possible spray patterns and their variations due to a change in the total flow rate through the nozzle are given in Yigit et al. (2011) and Pougatch et al. (2009). To investigate the effect of uncertainty in the spray pattern and the spray diameter, several spray patterns were constructed. In agreement with the function of the admixture concentration distribution inside turbulent jets given by Cushman-Roisin (2010), the following ratio of the spray flow rate at a distance r from the centre to the mean spray flow rate was used:

$$q_f(r) = Q_0/Q_m \cdot exp\left(-r^2/B\right) \qquad [7]$$

where Q_0/Q_m is the ratio of the maximal spray density to the mean spray density and coefficient B is chosen so that the total flow rate is described as follows:

$$F_{total} = \pi R_c^2 \cdot Q_m = \pi B \cdot Q_0 \left(1 - exp\left(-R_c^2/B\right)\right) \qquad [8]$$

The last expression was obtained by integrating Eq. [7] and multiplying by Q_m over the cloud area. Three pattern profiles are plotted in Fig. 3c.

The spray injection was divided into small surfaces separated along the radial and angular directions with constant steps, Δr and $\Delta\alpha$. The water flow from each surface was proportional to its surface area as follows:

$$F_p\left(r_j, \alpha_k\right) = \Delta\alpha \int_{r_j-\Delta r/2}^{r_j+\Delta r/2} q_f(r) \cdot Q_m r dr \qquad [9]$$

The centres of the surfaces (indicated with red circles) with the coordinates r_j and α_k are plotted in Fig. 3b for the case of four radial steps, N_R=4, and twelve angle steps, N_α=12. The F_p of each surface was then divided among droplet bins in accordance with the spray DSD. Each bin from each surface was simulated as one parcel, and each parcel was tracked separately.

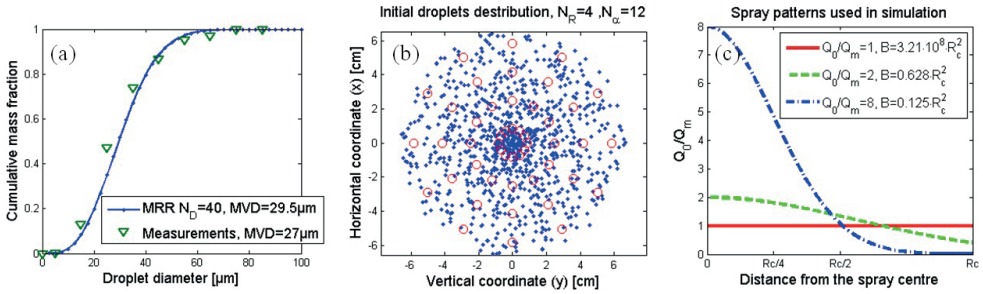

Figure 3. (a) Experimental cumulative DSD and examples of distributions used in the simulation. (b) Example of the injection surface discretisation. (c) Example of pattern profiles used in the simulations.

The cumulative DSD in the simulations was approximated using the modified Rosin-Rammler distribution as follows:

$$Q(d) = 1 - exp\left[(d/X)^q\right] \qquad [10]$$

where X=34.88 µm; q=10.1; and $Q(d)$ is the cumulative mass fraction of droplets with a diameter smaller than d. Fig. 3a shows the measured cumulative distribution and the cumulative DSD used in the simulations. In simulations, all bins were separated with constant step and with total number N_D. For example, in the case where N_D=40, the diameter ranges were specified with a step size of 2.5 µm as follows: D_i=2.5, 5...100 µm. Thus, the parcel representing diameter D_i from the surface j, k exhibited the following water mass flow rate:

$$\left[Q(D_i + 1.25\mu m) - Q(D_i - 1.25\mu m)\right] \cdot F_p\left(r_j, \alpha_k\right) \qquad [11]$$

Adjustments in Section 5.1 of the model will give the proper choice for N_D. The total number of parcels in each simulation was as follows:

$$N_{total} = N_R \cdot N_\alpha \cdot N_D \cdot N_{inj} \qquad [12]$$

where N_{inj} is the number of injections. The initial position of each parcel's interior surface was randomised:

$$\begin{aligned} r_{j,i} &= r_j - \Delta r / 2 + \Delta r \cdot rand(\ ) \\ \alpha_{k,i} &= \Delta\alpha \cdot k + \Delta\alpha \cdot rand(\ ) \end{aligned} \qquad [13]$$

where k is the angle index; j is the radius index and i is the bin index.

The initial spray horizontal velocity, V_{z0}, was set to 20 m/s. The transversal velocity was directed from the cloud centre, and its absolute value was proportional to the distance from the centre of the cloud:

$$V_t(r_i) = V_{z0} \cdot r_i / z_0 \qquad [14]$$

5. Results and Discussion

Calculations were performed in parallel using 10 processors; each simulation took approximately 5 h. Several simulations of the droplet flow were performed, most of which were used to obtain a setup of the O'Rourke's algorithm that would produce a stable result. The results are presented in the following order: 1) Adjustment of the model, 2) Examples of the spray cloud evolution and 3) Sensitivity studies.

Properties of the modelled spray are compared with available measurements of the LWC and the median volume diameter (MVD) at a distance of 4.35 m from the nozzle (TS2). The LWC was measured with an accuracy of 10-15% using a Cloud imaging probe manufactured by Droplet Measurement Technologies, Inc.

5.1. Adjustment of the Model

The literature contains little information on the setup of the O'Rourke algorithm. Several investigations were performed in this work to obtain stable solutions. The main goal was to obtain the accuracy needed for engineering simulations, treating an accuracy of 1 to 5% as acceptable. In addition, the simulations were performed on an unstructured mesh that did not create artefacts near a cell face (for examples of possible artefacts, see Schmidt and Rutland (2004)). It is important to note that the given result is likely only valid for this particular case, but the general logic and procedures can be used for any other spray flow simulation. The cases are described in Table 2, and the selected numerical parameters are highlighted. The convergence of the results depends strongly on the sampling window, which should be sufficiently small to resolve particular processes in the spray but large enough to enable averaging of the stochastic simulation. The applied sampling window was a 3.8 cm square.

- **Injections amount.** The transient mode was used for the simulation, and the simulated spray had a finite duration. The interdroplet interactions require that each droplet be surrounded by other droplets to simulate an infinite spray. A sufficient spray injection duration is needed to obtain such a condition. It was determined that 500 injections are enough to yield an accuracy of better than 2%.
- **The calculation and injection time step.** The injection time step affects the distance between two sequential injections. If this time step is too large, droplets from different injections will be in different cells and will not interact. The time step should be less than 1.5 ms, which was determined according to the ratio of the cell edge length (3 cm) to the airflow velocity in the TS2 (20 m/s). However, if the time step of injections or calculations is too small, numerical errors could arise and the probability of an interaction will be suppressed numerically. The results in Fig. 4a show that a good MVD profile is obtained when the time step is approximately 1 to 0.5 ms. The interdroplet interactions did not affect the LWC. The interdroplet interactions were weaker when the time step was increased or decreased by one order of magnitude.
- **Cloud spatial resolution.** Two cases were investigated, which yielded similar results. However, a greater number of cells (N_R=8, N_α=20) were used in later calculations because they resolved the radial variation of the initial pattern case (Q_0/Q_m=12) better.

This change did not affect the final result for a given turbulence level. However, pattern resolution becomes more important for lower turbulence.

- **Cloud bin resolution.** Fig. 4b shows that even the use of 10 bins yields good accuracy. When the number of bins is between 20 and 99, the agreement of the results is especially good where the LWC is greatest (vertical position of 0 to 2 cm, see Fig. 4b).
- **Mesh resolution.** The influence of the mesh resolution on the droplet flow was not investigated in this paper. It was assumed that the mesh was sufficiently fine to yield accurate results (the mesh size was 3 cm and the spray diameter at z=0.4 m was 13 cm).
-

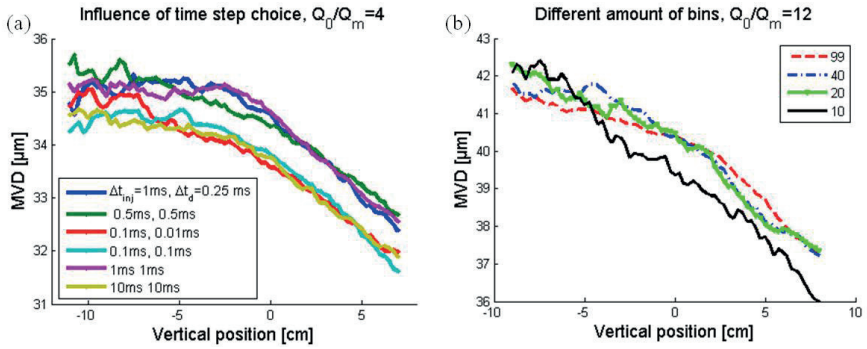

Figure 4. (a) Effect of the droplet injection step and calculation step on the MVD profile accuracy in plane the TS2. (b) Effect of the number of bins on the accuracy of the MVD profile calculation (100 bins in the range from 0 to 100 were used for plotting)**.**

Table 2. Summary of investigated cases that were used to obtain a stable solution

Cases	Δt_d[ms]	Δt_d [ms]	N_R	N_α	N_{inj}	N_d	Q_0/Q_m	L_T
Injection Amount	1.0	0.25	4	12	20,100, **500**,5000	56	4	6 cm
Time step	**1.0** 0.1 0.1 **0.5** **1.0** 10	**0.25** 0.01 0.1 **0.5** **1.0** 10	4	12	500	56	4	6 cm
Spatial resolution	1.0 0.5	1.0 0.5	4 **8**	10 **20**	500	56	12	6 cm
Bins resolution	0.5	0.5	8	20	500	99,40,**20**,10	12	6 cm
Resulting setup:	**1.0**	**1.0**	**8**	**20**	**500**	**20**		

In principle, for the given case of LWC, the errors in the DSD calculation did not strongly affect the vertical LWC profile. Table 2 shows the spray parameters (Q_0/Q_m, L_T) used for each investigation. The choice of numerical parameters is case-dependent; although the optimal numerical parameters for high concentrations will give good results for lower spray concentrations, the opposite is not true.

5.2. Flow and Evolution of the Spray

This section presents examples of the spray evolution for two turbulence conditions (L_T=20, 60 mm) and two types of patterns (Q_0/Q_m=1, 12). All conclusions are based purely on the model and thus, they are valid only if the model reliability is proven, which requires more data.

Fig. 5b shows the change of the cloud MVD averaged in the vertical plane (MVDA) at a given streamwise position when the spray flows along the tunnel. This value represents only the results of droplet scattering and coalescence and excludes the effects of the turbulent mixing. Less turbulence results in a higher MVDA because the spray spreads less. Most of the interactions occur within 1 m of the nozzle.

In the case of Q_0/Q_m=12, Fig. 5a shows a 7 µm increase of the MVD along the axis in the middle of the tunnel between positions z=0.5 m and z=0.8 m. Further along the tunnel, the MVD peak value decreases due to the turbulence dispersion and moves downward due to gravity. Kollar and Farzaneh (2007) also found that the turbulence affects the mixing of the droplets. Low turbulence results in vertical stratification of the MVD and high turbulence yields a more uniform profile.

The main factor affecting the LWC evolution is turbulence (Fig. 6). In the involved case of low LWC, the initial uncertainty of the cloud diameter and pattern does not affect the LWC at a distance of 4.35 m. In the case of comparatively high turbulence (2.6% in the TS2, L_T=60 mm), the difference in the vertical LWC profile between the two different patterns is less than the computational accuracy of 2%. However, the effect of the initial pattern on the MVD is significant. The initial pattern with Q_0/Q_m=12 gives a higher MVDA and a better agreement with the experimental value at z=4.35 m. Specifically, there is an 8% maximal relative divergence in this case in contrast to 23% in the case with Q_0/Q_m=1 (see Fig. 5a for L_T=60 mm).
The LWC profile peak first moves upwards and then downwards after z=1.5 m due to gravity (see Fig. 6). This effect reflects the non-uniformity of the inlet velocity profile (Fig. 1b). Higher air velocity in the lower part of the tunnel pushes droplets up. Later, the airflow mixes and becomes uniform (Fig. 2c). Thus, the position of the LWC peak is primarily related to air velocity non-uniformity, but the cloud diameter is related to the turbulence level.

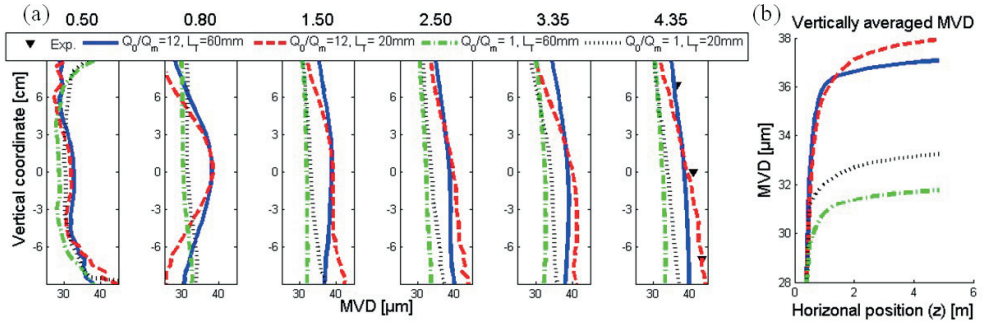

Figure 5. (a) Evolution of the spray vertical MVD profile along the tunnel (titles show the horizontal position of the spray along the tunnel). (b) Evolution of the horizontally averaged MVD along the tunnel.

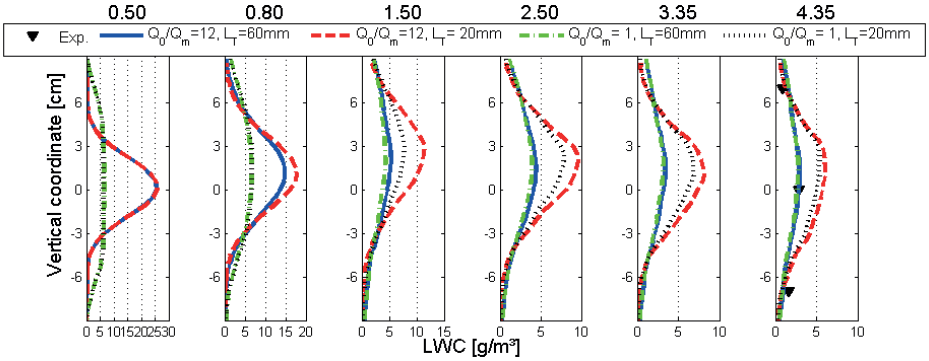

Figure 6. Evolution of the vertical LWC profile along the tunnel

5.3. Effect of Flow Pattern and Turbulence

Section 5.4 will show more clearly that the velocity profile is the main determinant of the position of the LWC maximum. Here, the effects of the turbulence and the spray pattern are shown.

The exact position of the maximum LWC is uncertain. The peak LWC (usually 1.5 cm above the centre of the tunnel) is compared with the measured values of the LWC in the centre of the TS2 in Fig. 7b and Fig. 8b. The experimental and computed MVD values are compared in the centre of the TS2. The obtained results (see Fig. 7a and Fig. 8a) show that the MVD is mainly affected by the initial flow pattern, while the effect from the turbulence is much weaker. On the other hand, the LWC is mostly affected by the turbulence dispersion (Fig. 7b). The effect of the flow pattern on the maximal LWC vanishes completely when the turbulence intensity in the test section is above 2.6% (L_T=60 mm). When the intensity is 1% (L_T=6 mm) the choice of the spray pattern can vary the maximal LWC value by up to 50% (Fig. 8b). In addition, Fig. 7c and Fig. 8c show the ratio of the LWC at a distance of 7 cm from the position of the LWC peak to the maximal LWC value. These figures show that the ratio is almost independent of the pattern and only related to turbulence. The offset between the curves of different patterns in Fig. 7c is within the range of computational accuracy.

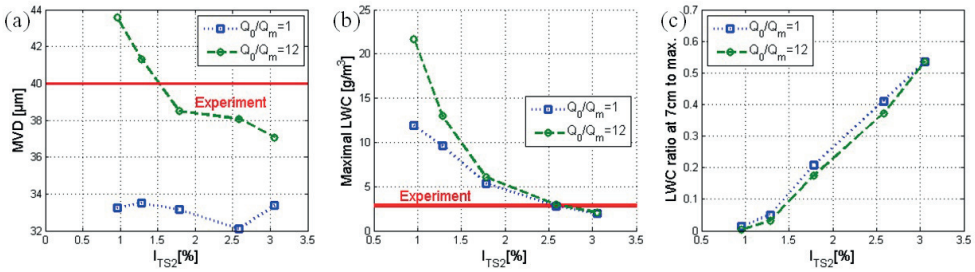

Figure 7. Effect of turbulence on the spray properties in the TS2 (z=4.35 m).

The best fit of the calculated results to the experimental data among the performed calculations was obtained when Q_0/Q_m=12 and L_T=60 mm. This case is further studied in the next section.

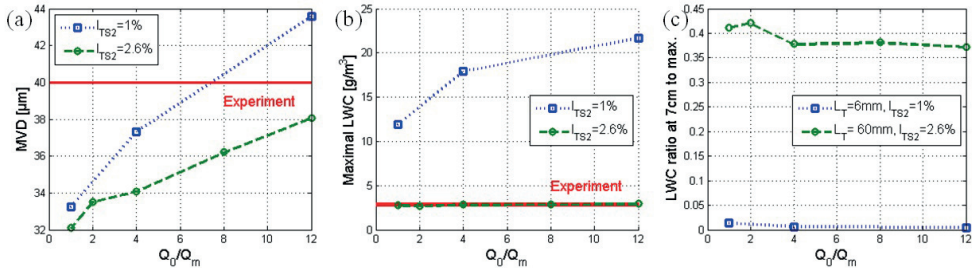

Figure 8. Effect of initial spray pattern (z = 0.4 m) on the spray properties in the TS2.

5.4. Effect of Flow Field

The inlet air velocity conditions used in the all of the previous calculations were changed to investigate their effects on the LWC. The velocity profile shown in Fig. 1b was replaced by a uniform profile with a constant velocity of 4.28 m/s (UV). The result of the UV simulation is shown in Fig. 9a-c with results calculated using the velocity profile shown in Fig. 1b (VP). Fig. 9a shows that the MVD does not depend on the velocity profile.

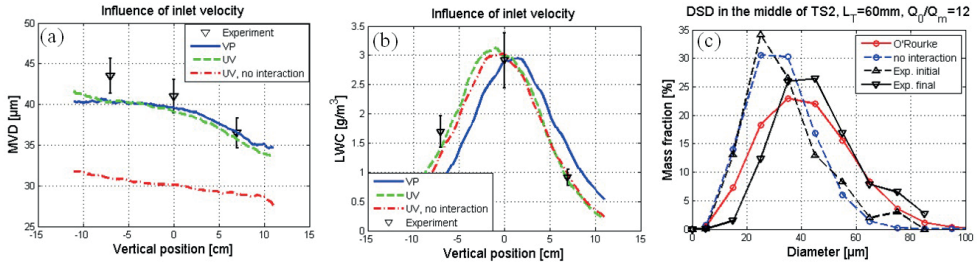

Figure 9. (a) MVD profiles for the three simulations (for the VP case, the measured velocity profile was used as a boundary condition, while for the UV case, a constant velocity was used in the inlet. (b) LWC profile. (c) Mass fraction distribution of droplets (simulations for the UV case).

Fig. 9a and Fig. 9b show a very good agreement between the simulation results of UV case and those of the experiments for both the MVD and LWC vertical profiles. Thus, issue at hand is whether the assumption that the velocity profile is horizontally uniform correct or should the VP be measured in more detail across the plane z=0, not only along the lines of x=0 and y=0. In addition, Fig. 9a-c show results for the case where the interdroplet interactions were not considered. As is clear, the exclusion of the interaction for the given case does not significantly affect the LWC profile, even though the difference in the MVD between these two cases is approximately 10 μm. Thus, for an LWC value of up to 10 g/m³, the interdroplet interaction can be neglected. The LWC value obtained in the UV case without this interaction lies above the profile of the UV case. This result shows the combined effects of droplet interactions and

gravity, even though these effects are very small in the given case. In addition, Fig. 9c shows that the UV case for the DSD in the middle of the TS2 agrees well with the experimental results.

5.5 Injection Spray Velocity

Two cases, Q_0/Q_m=12 and L_T=6 and 60 mm, were investigated because they yield different LWC behaviours. For each case, the initial spray velocity was set to 4, 20, and 50 m/s, and the results were compared. No significant effect on the LWC was observed, and the maximal difference between the vertical MVD profiles was less than 3 μm. Thus, we can conclude that the initial spray velocity does not affect the simulation results.

6. Conclusion

This paper described a 3D model of spray flow in a wind tunnel, considering the interactions between droplets using the O'Rourke algorithm. The numerical model setup was varied to obtain conditions that yield a stable solution; the setup is given in Table 2. Furthermore, this paper discusses the complexity of the spray flow modelling and the importance of boundary conditions. It was shown that there are insufficient available experimental data to properly validate the model. When parameters that are unavailable in the literature were set to certain values (specifically, Q_0/Q_m=12 and L_T=60 mm), the model provides a reliable estimate for the LWC and the DSD and for their vertical variations in the test section.

The model results imply the following:

- For a given case (MVD 30-50 μm and LWC less than 20 g/m³), the droplet interactions only weakly affect the final LWC and can be neglected in engineering calculations. The droplets are too small to exhibit significant height stratification, and the LWC is too low to induce intense droplet interactions. The created model reveal the effect of the interdroplet interactions on the DSD; in the case with Q_0/Q_m=12, the MVD increases by approximately 10 μm.
- A non-uniform air velocity profile at the spray bar affects the vertical position of the spray.
- The turbulence of the airflow affects the spray LWC dispersion. High turbulence (above 2.6% in the TS2) obscures the effect of the initial spray pattern on the final LWC. This result is useful for small-scale experiments because a uniform spray produces a uniform ice accretion on the objects, which is easier to model. The same effect is described by Marek and Olsen 1986.
- The most significant droplet interactions occur within 1 m of the nozzle. The initial pattern of the cloud has a stronger effect on the final MVD than turbulence does because most interactions occur close to nozzle exit.
- In the simulation, the initial spray velocity (z= 0.4 m) does not affect the result.

The information given above shows that for proper model validation, the following measurements should be performed and added to the existing data on spray LWC and DSD:

- More data should be collected related to the airflow and turbulence, especially when the spray is injected, including spatial variation along the tunnel.
- The spray pattern and the width of the cloud at z_0=0.4 m should be measured.

Acknowledgments

This work is part of the MARICE project related to sea spray icing on offshore structures and vessels. The project is a joint industry project between Det Norske Veritas, Statoil, the Norwegian University of Science and Technology, and the Research Council of Norway.

References

Abramovich G.N., 1963. The theory of turbulent jets. MIT Press

Cushman-Roisin B., 2010. Environmental fluid mechanics. John Wiley&Sons, Inc., New York

Faeth G.M., Hsiang L.-P., Wu P.-K., 1995. Structure and breakup properties of sprays. International Journal of Multiphase Flow, 21, Suppl., 99-127

Kollar L.E., Farzaneh M., Karev A.R., 2005. The role of droplet collision, evaporation and gravitational settling in the modelling of two-phase flows under icing conditions. Proc. of the 11th International Workshop on Atmospheric Icing of Structures, Montreal, Canada.

Kollar L.E., Farzaneh M., Karev A.R., 2006. Modeling droplets size distribution near a nozzle outlet in an icing wind tunnel. Atomization and Sprays, 16(6), 673-686

Kollar L.E., Farzaneh M., 2007. Modeling the evolution of droplet size distribution in two-phase flows. International Journal of Multiphase Flow, 33, 1255-1270

Marek C.J. and William A.O. Jr., 1986. Turbulent dispersion of the icing cloud from spray nozzles used in icing tunnels. Proc. of the 3rd International Workshop on Atmospheric Icing of Structures, Vancouver, Canada, 103-110.

O'Rourke P.J., 1981. Collective drop effects on vaporizing liquid sprays. PhD thesis. Princeton University, Princeton, New Jersey

Pougatch K., Salcudean M., Chan E., Knapper B., 2009. A two-fluid model of gas-assisted atomization including flow through the nozzle, phase inversion, and spray dispersion. International Journal of Multiphase Flow, 35, 661–675

Schmidt D.P. and Rutland C.J, 2004. Reducing grid dependency in droplet collision modelling. ASME Journal of Eng Gas Turb Power, 126, 227-255

Stallabrass J.R., 1980. Trawler icing a compilation of work done at N.R.C. Technical report National Research Council of Canada No 19372

Yigit C., Sozbir N., Yao S.C., Guven H.R., Issa R.J, 2011. Experimental measurements and computational modelling for the spray cooling of a steel plate near the Leidenfrost temperature. Journal of Thermal Science and Technology. TIBTD Printed in Turkey ISSN 1300-3615, 27-36

21st IAHR International Symposium on Ice
"Ice Research for a Sustainable Environment"
Dalian, China, June 11 to 15, 2012

Full-scale 3D CFD Simulation of Spray Impingement on a Vessel Produced by Ship-wave Interaction

Anton Kulyakhtin[1,4*], Olga Shipilova[2], Bradd Libby[2] and Sveinung Løset[1,3]
1. Norwegian University of Science and Technology, Trondheim, Norway
2. Det Norske Veritas, Oslo, Norway
3. Sustainable Arctic Marine and Coastal Technology (SAMCoT), Centre for Research-based Innovation (CRI), Norwegian University of Science and Technology, Trondheim, Norway
4. The University Centre in Svalbard (UNIS), Longyearbyen, Norway
**anton.kulyakhtin@ntnu.no*

This paper presents full-scale simulations of spray flow and its interaction with the hull and superstructure of a ship. Simulations are performed for one particular vessel, which was also chosen for future measurements of the spray properties produced by ship-wave interaction. Particular areas of equipment installation are of special interest. All of the simulations are conducted in ANSYS FLUENT using a mixed Eulerian-Lagrangian approach. The output of the simulations is the distribution of spray flow rate per unit area on the vessel surface. In the current work, ship dynamics are not included in the model. To estimate the generated spray, the empirical equation for the liquid water content of the droplet cloud in front of the ship is used. The model for the spray flow neglects thermodynamics and interactions between droplets. However, it accounts for the air flow field around the vessel, which is calculated using the Reynolds-averaged Navier-Stokes approach. The main goal of this paper is to demonstrate the potential of computational fluid dynamics to improve the prediction of icing rates via accurate spray flow calculations. The calculations are performed for several wind speeds, and the spray droplet size distribution is described by two different approaches: using one representative droplet size for the whole cloud and dividing the droplet size distribution into bins, each of which represents one droplet size.

1. Introduction

The marine icing of vessels may endanger the operations and even the stability of vessels. Icing is of particular interest because waters prone to icing host an increasing number of activities related to exploration and production of hydrocarbons. In addition, a detailed scientific understanding of this phenomenon and ability to predict icing is important because of operational issues and the frequency of ship accidents caused by ice formation on the ship deck and superstructure. The main body of research devoted to marine icing, also known as sea spray icing, was conducted in the 1970s, 1980s and early 1990s. Currently, the plans for increasing the exploration of the northern and Arctic seas have renewed interest in the problem of icing. Advanced computational fluid dynamics (CFD) techniques and new computer technologies allow the investigation of this phenomenon on a more detailed level than was possible previously.

The process of sea spray icing due to the ship-wave interactions can be divided into three main stages: 1) the generation of the sea spray due to the ship-wave interaction, 2) the flow of the spray (i.e. the cloud of water droplets) around the superstructure of the ship and 3) droplet impingement with the ship structure with the following water run-off and freezing.

In this work, we focus on the second stage of the process. The main purpose of the study is to determine how an accurate air flow simulation around a vessel can improve the prediction of the icing rate. We consider a particular ship, which represents supply vessels. It is approximately 100 m in length and has the bridge in the front of the main deck. A series of simulations is conducted in quasi-static mode that neglects the interaction of the ship with the sea and does not include dynamics of the ship. The liquid water content (LWC) and droplet size distribution (DSD) are the properties of the spray that we consider in this paper. The spray is injected in front of the vessel in the plane perpendicular to the ship heading. After the droplets are tracked in the air flow, the intensity of the water inflow on the ship is estimated from the amount of droplets interacting with the surface. For the first iteration, we assume a uniform spray distribution using the droplet size and LWC. The simulation results are presented as the ratio of the spray inflow per unit area on the ship surface to the flow rate per unit area of the injection, referred to as the *collection efficiency*, E, in the rest of the paper. Furthermore, the Zakrzewski function (Zakrewski, 1986) is used to estimate the spray inflow on the surface of the ship.

For comparison, we consider the case of a constant air flow speed over the ship. The influence of the inclusion of the turbulent fluctuations into the air movement when the droplets are tracked is also addressed. In the future, the developed CFD model will be validated with vessel measurements. Thus, the areas of the maximum and minimum droplet accumulation are of special interest for the equipment installation.

The paper is organised as follows. Section 2 gives the description of the proposed CFD model. Section 3 presents the results of the model applied to two wind speeds and two values of median volume diameter (MVD) for the spray. Next, the effect of the assumption on the air and droplet flows is addressed in Section 4. The dependence of the spray flow on MVD and DSD is discussed in Sections 5 and 6, respectively. In Section 7, the Zakrzewski function for the spray generation is included in the simulations.

2. Model Description

The CFD model applied in this work considers only dynamics. In the case of the spray generated by the ship–wave interaction, Lozowski et al. (2000) stated that effect of evaporation on droplet mass is negligible and therefore thermodynamics can be neglected. The model consists of two parts: 1) the air flow over the ship and 2) the movement of the cloud of droplets in the calculated air flow. A detail description of each part is given below.

The computational domain for the air flow simulations is a box, the bottom surface of which coincides with the water surface. We consider a 5 m draft of the ship. The coordinate system is associated with the ship. Initially, we assume that the ship has zero pitch and yaw. Along the *x*-axis of the ship, the length of the box from the centre to either edge is 4.2 ship lengths, *L*, giving an overall length of 8.4 *L*. In the *y*-axis of the ship (i.e. lateral direction), the width of the box from the centre to either edge is 3.9 *L*, giving an overall width of 7.8 *L*. The box height is approximately 1.5 *L*. The computational mesh consists of prismatic elements with finer resolution in the ship vicinity.

Reynolds averaging of the Navier-Stokes system is applied for the turbulence modelling in ANSYS FLUENT. All variables (velocity, pressure, energy, etc.) are substituted in the Navier-Stokes equations with their decomposition into the mean (or averaged) and fluctuating components. The new terms in the system represent the effects of turbulence, which should be defined from an additional set of equations. The *k*-ε model is one of the approaches used to determine turbulence and yields two additional equations: one for the turbulence kinetic energy *k* and one for the turbulence dissipation rate ε. The standard *k*-ε model is widely used for fully turbulent flows. In our work, we apply its modification based on renormalisation group theory, the RNG *k*-*ε* model. This model is more flexible and accurate due to the additional terms included in the system and the formula-based definition of the governing parameters in contrast to the standard *k*-ε model. Namely, the transport equations in RNG *k*- ε model are

$$\frac{\partial}{\partial t}(\rho k)+\frac{\partial}{\partial x_i}(\rho k u_i)=\frac{\partial}{\partial x_j}\left(\alpha_k \mu_{eff}\frac{\partial k}{\partial x_j}\right)+G_k-\rho\varepsilon \qquad [1]$$

for the kinetic energy and

$$\frac{\partial}{\partial t}(\rho\varepsilon)+\frac{\partial}{\partial x_i}(\rho\varepsilon u_i)=\frac{\partial}{\partial x_j}\left(\alpha_\varepsilon \mu_{eff}\frac{\partial \varepsilon}{\partial x_j}\right)+C_{1\varepsilon}\frac{\varepsilon}{k}G_k-C_{2\varepsilon}\rho\frac{\varepsilon^2}{k} \qquad [2]$$

for the dissipation rate. Here, ρ is the density, u_i are the velocity components, G_k is a source function due to the mean velocity gradients, and the quantities α_k and α_ε are the inverse effective Prandtl numbers for *k* and ε. For more details on calculating G_k, we refer the reader to the Theory Guide for ANSYS FLUENT.

Two wind speeds relative to the ship are considered: 15 and 25 m/s. It is assumed that the ship is heading into the wind. The boundaries in front and on sides of the ship are defined as the inlet. Here, the *x*-component of flow velocity is set to the considered wind speed, while two other components are equal to zero. Additionally, the free stream turbulence intensity is set to 15 % on

the inlet. The turbulent length scale of 20 m on the inlet is chosen to keep the turbulence properties constant in a mesh cell far from the ship. The boundary behind the ship is the outlet, where the outlet pressure is set. The sea surface and the ship surface are considered no-slip walls. The upper boundary (above the ship) is a wall with a zero-shear condition. The initial conditions in the domain are calculated from the inlet.

The details of the setup and procedure of the droplet flow calculation is given by Kulyakhtin et al. (2012). The droplets are tracked with the equation of motion in the Lagrangian frame of coordinates

$$\frac{d\mathbf{u}_d}{dt} = \mathbf{F}_d\left(\mathbf{u}-\mathbf{u}_d\right)+\frac{\mathbf{g}\left(\rho_d-\rho\right)}{\rho_d}, \qquad [3]$$

where $\mathbf{u}_d$ and ρ_d are the droplet velocity and density, respectively; $\mathbf{u}$ and ρ are the flow velocity and density and $\mathbf{g}$ is the gravitational acceleration, equal in our case to (0,0,-9.81). $\mathbf{F}_d$ is the drag force per unit droplet mass defined as

$$\mathbf{F}_d = \frac{3\mu C_d\, Re}{4\rho_d D_d^2} \qquad [4]$$

where μ is the molecular viscosity of the fluid in the flow, D_d is the droplet diameter, ***Re*** is the relative Reynolds number and C_d is the drag coefficient for a spherical particle.

For the initial conditions, droplets are injected 5 m in front of the ship bow. The cloud width in the *y*-direction is 2 beams of the ship and equal to 40 m. The initial speed of droplets is set to zero. The maximum cloud height is 21.6 m, which coincides with the highest point of the ship superstructure. Droplets are distributed uniformly inside the injection plane. The distance between droplets is set to 2 cm to minimise numerical errors. The minimum size of surface cells on the ship is 6 cm.

To simplify the result analysis, the top of the ship is split into 7 surfaces from the bow to the stern - *Deck, SF1, SF2, SF3, SB, BD1, BD2* - as shown in Fig. 1. It is important to note that the ship is split into surfaces in accordance with their height and distance from the spray injection. Later, the collection efficiency *E*, which is calculated as the ratio of the average spray inflow rate per unit area on each surface to the initial spray cloud spray flow rate per unit area, is analysed.

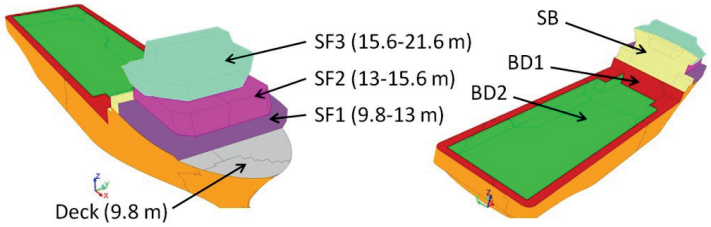

Figure 1. Division of the ship into the surfaces and the height extension above the sea level for the front surfaces.

3. Determination of Droplet Impingement on the Ship's Surface

In this section, the results for two wind speeds and two values of the median volume diameter (MVD) are presented (see Finstad et al. (1988) for the definition of MVD). The goal of the simulations is to study the dependence of the droplets' spreading and trajectories on the wind speed and MVD. Four simulations are performed for each wind speed (15 and 25 m/s) and droplet diameter (250 and 2000 μm) combination. Natural spray has exponential vertical distribution of LWC; thus, it is important to consider droplet trajectories and spray motion from different height levels. In each simulation, droplets are injected in one of the specified intervals: 0-9.8 m, 9.8-13 m, 13-15.6 m and 15.6-21.6 m. These intervals are chosen in accordance to the vessel structure, see Fig. 1. It is assumed that the LWC of the cloud is uniform, and DSD is presented by one representative size equal to MVD.

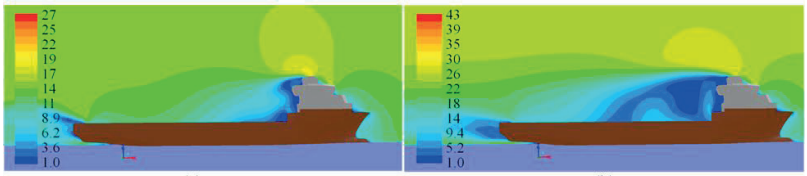

Figure 2. The velocity field over the top of the ship in the plane along the ship centreline: 15 m/s wind speed – (a), 25 m/s wind speed – (b).

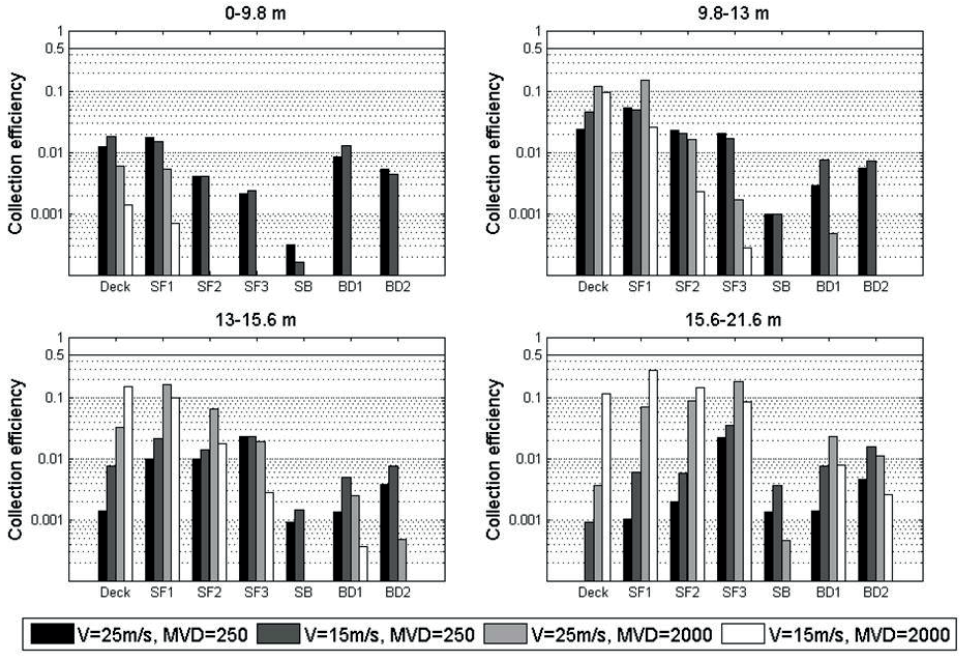

Figure 3. Collection efficiency E for wind speeds of 15 and 25 m/s and a MVD of 250 and 2000 μm. The value of E is represented for ship surfaces from the bow to the aft. Each bar plot presents results obtained for the droplets injected in the height interval.

Fig. 2a shows the calculated flow for the initial wind speed of 15 m/s in the plane along the centreline of the ship. The maximum flow velocity reaches 32 m/s for this wind speed. The stronger wind, 25 m/s, results in the maximum velocity of 44.5 m/s and stronger vorticity behind the bridge, see Fig. 2b. Figs. 3, 4 and 5 demonstrate the collection efficiency for both MVDs and both wind speeds with respect to the ship surfaces; see Fig.1 for the surface legend.

Fig. 3 gives a quantitative assessment of the water inflow on the ship surface. In general, smaller droplets, 250 µm MVD, produce more uniform spray inflow. Small droplets can easily flow around and over the superstructure of the ship. The 2000-µm-diameter droplets settle mostly in the ship front. The air flow generated by the stronger wind, 25 m/s, is able to lift droplets higher and results in a less uniform collection efficiency.

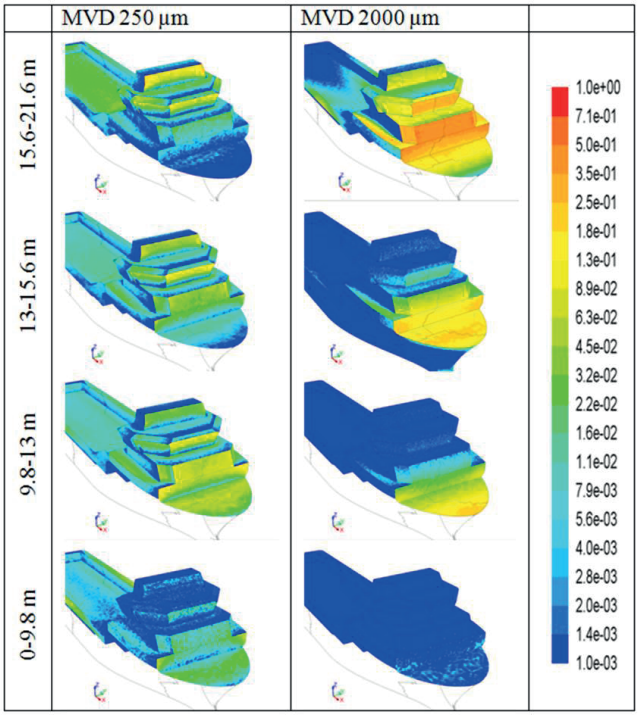

Figure 4. Collection efficiency *E* for a wind speed of 15 m/s and a MVD of 250 and 2000 µm.

Figs. 4 and 5 can be used to qualitatively analyse the water inflow distribution. First, the droplets accumulate on the sides of the ship, which is not intuitive considering that the ship heading is into the wind. The generated boundary layer in the air allows droplets to flow around the ship structure and to settle not only on the surfaces perpendicular to the heading. This behaviour is especially pronounced for the weaker wind speed, 15 m/s, and light droplets, 250 µm MVD.

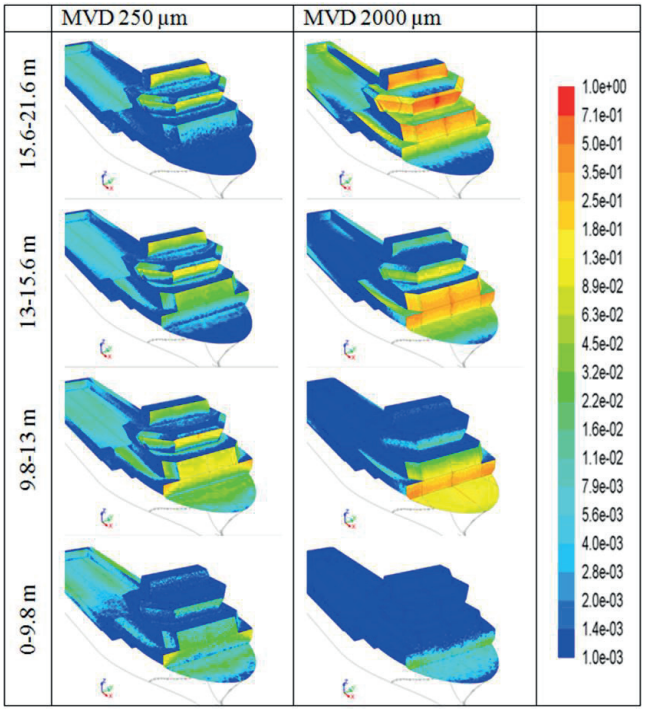

Figure 5. Collection efficiency *E* for a wind speed of 25 m/s and a MVD of 250 and 2000 µm.

Second, the flow and the profile of the water inflow behind the bridge are interdependent. In the case of a MVD of 250 µm, the 15 m/s wind speed gives a more uniform profile over the deck and its sides than the 25 m/s wind speed. The larger vorticity produced by the stronger wind results in a higher collection efficiency in the middle of main deck than on the sides. In the case of the heavy droplets, with a MVD of 2000 µm, it is worth emphasising the results for the highest cloud (15.6-21.6 m). Of the droplets that overflew the superstructure, the majority settled just behind the bridge for the 15 m/s wind, while the main accumulation region was shifted to the aft of the ship for the 25 m/s wind.

In summary, the results from this section indicate non-monotonic relationships between water inflow on the ship and relative wind speed and spray characteristics. A higher wind speed does not necessarily results in more icing if we assume independence of spray generation from wind speed. For example, the case of 15 m/s and 250 µm MVD gives a higher *E* for the injection height ranges 9.8-13 m and 13-15.6 m than the case of 25 m/s and 250 µm MVD. Ranges in wind speed and, most likely, temperature for which the icing rate is maximal may exist. From this point forwards, we focus on the moderate wind speed of 15 m/s relative to the ship; the wind speed of 25 m/s presents rather extreme sea conditions. Considering the assumed ship heading and the LWC of the spray, the actual wind and ship speeds can be estimated as 12 m/s (~23 knot) and 3 m/s (~5.8 knot), respectively.

4. Effect of the Flow Field Calculation Approach

This section is devoted to comparing the proposed model with the approach estimating the collection efficiency, where a uniform velocity field is assumed (see e.g. Lozowski et al. (2000)). Here, we concentrate on the 15 m/s wind speed and the MVD of 250 μm. Droplets of this size have small inertia and are therefore strongly affected by the air flow field. Note that the resulting difference will be smaller in the case of a larger MVD.

Fig. 7a shows that the assumption of the constant velocity overestimates highly the spray inflow on the front of the ship; see the black and white bars. At the same time, the constant velocity case gives no spray inflow on the back side of the ship's superstructure and main deck because they are sheltered by the superstructure; see Fig. 6a for a visualisation of the droplet paths.

In addition to the turbulent modelling of the air flow, it is also important to include the random nature of the turbulence into the droplet flow. According to the "ANSYS FLUENT Theory Guide", the stochastic approach introduces random fluctuations of the flow field when the equation of droplet movement, Eq. [3], is integrated; note that stochastic technique has been applied in the previous section. In other words, this approach uses both averaged, $\overline{\mathbf{u}}$, and fluctuating, $\mathbf{u}'$, components of the flow velocity, $\mathbf{u} = \overline{\mathbf{u}} + \mathbf{u}'$, while the non-stochastic approach uses only the averaged component, $\overline{\mathbf{u}}$. Stochastic droplet tracking assumes $\mathbf{u}'$ to be a discrete piecewise constant function of time. $\mathbf{u}'$ is kept constant on an interval of time needed to cross the turbulent eddy or equal to the eddy characteristic lifetime defined as

$$T_e = 0.15k/\varepsilon \qquad [5]$$

The results of the stochastic and non-stochastic droplet tracking in terms of collection efficiency are presented in Fig. 7a; compare the black and grey bars. Figs. 6b and 6c give the visual representation of the difference between the two methods. It can be seen that the model without fluctuations, when droplets flow in accordance with the averaged air flow, predicts lower values of E for all surfaces. In the case of random fluctuations, the droplet velocity can result in more frequent impingement on the ship surface. It is also worth mentioning that neither the constant velocity nor the non-stochastic approaches reproduce the water inflow on the back side of the structure.

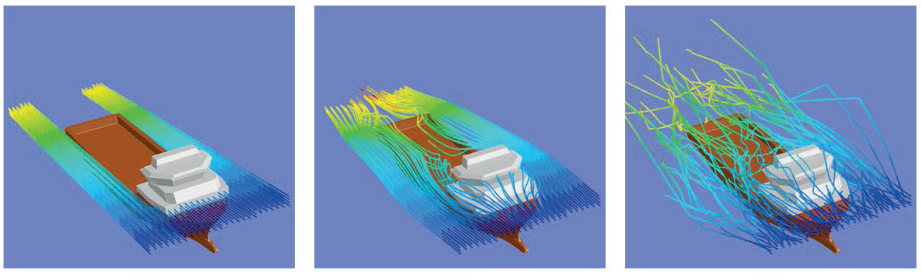

(a) (b) (c)

Figure 6. Droplet tracking: constant velocity field – (a), turbulent air flow with non-stochastic droplet tracking – (b), turbulent air flow with stochastic droplet tracking – (c).

5. Collection Efficiency Dependence on MVD

The resulting distribution of spray inflow depends highly on the spray droplet size. Many of the former offshore icing measurements have missed this parameter or have made assumptions about it based on subjective criteria. A series of simulations is conducted here to show the influence of the choice of droplet diameter.

Droplets are subjected to two counteracting forces from the flow field: gravity and drag. Gravity brings larger droplets down on the horizontal surfaces of the ship (which is why the E value for the Deck increases monotonically with MVD), and the flow field tries to move droplets around the ship. A larger droplet with higher inertia follows stream lines less and thus contributes to a higher collection efficiency. Fig. 7b presents E for different values of MVD. As can be seen, E increases with droplet size for the front surfaces (Deck, SF1, SF2 and SF3) due to the increase in inertia. This effect occurs until the diameter reaches a limit defined by gravity, and then the flight time of most of the droplets decreases. This finding also holds for the back side of the ship, where large droplets (2 mm and 5 mm) cannot produce any ice accretion because they give negligible spray inflow on the SB, where E is less than 10^{-4}. The possibility of ice accretion on SB increases with a decrease in droplet diameter. Thus, small droplets can be a key related to prediction of where on a ship icing may occur. Small droplets do not confer large amounts of water; however, they can reach the areas of primary concern, for example, safety boats and the deck behind the bridge, which can become slippery and represent a hazard for a crew working with cargo.

To conclude this series of simulations, an improper choice of MVD gives an error in the spray inflow of several hundred per cent. For example, the case of 2000 μm MVD gives for SF2 an almost 3-fold-higher inflow than the case of 500 μm MVD. If such uncertainty is introduced in the very beginning, the thermodynamics of the ice accretion would not have any importance.

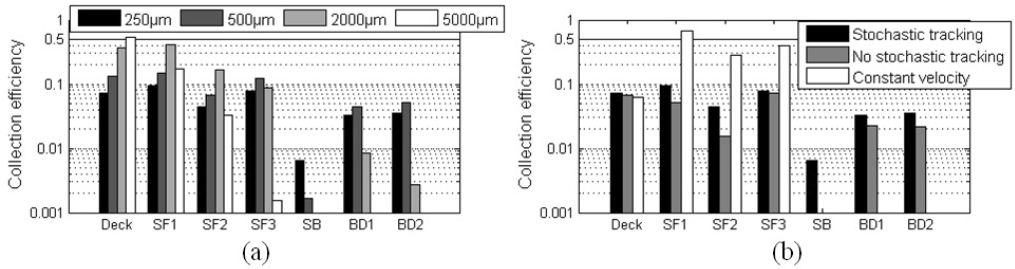

Figure 7. Collection efficiency for different MVD – (a) and different droplets flow modelling approach – (b).

6. Effect of Droplet Size Distribution

All previous simulations in this study have used one representative droplet diameter equal to the MVD. However, natural spray is represented by a spectrum of droplet sizes; see Ryerson (1995) for an example. This section demonstrates an effect of droplet size distribution on the resulting water inflow on the ship surface.

Two cumulative mass distributions, $Q(D)$, of spray droplet diameters, D, are created based on the modified Rosin-Rammler function defined as

$$Q(D) = 1 - exp\left[(D/X)^q \right] \quad [6]$$

where q and X are parameters; see Kulyakhtin et al. (2012) for details. The parameters are 1) q=25, X=1280 (narrow spectrum) and 2) q=12, X=1430 (wide spectrum). The obtained distributions have the same MVD of 1005±1 μm and are shown in Fig. 8a. Each distribution is divided into 12 bins. One bin represents 2 million droplets uniformly distributed in the injection plane of a specific diameter.

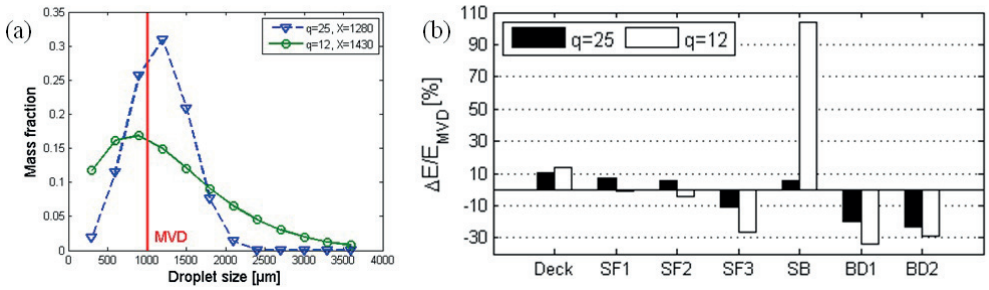

Figure 6. Effect of the droplet size distribution: DSD used in simulations – (a); relative divergence of E from the case of one representative droplet diameter – (b).

The collection efficiencies for the given distributions are compared with results from the DSD represented by one diameter equal to the MVD. Fig. 8b shows their relative divergence from the case of one representative droplet size in terms of $\Delta E/E_{MVD}$. The biggest difference is found for the SB surface, where E is in the range from 0.0004 to 0.001. The result for the SB is reasonable, as the previous section has shown that smaller droplets yield a higher collection efficiency there, and the distributions q=12 and q=25 contain droplets smaller than the MVD. The biggest difference is for the case q=12, which has a high mass fraction 12% of droplets with 300 μm diameters; see Fig. 8a. Regarding the remaining surfaces, the results show that the divergence is not higher than 35%, and q=12 gives higher divergence for most of the surfaces, which is directly related to the spectrum width.

7. Application of the Model to Spray Inflow Calculation

The most challenging subject in modelling marine icing is spray generation. Few data are available on this issue. The model describing LWC with respect to the significant wave height and the ship speed relative to the waves was presented by Zakrzewski (1986). This function was developed for Soviet medium-sized fishing vessels. This section shows an example of the application of the proposed CFD model together with this empirical equation for the spray generation to predict the sea spray inflow.

The spray generation function gives the following value of LWC, Q (kg/m³):

$$Q(z) = 6.46 \cdot 10^{-6} H_s \cdot V_{rw}^2 \cdot exp(-z/1.82), \quad [7]$$

where z is the height above the ship deck (m), H_s is the significant wave height (m) and V_{rw} is the ship speed relative to waves (m/s). The wave height and relative ship speed are calculated by the equations of Zakrzewski (1986), based on the wind and ship speeds.

Simulations are performed for a ship speed of 3 m/s and wind speed of 12 m/s. Two different yaw angles, 0 and 15°, are considered to clarify the effect of the ship yaw. The following wind speeds are set on the boundaries of the calculation domain: (case 1) V_x=15 m/s and V_y=0 m/s for a yaw of 0° and (case 2) V_x=14.6 m/s and V_y=3.11 m/s for a yaw of 15°. The relative ship speed V_{rw} is calculated using the following equation

$$V_{rw} = 1.559 T_s + V_s \, cos(\pi - \alpha), \quad [8]$$

where T_s is the significant wave period (s), V_s is the ship speed and α is the angle between the ship heading and wave phase vector. Eqs. [7] and [8] result in Q ratio in Cases 1 and 2 that is equal to 1.01; thus, the effect of the ship heading relative to the waves on the spray generation can be neglected in the cases considered.

The droplet size is set equal to 1.75 mm according to Zakrzewski et al. (1993). Fig. 9 presents the vertical distribution of the flow rate per unit area in the injection plane, which is in front of the ship at the position of the bow tip. The sheet spreads from the vessel deck up to ship height in vertical direction and has 2 ship widths in horizontal direction perpendicular to ship movement. This setup is used for both cases. Fig. 9b compares the obtained flow rate per unit area for the different surfaces of the ship. The spray inflow on the ship surfaces is smaller for a 15° yaw than for zero yaw, except on the SB surface. On the SB, the case of the 15° yaw gives a 3-fold-higher spray inflow, which could be a concern for this vessel because the rescue boats are placed there.

Fig. 10 gives the qualitative spray distribution. One can see that the pictures are very similar for both considered cases: the only difference is that Case 2 gives a larger spray inflow on one side of the ship. In addition, both the model predictions show a higher spray concentration closer to the corners of the front part of the vessel and in the middle of the SF1 and SF2 surfaces.

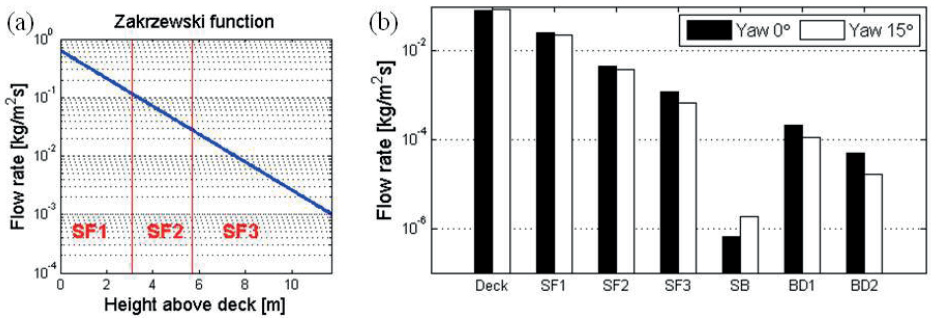

Figure 7. Spray flow rate vertical distribution for the Zakrzewski generation function – (a); spray flow rate distribution on the ship surface for different yaw angles – (b).

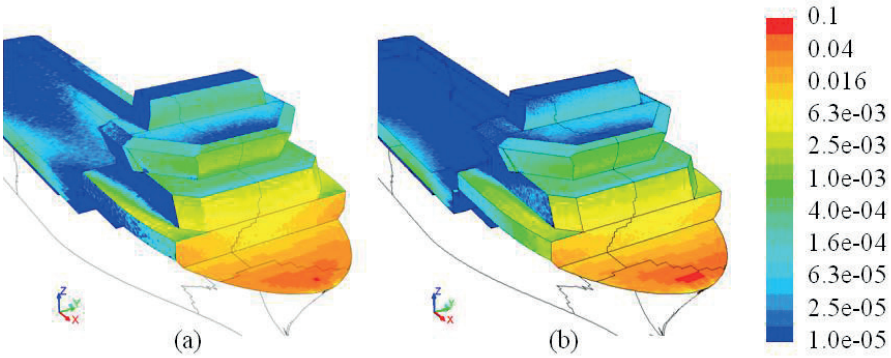

Figure 8. Flow rate distribution: Case 1, 0° yaw – (a); Case 2, 15° yaw – (b).

8. Conclusions

The paper presents the capabilities of CFD to improve the prediction of ice accretion by accurate modelling of droplet flow around complex structures. The paper describes several important factors that should be taken into account when one models spray inflow:

- Air flow simulations give more detailed water inflow distribution. Features such as the sides of the structure accumulate a significant amount of water droplets.
- Unlike the classical approach, the turbulent flow method predicts that droplets flow over and around the superstructure and impinge on the aft and the back side of the superstructure. The turbulent flow can lift droplets that are below deck and bring them to the rear structure of the ship, increasing spray inflow by several times due to the exponential vertical profile of spray concentration.
- The uncertainty of the spray MVD can result in errors of several orders of magnitude in the spray inflow.
- Approximation of the DSD spectrum using the constant droplet size determined by MVD can result in 10-50 % error and, for some areas of the ship, can give errors even on the order of 100 %.
- The preliminary results based on Zakrzewski's spray concentration function indicated that the two different yaw angles studied here have approximately the same spray inflow.

It should be emphasised that the calculations show a collection efficiency of less than 70% overall and approximately 10% for most areas in the front part of the vessel. Thus, the measured spray flow and LWC should be scaled according to the flow field when these data are used for simulation. To clarify, assume that the spray on the deck of the ship has been measured. The obtained values were already affected by the flow field after the spray generation. Thus, these values cannot be used in simulations for another ship with a different superstructure and deck height. The measured values could be scaled based on both measurements and the flow field simulation for the particular vessel.

This approach can be further used to estimate icing and to make recommendations for ship construction and ship manoeuvring in waters prone to icing.

Acknowledgements

The work presented in this paper is a part of MARICE, a joint industry project between Det Norske Veritas, Statoil, Norwegian University of Science and Technology and the Research Council of Norway, related to marine icing on offshore structures and vessels.

References

Finstad K.J., Lozowski E.P, Makkonen L., 1988. On the median volume diameter approximation for droplet collision efficiency. Journal of the Atmospheric Science, 45 (24), 4008-4012.

Lozowski, E.P, Szilder, K., Makkonen, L., 2000. Computer simulation of marine ice accretion. Phil. Trans. R. Soc. Lond. A 358, 2811-2845.

Kulyakhtin, A., Kollar, L., Løset, S., Farzaneh M., 2012. Numerical simulations of 3D spray flow in a wind tunnel with application of O'Rourke's interaction algorithm and its validation. Proc 21th IAHR International Symposium on Ice, Dalian, China (In press).

Ryerson C.C., 1995. Superstructure spray ice accretion on a large U.S. Coast Guard cutter, Atmospheric Research, 36, 321-337.

Zakrewski W.P., 1986. Icing of fishing vessels. Part I: Splashing a ship with spray. Proc. IAHR Ice Symposium, Iowa City, Iowa, 2-3, 179-194.

Zakrzewski, W.P., Lozowski, E.P., Thomas, W.L., Bourassa, M., Szilder, K., Kobos, A., 1993. A three-dimensional time-dependent ship icing model. Proc. 12th POAC, Hamburg, Germany, 2-2, 857-873.

Proceedings of the Twenty-third (2013) International Offshore and Polar Engineering **www.isope.org**
Anchorage, Alaska, USA, June 30–July 5, 2013

ISBN 978-1-880653-99–9 (Set); ISSN 1098-6189 (Set)

Measurements of Thermodynamic Properties of Ice Created by Frozen Sea Spray

Anton Kulyakhtin[1,3], Sergey Kulyakhtin[1,2] and Sveinung Løset[1,2,3]
[1] Norwegian University of Science and Technology (NTNU), Trondheim, Norway
[2] Sustainable Arctic Marine and Coastal Technology (SAMCoT), Centre for Research-based Innovation (CRI), Trondheim, Norway
[3] The University Centre in Svalbard (UNIS), Longyearbyen, Norway.

ABSTRACT

A field simulation of ice accretion has been performed in the harbour area of Longyearbyen, Spitsbergen, during the winter of 2011. Cylinders with diameters of 10, 20, 40 and 100 mm were exposed to a freezing artificially created periodic spray. This paper presents the density, crystalline structure and salinity of the accreted glaze ice. Hydrostatic weighing was used to measure the ice density, which is a well-established method in fields not related to ice. The method is simple, does not require special equipment and can be accurate to better than 1%. The dependence of the ice properties from the weather conditions is discussed. The experiments demonstrated that the ice salinity was smaller on the larger vertical objects.

KEY WORDS: Accretion; ice; density; icing; sea spray.

INTRODUCTION

No much data are available in the literature related to the properties of ice formed by freezing sea spray with high concentration. A detailed description of the properties of ice accreted on a real vessel can be found in the work of Ryerson and Gow (2000). Some data on the salinity of ice accretion are available in a study by Fukusako et al. (1989).

The ice salinity is important for the ice adhesion, according to Makkonen (2012). The salinity also defines the ice strength and is important to understand salt entrapment and the growth of saline ice. This knowledge is required for modelling ice accretion, which can be further used to estimate the icing load. The salinity measurements were produced in the given experiments for these reasons.

The measurements were obtained in the harbour area of Longyearbyen, Spitsbergen, and a detailed description of the experimental setup is given in the work of Kulyakhtin et al. (2012). The measurement was conducted for up to 2.5 hours, which is a relatively long time of measurement. The spray inflow resulted in a wet icing formation that was unknown; therefore, the data for this formation were not analysed previously. The recent results in Kulyakhtin et al. (2013) proved that in a "thermally limited" (TL) conditions, the ice accretion is almost independent of the spray's flow rate and period. Therefore, the experimental results were revised based on the improved knowledge, and an analysis of the ice properties was attempted. The scattering and the limited amount of data complicated the analysis. The results and discussion are therefore combined in this paper; however, a few important observations have been made. The results indicate the ice growth process and the drainage of the salt solution.

ICE ACCRETION RATE THEORY

There are two main scenarios of ice accretion in accordance with the factors limiting the growth rate. The first scenario is the "mass limited" (ML) scenario, in which the total water mass arriving on the cold surface can be frozen due to the cooling; the water mass is therefore the limiting factor for the accretion rate. The second scenario, the TL scenario, represents conditions when the water impingement on the surface is high and the heat fluxes are unable to freeze all of the water; as a result, some of the water runoff representing the "wet" icing conditions. The existence of the unfrozen water and the water-ice interface requires that the temperature of the liquid film equals the freezing temperature. The temperature of the sea water is defined by the water's salinity, which can be increased due to salt expulsion from the forming ice. The equation describing the ice growth in the TL scenario in the case of continuous spray was given by Makkonen (1987). Kulyakhtin et al. (2013) showed that in the wet icing case, the accretion rate is independent of the spray period and the water amount arriving per spray event for the conditions in Longyearbyen. This finding is true even if the conditions are TL only on average, i.e., even if most of the ice surface is dry between the sprays. This result means that the "wet formed" ice should be independent of the amount of water that arrived and should depend purely on the heat fluxes. Thus, if the conditions are proven to be TL, the results in the paper by Kulyakhtin et al. (2012) can be analysed based on the freezing conditions. Such an analysis is performed in this paper, and the ice properties are discussed.

Kulyakhtin et al. (2013) simplified the equation from Makkonen (1987) and showed that the main heat flux sources in the experiment were convection and evaporation. It was shown that the radiation can be neglected; however, the heat flux from cooled spray is uncertain. According to Kulyakhtin et al. (2013), the ice accretion growth rate per

unit area in the TL conditions can be estimated using the following equation:

$$I_{calc} = \left(Q_c + Q_e\right) / \left[l_f \left(1 - k\right)\right] \quad (1)$$

where Q_e and Q_c are the evaporative and convective heat fluxes, respectively, l_f is the latent heat of pure ice freezing and k represents the mass of entrapped unfrozen brine in the ice and according to Makkonen (1987) and Makkonen (2010) can be assumed to be constant and equal approximately to 0.26.
The convective heat flux is as follows:

$$Q_c = h\left(T_i - T_a\right) \quad (2)$$

Where T_a is the air temperature and T_i is the temperature of the accretion surface equal to the freezing temperature. In Adventfjord, the water salinity is approximately 34 ppt, and the freezing temperature can therefore be set as a constant equal to -1.9 °C for approximate calculations, which neglects the variation of the salt concentration during freezing. h is the heat transfer coefficient described by the following formula:

$$h = \frac{Nuk_a}{D} \quad (3)$$

Where k_a is the heat conductivity of air, D is the cylinder diameter and Nu is the Nusselt number, which is a dimensionless characteristic of the heat transfer. This number depends on the Reynolds number (Re), the surface roughness, the free stream turbulence and the surface geometry.

The convective heat transfer of cylindrical objects is well studied, and the physics is described in Achenbach (1977). The experiments performed in Longyearbyen lie in the Reynolds number range from $3.5 \cdot 10^3$ to $8.5 \cdot 10^4$. According to Achenbach (1977), this range corresponds to the subcritical flow regime, and only in the case of the 104-mm cylinder can we expect a transition to the critical flow regime due to the surface roughness and icicles. The subcritical flow regime is characterised by a laminar separation of the boundary layer and a lack of significant effect from the surface roughness on the heat transfer. Of course, icicles can induce an additional heat transfer; however, this effect is neglected here, and the averaged heat transfer across the whole cylinder can be calculated according to Achenbach (1977):

$$Nu = 0.18 \cdot Re^{0.63} \quad (4)$$

In addition, according to the figures presented by Achenbach (1977), the heat transfer from the windward side is approximately equal to the heat transfer from the lee side. Thus, the same Eq. 4 is used to calculate the heat transfer from a stationary cylinder when the ice grows only on the windward side.

The evaporative heat flux per unit area is as follows:

$$Q_e = \frac{\varepsilon l_v}{p c_p} \left(\frac{Pr}{Sc}\right)^{0.63} h\left(e_s\left(T_i\right) - r_H \cdot e_s\left(T_a\right)\right) \quad (5)$$

Where ε is the molar weight ratio of water to air, l_v is the latent heat of water evaporation, p is the atmospheric pressure, c_p is the specific heat capacity of air, Pr is the Prandtl number, Sc is the Schmidt number, r_H is the relative humidity of air and $e_s(T)$ is a function of temperature that describes the saturated water pressure for a given temperature; Kulyakhtin et al. (2013) presents further details.

Eqs. 1-5 can provide an estimate of the ice accretion rate in the performed experiments.

EXPERIMENTAL SETUP AND MEASUREMENT PROCEDURE

Our experiment was performed in the harbour area of Longyearbyen in open air conditions. Details of the experimental setup can be found in the study by Kulyakhtin et al. (2012). The ice accretion was generated by periodic spray (a period of 33 sec and a duration of 2.5 sec) on cylinders with lengths of 60 cm and diameters of 10, 20, 40 and 104 mm. The water was pumped directly from the fjord and had a salinity of 33-34 ppt. The water sprayed a distance of 5.2 m from the cylinder and was carried by the wind, which unfortunately fluctuated; as a result, the amount of impinging spray on the cylinders per spraying event is uncertain. Thus, the results here are analysed against the weather conditions based on the assumption that in a TL scenario, the ice accretion rate is independent of the spray amount. The weather conditions were measured by a weather station, which included temperature, humidity and wind sensors.

Measurements were performed on stationary (ACC) and rotating cylinders (LWC). The goal of the LWC measurements was to measure the liquid water content of the spray, assuming the validity of ML scenario. However, it will be shown later that the approach was wrong and that the measured accretion rate on the rotating cylinders is predicted well by Eq. 1, which corresponds to the TL scenario. The measured ice accretion rate was calculated as follows:

$$I_{\exp} = \frac{\Delta m}{t_{\exp} \cdot \left(\pi D / 2\right) \cdot L} \quad (6)$$

Where Δm is the total accretion mass, t_{exp} is the experiment duration and L is the cylinder length.

The ice samples for the salinity and density analysis were collected from the cylinder and from the "base", which is the leg of the construction supporting the cylinder (Fig. 1). The amount of spray arriving on the base was higher, and the duration of the accretion process is longer. It was therefore interesting to investigate the "base" ice.

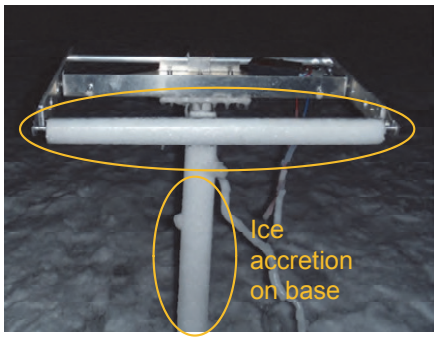

Fig. 1. The photo shows the cylinder that was used to accumulate ice and the leg, which was exposed to the spray in addition to cylinder. The

ice from the leg was also collected for analysis.

The ice samples were split into pieces. A fraction of the samples was used to measure the salinity only. This measurement was performed after melting the ice at a temperature of approximately 22 °C. The remaining samples were moved after the experiment into the freezer with a temperature below -18 °C, where the samples were stored until their density was measured in the cold lab.

The density measurements require a high accuracy. For instance, the range of the measured densities was from 853 to 955 kg/m3, which is a variation of only 11%. Therefore, it is reasonable to perform measurements only if we can reach an accuracy of better than 1%; to make any reliable analysis, a 0.1% accuracy is required. The density measurements usually consist of mass and volume measurements, and the main uncertainty is introduced by the volume; this uncertainty is due to both the possible complicated shape of the sample and to the inaccuracy of the measurement technique.

The density was measured using hydrostatic weighing (Fig. 2). The ice sample was tied by a thin thread, and the thread end was hung on a hook on the bottom of an electronic scale. In this way, the sample mass was measured in the air (M_{air}), and its mass was then measured when it was submerged below the surface of liquid paraffin (M_{par}). The effect of the thin thread's volume on the accuracy of the density measurements was negligible. Paraffin with a density (ρ_{par}) of approximately 770 kg/m3 was chosen as the working liquid because this material is lighter than the ice. The ice mass was calculated from the following equation, which comes from Archimedes' law:

$$\rho_{ice} = \frac{M_{air}}{M_{air} - M_{par}} \cdot \rho_{par} \tag{7}$$

The accuracy of the measured mass can be estimated in the following way:

$$\frac{\delta\rho_{ice}}{\rho_{ice}} \le \frac{M_{par}}{M_{air} - M_{par}} \cdot \frac{\delta M_{air}}{M_{air}} + \frac{M_{par}}{M_{air} - M_{par}} \cdot \frac{\delta M_{par}}{M_{par}} + \frac{\delta\rho_{par}}{\rho_{par}} \tag{8}$$

Considering that the absolute magnitude of the mass measurement error is equal for the measurements in the paraffin and in the air, we can rewrite the above equation:

$$\frac{\delta\rho_{ice}}{\rho_{ice}} \le \frac{2\rho_{ice} - \rho_{par}}{\rho_{par}} \cdot \frac{\delta M_{air}}{M_{air}} + \frac{\delta\rho_{par}}{\rho_{par}} \tag{9}$$

Using the extreme values of the ice and paraffin densities encountered during the experiments, we can estimate the coefficient in Eq. 9:

$$\frac{\delta\rho_{ice}}{\rho_{ice}} \le 1.5 \cdot \frac{\delta M_{air}}{M_{air}} + \frac{\delta\rho_{par}}{\rho_{par}} \tag{10}$$

The samples with masses of approximately 50-250 g were used for the density measurements, and the scale had an accuracy of better than 0.1 g, which means that the relative error input from the mass measurements was less than 0.3%.

The ice density was measured on three different days. The temperature in the lab was unfortunately different on those days: -4, -5.9 and -10 °C. An attempt was also made to perform measurements at -18 °C to avoid salt drainage; however, the paraffin had a higher freezing point.

In contrast to the mass measurements, the paraffin density was measured using a graduated cylinder, which had an accuracy of 1%. This is the maximal accuracy for this type of equipment. The paraffin density measurement was repeated using three different cylinders each day; however, the authors cannot guarantee an accuracy of better than 1%. The measured paraffin density used for the ice density calculation was the following:
766.2 kg/m3 at -4 °C
767.7 kg/m3 at -5.9 °C
770.9 kg/m3 at -10 °C

In addition, the equations presented by Cox and Weeks (1983) show that the saline ice density changes substantially with a change of the lab temperature. Calculations show that the ice density decreases by 2.4, 1.5 and 0.5% when the temperature drops from -4 to -10 °C if the ice salinity is 38, 25 and 9 ppt, respectively.

In summary, the ice density was measured with an accuracy of better than 1.3%. The resolution of the data obtained on the same day was better than 0.3%. However, the density measured on different days cannot be compared directly due to temperature variations. The proposed method can have a better accuracy if the density of the liquid used to measure the ice density is known or measured more accurately. For example, this measurement can be performed using an aerometer, which is cheap and precise.

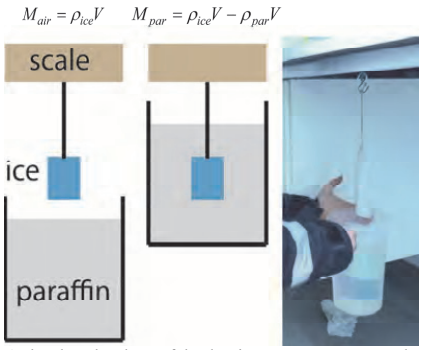

Fig. 2. A sketch and a photo of the density measurement procedure.

RESULTS AND DISCUSSION

Accretion Rate

The scatter plot in Fig. 3 compares the measured ice accretion rate, Eq. 6, with the rate predicted by Eq. 1. In general, the point distribution supports the theory because the ice accretion cannot be higher than that predicted by the TL scenario, and this fact is demonstrated in Fig 3. Most of the values are predicted well by the theory, and most of the measuring conditions therefore corresponded to the TL scenario. This result also means that the correct heat transfer function was used. There are only three points that lie substantially above the curve; however, the difference is not greater than 42% from the value predicted by the theory.

The points lying below the curve correspond to the ML scenario. These points are enclosed in orange squares. The choice of ML cases was subjective and based only on the divergence of the results. The ACC

points marked as ML correspond to measurements performed on the 21st of February on 40- and 20-mm cylinders in relatively cold conditions with an air temperature below -14 °C. It is quite possible that the spray did not reach the cylinder due to the wind direction fluctuations, thus limiting the ice growth rate. The accretion rate on the 10-mm cylinder measured on the 8th of March resulted only in 19 g of ice, possibly for the same reasons. In addition, the LWC measurements performed on the 24th of March reflect the 8 m/s wind speed. In that case, the spray overflew above the cylinder, and thus only a small amount of water was frozen on the cylinder.

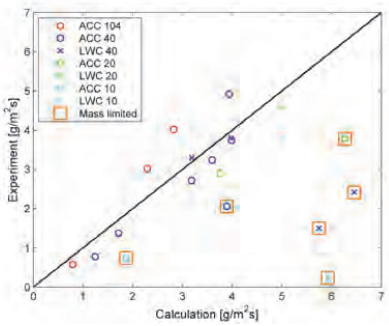

Fig. 3 Comparison of the measured ice accretion with that calculated using Eq. 1.

As a result, the mean absolute relative divergence of the experiments classified as the TL scenario from Eq. 1 is 20%, and the max error is 42%, which is a good agreement. Fig. 4 shows the divergence of the cases classified as TL from the theory. The good agreement of the LWC measurements with the theory shows that the assumption of Kulyakhtin et al. (2012) that the rotating cylinder can be used to measure the LWC of the dense periodic spray, is wrong.

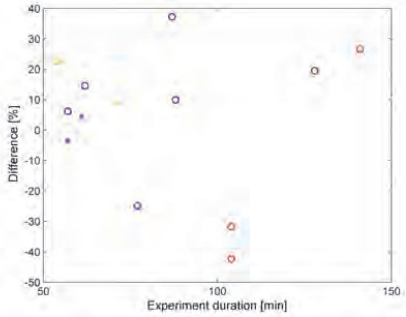

Fig. 4 Relative difference of the experimental ice accretion from that obtained using Eq. 1.

The three points lie above the curve. This can be due to the neglect of the radiative heat flux and the heat flux from droplets cooling. Or the increased heat transfer is possibly due to the growth of icicles or to the duration of the experiment, which involves a substantial change of the ice accretion shape (Kulyakhtin et al. (2012) present pictures of ice accretion). These effects are amplified in the case of faster growth, which corresponds to colder conditions. In Fig. 4, one can see several cases with a longer duration that give a better agreement with the theory. However, the simplified theory can be used to predict the maximal ice accretion rate well, even for the experiments with a 140-min duration, with an accuracy of better than 50%. In addition, the divergence can be explained by the inaccuracy of the measurements and not by the inaccuracy of the theory.

As most of the values belong to the TL scenario, we can compare the ice properties obtained in TL scenarios based on the weather parameters; this comparison is performed in the following subsections.

Crystalline structure

The experiments gave a glaze ice accretion. The ice was transparent in the beginning, and it became milk-white when it became thicker, as described by Fukusako et al. (1989). Thin sections were made in the lab at a temperature of -20 °C, but it was still quite difficult to obtain thin samples due to the high ice salinity. The ice was very fragile. The slice thickness was less than 0.7 mm at the moment the pictures were taken in the case of cylinders and approximately 1.2 mm in the case of the "base" ice.

There was no difference observed in the crystalline structure between the samples obtained on the 40- and 104-mm cylinders or on the base, except that only the base samples had cracks in the plane perpendicular to the growth direction.

Fig. 5 shows the crystalline structure of the ice in thin sections photographed under polarised light. The measured grain size was from 0.1 mm to 0.7 mm, which means that even in our case of a very thin layer of thin sections, we had several layers of grains in the ice plate with a 0.7-mm thickness. The grains are approximately round, are uniformly distributed and do not have any preferable direction of growth, which can be related to the heat flux. Ryerson and Gow (2000) also did not find any preferable orientation of the ice crystals, and only the icicles' crystals had elongation, according to their work. Ryerson and Gow (2000) presented a slightly larger grain size, i.e., ranging from 0.6 mm to 2 mm, for the ice from the real vessel.

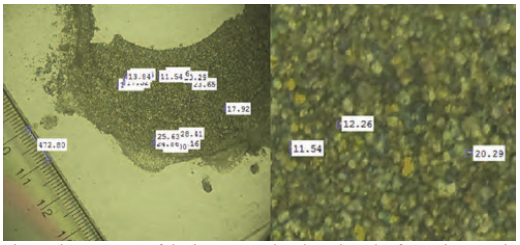

Fig. 5 The structure of the ice accumulated on the 5th of March at an air temperature of -16°C and a wind speed of 4 m/s.

Salinity

These experiments were first attempt, and different techniques were used to reveal any interesting dependencies. Thus, the salinity was sometimes measured from the whole cylinder, whereas the ice was split along the stagnation point in other cases. Usually, several samples were taken from the same cylinder and measured separately to investigate the accuracy and spreading of the results.

In addition, icicles were cut separately, and their salinities for a few

cases are given in Table 1. The values cannot be used for any analysis; however, these values clearly demonstrate the existence of water drain and that the icicles are more saline than the water sprayed.

Table 1. Salinity of icicles.

Air temperature [°C]	-16.2	-4.2	-11.4	-11.2	-3.7
Wind speed [m/s]	3.8	5.5	7.5	5.4	5.6
Exp. duration [min]	88	87	104	104	141
Cyl. diameter [mm]	40	40	104	104	104
Salinity [ppt]	51.2	47.3	40.9	32.5	27.3

To investigate the salt expulsion, the ice surface of the 4 samples were cut vertically into two pieces (to ensure that there was no influence of the vertical salt concentration variation), and the surface of one piece was cleaned with a knife, removing 2-3 mm of ice. The difference in the ice salinity of the cleaned samples and the samples without cleaning is given in Table 2. The salinity of the cleaned samples was expected to be lower, and the highest salt concentration solution or ice was predicted to be on the surface of the sample, especially at higher temperatures. However, the result is the opposite of that predicted, and the difference obtained was smaller or on the level of the spatial non-uniformity or the measurement error of the salinity, as shown below.

Table 2. Difference in the salinity of ice with a cleaned surface. The minus sign means that the ice salinity without cleaning was higher.

Air temperature [°C]	-11.2	-3.7	-5.4	-11.2
Cylinder diameter [mm]	104	40	40	40
Salinity difference [ppt]	-0.4	0.6, 0.4	2.1	-0.7

In addition, the thick ice samples from the 104-mm cylinder were cut parallel to the cylinder surface in two parts, and the salinity is shown in Table 3. The difference was less than 2.5 ppt and was lower than the spatial scattering of the salinity along the cylinder.

Table 3. Salinity profile in the ice accretion on the cylinder with a 104-mm diameter at a temperature of -11 °C.

Date, sample location on cylinder	24/02, overall		28/02, bottom		28/02, top	
Thickness range [mm]	0-12	12-25	0-14	14-22	0-11	11-20
Salinity [ppt]	18.95	22.3	19.6	21.7	17.2	16.66

We can conclude that there is no strong effect of the surface brine salinity's increase with time and that there is no strong evidence of salt expulsion and of the brine channels draining in the measurements with a duration of less than 2 hours.

For the LWC measurements on the rotating cylinders, the ice salinity ranged from 31 ppt to 35 ppt and was close to the sprayed water salinity, which was why Kulyakhtin et al. (2012) erroneously assumed that the measurements on the rotating cylinders were suitable for LWC measurements. It was assumed that if the salinity is similar to the water salinity, there is no dripping off; however, the reason was most likely the rotation and mixing of the fluid film.

When the surface effects and the effects from icicles were excluded from the analysis, the next step was to analyse the dependence of the obtained salinity from the weather conditions. For Kulyakhtin et al. (2013), the experimental salinity had a tendency to increase with the calculated ice accretion rate. The data obtained here are plotted in Fig. 6.

The obtained values are quite scattered. Several samples were taken from the cylinder along its length, and Fig. 6 shows that the difference is up to 2 ppt. These samples provide a trusted interval of our data for comparative analysis. In addition, the ice was split along the stagnation line of the cylinder, and the ice salinity was measured from the bottom and the top of the cylinder. The ice was 1-3 ppt more saline on the bottom than on the top of the cylinder on both the 104-and 40-mm cylinders. The overall salinity was closer to the salinity on the bottom because there was more ice below the stagnation line.

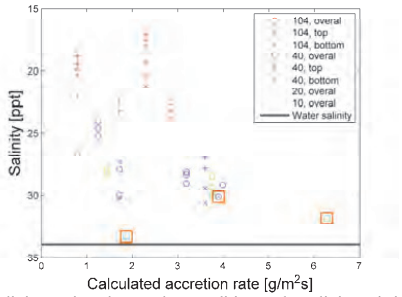

Fig. 6. Salinity against the weather conditions. The salinity axis is reversed to simplify the understanding that there is a tendency to have more saline ice on the cylinder's bottom comparing to the top.

The data are too few to give any solid conclusion regarding the effect of the ice accretion rate on the ice salinity, and no such conclusion is made here. No clear temperature effect was observed too. However, the results quite clearly show that the salinity of the 104-mm cylinder is, on average, 5 ppt lower than the salinity of the 40-mm cylinder. The 20-mm cylinder does not repeat this tendency relative to 40-mm cylinder, and the 10-mm cylinder gave a very high salinity. Szilder (1994) wrote that the pendant droplet will detach from the cylinder when the droplet reaches critical mass, which is determined by capillary effects. Thus, it is likely easier to collect a droplet with critical mass on the bottom of the larger cylinder due to the larger total surface that collects spray. Increased draining can result in the decreased overall salinity of the samples. In addition, gravity moves the liquid over a longer distance for the bigger cylinder due to the cylinder's curvature. The difference in the gravity effect may become weaker when the 40- and 20-mm cylinders are compared.

The dependence of the salinity on the cylinder's diameter was not obtained by Kulyakhtin et al. (2013) when the duration of the experiment was approximately 20 min. Thus, the stratification of the salinity likely requires more than 50 min, as in the given experiments. Fig. 7 shows the salinity against the experiment's duration. The distribution of the points does not support the suggestion that the salinity varies with time. Each point set for the 104- and 40-mm cylinders lies on a certain level that is most likely determined by the cylinder's size, and the level seems to be independent of time.

The main conclusions are as follows:

- There is a stratification of salinity in the ice related to the geometry of the object.
- The salinity variation is relatively small, and the magnitude of the measurements' uncertainty was that of the observed salinity variation (i.e., 2-3 ppt).
- The amount of influencing parameters complicates the data analysis. Thus, a comparison should be made based on a certain ice growth theory in a way similar to the analysis of the ice accretion rate. As shown here, the correct theory can show systematics in the data that were initially treated as totally scattered by the

experimental uncertainties.

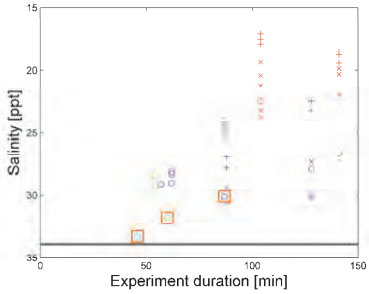

Fig. 7 Salinity against the experiment's duration. Symbols as in Fig. 6.

The discussion below related to the ice salinity accreted on the support construction ("base") is rather authors' personal understanding of the ice growth and attempt to understand the measurement results. In principle, this discussion is not supported by a solid theory and requires a more comprehensive investigation.

The ice from the supporting leg was taken at the end of certain measurement days. The ice on the legs accreted over 2 to 6 hours. The thickness was different on different days and varied vertically. Fig. 8 shows detailed measurements performed on the 5th of March. The ice accreted on the leg was cut into pieces with a 20-cm height in the vertical direction. Each sample was then cut perpendicular to the growth direction in slices with thicknesses of 1-2 cm to observe whether there was any reflection of salt drainage.

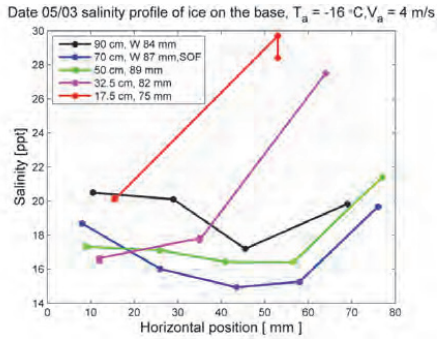

Fig. 8. Horizontal profiles of the salinity on the different heights of the ice accreted on the support leg.

The legend shows the position above the base foundation, which was 10 cm above the ground, and the total ice width at this height. The distribution of the thickness depended on the cooling and the wind speed. The wind speed determined the position of the spray's maximal concentration. The water was pumped directly from below the level ice into the system. The water was at freezing temperature and could only cool down further while flying to the base, thus inducing more ice freezing. It is therefore expected that on the 5th of March, the maximal water inflow was at a height of approximately 50 to 70 cm, where the width was maximal. This phenomenon can also explain the lower ice salinity due to the higher water amount, which dissolves salt and moves it downward; this behaviour explains the higher average salinity over the thickness at the 90-cm height.

The thickness of the base walls was thicker than the wall thickness of the cylinders, and the base therefore had a higher heat capacity. Thus, the ice accreting on the base was possibly exposed longer to the cooling stored by the material and transferred by heat conduction (explanation of this theory is in Kulyakhtin et al., 2013). The ice isolates the water-ice interface from the cooling, which comes from the metal surface. The decreased heat outflow decreases the growth rate and, as a result, entrapped ice. The high salinity values close to the ice surface represent the ice that likely did not have sufficient time to expel salt. However, that ice fraction is not a thin layer; the surface of the sample marked as SOF in the figure legend was cleaned of several millimetres of ice. However, the resulting salinity distribution is in good agreement with the neighbours. These values are especially large at the bottom of the base. All of the draining salt solution moved there, thus resulting in a high salinity. It is also clear that the amount of water arriving there was smaller, resulting in a smaller accretion thickness.

There can be another explanation of the salinity minimum at approximately 40-50 mm horizontal position. It is common to treat spongy ice accretion as non-heat-conducting. However, this assumption can be wrong if the ice thickness is small. Using the weather parameters from the 5th of March and Eqs. 2-5, we can estimate the convective and evaporative heat transfer by assuming the base as a 5-cm-diameter cylinder. We then assume that the base surface temperature is equal to the air temperature. We divide the product of the ice's heat conductivity and the difference between the surface and the freezing temperatures by the sum of the convective and evaporative heat fluxes. As a result, we obtain the thickness of the ice when the conductive heat flux and sensible heat fluxes are equal. We also assume no effect of the sponginess on the heat conductivity. The obtained ice thickness is 38 mm, which is very close to the position of the measured salinity minimum in Fig. 8. This means that in the beginning, the ice was likely growing mainly due to the heat conduction, as the ice was stronger and the growth mechanism was similar to the sea-level ice growth. When the ice became thicker, it decreased the heat conductivity, and the salinity became smaller in the upper part and higher on the lower positions. After the ice passed 40 mm in thickness, the convective and evaporative heat fluxes started to rule the growth process and created conditions for the spongy ice formation, i.e., when the water-ice interface is cooled more from the air, the temperature gradient changes its sign, resulting in more favourable conditions for a faster freezing front propagation and dendrites growth. As the ice becomes thicker, the temperature gradient increases, resulting in the higher salinity. Additional salinity profiles are shown in Fig. 9, and only the second theory explains well the black curve corresponding to the 28th of February. In addition, the difference in the salinity profiles can be explained by variations in the wind speed.

The third explanation of the salinity profile comes from the wind speed and direction variation and the spray amount impingement. In addition, the measurements on the 5th of March were performed over 4 hours, after which there was a 1-hour pause before measurements were resumed for another 1.5 hours. The pause can explain the minimum ice salinity at 3/5 of the thickness.

On the 24th of February (blue curve in Fig. 9), there was no long pause in the measurements, and the thickness after which the sensible heat could overtake the freezing process was 25 mm, which is similar to the position of the measured salinity minimum. However, the minimum of this measurement is on the level of the measurements' uncertainties.

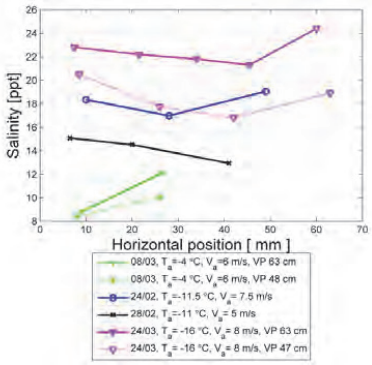

Fig. 9 The horizontal salinity distribution inside the ice. VP marks the vertical position above the base foundation. The vertical position from which the samples on 24/02 and 28/02 were taken is unknown.

Fig. 10 shows the vertical distribution of the ice salinity. The samples from the bottom had a higher salinity. At the same time, the overall salinity distribution seemed to be quite complicated and can be explained by the discussion given above. The only clear conclusion that can be given is that the longer vertical extension of the construction results in better salt runoff and thus a lower salinity compared to the cylinders.

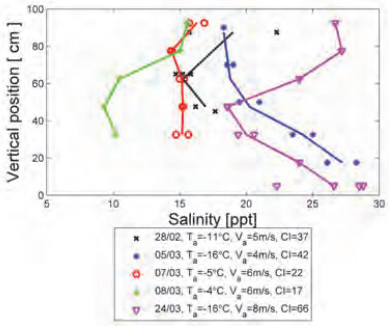

Fig. 10 Vertical salinity profiles on the base. CI means cooling index which is the product of the mean air velocity in the power of 0.63 and the difference of the water freezing temperature and the air temperature.

Density

The ice density can vary due to salt entrapment and the inclusion of air pockets. Ryerson and Gow's (2000) measurement of the density of the ice accreted onboard the USCGC Midget was 690-920 kg/m3, and the values presented in their work from other authors' research ranged from 620 to 967 kg/m3. The fresh ice density without air entrapment is approximately 920 kg/m3, which means that some of these researchers' samples might have a relative air entrapment volume of approximately 30%, which is a high value. It was therefore interesting to analyse the density and air entrapment.

The density of the ice is plotted against the salinity in Fig. 11. The density of saline ice has a strong dependence on the surrounding temperature. We did not have a good control of the temperature in the lab; thus, the three curves show the theoretical density of the ice without air entrapment for the different laboratory temperatures. The curves were calculated using the equations of Cox and Weeks (1983). The measured densities were well predicted from the measured salinities using the equations. The calculated relative air entrapment volume using the equations of Cox and Weeks (1983) was 0.5% to 4.5% and was on the level of the measurement errors. This result means that the ice did not contain a high volume of the entrapped air and that there was no density dependence on the ice growth conditions except those related to the ice salinity.

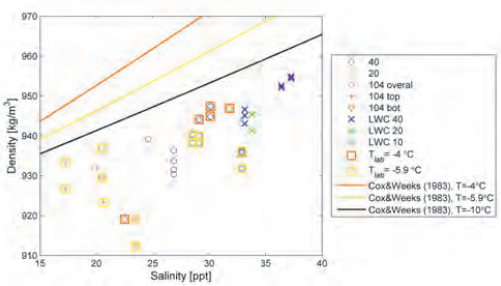

Fig. 11 The ice density against the ice salinity. The points are enclosed in squares to describe the lab temperature at which the density was measured. The points without coloured squares correspond to the -10 °C temperature in the lab.

The vertical distribution of the air entrapment in the samples from the base is shown in Fig. 12. The obtained values do not show any systematics or trends. However, compared to the samples from the cylinder, the air content varies from 1% to 10%, and most of the values range from 3 to 7%, resulting in less dense ice. As previously noted, the samples from the base had cracks in the planes perpendicular to the growth direction. In addition, the higher air entrapment can be explained by the brine draining and the substitution of the volume occupied by saline water with the air.

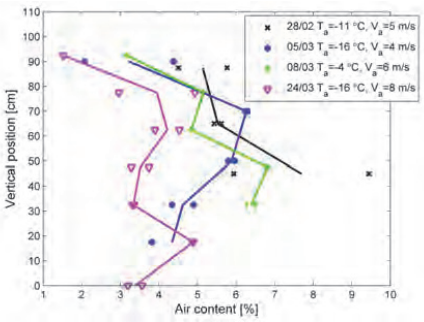

Fig. 12. Vertical profiles of air entrapment in the ice from the base.

In general, the measured densities ranged from 853 to 955 kg/m3 and were smaller than the values given by Ryerson and Gow (2000). The difference is so large that it cannot be explained by the different temperature conditions during the measurements but only by the

different air entrapment or the measurement accuracies. It is also important to note that the technique used here to measure the ice density had a precision of 1.3%.

CONCLUSIONS

The paper presented a reanalysis of the earlier obtained data by Kulyakhtin et al. (2012) in a small-scale field experiment. Most of the measurements corresponded to the thermally limited scenario and were predicted with a mean divergence of 20% and a maximum of 42% using analytical equations with the heat transfer function proposed by Achenbach (1977). The durations of the measurements were relatively long, lasting up to 140 min; however, the ice accretion rate was well predicted, though the shape of the accretion changed substantially with time.

The ice properties accreted on the metal cylinders and supporting construction were studied. The ice on the support construction accreted over a time of up to 6 hours. The salinity study showed the following results:

- The icicles' salinity was higher than the sea water's salinity.
- No salinity profiles were found inside the ice accreted on the 100-mm-diameter cylinder accreted over 104 min at a temperature of -11°C.
- The variation of the salinity along the ice growth direction of the samples on the supporting construction was relatively small and comparable to either the measurement errors or the spatial salinity variation in general (2 ppt). However, a significant vertical salinity variation was observed.
- A decrease of the ice salinity was observed on the bigger cylinders and on the support construction, which was most likely related to the fluid dynamics flow under the gravity effect.

The ice was denser (853 - 955 kg/m^3) in the small-scale experiments than in the field (690-967 kg/m^3). However, the saline ice density is strongly dependent on the laboratory temperature where the density was measured and should be recalculated into the air volume entrapment for the analysis. The ice from the cylinders contained small percentages of air volume (0.5-4.5%). The ice accreted on the construction on average had a higher air volume entrapment (3-7%), which can be explained by the salt drainage and the salt's substitution by air.

In addition, this work presented a technique for high-quality density measurements that can result in an accuracy of better than 1%.

ACKNOWLEDGEMENTS

The work presented is part of MARICE, which is a joint industry project between Det Norske Veritas, Statoil, the Norwegian University of Science and Technology and the Research Council of Norway, which studies marine icing on offshore structures and vessels. The authors wish to thank Aleksey Shestov and Gerd Irene Sigernes for their help in organising the laboratory work.

REFERENCES

Achenbach, E (1977). "The Effect of Surface Roughness on the Heat Transfer from a Circular Cylinder to the Cross Flow of Air," *Int J Heat Mass Transfer*, Vol 20, pp 359-369.

Cox, GFN, and Weeks, WF (1983). "Equations for Determining the Gas and Brine Volumes in Sea-Ice Samples," *J Glaciology*, Vol 29, No

Fukusako, S, Horibe, A, and Tago, M (1989). "Ice Accretion Characteristics along a Circular Cylinder Immersed in a Cold Air Stream with Seawater Spray," *Experimental Thermal Fluid Science*, Vol 2, pp 81-90.

Kulyakhtin, A, Løset, S, and Kollar, L (2012). "Small-Scale Simulation of Seawater Icing in Natural Field Conditions," *Proc 21th IAHR Int Symposium on Ice*, Dalian

Kulyakhtin, A, Kulyakhtin, S, and Løset, S (2013). "Field small scale study of icing created by periodic spray", *Cold Regions Science and Technology* (submitted).

Makkonen, L (1987). "Salinity and Growth Rate of Ice Formed by Sea Spray," *Cold Regions Science and Technology*, Vol 14, pp 163-171.

Makkonen, L (2010). "Solid fraction in Dendritic Solidification of a Liquid," *Applied Physics Letter*, Vol 96, 091910

Makkonen, L (2012). "Ice Adhesion – Theory, Measurements and Countermeasures," *J Adhesion Sceince and Technology*, Vol 26, pp 413-445.

Ryerson, CC, and Gow, AJ (2000). "Ship Superstructure Icing: Crystalline and Physical Properties," *U.S. Army Cold Regions Research and Engineering Laboratory* Tech. Report TR-00-11, 42 pp.

Szilder, K, (1994). "Simulation of Ice Accretion on a Cylinder due to Freezing Rain," *J Glaciology*, Vol 40, No 136, pp 586-594.

Journal of Fluids and Structures 48 (2014) 280–294

Contents lists available at ScienceDirect

Journal of Fluids and Structures

journal homepage: www.elsevier.com/locate/jfs

Numerical simulation of droplet impingement and flow around a cylinder using RANS and LES models

Anton Kulyakhtin [a,*], Olga Shipilova [b], Michael Muskulus [a]

[a] Department for Civil and Transport Engineering, Norwegian University of Science and Technology (NTNU), Høgskoleringen 7A, 7491 Trondheim, Norway
[b] Arctic Technology, DNV Research & Innovation, Det Norske Veritas (DNV), P.O. Box 300, 1322 Høvik, Norway

ARTICLE INFO

Article history:
Received 15 May 2013
Accepted 17 March 2014
Available online 18 April 2014

Keywords:
Collision efficiency
Particle and droplet flow
Cylinder
RANS
LES

ABSTRACT

The paper is devoted to the numerical modeling of droplet impingement on a cylinder and droplet transport behind it at a Reynolds number of 1.6×10^4. The objectives are to investigate the ability of different turbulence models to predict the collision efficiency and the droplet distribution in the wake in order to find the computationally most efficient way to achieve reliable results. The solutions of potential theory and four different RANS models are compared using the one obtained with Large Eddy Simulation as reference. The results show that the collision efficiency of the cylinder is predicted well by both potential theory and all considered RANS models for the given Reynolds number and droplet diameters of 13, 17, and 45 μm. However, only the RNG k–ε model with enhanced wall treatment results in the droplet flow in the wake behind the cylinder being similar to the results obtained by LES.

1. Introduction

Modeling of a turbulent flow combined with particle or droplet transport can be found in many industrial applications, for instance, in engine combustion, painting or snowdrift. This work has been motivated by investigations in the field of marine (or sea spray) icing of vessels. Ice accretion on a vessel results from freezing water transported by wind in the form of droplets. To eliminate negative operational issues and to reduce the frequency of ship accidents caused by ice forming on the ship deck and superstructure, it is important to have a physical understanding and the ability to predict icing.

The rate of ice accretion depends on the amount of water impinging on surfaces, which is determined by the air flow around and along the structure of interest. The classical approach used in icing estimation assumes either a uniform air flow field around large structures (Lozowski et al., 2000) or reduces the problem to potential flow; the structure is approximated by simple, well-understood geometries such as cylinders (Jones and Andreas, 2012). Makkonen et al. (2001) used potential theory with a panel method to calculate ice accretion on the front parts of wind turbine blades. To model the ice accretion on a complete aircraft, Nakakita et al. (2010) applied a two-phase model in which water droplets were represented as a second fluid dissolved in air. The complexity of vessel superstructure (which, in addition to the bridge in the front or rear part of the ship hull, can include various elements such as cranes, helicopter decks, antennas, etc.) results in a complicated, turbulent air flow with still regions and vortices. In Kulyakhtin et al. (2012b) and Shipilova et al. (2012), the steady RNG k–ε

* Corresponding author. Tel.: +47 45 06 34 10; fax: +47 73 59 70 21.
E-mail address: anton.kulyakhtin@ntnu.no (A. Kulyakhtin).

http://dx.doi.org/10.1016/j.jfluidstructs.2014.03.007
0889-9746/

Fig. 1. The ice accreted on the starboard side of the Coast Guard vessel *Nordkapp* on 27.02.1987 while the vessel was moving against the waves.

RANS model was applied to approximate the turbulent flow around the ship superstructure. The model was able to predict the ice accretion on the sides and the back of the superstructure while the ship was heading into the wind. This situation can be observed in reality (Fig. 1).

The calculated flow field yields transport of water droplets over and around the superstructure and droplet impingement on the aft and the back side of the superstructure. Since this approach is quite advanced for the field of marine icing, it requires a more rigorous validation. A direct comparison with observations presents substantial difficulties due to the limited amount of available empirical data on ice accretion, water inflow, and the flow field around vessels.

In this work, turbulent cross flow over a circular cylinder is considered to justify the choice of the turbulence model and to estimate the level of error introduced into ice accretion estimations performed with it. Although a large-scale vessel and the small-scale numerical experiment performed here correspond to different Reynolds numbers (Re), a cylinder in subcritical flow has been chosen to facilitate the understanding of the physical processes, mainly because it has a smaller number of affecting parameters. The effect of both surface roughness (Achenbach, 1977) and free stream turbulence (Sadeh and Saharon, 1982) on the air flow is weak when Re is substantially smaller than 1.0×10^5. In addition, small parts of the ship superstructure, such as antennas and ventilation systems, are exposed to this flow regime.

In the estimation of the ice accretion rate, the water flux due to sea spray is defined by the percentage of droplets impinging on the surface, i.e., by the collision efficiency. The air flow that delivers droplets to an object can be obtained by different approaches. The simplest possibility is based on the assumption of inviscid, irrotational flow, i.e., an approach based on potential theory. For example, Finstad et al. (1988) considered the case of a cylinder with droplet trajectories affected by the drag force while the droplets were approaching the cylinder. Makkonen and Stallabrass (1987) performed experiments in a wind tunnel with Re ranging from 1.3×10^4 to 1.7×10^5; the measured collision efficiency showed good agreement with the values calculated by Finstad et al. (1988). However, Yoon and Ettema (1993) measured the collision efficiency at a Re of 4.0×10^4 and found that the calculations by Finstad et al. (1988) overestimated it by approximately 100%.

In addition, gradients and curvatures of the streamlines observed in these experiments were steeper than the ones predicted by potential theory. According to Yoon and Ettema (1993), the existence of separated flow and the location of the separation point might significantly affect the flow field, and thereby the collision efficiency. Potential theory is not able to represent flow separation and the ensuing wake.

To include features such as separation and the wake behind the structure, turbulence models based on Reynolds averaging of the Navier–Stokes equations (RANS) can be employed. This class of models is computationally efficient and widely used for engineering applications. However, the suitability of a particular numerical model inside this class depends, among other things, on the flow regime. In the current work, three different RANS models are considered, namely, *the renormalization group* (*RNG*) *k–ε model* with both the *standard wall function* (*SWF*) and the *enhanced wall treatment* (*EWT*), the *transition shear-stress transport* (*SST*) model, and the *Reynolds-stress model* (*RSM*) with a *stress-omega submodel*.

According to Ong et al. (2009), the transient RNG k–ε model with SWF performs well in the case of transcritical and supercritical flow. Moreover, it requires a rather low resolution of the boundary layer. Namely, the non-dimensional wall distance $y^+ = u_* y/\nu$ should be higher than 30. Here u_* is the local friction velocity near the wall, y is the distance, and ν is the local kinematic viscosity of the fluid. However, according to Benim et al. (2008), this model cannot predict vortex shedding for the subcritical flow and, therefore, only the steady-state version of the model was used. Lad et al. (2010) conducted measurements and modeled the spray flow in the wake of a cylinder with the k–ε model at $\mathrm{Re} = 2.6 \times 10^3$. Yoon et al. (2006) performed calculations with the k–ε model at $\mathrm{Re} = 8.0 \times 10^3$. The droplet interaction with the cylinder and the droplet diameter distribution in the wake were measured. However, no investigation or comparison was performed with regard to the droplet concentration in the wake.

More sophisticated variants of RANS models are the RNG k–ε EWT, the transition SST, and the k–ω SST models, which require the first layer of the mesh to have $y^+ \approx 1$, i.e., a much finer mesh is needed. According to Benim et al. (2008), the k–ω SST model can reproduce the shedding of the larger vortices at $\mathrm{Re} = 1.0 \times 10^4$. The three-dimensional (3-D) k–ω SST model is able to predict the drag coefficient, C_d, quite accurately, whereas the two-dimensional (2-D) model typically overestimates C_d. Unfortunately, to the knowledge of the authors, there is no available data on the droplet distribution in the close or far wake of a cylinder for either the transition SST or for the k–ω SST model.

Therefore the first objective of the current work was to investigate the ability of different turbulence models to predict collision efficiency. In addition, the possibility of droplet impingement on the cylinder sides and back was examined. This work is also meant to find the computationally cheapest model able to produce reliable results. The second objective focuses on the suitability of different turbulence models for calculating the droplet distribution in the wake, which is important during ice accretion estimation for complex structures, such as ship superstructures.

The results of this work are based on a test case that allows a comparison with the experiments reported by Makkonen and Stallabrass (1987) and simulation results for the air flow field presented in Benim et al. (2008) for $\mathrm{Re} = 1.0 \times 10^4$. The Large Eddy Simulation (LES) model with Smagorinsky–Lilly subgrid parameterization following Benim et al. (2008) was used to obtain a reference solution for validation. Section 2 describes details of the turbulence models considered and the approach used for the droplet transport and water flux evaluation. The calculations were performed for the case of a cylinder of diameter $d = 10.24$ mm in 20 m s^{-1} wind speed, which corresponds to $\mathrm{Re} = 1.6 \times 10^4$ (see Section 3). The main findings are presented in Section 4.

2. Methods

2.1. Numerical model of air flow

RANS models are distinguished by the way the Reynolds stresses are evaluated and what empirical coefficients are used. The RNG k–ε model is based on the Boussinesq eddy viscosity assumption, according to which the deviatoric Reynolds stress is proportional to the mean rate of strain (Pope, 2000), and uses two additional equations for the turbulence kinetic energy and its dissipation to obtain closure. To simulate near wall flow the RNG k–ε model uses the SWF, which implements the "law of the wall", i.e., reproduces the empirically observed logarithmic velocity profile near a flat wall in the fully turbulent flow regime. The SWF performs poorly for flow with strong pressure gradients that result in flow separation (ANSYS, 2009). Another possible approach is to use the EWT, which numerically resolves the viscous sublayer, when used on a fine enough mesh. The method is able to simulate both laminar and turbulent boundary layers and takes into account the pressure gradient (ANSYS, 2009). The transition SST (later referred to as SST) also applies the Boussinesq assumption, resolves the near wall viscous sublayer, and uses closure equations for the turbulence kinetic energy and dissipation. In addition, the SST uses two correlation-based transport equations for intermittency and transition onset criteria to predict the transition of the flow from laminar to turbulent that is observed in experiments (Menter et al., 2006). The RSM model uses four and six transport equations for the individual Reynolds stresses in the 2-D and 3-D cases, respectively, and one equation for modeling the dissipation. The coefficients in the transport equations of the RANS models were chosen empirically to optimally reproduce certain properties of benchmark flows. Therefore, the quality of the models' predictions is highly dependent on flow type and the parameters of interest. In contrast to the RANS models, the LES model explicitly resolves the large length scales of the turbulent flow. It therefore requires a much finer mesh resolution. However, the Smagorinsky–Lilly subgrid model used with LES only consists of one equation (Kim et al., 2014). The models are implemented within the

ANSYS FLUENT software package and we refer the reader to the Fluent Theory Guide for further details and references (ANSYS, 2009).

The air density and viscosity were set to $1.315\,\mathrm{kg\,m^{-3}}$ and $1.7\times10^{-5}\,\mathrm{kg\,m^{-1}\,s^{-1}}$, respectively. These properties correspond to air at a temperature of $-4.5\,^{\circ}\mathrm{C}$. The direct comparison of the simulation results to the validation case by Makkonen and Stallabrass (1987) is complicated due to the change of the effective cylinder diameter in the experiments due to the ice growth. However, those results agree with the calculations of Finstad et al. (1988) quite well. Therefore we compare our results with results of Finstad et al. (1988) and the potential solution. For the latter, the analytical solution of Morsi and Alexander (1972) is projected onto the mesh used by the turbulence models.

The flow field predicted by the models is compared with respect to the following parameters. First, the pressure coefficient is considered (Zdravkovich, 1997):

$$C_p=\frac{p-p_\infty}{0.5\rho_a U_\infty^2}. \tag{1}$$

Here p is the local pressure, p_∞ is the far-field or reference pressure, and ρ_a is the air density. Variation of the pressure describes changes in the air velocity magnitude. The skin drag is negligible compared with the body drag for the cylinder at $\mathrm{Re}=1.6\times10^4$ (Zdravkovich, 1997). Therefore integration of C_p along the cylinder surface results in the C_l(lift) and C_d(drag) coefficients. Next, the separation point α_S and the Strouhal number (St) are compared. The latter represents the non-dimensional shedding frequency of vortices:

$$\mathrm{St}=\frac{fd}{U_\infty}, \tag{2}$$

where f is the shedding frequency and d is the cylinder diameter. The location of the separation point α_S is the position where the wall shear stress on the cylinder changes sign, per Sadeh and Saharon (1982).

The length of the eddy formation region is defined by the minimum of the local pressure coefficient L_f behind the cylinder, and is given in terms of distance from the cylinder center (Zdravkovich, 1997). However, many factors both externally prescribed to the flow as, for example, the inlet turbulence level and external sounds (Zdravkovich, 1997), as well as factors developing internally in the flow as, for example, acoustic resonance (Mohany and Ziada, 2011) affect the value of L_f. Comparing this value is therefore not very reliable.

2.2. Numerical model of droplet flow

The droplet flow is described by the following equation (Lozowski et al., 2000):

$$\frac{d\vec{V}_d}{dt}=-\frac{3}{4}\frac{C_{pd}}{d_d}\frac{\rho_a}{\rho_w}\left|\vec{V}_d-\vec{U}_a\right|(\vec{V}_d-\vec{U}_a)-\vec{g}\left(\frac{\rho_a}{\rho_w}-1\right). \tag{3}$$

Here $\vec{V}_d$ is the droplet velocity, t is time, C_{pd} is the droplet drag coefficient (which depends on the relative Reynolds number of the droplet), d_d is the droplet diameter, ρ_w is the droplet density (set to $1.0\times10^3\,\mathrm{kg\,m^{-3}}$), $\vec{U}_a$ is the velocity of air, and $\vec{g}$ is the acceleration due to gravity. In our case the effect of gravity was neglected, and the droplets are exposed only to viscous drag. The concentration of droplets is assumed to be small, and thus interactions between them and their influence on the air flow were neglected. FLUENT's built-in discrete-phase model (DPM) is used to calculate the trajectories of the droplets. $\vec{U}_a$ in Eq. (3) can be split into a sum of an average velocity and velocity fluctuations. The velocity fluctuations are realizations of a Gaussian random variable with standard deviation proportional to the square root of turbulence kinetic energy. The values obtained are constant during a period of time inversely proportional to the specific dissipation rate (ANSYS, 2009).

The droplets in the flow are assumed to be spherical. Yoon and Ettema (1993) estimated a possible effect from non-sphericity of droplets. They tested ellipsoidal droplets with a ratio of the principal axes equal to 2. This resulted in a change of drag coefficient by 35%, whereas the resulting collision efficiency was changed by less than 1%. Thus, for our purposes, the effect of non-sphericity can be neglected.

2.3. Collision efficiency

To define the ice accretion rate, the water flux to which the structure is subjected has to be known. According to Stallabrass (1980) the water flux is described as

$$M=E_c UwA, \tag{4}$$

where U is the free stream air flow velocity relative to the obstacle,w is the liquid water content (LWC), E_c is the collision efficiency, $A=L_c d$ is the front projected area, and $L_c$is the cylinder length. The LWC is given by the total mass of water droplets per unit volume of air. The collision efficiency represents the ratio of droplets that interact with the object compared with the total concentration in the undisturbed air.

3. Numerical set-up and procedures

The domain size and the mesh structure are based on the paper of Benim et al. (2008), which considered flow at $Re = 1.0 \times 10^4$. It was found that the blockage effect on the drag coefficient is small when the domain width is 12 times larger than the cylinder diameter. Here the ratio of the tunnel width to the cylinder diameter is 16. The mesh used for 2-D simulations is sketched in Fig. 2. The domain is 16 by 24 diameters (d), and it was split into several regions to better control mesh construction. The 3-D mesh is πd wide in the direction perpendicular to the plane shown in Fig. 2. The origin of the coordinate system is in the cylinder center. The mesh in the circle with diameter $8d$ was refined close to the cylinder in the radial direction. The cylinder was split into four sectors; the ends of these sectors correspond to the corners of the 16 by 16 diameter subdomain. Each sector was split into 64 nodes on the boundary, except for the refined LES mesh. The same was done in the direction perpendicular to the air flow. The rest of the 16 by 16 diameter subdomain was meshed in the radial direction. The boundaries in front of the outlet were realized with equidistant nodes.

The mesh parameters are summarized in Table 1. The calculations with the RNG k–ε SWF model were performed on meshes marked as "k–ε SWF". The rest of the 2-D models, including the RNG k–ε EWT, were performed on meshes marked as "2-D". Refined meshes used for verification of grid resolution independence are marked by a star (*). In the 3-D case, only the results of the LES model were verified on another mesh. Due to the high computational cost, only part of the refined 3-D* mesh (see Table 1) is finer, whereas other parts of it are coarser than the 3-D mesh.

The left boundary was modeled as a velocity inlet, with velocity equal to 20 m s^{-1}. The turbulence intensity was set to 0.1%, according to Benim et al. (2008). The viscosity ratio was chosen to minimize the decay of inlet turbulence intensity and equals 0.3. The surface of the cylinder is assumed to be smooth. The boundaries perpendicular to the z-axis were periodic, and the symmetry boundary condition was used on the upper and lower boundaries (Fig. 2).

The pressure–velocity calculation is coupled by the SIMPLE scheme. The second-order upwind scheme is used for spatial discretization, and the second-order implicit scheme is used for the transient formulation. Calculations were performed with double accuracy, and the residuals (i.e., with respect to continuity of the solution, momentum equations, etc.) were performed within 1.0×10^{-5} relative error as the criterion for convergence of the solution.

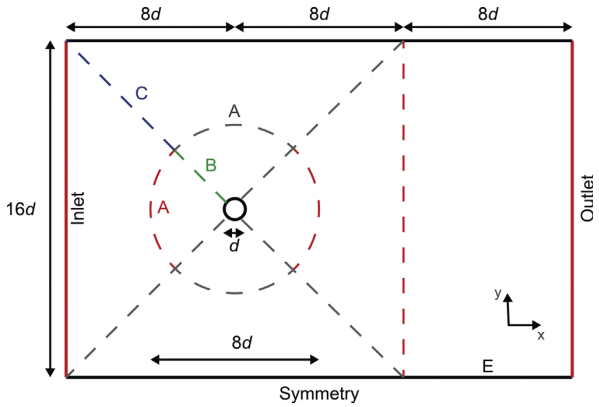

Fig. 2. The calculation domain, boundaries and grid topology. A, B, C, and E mark mesh edges with different topology. The dimensions of the domain are given in terms of the cylinder diameter d, the details are presented in Table 1.

Table 1
Mesh parameters used for modeling. See Fig. 1 for the location of mesh parts A, B, C, and E. N – number of elements; GR – growth rate; FE – first element height, the value is in cylinder diameters.

		k–ε SWF	k–ε SWF[a]	2-D	2-D[a]	3-D	3-D[a]
A	N	64	64	64	64	64	90
B	N	21	45	125	300	300	240
	FE [d]	0.06	0.06	0.001	5×10^{-4}	5×10^{-4}	0.001
	GR	1.10	1.01	1.04	1.016	1.016	1.01843
C	N	12	35	30	40	40	40
	GR	1.11	1.04	1.04	1.056	1.056	
E		32	32	32	32	32	64
	N, along z-axis	N/A	N/A	N/A	N/A	66	60
	N, total [× 1000]	9.7	20	41	87	87 × 66	87 × 60
	Max y^+	35	35	1.2	0.61	0.61	1.2

[a] Meshes used for verification of results.

The Strouhal number for $Re = 1.6 \times 10^4$, according to experiments reported in Zdravkovich (1997), is in the range 0.20–0.22. Thus the expected period of vortex shedding $T_v$and thereby of periodic fluctuations of the lift force is 2.32–2.56 ms. The time step used was 0.025 ms (approximately 100 steps per T_v) for the 2-D RANS models and 0.01 ms (approximately 250 steps per T_v) for the LES and 3-D RANS models. This is a relatively large time step compared with, for example, Ong et al. (2009), in which 5000 steps per T_v was used. The Courant number across the domain, corresponding to the 0.025 ms time step, is less than 15 for the SST model. To test the correctness of the chosen time step in case of the 2-D SST model, the time step was decreased down to 0.01 ms and 0.003 ms, which resulted in a change of the drag coefficient of less than 5%. For the final simulation, the 0.025 ms time step was used in order to speed up the simulations. Stable periodic numerical solutions were obtained after approximately $10–30T_v$, depending on the model.

The droplets were injected from a plane (or line in the 2-D simulations) normal to the air flow direction and at a distance of $7.75d$ in front of the cylinder center, with an initial speed of 20 m s^{-1} along the x-axis. Inside the injection plane droplets were spread uniformly within the range of $-0.75d$ to $0.75d$ along the y-axis. The width of the cloud was chosen as a compromise between decreasing the number of tracked droplets and at the same time minimizing the effect of the finite cloud width on the collision efficiency.

In the case of the steady RNG k–ε model 1.0×10^5 droplets were injected. Calculations with 1.0×10^6 droplets resulted in a difference in the collision efficiency of less than 0.1% in the case of the RNG k–ε model and a 17.1 μm droplet size.

In the case of the transient 2-D RNG k–ε and SST models, 1.0×10^3 droplets were injected at each time step from the plane; the total amounted to approximately 1.0×10^5–3.0×10^5 droplets per simulation. These injections were performed at discrete times, and the number of injections N_{inj} varied in such a way that the total injection duration was an integer multiple of T_v. In case of the 3-D models, 400 droplets were spaced along the y-axis, 40 droplets were spaced along the z-axis, and were injected 50–100 times per period of the lift force, for a total of approximately 3.0×10^5 droplets.

The droplets were tracked with the same 0.025 ms time step in all cases. The collision efficiency is calculated as

$$E_c = \frac{N_{int}}{(N_{pl}/1.5d)N_{inj}d}, \tag{5}$$

where N_{int} is the total number of droplets that interacted with the cylinder during the simulation and N_{pl} is the number of droplets per injection. A special user-defined function was developed to count the number of droplets that interacted with the cylinder.

The local collision efficiency is given by

$$E_\alpha = \frac{N_\alpha}{((d/2)\Delta\alpha)}\frac{d}{N_{int}}, \tag{6}$$

where N_α is the number of droplets interacting with the cylinder at angle α within a sector of size $\Delta\alpha$.

4. Results

4.1. Air flow field

The main flow characteristics predicted by the different models are summarized and compared with data available in the literature in Table 2.

In general, all the models (including potential theory) show a similar distribution of pressure in front of the cylinder (along the x-axis; see Fig. 3). However, behind the cylinder the models predicted different flow fields. The RNG k–ε model

Table 2
The parameters of the flow field obtained by different models and in experiments.

	C_d	C_d (STD)	C_l (STD)	St	α_S[deg]	$L_f[D_c]$
2-D RNG k–ε, SWF	0.24	N/A	N/A	N/A	151.4	0.74
2-D RNG k–ε, EWT	0.513	0.001	0.087	0.27	98.0	0.76
2-D SST	1.66	0.11	1.49	0.23	94.8	0.94
3-D SST	1.42	0.06	0.92	0.20	87.6	0.78
3-D RSM	1.49	0.10	1.02	0.19	89.1	0.97
3-D LES	0.99	0.03	0.10	0.21	83.7	1.6
Literature, Experiments						
Son and Hanratty (1969), $Re = 1.6 \times 10^4$					82	
Zdravkovich (1997)	1.1–1.2	0.1	0.2–0.7	0.2–0.22	81–90	1.0[a]
Achenbach and Heinecke (1981)[b]	1.4			0.21		
Humphreys (1960)	1.1–1.2	0.05–0.15				

[a] When the aspect ratio is high. It increases with a decrease in the aspect ratio. It is also strongly affected by external sounds and turbulence intensity (Zdravkovich, 1997).

[b] The blockage ratio is high (0.167). The values are presented without blockage correction.

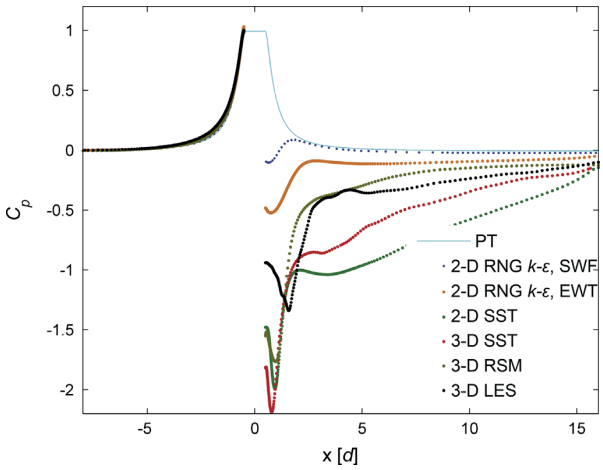

Fig. 3. Pressure coefficient distribution from different models, along the x-axis. PT – potential theory, SWF – standard wall function, EWT – enhanced wall treatment. RNG k–ε, SST, RSM, and LES are different turbulence models.

with SWF showed results similar to those obtained by potential flow, whereas the other RANS models and LES differ, while being similar to each other. If the droplets were to interact only with the cylinder front, all of the models would predict the collision efficiency well, even though the predicted position of the separation point and the structure of the wake would be different.

The SWF assumes that the boundary layer is turbulent everywhere on the cylinder. At a Reynolds number on the order of 10^4 the flow separates from the laminar part of the boundary (Achenbach, 1975). In this flow regime, the RNG k–ε model with SWF therefore cannot predict vortexes (which was also tested numerically in transient simulations), and only the steady 2-D RNG k–ε model with SWF is therefore considered. The separation point was predicted incorrectly (Fig. 4 and Table 2). The values obtained are similar to those for the transcritical and supercritical flow regimes, i.e., the RNG k–ε with SWF is not adequate for the considered regime. Incorrect prediction of the separation point and the base pressure explains the smaller drag coefficient, compared with experimental results (Table 2). The result improves when the RNG k–ε model is used with EWT. The vortexes have a frequency that is 35% higher than the one experimentally measured. However, the values of C_d and C_l are lower than the experimental ones, and α_S is shifted 16° in the leeward direction.

The LES model shows the best agreement with the experimental data. The drag coefficient, the location of the separation point, and the Strouhal number are in good agreement (see Table 2). The drag coefficient predicted by the LES and 3-D RANS models exhibits some non-periodic oscillations, compared with the 2-D RANS results, which is a three-dimensional effect in agreement with experiments (Humphreys, 1960). However, the frequency analysis revealed only one strong peak corresponding to the main shedding frequency. The local pressure distribution on the cylinder surface is a bit higher than in the experiments. It is also important to note that Table 2 gives the standard deviation of the drag and lift coefficients, whereas the experimental results are given in terms of the amplitude of oscillations, i.e., it is normal that the values are lower. However, the LES predicts smaller lift oscillations than measured. In addition, the position of the pressure minimum L_f is registered further behind the cylinder than in the experiments.

The 2-D SST model predicts α_S shifted only by approximately 10°, St is only 10% overpredicted, and L_f is in excellent agreement with the experiments. The value of C_d is approximately 40% higher than the average value in the experiments; however, the local pressure distribution is similar to the experimental one. It has an almost constant shift in the base pressure compared to LES, starting 20–30° before the separation point. This explains the overestimation of the drag coefficient. In general, the 2-D SST model can predict the main features of the flow.

As shown by the pressure distribution in Figs. 3 and 4, the mean flow field in front of the cylinder, as calculated by the different models, is quite similar. Due to the low inlet turbulence intensity (0.1%), the fluctuations of velocity in front of the cylinder are quite small compared to the mean values. At the same time, the turbulence level in this region predicted by the RNG k–ε model with SWF is higher than one predicted by SST for the same reason; the model with SWF assumes a fully turbulent boundary flow close to the wall region. For example, the turbulence intensity at the point $0.5d$ before the front stagnation point predicted by RNG k–ε with SWF is 40 times higher than the inlet turbulence. The turbulence intensity at that point is only a few percent different from the inlet turbulence when RNG k–ε with EWT, SST, or RSM models are used.

The 3-D SST and 3-D RSM show flow field properties similar to those of 2-D SST but agree with the experiments even better than the 2-D RANS models. In general, the SST and RSM models produce vortexes that cross the x-axis right behind the cylinder (see Fig. 5b). The LES approach results in a shadow zone behind the cylinder (Fig. 5c) that is similar to the one calculated by the RNG k–ε model with EWT (Fig. 5a).

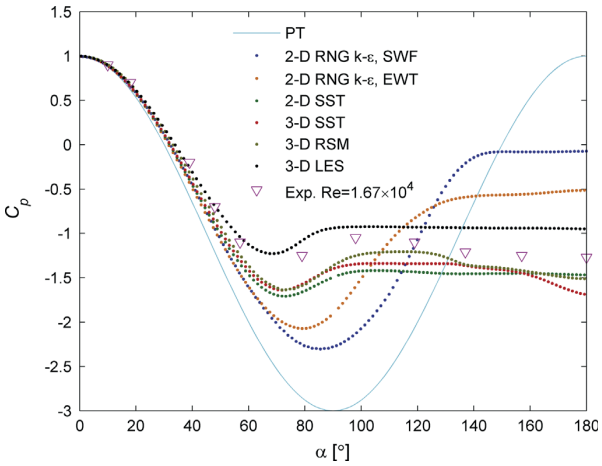

Fig. 4. Pressure coefficient distribution on the cylinder surface. The experimental values were taken from Zdravkovich (1997). See Fig. 3 for abbreviations used.

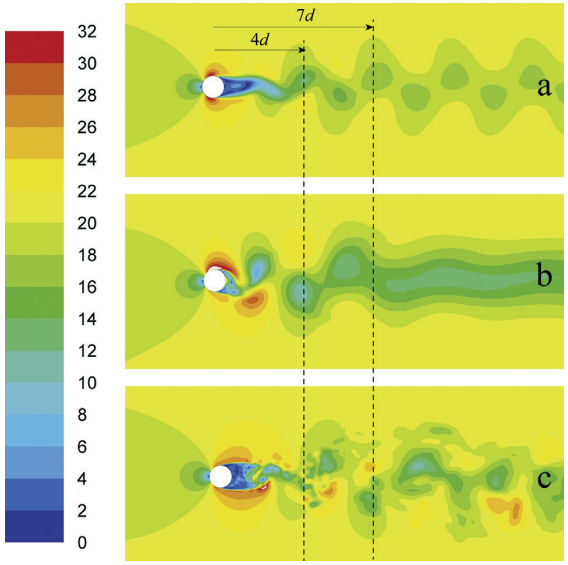

Fig. 5. Instant velocity magnitude: (a) RNG k–ε with EWT; (b) RSM; and (c) LES.

4.2. Collision efficiency

Table 3 shows the obtained collision efficiencies. The values reported here are larger than the ones obtained in the time-dependent simulations of Makkonen and Stallabrass (1987). The reason is that those authors took into account the true instantaneous cylinder diameter during the ice growth, whereas here only the initial diameter is used. The smallest difference in collision efficiency to the results obtained by Finstad et al. (1988) is revealed for the biggest droplet size, namely 45 μm. A clear trend of decreasing collision efficiency is observed when more sophisticated turbulence models are used.

Fig. 6 shows the spatial distribution of E_α for each sector ($\Delta\alpha$=0.027 rad) on the cylinder surface, obtained by LES and Eq. (6). Note that the decrease of the local collision efficiency with increasing angle is not very representative for the physical process of ice aggregation because the projection of the sector $\Delta\alpha d/2$ on the surface normal to the flow direction decreases with increasing α. However, Fig. 6 demonstrates explicitly the contribution of each angle to the total collision efficiency. Approximately 90% of droplets (for all considered droplet diameters) interact with the cylinder before the angle of 50°, which is another 30° before flow separation occurs.

Table 3
The collision efficiency predicted by the use of different turbulence models for three different droplet diameters.

Droplet size	13.1 μm	17.1 μm	45 μm
Makkonen and Stallabrass (1987)			
Experiment	0.46	0.56	–
Calculation	0.43	0.53	–
Based on Finstad et al. (1988)	0.459	0.614	0.881
Numerical modeling			
PT, CFD	0.498	0.615	0.889
2-D RNG k–ε, SWF	0.50	0.615	0.89
2-D RNG k–ε, EWT	0.477	0.601	0.886
2-D SST	0.476	0.600	0.887
3-D SST	–	0.599	–
3-D RSM	–	0.596	–
3-D LES	0.461	0.586	0.883

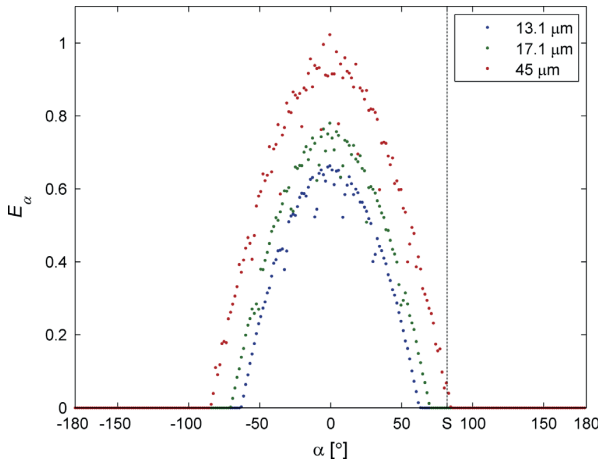

Fig. 6. Spatial distribution of E_c along the cylinder surface calculated by LES for different droplet diameters. S on the x-axis marks the separation point.

The maximal angles at which droplets impinge are 62°, 69°, and 84° for 13.1 μm, 17.1 μm, and 45 μm, respectively, and these values are in agreement ($\pm 0.5°$) with the results of Finstad et al. (1988). An important observation is that for the given Reynolds number and droplet diameters, the droplets impinge in the laminar boundary region, well before the separation point (Table 2). This explains the good agreement with the results of potential flow theory and the weak influence of the separation point and turbulence models on E_c. E_c is also insensitive to the injection duration (relative to T_v), in contrast to the droplet distribution behind the cylinder (see below). The RNG k–ε model with SWF predicts higher levels of turbulence, as was mentioned before, but this does not have a significant effect on E_c.

In general, all models show good agreement with the results of Finstad et al. (1988), the differences are less than 8%. The introduction of turbulence models therefore cannot substantially improve the prediction of E_c on the frontal parts of objects, if droplets are not expected to impinge behind the separation point. The computationally cheapest techniques, namely, potential flow or the RNG k–ε model, can calculate E_c reliably in such cases.

An important requirement is that droplets are inserted into the domain from a far enough distance. For example, Finstad et al. (1988) injected droplets at a distance 10d from the cylinder, and E_c diverged by 0.7% when the droplets were injected at a distance of 20d instead. Table 4 shows the relative difference in E_c obtained when droplets are injected at a shorter distance compared with the case when droplets are injected at the 7.75d distance with the 2-D SST model. Even the distance of two diameters leads to relatively reliable results. The difference grows, however, when the droplet diameter decreases.

4.3. Droplets distribution in the wake

Fig. 7 presents examples of droplets motion (each point represents a droplet) in the cylinder wake predicted by LES, for two different moments in time; the second plot shows the situation 1.55 ms (a fraction of 0.65 of the vortex shedding

Table 4
Relative overprediction of the collision efficiency due to a decrease of the injection distance relative to a 7.75*d* injection distance for droplets with different diameters.

Injection distance (μm)	4 diameters (%)	2 diameters (%)	Finstad et al. (1988) (%)
7	1.1	7.1	11.8
13.1	1.1	6.7	4.4
17.1	1.2	5.8	1.6
45	–	–	0.75

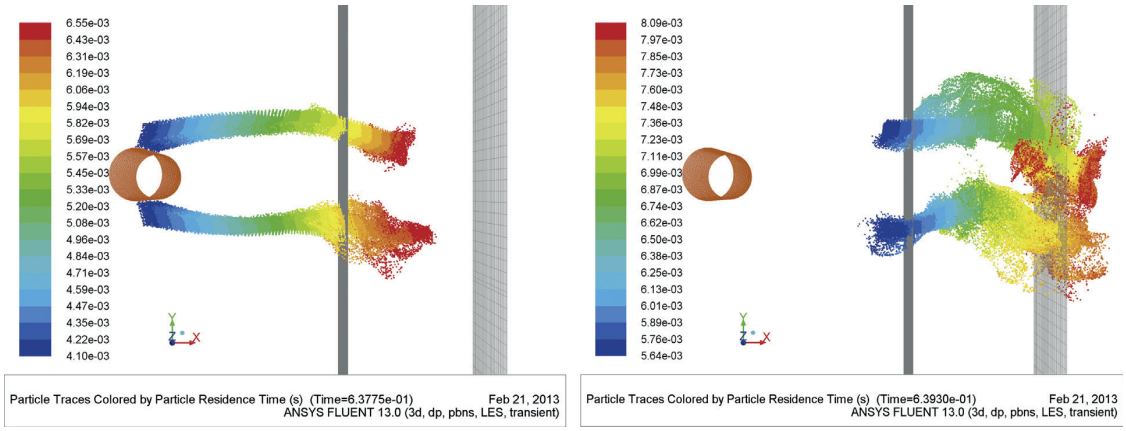

Fig. 7. 17.1 μm droplet flow in the cylinder wake predicted by 3-D LES at two moments of time. The color represents the time the droplet spent in the domain after injection. Surfaces at 4*d* and 7*d* distances behind the cylinder are marked by gray lines. (For interpretation of the references to color in this figure legend, the reader is referred to the web version of this article.)

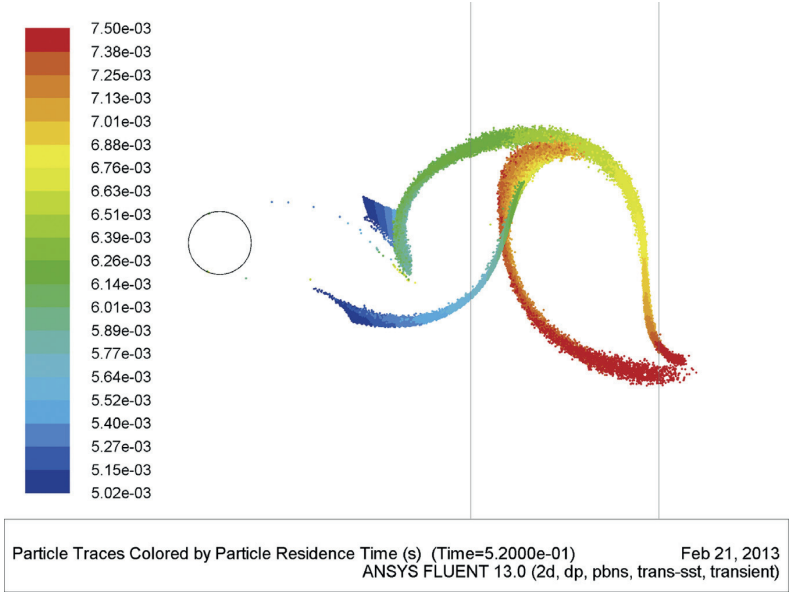

Fig. 8. 17.1 μm droplet flow in the cylinder wake predicted by 2-D SST. The color represents the time the droplet spent in the domain after injection. Surfaces at 4*d* and 7*d* distances behind the cylinder are marked by gray lines. (For interpretation of the references to color in this figure legend, the reader is referred to the web version of this article.)

period) later than the first one. The figures demonstrate the existence of a shadow region behind the cylinder that is free from droplets. This region ends only at a distance of approximately 7*d* behind the cylinder, when droplets become involved in vortexes.

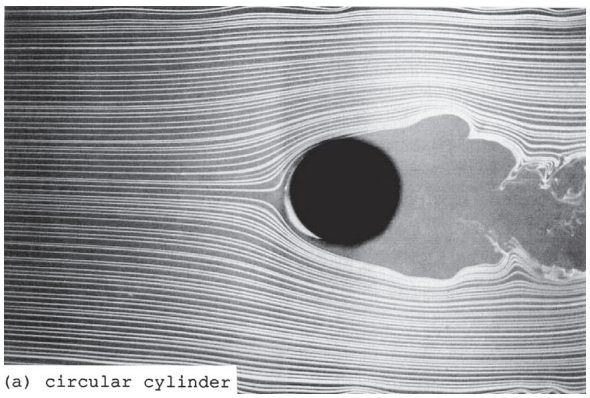

Fig. 9. Flow pattern around circular cylinder at $Re = 3 \times 10^4$, reprinted from Yoon and Ettema (1993), ©1993, with permission from Elsevier.

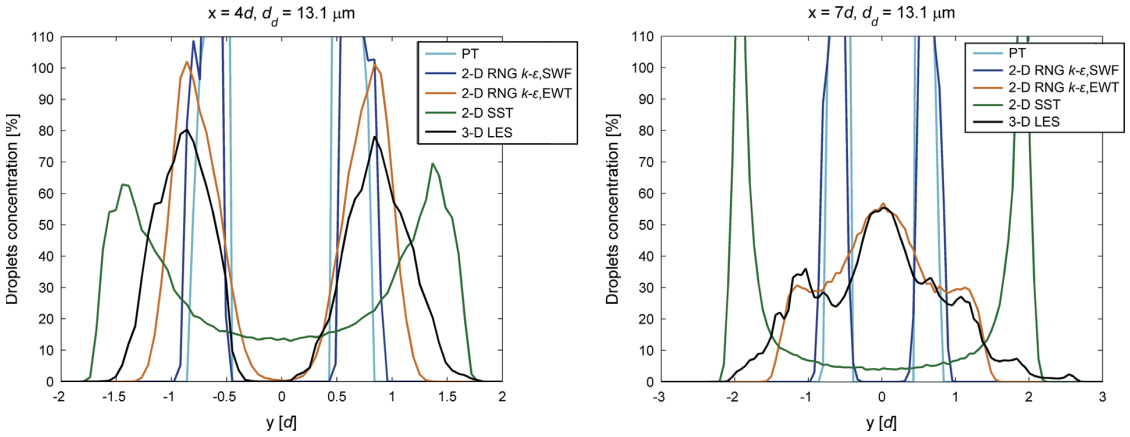

Fig. 10. 13.1 μm droplet distributions in the wake of the cylinder, predicted by different models. PT – potential theory, SWF – standard wall function, EWT – enhanced wall treatment. RNG k–ε, SST, RSM, and LES are different turbulence models.

Fig. 8 shows results obtained with the 2-D SST model. The droplets cross the central axis right behind the cylinder, and this pattern repeats itself, with the droplets following the streamlines around large vortexes. The structure of the flow is substantially different from the one predicted by LES (Fig. 5c). No data were found in the literature regarding the droplet distribution in the wake close to the cylinder. The only evidence of this phenomenon is the picture of smoke flow around a cylinder at $Re = 3.0 \times 10^4$ in Fig. 9. As will be shown later, smaller droplets mix more strongly and cross the x-axis for the first time earlier than larger ones. We therefore expect stronger mixing of smoke than mixing of droplets (of our sizes). According to Fig. 9, the smoke is not mixed for at least $2.5d$ behind the cylinder (the flow further downstream is not visible), which supports the predictions by LES and is in conflict with the results obtained by the SST model. It seems that the small vortexes predicted by LES pre-empt droplet entrapment into larger vortexes.

The LES results in Figs. 10–12 illustrate the distribution of droplet concentration, which is the ratio of the time-averaged droplet flow per unit area through the considered plane to the droplet flow per unit area through the injection plane, at distances of $4d$ and $7d$ behind the cylinder. The droplet distribution obtained by LES with one and two periods of injections is in good agreement, even though the flow field calculated with LES is not (regularly) periodic and exhibits random fluctuations. Therefore complete symmetry and similarity of the LES results is not expected because this would require longer-term averaging. As mentioned earlier, droplets do not become entrapped and advected by vortexes before a distance of $7d$. For the 45 μm droplet diameter at this distance, the maximum concentration is not yet found at the central axis due to the higher inertia of the droplets. It is also clear that smaller droplets disperse easier in the turbulent flow.

Both potential theory and the RNG k–ε model with SWF predict a shadow region behind the cylinder that stretches along the whole domain. Only in the case of 45 μm droplets give these models results comparable to the LES simulations. This is the case in which droplets are heaviest and therefore relatively unaffected by the flow, i.e., when the droplet distribution can be well predicted by analytical methods. The RNG k–ε model with SWF predicts a slightly larger distance between the regions of maximum concentration relative to potential theory. The reason is the flow separation and the shadow region

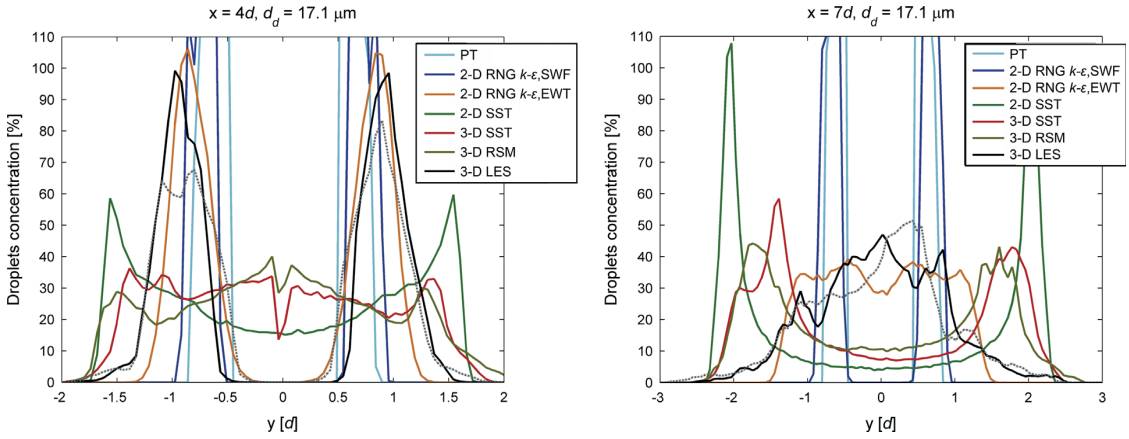

Fig. 11. 17.1 μm droplet distribution in the wake of the cylinder, predicted by different models. See Fig. 10 for abbreviations used.

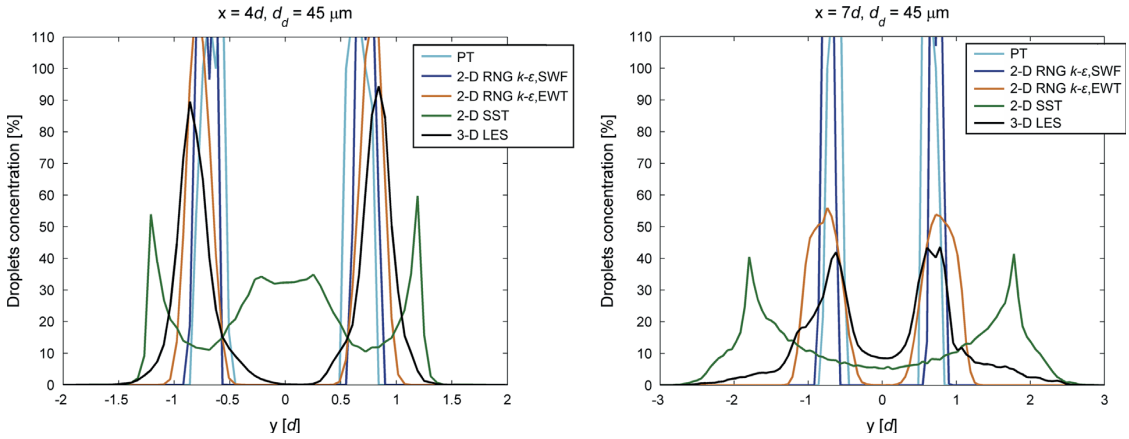

Fig. 12. 45 μm droplet distribution in the wake of the cylinder, predicted by different models. See Fig. 10 for abbreviations used.

predicted by the RNG k–ε model; the droplets are not forced by the flow to move closer to the central axis. The results obtained by the RNG k–ε model with EWT are in good agreement with the LES simulations, with little dependence on the droplet diameter. This result is remarkable because the RNG k–ε model with EWT exhibits characteristics around the cylinder quite different from what is obtained for LES (Section 4.1). However, the velocity shadow behind the cylinder (Fig. 5) is similar for both LES and RNG k–ε with EWT. The shadow region keeps droplets away from crossing the x-axis and approximately extends to the distance of $4d$.

In contrast, the 2-D SST, 3-D SST, and 3-D RSM models predict large high-velocity vortex structures which cross the x-axis immediately after the cylinder. The droplets follow the main streamlines, thus either resulting in the maximum droplet concentration occurring on the sides (Figs. 10 and 11; on the right) or resulting in a relatively uniform distribution within a certain width. The variation of the distribution of droplets in planes perpendicular to the x-axis is periodical along the x-axis (see Fig. 8).

5. Discussion

The discrepancy in the collision efficiency between results presented in the current paper and results of Finstad et al. (1988) is small. The largest difference was obtained in the case of a 7 μm diameter droplet and was 11.8%. This difference is due to numerical errors. The results of Finstad et al. (1988) are based on fitting a regression curve to numerical results, and the observed discrepancy is explained by the residuals of this fit. Repeating the numerical calculation on which Finstad et al. (1988) based their fit, the discrepancy drops to only a few percent. In general, the results here do not support the suggestion of Yoon and Ettema (1993) that turbulent flow produces a different collision efficiency.

The effect of turbulence intensity on the flow field is weak for the cases of the authors' interest (see Section 1), although the turbulence intensity can affect the concentration and size distribution of droplets in front of a cylinder (Kulyakhtin et al., 2012a). During the experiments of Makkonen and Stallabrass (1987), the level of turbulence was approximately equal to 3.5% in the test

chamber. Detailed data describing the turbulence and flow field development were not available in the paper, thus exact or detailed modeling of their experiment was impossible. In our calculations, the turbulence intensity was set to 0.1%. We would have preferred to replicate the experiment with the same value of turbulence intensity, but the assumptions used in most of the RANS models, with the exception of the RSM, do not fit these conditions. The reason is as follows:

Turbulence intensity does not scale with Reynolds number. The characteristic size of turbulent eddies can be estimated using the relations of the k–ε model for the turbulence length scale (l_T) from Pope (2000):

$$l_T = 1.5\frac{\mu_a}{\rho_a U_\infty I}\left(\frac{\mu_t}{\mu_a}\right), \tag{7}$$

where μ_a is the air viscosity, μ_t is the turbulent viscosity, and I is the turbulence intensity. Eq. (7) results in a size of 0.3 mm in the case of I equal to 0.1%, for a viscosity ratio of 0.3. In the case of I equal to 3.5%, and if the viscosity ratio is chosen to be 460 to keep the level of turbulence from decreasing too quickly, the length scale is 12 mm, which is comparable to the cylinder size. The Boussinesq approach, however, assumes μ_t as an isotropic scalar value, which is contradictory for the given situation. In addition, the size of inlet turbulent eddies is comparable to the size of vortexes shed from the cylinder, and in reality interference occurs. Therefore the RNG k–ε and SST models cannot be applied. The LES model, in the case of I equal to 3.5%, showed approximately the same values for collision efficiency and droplet distribution in the wake as LES with I equal to 0.1%; however, small, non-periodic deviations were observed. The LES calculations performed with no inlet turbulence intensity resulted in less than a 1% difference of air and droplet flow from the ones obtained with 0.1% inlet turbulence.

The angle at which flow separation occurs is always above 75° in the Reynolds number range from 1.0×10^4 to 5.0×10^6, with its lowest value around $\mathrm{Re}=1.0\times10^5$, depending on turbulence intensity and the surface roughness (Achenbach, 1968; Zdravkovich, 1997). This means that potential theory can also be used for flow regimes other than the ones considered here. The only parameter that could possibly affect the results is the transition from a laminar to a turbulent boundary layer. Therefore it would be interesting to investigate droplet interaction with the cylinder in cases in which the transition point is located at less than 50°.

Flow separation moves the non-interacting droplets even further away from the cylinder surface. Because the flow does not attach to the surface after separation, there are no impinged droplets on the sides and on the back of the cylinder. This means specifically that vortexes shed from the cylinder cannot bring droplets to the back of the cylinder. The calculated ice accretion on the sides described in Kulyakhtin et al. (2012b) may however be explained by the flow field around a rectangular cylinder (see, for example, Okajima, 1982; Shimada and Ishihara, 2012) in which the flow separates at the leading edge and later reattaches, or by the interaction between wake behind structural elements and the boundary layer along the walls (see, for example, He et al., 2013).

As was shown here, any of the models predict the collision efficiency well. However, the droplet flow in the wake is different for each model. It seems that LES provides the physically most reasonable result. The 2-D k–ω SST model (Menter, 1994; Rastgou and Saedodin, 2013) was additionally tested, and it exhibited results similar to the 2-D transition SST model. In general, the reasonable agreement between the droplet distribution in the wake obtained by using the RNG k–ε model with EWT, and the results obtained by LES show that flow parameters such as the distribution of the local pressure coefficient, L_f (where significant differences could be observed) are not indicative of the models' ability to predict the behavior of the wake. It is therefore required to consider the spatial distribution of the wake velocity. Unfortunately, there is no representative non-dimensional number that can be used to characterize this behavior of the flow.

These conclusions, in terms of the suitability of the models for estimating collision efficiency, can be reasonably extended to other flow regimes. However, the result obtained for the droplet flow in the cylinder wake is most likely valid only within the considered flow regime; i.e., the RNG k–ε model with SWF, the transition SST, and the RSM models can be expected to perform better at higher Reynolds numbers.

6. Conclusions

The main focus of this work was an evaluation of different approaches for modeling droplet flow in air, which is particularly important for the problem of icing estimation. The modeling consisted of two stages: simulation of the air flow and simulation of the droplet transport in it. Primarily the first stage was investigated. A simple example of subcritical flow around a cylinder was considered. The predicted flow was evaluated on the basis of flow field properties, the collision efficiency, and the droplet distribution in the wake. The results of several turbulence models (RANS 2-D RNG k–ε with SWF, unsteady RANS 2-D RNG k–ε with EWT, 2-D and 3-D transition SST, 3-D RSM, and LES) were compared with predictions by potential theory. A particular case was studied, with a cylinder of diameter 10.24 mm in a 20 m s^{-1} air flow, chosen due to the existence of experimental data for the collision efficiency. The main findings are:

- A total of 90% of the droplets interact within angles of $\pm 50°$ from the stagnation point. The maximal impingement angle is in good agreement with potential theory. This is partially due to the location of the separation point at 82°, which is further than the maximal impingement angle.
- All models studied predict similar values for the collision efficiency, with a difference of less than 8%. Thus, any model can be used in cases where droplets are expected to impinge only on the front of a structure (when flow separation does not have an effect).

– Both the SST and RSM models predict similar flow and droplet behavior behind the cylinder, but different from the LES prediction. Only the 2-D RNG k–ε model with EWT was able to exhibit droplet distributions similar to the ones predicted by LES, even though the separation point, vortex shedding frequency, and drag coefficient obtained are very different.

Both the RNG k–ε model with SWF and potential theory predict a shadow region free of droplets behind the cylinder along the flow direction for a distance greater than 16 diameters. The transition SST and RSM models predict large vortexes, which droplets follow, with only small deviations due to their inertia, and there is no such region free of droplets after one diameter behind the cylinder. The LES simulations resulted in the most reasonable behavior, such as a shadow region free of droplets that extends to a distance of approximately 7d for the given combination of cylinder and droplet diameters.

It would be interesting to investigate the transport and accretion processes for higher Reynolds numbers (with no laminar boundary layer) in the front of the cylinder and for rectangular objects. In the latter case, it would also be possible to investigate droplet impingement on the sides, which was not found in the case of circular cylinders.

Acknowledgements

This work is part of MARICE, a joint industry project between Det Norske Veritas, Statoil, the Norwegian University of Science and Technology, and the Research Council of Norway, which studies marine icing on offshore structures and vessels. The authors wish to thank Dr. Lasse Makkonen for valuable comments and Prof. Sveinung Løset for sharing his picture of ice accretion on K/V *Nordkapp*.

References

Achenbach, E., 1968. Distribution of local pressure and skin friction around a circular cylinder in cross-flow up to Re$=5\times10^6$. Journal of Fluid Mechanics 34, 625–639.
Achenbach, E., 1975. Total and local heat transfer from a smooth circular cylinder in cross-flow at high Reynolds number. International Journal of Heat and Mass Transfer 18, 1387–1396.
Achenbach, E., 1977. The effect of surface roughness on the heat transfer from a circular cylinder to the cross flow of air. International Journal of Heat and Mass Transfer 20, 359–369.
Achenbach, E., Heinecke, E., 1981. On vortex shedding from smooth and rough cylinders in the range of Reynolds numbers 6×10^3 to 5×10^6. Journal of Fluid Mechanics 109, 239–251.
ANSYS, 2009. FLUENT 12.0 Theory Guide, Cannonsburg.
Benim, A., Pasqualotto, E., Suh, S., 2008. Modelling turbulent flow past a circular cylinder by RANS, URANS, LES and DES. Progress in Computational Fluid Dynamics 8, 299–307.
Finstad, K.J., Lozowski, E.P., Gates, E.M., 1988. A computational investigation of water droplet trajectories. Journal of Atmospheric and Oceanic Technology 5, 160–170.
He, G., Pan, C., Wang, J., 2013. Dynamics of vortical structures in cylinder/wall interaction with moderate gap ratio. Journal of Fluids and Structures 43, 100–109.
Humphreys, J.S., 1960. On a circular cylinder in a steady wind at transition Reynolds numbers. Journal of Fluid Mechanics 9, 603–612.
Jones, K.F., Andreas, E.L., 2012. Sea spray concentrations and the icing of fixed offshore structures. Quarterly Journal of the Royal Meteorological Society 138, 131–144.
Kim, S., Wilson, P.A., Chen, Z.-M., 2014. Numerical simulation of force and wake mode of an oscillating cylinder. Journal of Fluids and Structures 44, 216–225.
Kulyakhtin, A., Kollar, L.E., Løset, S., Farzaneh, M., 2012a. Numerical simulations of 3D spray flow in a wind tunnel with application of O'Rourke's interaction algorithm and its validation. In: Proceedings of the 21st IAHR International Symposium on Ice, Dalian, China, pp. 1154–1167.
Kulyakhtin, A., Shipilova, O., Libby, B., Løset, S., 2012b. Full-scale 3D CFD simulation of spray impingement on a vessel produced by ship–wave interaction. In: Proceedings of the 21st IAHR International Symposium on Ice, Dalian, China, pp. 1129–1141.
Lad, N., Muhamad Said, M., Aroussi, A., Adebayo, D., 2010. Experimental and computational characterisation of atomised spray flow around a circular cylinder. Progress in Computational Fluid Dynamics 10, 232–238.
Lozowski, E.P., Szilder, K., Makkonen, L., 2000. Computer simulation of marine ice accretion. Philosophical Transactions of the Royal Society of London, Series A 358, 2811–2845.
Makkonen, L., Laakso, T., Marjaniemi, M., Finstad, K.J., 2001. Modelling and prevention of ice accretion on wind turbines. Wind Engineering 25, 3–21.
Makkonen, L., Stallabrass, J., 1987. Experiments on the cloud droplet collision efficiency of cylinders. Journal of Climate and Applied Meteorology 26, 1406–1411.
Menter, F., Langtry, R., Likki, S., Suzen, Y., Huang, P., Volker, S., 2006. A correlation-based transition model using local variables—Part I: model formulation. Journal of Turbomachinery 128, 413–422.
Menter, F.R., 1994. Two-equation eddy-viscosity turbulence models for engineering applications. AIAA Journal 32, 1598–1605.
Mohany, A., Ziada, S., 2011. Measurements of the dynamic lift force acting on a circular cylinder in cross-flow and exposed to acoustic resonance. Journal of Fluids and Structures 27, 1149–1164.
Morsi, S., Alexander, A., 1972. An investigation of particle trajectories in two-phase flow systems. Journal of Fluid Mechanics 55, 193–208.
Nakakita, K., Nadarajah, S., Habashi, W., 2010. Toward real-time aero-icing simulation of complete aircraft via FENSAP-ICE. Journal of Aircraft 47, 96–109.
Okajima, A., 1982. Strouhal numbers of rectangular cylinders. Journal of Fluid Mechanics 123, 379–398.
Ong, M.C., Utnes, T., Holmedal, L.E., Myrhaug, D., Pettersen, B., 2009. Numerical simulation of flow around a smooth circular cylinder at very high Reynolds numbers. Marine Structures 22, 142–153.
Pope, S.B., 2000. Turbulent Flows. Cambridge University Press, Cambridge.
Rastgou, H., Saedodin, S., 2013. Numerical simulation of an axisymmetric separated and reattached flow over a longitudinal blunt circular cylinder. Journal of Fluids and Structures 42, 13–24.
Sadeh, W.Z., Saharon, D.B., 1982. Turbulence Effect on Crossflow Around a Circular Cylinder at Subcritical Reynolds Numbers. NASA Contractor Report 3622.
Shimada, K., Ishihara, T., 2012. Predictability of unsteady two-dimensional $<i>k</i>/i> - <i>\varepsilon</i>/i>$ model on the aerodynamic instabilities of some rectangular prisms. Journal of Fluids and Structures 28, 20–39.
Shipilova, O., Kulyakhtin, A., Tsarau, A., Libby, B., Moslet, P., Loset, S., 2012. Mechanism and dynamics of marine ice accretion on vessel archetypes. In: Proceedings of OTC Arctic Technology Conference, Houston, Tx, USA. Paper OTC-23762.

Son, J.S., Hanratty, T.J., 1969. Velocity gradients at the wall for flow around a cylinder at Reynolds numbers from 5×10^3 to 10^5. Journal of Fluid mechanics 35, 353–368.
Stallabrass, J., 1980. Trawler Icing: a Compilation of Work Done at NRC. National Research Council Canada 19372.
Yoon, B., Ettema, R., 1993. Droplet trajectories and icing-collision efficiencies for cylinders determined using LDV. Cold Regions Science and Technology 21, 381–397.
Yoon, S., DesJardin, P., Presser, C., Hewson, J., Avedisian, C., 2006. Numerical modeling and experimental measurements of water spray impact and transport over a cylinder. International Journal of Multiphase Flow 32, 132–157.
Zdravkovich, M., 1997. Flow Around Circular Cylinders, vol. 1: Fundamentals. Oxford University Press, Oxford.

Cold Regions Science and Technology 104–105 (2014) 33–44

Contents lists available at ScienceDirect

Cold Regions Science and Technology

journal homepage: www.elsevier.com/locate/coldregions

A time-dependent model of marine icing with application of computational fluid dynamics

Anton Kulyakhtin *, Andrei Tsarau

Department for Civil and Transport Engineering, Norwegian University of Science and Technology (NTNU), Høgskoleringen 7A, 7491, Trondheim, Norway

ARTICLE INFO

Article history:
Received 22 December 2013
Accepted 2 May 2014
Available online 10 May 2014

Keywords:
Icing
Freezing
Sea spray
Ice accretion
Heat transfer
Droplet flow

ABSTRACT

A tool predicting the spatial distribution of ice is required to take precautions against icing in the design of offshore structures. This paper presents a 3-dimensional time-dependent model of icing caused by sea spray, called MARICE. The novelty of MARICE is that a computational fluid dynamics (CFD) solver is used to resolve the details of the airflow and heat transfer from the structure, to track the spray flow in the air, and to calculate the spatial distribution of the ice thickness on the structure. Two case studies illustrate the advantages of MARICE. In the first case study, the heat transfer was calculated on a structure with complex geometry, for which empirical formulas are hardly applicable. In the second, the MARICE, RIGICE04, and ICEMOD icing models predicted the time-series of ice accretion on a 90-m-diameter cylindrical structure. MARICE and RIGICE04 calculated similar total ice loads, which were higher than those calculated by ICEMOD. Both RIGICE04 and ICEMOD underestimated the heat transfer by a factor of 2–5 compared to MARICE; however, RIGICE04 applies a greater spray flux than the other two models.

1. Introduction

Wind and the interaction of waves with a marine structure lift water droplets into the air when the wind speed exceeds 9 m s^{-1} (Horjen and Vefsnmo, 1985). If the air temperature is below the freezing temperature of seawater, droplets freeze on the structure surface. Those conditions lasting for more than 3 days happen on average 3 times per year in Norwegian Arctic seas (Smirnov in Nauman (1984)). Ice accumulation, i.e., icing, may seal rescue equipment and doors, and clog ventilation systems, which may cause gas accumulation and increase the risk of explosion. A slippery deck caused 22% of crew injuries (Jørgensen, 1982). Structures such as semisubmersibles are sensitive to overloading because of the low ratio between rig water surface area and displacement (Nauman, 1984). However, only three events are known in which the total ice load was higher than 100 tonnes and drilling operations were interrupted (Brown and Mitten, 1988; Ryerson, 2008). To take precautions against icing, numerical models can be used for the structure design and the early detection of icing danger.

The rate of ice accretion is defined mainly by the spray flux and heat transfer (Lozowski et al., 2000), and both must be accurately predicted. Existing icing models, e.g., ICEMOD and RIGICE04, simplify the structure and decompose it into cylindrical and flat components (Horjen, 1990, 2013; Lozowski et al., 2002). The airflow field around a component is assumed to be unaffected by other parts of the structure, and the heat transfer is approximated using empirical equations (Horjen, 1990; Lozowski et al., 2000). In reality, the upwind components create shadow regions or regions of accelerated flow in front of the downwind components, and the heat transfer from the surface of the downwind components becomes different from the heat transfer described by empirical equations. Thus, the complex airflow cannot be decomposed.

The physics of spray generation is complex and cannot be reproduced by existing physical models. Lozowski et al. (2000) and Mitten (1994) modelled spray generation by wave–structure interaction using linear wave theory. However, this approach seems to be inadequate to represent violent water flow. Most models of marine icing use an empirical equation of spray flux for both vessels (Horjen, 1990; Zakrzewski, 1986) and offshore structures (Brørs et al., 2009; Forest et al., 2005; Jones and Andreas, 2012). ICEMOD prescribes the vertical distribution of the spray flux on the structure surface (Brørs et al., 2009). Not all generated droplets settle on the structure surface. Some of them are deflected by airflow and fly around the structure. Therefore, other models use empirical equations to describe spray generation and then track droplets in a constant uniform wind field (Lozowski et al., 2000) or in the airflow around single cylindrical components, calculated using potential flow theory (Finstad et al., 1988a; Jones and Andreas, 2012). In both approaches, the number of droplets that interact with the structure defines the spray flux on the structure surface.

This paper presents an icing model called MARICE. In MARICE, the spray generation is described by empirical relations, as in previous models. The advantage of MARICE is the application of CFD to calculate the turbulent airflow, heat transfer, and trajectories of the droplets around the complete geometry of the structure (Kulyakhtin et al., 2012; Nakakita et al., 2010). In addition, the model of the water film

* Corresponding author. Tel.: +47 45063410; fax +47 73 59 70 21.
E-mail address: akulyahtin@gmail.com (A. Kulyakhtin).

http://dx.doi.org/10.1016/j.coldregions.2014.05.001
0165-232X/

Notation

b	thickness of the ice accretion
b_{eff}	portion of the accreted ice thickness, which affects the growth of new ice
C_d	drag coefficient for a spherical particle
c_a, c_i, c_w	specific heat capacity of the air, ice, and water film at constant pressure, respectively
D_d	droplet diameter
D_{80}	droplet diameter at an air humidity of 80%
D_{st}	representative structure diameter
$e_s(T)$	saturated water pressure
e_0	27.03 Pa K^{-1}
E_0	−6803 Pa
E_g	combination of terms, see Eq. (9)
F_{HV}	spray flux on the structure wall generated by the wave–structure interaction
F_{JA}	spray flux in the air generated by the wind
F_g	combination of terms, see Eq. (10)
G	Combination of terms, see Eq. (5)
$\mathbf{g}$	gravitational acceleration
h	heat transfer coefficient at the air–water interface/ structure surface
H_s	significant wave height
H	upper limit of the source region of the wind-generated spray
k	Karman constant
k_a, k_w	thermal conductivity of the air and water, respectively
k_{HV}	0.0588 $s^{0.667}$ $m^{-0.667}$
k_R	wave number
L_e, L_f	latent heat of evaporation and fusion of pure water, respectively
M_{HV}	6.28×10^{-4} kg m^{-3}
p	atmospheric pressure
Pr	Prandtl number
Q_c, Q_d, Q_e, Q_r	heat fluxes due to convection, heat capacity of the impinging droplets, evaporation, and radiation, respectively.
RH	relative humidity of the air
R_M	maximal wave run-up
Re	Reynolds number
$\mathbf{s}_1$, $\mathbf{s}_2$	surface coordinates in the principal directions
$\mathbf{s}_3$	normal vector to the surface
Sc	Schmidt number
S_{sp}, S_w	salinities of the sea spray and water film, respectively
S_w^{max}	maximal salinity of the water film for the given ait temperature
S_{JA}, S_{HV}	salinity of the wind-generated and wave-interaction sprays, respectively
T_a, T_w	temperature of the air and of the water film at the air–water interface, respectively
T_f	freezing temperature of the water film
T_{JA}, T_{HV}	temperatures of the wind-generated and wave-interaction spray when they arrive at the air/water interface, respectively
u^*	frictional velocity near the wall or the sea surface
$\mathbf{u}_T$	fluctuating velocity due to turbulence
$\mathbf{U}$	mean air velocity
U_{10}	wind speed at the 10 m height
$\mathbf{V}_d$	droplet velocity
V_g	terminal fall velocity of the droplet
y	distance from the structure wall of the closest mesh cell
y^+	non-dimensional distance from the structure wall of the closest mesh cell
z	height above mean sea level
z_{HV}	equals $(2z/H_s) - 1$
ε	molar weight ratio of water to air
η	water film thickness
θ	temperature of the water film at the air–water interface
ν_a, ν_w	kinematic viscosities of the air and water, respectively
ρ_a, ρ_i, ρ_w	densities of the air, ice and water, respectively
σ	Interfacial distribution coefficient, ratio of unfrozen water mass entrapped into the ice accretion to the mass of the ice accretion
τ_{dur}, τ_{per}	Duration and period of spray pulses, respectively
τ_{wave}	period of swell wave
ϕ	angular position from the windward stagnation point in degrees or angle between the normal vector to a surface and the wind direction
ψ	angle between the line that connects the centre of the structure with the rescue boats and upwind direction
ω_T	specific turbulence dissipation

dynamics and freezing is applicable to any arbitrary surface. MARICE incorporates a modified model of fresh water freezing developed by Myers and Charpin (2004), which we enhanced by adding a conservation equation of salinity, similar to Horjen (1990).

The advantages of MARICE are shown by two case studies in Section 3. The first study shows the ice accretion on the West Hercules drilling rig, which is a four-legged semisubmersible. The air and spray flow around a multi-leg structure are difficult to estimate without CFD. The first study also shows that the ice accretion on large parts of the structure is caused only by spray generated by wave–structure interaction. The second study presents a time-series of the ice accretion on a Floating Production Storage and Offloading unit (FPSO), which is a 90-m-diameter cylinder, and shows that compared to MARICE, ICEMOD and RIGICE04 underestimate the heat transfer from the surface of such large structures.

2. Model description

2.1. Model structure

MARICE calculates ice accretion based on the input parameters, i.e., the structure geometry and meteorological and oceanographic data (metocean). MARICE uses a finite volume CFD solver, FLUENT (ANSYS, 2009), to calculate the airflow, heat transfer from the structure and flow of droplets. The airflow is key to the correct estimation of icing because the airflow controls the heat transfer from the structure surface and the spray flow (Fig. 1). Furthermore, the heat transfer and spray flux on the structure surface are used as an input for the freezing module, which was implemented using User Defined Functions in FLUENT (ANSYS, 2009).

The airflow around a structure is calculated using a system of continuity, momentum and turbulence equations (ANSYS, 2009; Pope, 2000). The airflow modelling consists of choosing the turbulence model and mesh construction. The user can choose among several turbulence models available in FLUENT, including the Reynolds-averaged

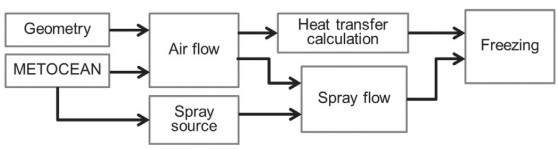

Fig. 1. Modelling procedures.

Navier–Stokes (RANS) and Large Eddy Simulations. The airflow is calculated in the reference frame of the structure, and the sea surface is modelled as a flat frictionless wall, i.e., the structure motion and the effect of the sea waves on the airflow are neglected. The change of the structure geometry, which the air is moving around and which is caused by the ice growth, is also neglected because the size of the offshore structures is significantly larger than the typical maximal ice thickness (10 cm, according to Brown and Mitten (1988)).

The heat transfer coefficient is independent of the temperature in the case of forced convection (Kays et al., 2005) but varies with the wind speed. When the airflow is obtained for certain wind conditions, the distribution of heat transfer coefficients on the structure surface is calculated from the energy balance equation.

2.2. Spray flux

Spray is generated by the interaction of waves with the structure and by the lifting droplets from wave crests. In MARICE, there are two ways to calculate spray flux on the surface, i.e., either prescribe spray flux on the surface of the structure or calculate spray flux based on droplet trajectories and the number of droplets interacting with the structure using the Discrete Phase Model (DPM) (ANSYS, 2009) from their initial state, i.e., the initial spatial distribution and velocities of the droplets after generation. Several empirical equations describe spray generation or spray flux on the structure surface and are based on different measurements (Forest et al., 2005; Horjen and Vefsnmo, 1985; Jones and Andreas, 2012; Lozowski et al., 2002). Any of those equations can be used in MARICE. The interaction-generated spray flux was measured only on the structure walls; therefore, all functions obtained describe the spray flux on the wall, and DPM is not used.

To test the model, we used the equations of Horjen and Vefsnmo (1985) to describe spray generation by the wave–structure interactions. The spray flux on the structure wall (F_{HV}) is non-zero during the pulses with a duration, τ_{dur}, of 2 s and a period, τ_{per}, of two wave periods and is as follows (Horjen and Vefsnmo, 1985):

$$F_{HV}(z) = \frac{M_{HV} U_{10} \tau_{per}}{\tau_{dur}} \frac{1-\left(1-10^{-2}U_{10}\right)\exp\left(-\left(\frac{4z_{HV}+2}{9}\right)^2\right)}{\exp\left(k_{HV}U_{10}^{0.667} z_{HV}^2\right)} \cos(\phi) \quad (1)$$

where $M_{HV} = 6.28 \times 10^{-4}$ kg m^{-3}, $k_{HV} = 0.0588$ s$^{0.667}$ m$^{-0.667}$, $z_{HV} = (2z/H_s) - 1$, H_s is the significant wave height, z [m] is the height above mean sea level, ϕ is the angle between the normal vector to a surface and the wind direction, and U_{10} [m s^{-1}] is the wind speed at $z = 10$ m.

The wind creates spray far away from the structure. In the model, droplets are ejected at the distance where the wind field is undisturbed by the structure, i.e., approximately 8 structure sizes or less, depending on the droplet size (Kulyakhtin et al., 2014). There, the spray concentration distribution with droplet diameter and height is as follows for a relative humidity of 80% (Jones and Andreas, 2012):

$$\frac{dC(D_{80},z)}{dD_{80}}\left[\frac{1}{\mathrm{m^3 \mu m}}\right] = \left(\frac{z}{H}\right)^{\frac{V_g}{ku_*}} \begin{cases} \dfrac{7\cdot 10^4 U_{10}^2}{D_{80}} \exp\left(-\dfrac{1}{2}\left[\dfrac{\ln(D_{80}/0.6)}{\ln 2.8}\right]^2\right), \text{if } U_{10} < 19 \text{ m s}^{-1} \\ \dfrac{30U_{10}^4}{D_{80}} \exp\left(-\dfrac{1}{2}\left[\dfrac{\ln(D_{80}/0.6)}{\ln 4}\right]^2\right), \text{if } U_{10} \geq 19 \text{ m s}^{-1} \end{cases} \quad (2)$$

where D_{80} [μm] is the droplet diameter at an air humidity of 80%, u^* is the frictional velocity close to the sea surface, $k = 0.4$ is the Karman constant, and H defines the upper limit of the source region. When $U_{10} > 19$ m s^{-1}, $H = 0.5H_s$, and when $U_{10} < 19$ m s^{-1}, $H = 1$ m. V_g is the terminal fall velocity of the droplet. The vertical distribution of the spray flux in the air generated by the wind, $F_{JA}(z)$, is obtained by integrating Eq. (2) multiplied by U_{10} over the range of droplet diameters from 10 to 200 μm for $U_{10} < 19$ m s^{-1} and up to 400 μm otherwise, following Jones and Andreas (2012). Droplets greater than 400 μm in diameter are too large to be lifted by the turbulence and fall down to the sea rapidly (Andreas, 1990).

After having been ejected, each droplet moves in the air, and its trajectory is affected by the air drag force and gravity (ANSYS, 2009; Lozowski et al., 2000):

$$\frac{d\mathbf{V}_d}{dt} = -\frac{3}{4}\frac{C_d}{D_d}\frac{\rho_a}{\rho_w}|\mathbf{V}_d - (\mathbf{U}+\mathbf{u}_T)|(\mathbf{V}_d - (\mathbf{U}+\mathbf{u}_T)) - \mathbf{g}\left(\frac{\rho_a}{\rho_w} - 1\right) \quad (3)$$

where $\mathbf{V}_d$ is the droplet velocity; D_d is the droplet diameter; C_d is the drag coefficient for a spherical particle; ρ_a and ρ_w are the densities of air and water, respectively; $\mathbf{g}$ is the gravitational acceleration; $\mathbf{U}$ is the mean air velocity; and $\mathbf{u}_T$ is the fluctuating velocity due to turbulence. Eq. (3) is a first order Lagrangian stochastic model of droplet flow in the turbulent air (Thomson and Wilson, 2013). The magnitude of $\mathbf{u}_T$ is 8–10% of the magnitude of $\mathbf{U}$ in the free-stream natural airflow (Türk and Emeis, 2010). The turbulence causes droplet levitation in the air (Andreas, 1990) and is modelled as a stochastic process. $\mathbf{u}_T$ takes random values described by a Gaussian distribution that has a standard deviation proportional to the square root of the local turbulence kinetic energy (ANSYS, 2009). $\mathbf{u}_T$ is a constant vector over the time required to cross a turbulent eddy or equal to the eddy characteristic lifetime $0.15/\omega_T$, where ω_T is the specific turbulence dissipation.

The number of droplets in 1 m^3 of the air is very high (>10^5) (Jones and Andreas, 2012; Ryerson, 1995), and therefore, to reduce computational time, droplets with similar coordinates, velocities, temperatures and diameters are combined into a parcel. The total number of parcels is 10^6–10^7. The DPM calculates the trajectory of each parcel individually until the parcel escapes from the computational domain or interacts with a cell on the structure surface. The number of parcels interacting with the cell defines the spray flux in the cell.

2.3. Freezing

2.3.1. Thermal problem

The sea spray, which arrived at the surface of the structure, freezes due to four main heat fluxes at the air–water interface (Fig. 2): convection, Q_c; evaporation, Q_e; heat capacity of the impinging spray, Q_d; and radiant heat flux, Q_r. The aerodynamic heating and kinematic energy of the droplets are neglected (Lozowski et al., 2000).

$$Q_c = h(T_w - T_a) \quad (4)$$

where h is the heat transfer coefficient, which was calculated in the airflow simulation, T_w is the temperature of the water film at the air–water interface, and T_a is the air temperature.

$$Q_e = h\left(\frac{\mathrm{Pr}}{Sc}\right)^{0.63} \frac{\varepsilon L_e}{pc_a}(e_s(\theta) - RH \cdot e_s(T_a)) = G(e_s(\theta) - RH \cdot e_s(T_a)) \quad (5)$$

where ε is the molar weight ratio of water to air, L_e is the latent heat of water evaporation, p is the atmospheric pressure, c_a is the specific heat capacity of the air, Pr is the Prandtl number, Sc is the Schmidt number, RH is the relative humidity of the air, and $e_s(T)$ is the saturated water pressure, which has been linearised by Myers (2001):

$$e_s(T) = E_0 + e_0 T \quad (6)$$

where $e_0 = 27.03$ Pa K^{-1} and $E_0 = -6803$ Pa. The saturated pressure depends on the water salinity. The maximum salt content in unfrozen water is 237‰ at the temperature of −17 °C (Schwerdtfeger, 1963), i.e., the lowest temperature in the case studies presented below. This salinity causes only a 13% decrease in $e_s(T)$ (Makkonen, 1987). The

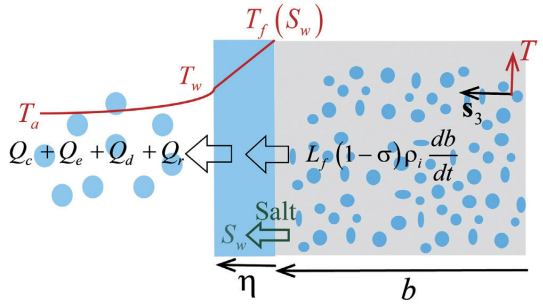

Fig. 2. The temperature gradients, heat and salt fluxes in the one-dimensional icing process.

prevailing heat flux is convection (Kulyakhtin et al., 2013), and therefore, the effect of salinity is neglected.

The thermal balance of the water film is affected by the internal energy of the sprays generated by the wave–structure interaction and the wind:

$$Q_d = c_w F_{HV}(T_w - T_{HV}) + c_w F_{JA}\left(T_w - T_{JA}\right) \tag{7}$$

where c_w is the specific heat capacity of water, and T_{HV} and T_{JA} are the temperatures of the wave–interaction and the wind-generated sprays at the air–water interface, respectively. To save computational time, the droplet thermodynamics during the flight were not simulated in the case studies. The temperature of the wind-generated spray was set to the air temperature because the wind-generated droplet has a typical diameter less than 100 μm, and the droplet temperature reaches T_a in less than 0.1 s (Andreas, 1990). The temperature of the wave-interaction spray arriving at the surface is uncertain because droplets are large (1–2 mm), they fly in the dense mixture with other droplets and the start position of the droplet is uncertain. The time required for the droplet temperature to decrease to the air temperature is comparable to the flight time (Andreas, 1990; Kulyakhtin and Løset, 2011). The flight time is uncertain and is higher for the droplets reaching higher parts of the structure. Therefore, the temperature of the spray arriving at the surface should be considered to be in the range between the air temperature and sea surface temperature. In the case studies, the temperature of the wave-interaction spray was set to the freezing temperature for simplicity.

The long wave radiation, which is less than 9% of Q_c under typical weather conditions (Kulyakhtin et al., 2013), and the short wave radiation are not currently considered for simplicity.

As in the previous models of icing (Lozowski et al., 2000; Makkonen, 1987, 2010), we assume no heat conduction through the ice. The heat fluxes from the air–water interface are conducted by the water film to the freezing interface (water–ice). The conduction is the main heat transfer mechanism in the water film, and the temperature gradient is linear when the water film thickness,η, is less than 3 mm (Myers and Charpin, 2004):

$$\frac{T_w - T_f}{\eta} = -\frac{Q_c + Q_e + Q_d}{k_w} = E_g - F_g T_w \tag{8}$$

where T_f, η and k_w are the freezing temperature, thickness and thermal conductivity of the water film, respectively; E_g and F_g are combinations of terms independent of the water film temperature, defined as follows:

$$E_g = \frac{c_w F_{HV} T_{HV} + c_w F_{JA} T_{JA} + hT_a + G[-E_0(1-RH) + e_0 RH \cdot T_a]}{k_w} \tag{9}$$

$$F_g = \frac{c_w\left(F_{HV} + F_{JA}\right) + h + Ge_0}{k_w} \tag{10}$$

The temperature gradient in Eq. (8) can be rewritten in terms of the freezing temperature, T_f (Myers and Charpin, 2004):

$$\frac{T_w - T_f}{\eta} = \frac{E_g - F_g T_f}{1 + F_g \eta} \tag{11}$$

The increase in the ice thickness, db/dt, is calculated from the heat balance at the ice/water interface:

$$\rho_i L_f (1-\sigma)\frac{db}{dt} = -k_w \frac{T_w - T_f}{\eta} = -k_w \frac{E_g - F_g T_f}{1 + F_g \eta} \tag{12}$$

where $\rho_i = 900\ \mathrm{kg\ m^{-3}}$ is the ice density, L_f is the latent heat of fusion of pure ice and $L_f(1-\sigma)$ is the latent heat of fusion of the saline ice accretion (Makkonen, 1987). When the water film is colder than the freezing temperature (Fig. 2 and Eq. (8)), the ice entraps liquid water between the dendrites. The ratio of entrapped liquid water mass to the mass of ice accretion is $\sigma = 0.3$ (Makkonen, 2010).

When the water film with salinity S_w freezes, the ice entraps only a portion of the salt, σS_w, and the rest is rejected into the solution (Makkonen, 1987; Szilder et al., 1995). We assume that the rejected salt rapidly diffuses in the water film in the direction perpendicular to the ice/water interface with no salt diffusion into the ice. As a result, S_w increases and decreases the freezing temperature (Fig. 2), which is dependent on salt concentration (Schwerdtfeger, 1963):

$$S_w = \begin{cases} -0.0182 \cdot T_f, \text{if } 0^\circ\mathrm{C} \geq T_f > -8.2^\circ\mathrm{C} \\ 0.149 - 0.01 \cdot \left(T_f + 8.2\right), \text{if} -8.2^\circ\mathrm{C} \geq T_f > -23^\circ\mathrm{C} \end{cases} \tag{13}$$

where S_w is non-dimensional and T_f is in [°C]. In the case of periodic spray, the water film salinity increases above the spray salinity, S_{sp}, after each spray event due to freezing (Fig. 3) until the water film salinity reaches the maximum, $S_w^{\max}$. The freezing temperature of the water film with salinity $S_w^{\max}$ is equal to the air temperature. The ice formation stops because the film cannot be colder than the air, and there is also no temperature gradient in the water film and, therefore, no heat flux. The system stays in this thermal balance until the next spray event, when the salinity of the water film is diluted by the next spray event, and the freezing starts again.

The water freezes with all salt contained in it only when the temperature is below −23 °C. The air temperature is usually higher than −23 °C under offshore conditions; i.e., the ice is covered by the water film all the time. Therefore, MARICE considers only wet ice accretion, in contrast to Myers and Charpin (2004).

For simplification, the system is assumed to come immediately to a new thermodynamic balance when T_f changes, and no heat flux is spent to change the temperature of the ice and water. The validity of this assumption will be discussed in Section 4.

MARICE assumes certain material parameters to be constant. However, these assumptions have small effect on the accreted ice mass. The density and thermal conductivity of saline water vary within 4 and 1%, respectively, with changes in salinity; the density of saline ice without air entrapment varies by less than 6% under typical conditions (Sharqawy et al., 2010). In nature, the variation is higher due to entrapment of the air. The density of the accreted ice on a Coast Guard vessel varied within 25% of the average value (Ryerson and Gow, 2000). However, the mass of the accreted ice is defined by thermodynamics, Eq. (12), and the ice density is only a multiplication factor that is used to calculate the ice thickness.

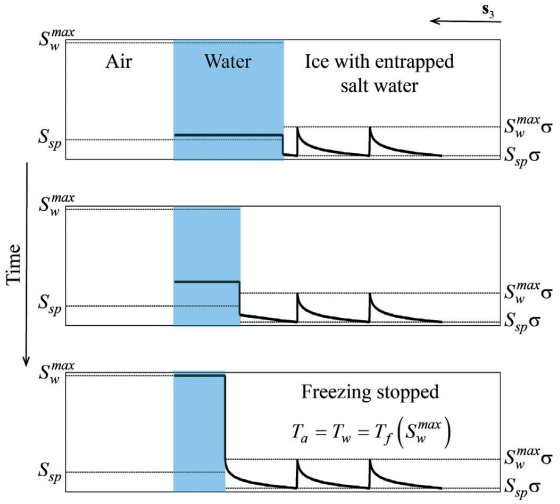

Fig. 3. Sequential variation of ice and water salinities during one spray period. S_{sp} is the average spray salinity of the sprays generated by the wind and wave-interaction.

2.3.2. Water flow

On the structure surface, the problem is not one-dimensional. The water film is moved by gravity along the ice surface (Fig. 4). In addition, the film thickness, η, decreases due to freezing and increases when spray arrives (Myers and Charpin, 2004):

$$\rho_w \frac{\partial \eta}{\partial t} + \rho_w \nabla \cdot (\mathbf{Q}\eta) = -\rho_i \frac{db}{dt} + \left(F_{JA} + F_{HV}\right) \tag{14}$$

where $\partial\eta/\partial t$ is the time derivative of η, $\nabla \cdot ()$ is the divergence operator on the structure surface and ρ_w is the density of the water film. The flow of the thin water film is defined by the balance of the viscous forces resisting gravity and is defined by lubrication theory (Myers, 1998):

$$\mathbf{Q} = \left[-\frac{\eta^2}{3\nu_w}\left(\mathbf{g}\cdot\mathbf{s}_1 + \frac{\partial \eta}{\partial s_1}\mathbf{g}\cdot\mathbf{s}_3\right), -\frac{\eta^2}{3\nu_w}\left(\mathbf{g}\cdot\mathbf{s}_2 + \frac{\partial \eta}{\partial s_2}\mathbf{g}\cdot\mathbf{s}_3\right)\right] \tag{15}$$

where ν_w is the kinematic viscosity of water (which varies by less than 5% due to change of salinity, Sharqawy et al. (2010)), $\mathbf{s}_1$ and $\mathbf{s}_2$ are the surface coordinates in the principal directions and $\mathbf{s}_3$ is the vector normal to the surface. The wind shear stress on the water film is currently neglected in the model. Only gravity, which is the main driving force in marine icing, is considered. The wind stress affects the distribution of the ice on the surface, whereas gravity decreases total ice mass on the structure. Gravity moves water down along the structure, where the ice does not accrete due to wave washing. In addition, the air/water surface tension, which likely affects the water movement, is not included in Eq. (15) because the tension depends on the small details and surface roughness of the ice. The small details cannot be modelled because the size of the surface elements is kept larger than 0.1–1 m in the case of a full scale structure due to limited computational capacity.

2.3.3. Salt flow

The water flow transports salt along the surface, and the diffusion is neglected. In addition, the salt mass changes due to the spray and the ice growth:

$$\rho_w \frac{\partial(\eta S_w)}{\partial t} + \rho_w \nabla_s \cdot (\mathbf{Q}\eta S_w) = -\rho_i \frac{db}{dt}(\sigma S_w) + \left(F_{HV}S_{HV} + F_{JA}S_{JA}\right) \tag{16}$$

where S_w is the salinity of the water film, S_{HV} and S_{JA} are the salinities of wave-interaction and wind-generated sprays, respectively. S_{HV} is equal to sea salinity (35‰) and S_{JA} is discussed in Section 4.

2.3.4. Wave washing

The ice does not accrete below the maximal wave run-up, R_M, because the ice is mechanically removed by sea waves (Mitten, 1994):

$$R_M = \begin{cases} 0.5H_s\left(2.0589 + 2.3292k_R D_{st} - 1.3194(k_R D_{st})^2\right) - 0.5H_s, \text{for } k_R D_{st} < 0.9 \\ H_s, \text{for } k_R D_{st} \geq 0.9 \end{cases} \tag{17}$$

where k_R is the wave number, and D_{st} is the representative diameter of the structure or one of the columns for a multicolumn structure at the water line. Eq. (17) agrees well with the results of Sarpkaya and Isaacson (1981) based on linear wave theory.

In summary, the system of Eqs. (12), (14), and (16) is solved on a 2-dimensional mesh on the curved surface of the structure to predict the ice growth. In Eq. (12), the water film thickness and freezing temperature vary with time. The ice accretion rate is calculated with a precision of 5% for each weather condition by running the freezing module for 20 spray events with a time step of 0.1 s.

3. Case studies

3.1. West Hercules

To show the complexity of the airflow around a real structure and the capabilities of MARICE, the ice accretion rate was calculated on the West Hercules drilling rig, which operates in the Norwegian offshore sector and is exposed to icing. West Hercules is a semisubmersible that consists of four pontoons, a main deck, a bridge, and rescue boats (Fig. 5). The latter were represented by a triangular horizontal wedge.

Three extreme conditions were studied, which are taken from the metocean design basis by Gaches et al. (2013) for the Johan Castberg field (72°N, 20°E): (a) $T_a = -9$ °C and $U_{10} = 33$ m s^{-1}, (b) -17 °C and 33 m s^{-1}, and (c) -17 °C and 20 m s^{-1}; with 0, 30, 45 and 90° orientations of the structure against the wind. The orientation angle (ψ) is the angle between the line that connects the centre of the structure with the rescue boats and the upwind direction (Fig. 5). The turbulence intensity in the air was set to 10%, and the relative humidity was set to 80%. The wave height and wave period were calculated from the fifth-degree polynomials of U_{10} (Zakrzewski, 1986).

3.1.1. Numerical setup

The airflow was calculated using the steady RANS turbulence k − ω SST model, which is based on the Boussinesq eddy viscosity assumption (Pope, 2000). The computational domain extended approximately 250 m in the windward direction and 500 m in the leeward direction from the centre of the structure. The domain width was 500 m and the height was 70 m. The unstructured computational mesh was generated in STAR-CCM+ (CD-adapco, 2010), which contained 7.6 million tetrahedral cells with an edge length of less than 5 m. To improve the resolution of the airflow, the finer cells with an edge size of less than 1 m were used within a distance of 10–15 m from the surface of the structure. 12 prism cells were placed in the boundary layer near the wall. The distance between the centres of the cells in the direction perpendicular to the wall was expanding by a geometric expansion factor of 1.5. The non-dimensional distance from the structure wall of the closest mesh cell, $y^+ = u^* y/\nu_a$, was less than 500, except for some corner elements. Here, u^* is the local friction velocity near the wall, y is the distance from the wall. Sufficiency of the mesh resolution was verified by the calculation on the mesh with cells twice small in size. The difference in the total and local heat transfer was less than 1% and 20% between the two meshes, respectively.

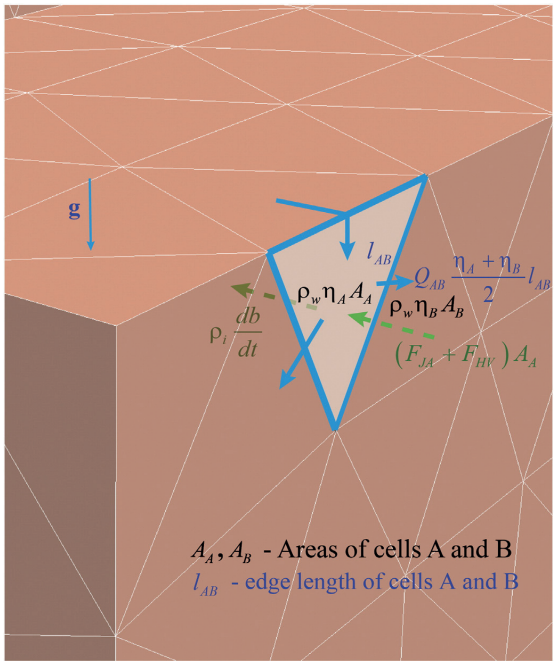

Fig. 4. Illustration of the water film flow on the surface mesh of the structure.

3.1.2. Spray fluxes

To determine the primary source of icing, we compared the interaction-generated (Eq. (1)) and wind-generated spray fluxes (Eq. (2)). For $U_{10} = 20$ and 33 m s^{-1} (Fig. 6), the wind-generated spray flux is greater than the time-averaged interaction spray flux at the elevations above 18 and 22.5 m, respectively, i.e., at an elevation of the rescue boats and the main deck. However, Eq. (2) represents a spray concentration far from the structure, and only a portion of this spray will settle on the structure walls. In contrast, Eq. (1) describes the spray flux generated by the wave–structure interaction which already arrived on the structure walls.

To estimate the portion of the wind-generated spray flux that interacts with the structure, we calculated droplet trajectories for $U_{10} = 33$ m s^{-1}.

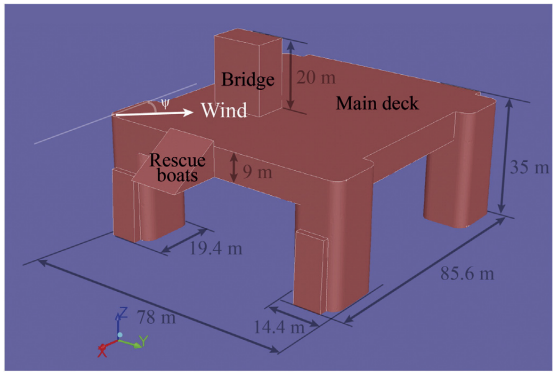

Fig. 5. Geometry of the West Hercules drilling rig.

The droplets were ejected according to the results of the studies of Kulyakhtin et al. (2014). Droplets were introduced as a vertical wall perpendicular to the wind direction and located 2.5-structure-widths upwind from the structure. The wall extended from $0.5H_s$ to 70 m in the vertical direction and had a width of 1.5-structure-widths in the horizontal direction perpendicular to the wind. The wall was split into 8 million squares with an edge length of 3 cm. Each square ejected one parcel with an initial speed of U_{10} with mass flux as in Eq. (2). The diameter of the droplets was equal to a Median Volume Diameter (MVD) (Finstad et al., 1988b) that was calculated for each square from Eq. (2) and varied with height.

In addition for verification purpose, the spray inflow was calculated by ejecting 16 parcels from each square. The diameters of the parcels were uniformly distributed from 10 to 400 μm, and the mass flux for each parcel was calculated by Eq. (2). The total spray inflow obtained with MVD agreed within 1% with that obtained with the droplet-diameter spectrum and showed that MVD is a good representation of the diameter spectrum given by Eq. (2). However, MVD is a good representation only for small droplets, as here, or less than 200 μm, as in Finstad et al. (1988b). MVD is not a good representation when the droplet spectrum is wide and the droplet trajectories are strongly affected by gravity, i.e., when MVD ~ 1000 μm (Kulyakhtin et al., 2012).

The MVD of the wind-generated spray at an elevation of 15 m is approximately 50 and 80 μm for $U_{10} = 20$ and 33 m s^{-1}, respectively. Such small droplets easily follow the air streamlines around the large structure, and only a small portion of them interacts with the structure. We determined that at an elevation of 26 m (the bottom of the rescue boats), the spray flux to the surface is $4 \cdot 10^{-5}$ kg m^{-2} s^{-1} (Fig. 7), which is only 4% of the spray flux in undisturbed air (Fig. 6) and is 5 times lower than the time-averaged spray flux due to wave-interaction ($2.1 \cdot 10^{-4}$ kg m^{-2} s^{-1}) at the elevation of 26 m. The spray flux of $4 \cdot 10^{-5}$ kg m^{-2} s^{-1} can produce a maximum ice growth rate of 0.2 mm hr^{-1}. A similar result was obtained for $U_{10} = 20$ m s^{-1}, and thus, the wind-generated spray is henceforth neglected because it produces insignificant spray flux to the structure.

3.1.3. Ice accretion

The wave–structure interaction spray was introduced on all of the windward walls. However, significant ice grew only on the pontoons (Fig. 8). The ice grew fast close to the corners where the heat transfer was high due to accelerated airflow (Fig. 8). The heat transfer was low in the shadow regions, behind the corners, and in the middle of the surfaces perpendicular to the airflow.

The structure parts had a complex effect on the heat transfer to each other. Aft Pontoons were in the shadow of Front Pontoons for $\psi = 90°$ (Fig. 8). However, the heat transfer on the windward side of Aft Pontoons was 24% higher than the heat transfer on Front Pontoons (Fig. 9) because a stagnation zone existed on the windward sides of Front Pontoons but did not occur on Aft Pontoon. A shadow region behind Front Pontoons created a possibility for the air, which flew between Front Pontoons, to not only move between Aft Pontoons but also move along the windward sides of Aft Pontoons (Fig. 10). The higher heat transfer resulted in the higher ice accretion on Aft Pontoons compared to Front Pontoons (Fig. 8).

For $\psi = 0°$, the heat transfer on Aft Pontoons was only 9% greater than the heat transfer on Front Pontoons because the area of the pontoons perpendicular to the airflow was smaller (Fig. 10).

The total increase of the ice load was significant for $\psi = 0°$:

a) 4.1 t h^{-1}, for $T_a = -9$ °C and $U_{10} = 33$ m s^{-1};
b) b) 5.5 t h^{-1}, for $T_a = -17$ °C and $U_{10} = 33$ m s^{-1};
c) c) 2.4 t h^{-1}, for $T_a = -17$ °C and $U_{10} = 20$ m s^{-1};

and is comparable to the ice accretion on the Ocean Bounty rig when the drilling fluid was discharged to ensure the stability of the rig (Nauman, 1984). However, the stability threshold depends on the particular structure size and geometry.

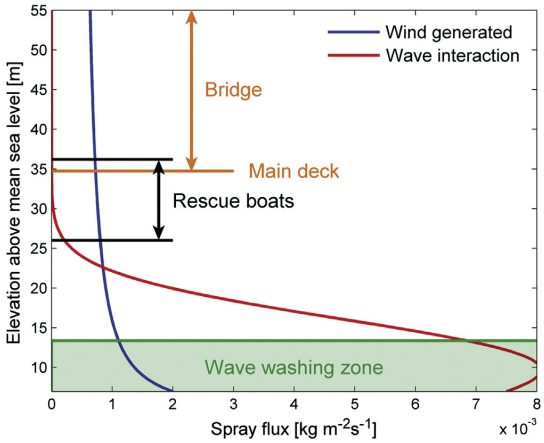

Fig. 6. Time-averaged wind-generated and wave–structure interaction-generated spray fluxes for $U_{10} = 33$ m s^{-1}. In the wave washing zone, there is no icing.

The ice accretion rate is expected to increase with the increase of the total spray flux, which is proportional to the projection of the structure area to the plane perpendicular to the wind (Eq. (1)). However, the ice accretion also depends on the heat transfer, which is proportional to the airflow speed. The airflow near the structure is slower for the larger projection than for the smaller one for the same wind conditions. Therefore, the total ice load changed less than the projection when ψ changed (Fig. 11).

3.2. Floating production storage and offloading unit (FPSO)

The goal of this section is to compare MARICE with existing icing models, steady model of Makkonen (1987), ICEMOD and RIGICE04. To do that, we used the same metocean data and a structure as Brørs et al. (2009). Using ICEMOD, Brørs et al. (2009) calculated the time-series of the ice accretion on the FPSO, which is a vertical cylinder with a diameter of 90 m and extends to 30 m above sea level. The weather conditions were for the location 71.23°N 22.21°E for the period from 15.12.1995 to 15.01.1996.

3.2.1. Numerical setup and assumptions

CFD calculations give detailed spatial distributions of the accreted ice, but they are time consuming and the exact time depends on the mesh resolution. The freezing module of MARICE uses approximately 30 s to compute 1 s of the real freezing process. Therefore, the time-series of the ice accretion were composed from the average accretion rates obtained for the conditions within 3-h intervals. The accretion rates in each 3-h interval were taken from the data massive containing the accretion rates pre-calculated for the set of T_a and U_{10}.

In reality, the icing depends not only on T_a and U_{10} but also on the sea temperature, sea wave conditions and air humidity. The sea temperature was not available in metocean, and it was set to the freezing temperature of seawater with a salinity of 35‰.

Sea waves depend on the wind. The following curves fitted the significant wave height, H_s, and period of swell wave, τ_{wave}, from metocean well:

$$H_s = 0.5459U_{10} - 2.776, \text{ determination coefficient } 0.72 \quad (18)$$

$$\tau_{wave}(H_s) = -0.1032H_s^2 + 2.082H_s + 3.771, \text{ determination coefficient } 0.73 \quad (19)$$

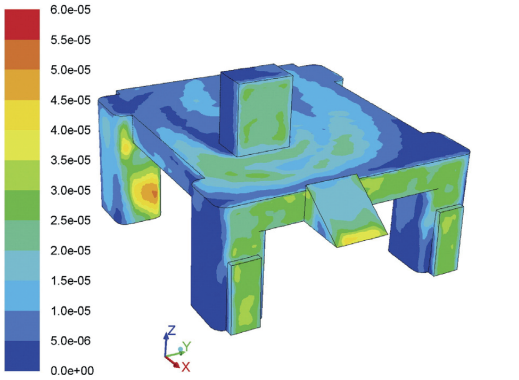

Fig. 7. Wind-generated spray flux [kg m^{-2} s^{-1}] on the surface of West Hercules for $\psi = 0°$ and $U_{10} = 33$ m s^{-1}.

Eqs. (18) and (19) were used to represent the sea state instead of real data (Fig. 14) and the wave direction was set along the wind direction.

The air humidity during icing days was between 50 and 75%. Therefore, a constant humidity of 60% and a constant pressure were used in the calculations, which caused an error of less than 9% (Kulyakhtin et al., 2013). The melting process was simplified by two conservative assumptions: the ice starts to melt when $T_a > -1.9$ °C, and energy of the same magnitude was required for ice to melt as to freeze. In reality, the melting temperature and latent heat of the ice depends on its salinity (Schwerdtfeger, 1963; Szilder et al., 1995), i.e., on the air temperature at which the ice was created.

In such a way, the accretion rate on the surface of the FPSO was calculated on a 3-dimensional mesh with vertical and horizontal sizes of the cells of 0.6 and 1.1 m, respectively, and only for a matrix of T_a (−9, −6, −4, −2.5 °C) and U_{10} (9, 12, 15, 22 m s^{-1}), which included the minimal and maximal values during icing conditions. The accretion rate for intermediate T_a and U_{10} was obtained using bilinear interpolation.

To obtain the heat transfer coefficient the airflow was calculated on a different mesh because the airflow around a cylinder can be described well as 2-dimensional. The numerical domain was 8 diameters of the structure in the windward direction, 20 diameters in the leeward direction, and 16 diameters in width. A block structured mesh consisting of rectangular elements was generated using ICEM CFD (ANSYS, 2012). y^+ was less than 300. The airflow was verified on a mesh with cells twice as small. For $U_{10} = 9$ m s^{-1}, the airflow was additionally verified

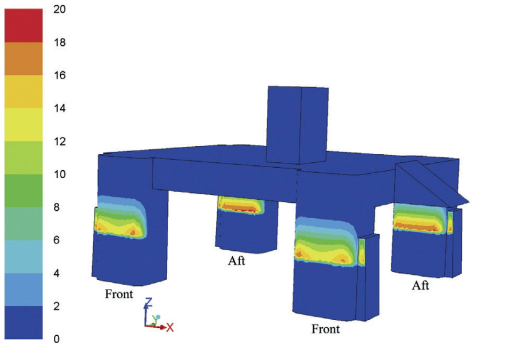

Fig. 8. Ice accretion rate [mm h^{-1}] on West Hercules at $T_a = -17$ °C, $\psi = 90°$ and $U_{10} = 33$ m s^{-1}.

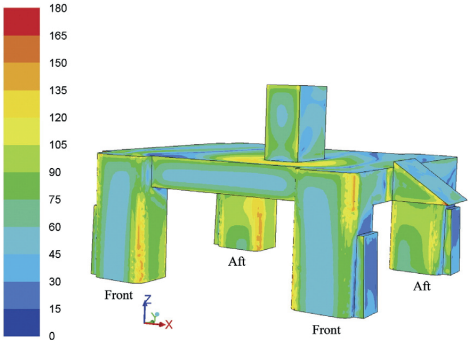

Fig. 9. The heat transfer coefficient [W m^{-2} K^{-1}] on the surface of West Hercules for $\psi = 90°$ and $U_{10} = 33$ m s^{-1}.

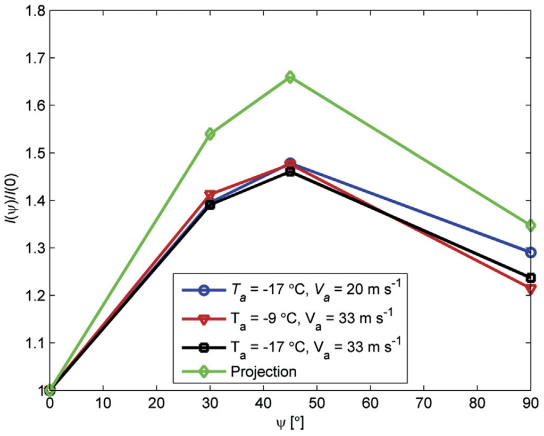

Fig. 11. The increase of the total ice load depending on the different orientations (ψ) of West Hercules. $I(\psi)$ is the total ice load for orientation angle ψ.

on a mesh with $y^+ < 1$. We applied the transient RANS k − ω SST model with a numerical time step less than 0.005 of the vortex-shedding period.

The average heat transfer coefficient obtained was in an excellent agreement (determination coefficient was 0.986) with the following fitting curve for the velocities 3, 9, 12, 15, and 22 m s^{-1}, which was used to transfer values to the mesh of the freezing module:

$$h = \frac{k_a}{D_{st}} \begin{cases} \left(-1.82\cdot 10^{-8}\phi^3 + 9.18\cdot 10^{-7}\phi^2 + 1.49\cdot 10^{-4}\phi + 8.39\cdot 10^{-3}\right) Re^{0.86}, \phi < 130^\circ \\ \left(-5.85\cdot 10^{-8}\phi^3 + 2.74\cdot 10^{-5}\phi^2 - 4.18\cdot 10^{-3}\phi + 0.212\right) Re^{0.86}, \phi \geq 130^\circ \end{cases} \quad (20)$$

where D_{st} is the structure diameter, k_a is the thermal conductivity of the air, and ϕ is the angular position from the windward stagnation point in degrees. Re $= U_{10} D_{st}/\nu_a$ is the Reynolds number.

3.2.2. Verification of the importance of calculating the water film motion

To verify the importance of the modelling of the water film flow, we compared results of MARICE with the results of the model in which the freezing module is substituted by a steady model of Makkonen (1987). The steady model had several simplifications: (a) it assumes no motion of the water film; (b) the pulsed spray Eq. (1) is substituted by the continuous spray flux of $F_{HV}\tau_{dur}/\tau_{per}$; (c) the heat transfer is as in Eq. (20); and (d) the water that does not freeze disappears from the surface. The ice accretion rate in each cell was calculated as:

$$\frac{db}{dt} = -k_w \frac{E_g - F_g T_f(S_w)}{\rho_i L_f (1-\sigma)} \quad (21)$$

Eq. (21) neglects a temperature gradient in the water film in contrast with Eq. (12). T_f was calculated from a second-order ordinary equation that was obtained by combining Eq. (21) with the following equation for the accretion fraction (Makkonen, 1987):

$$\frac{\rho_i db/dt}{F} = \left(1 - \frac{S_{HV}}{S_w}\right) \frac{1}{1-\sigma} \quad (22)$$

where S_w was replaced by Eq. (13).

As expected, the steady model predicted a higher total ice accretion than MARICE because, when water does not move, it has more time for freezing. The steady model predicted an up-to-24%-greater total accretion rate at $T_a \leq -4$ °C, and the difference was 35%–60% at $= -2.5$ °C.

The difference between the local ice accretions predicted by the steady model and by MARICE was within 13% at $T_a \leq -6$ °C, and the range of the time-averaged spray flux was from 0 to $4 \cdot 10^{-3}$ kg m^{-2} s^{-1} (which corresponds to an instant spray flux of up to 0.1 kg m^{-2} s^{-1}) (Fig. 12). Good agreement of MARICE with the model that neglects water motion for the wide conditions indicates that the choice of a model describing the water film dynamics is not important. MARICE, ICEMOD and RIGICE04 use different water film models. However, they must predict similar ice accretion rates if they use similar heat and spray fluxes. This result also means that in the range of conditions considered, the steady model of Makkonen (1987) can be used to predict ice accretion instead of computationally expensive numerical models.

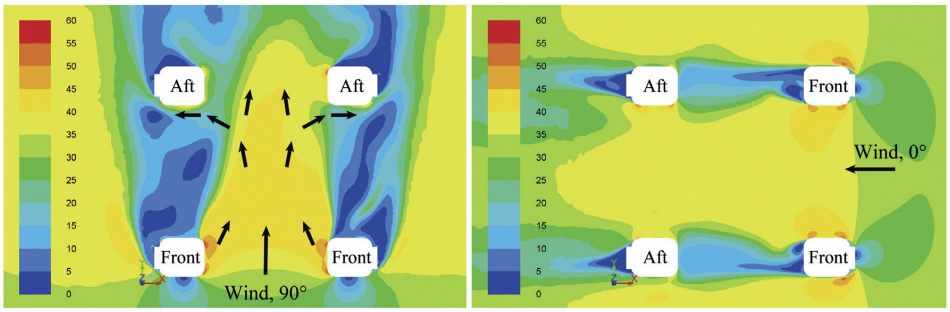

Fig. 10. Wind speed [m s^{-1}] in a horizontal plane z = 15 m, middle of pontoons.

The steady model also predicted a greater local ice accretion than MARICE under most conditions (Fig. 12). For the same temperature, the largest difference between the models was for $U_{10} = 22$ m s^{-1} (Fig. 13) because the period-averaged spray flux and spray period were the greatest. The local difference was less than 8% and 13% at T_a of −9 and −6 °C, respectively. At these temperatures, the freezing was fast enough that the unfrozen water that was shed to the lower computational cells had salinity too high to freeze and, therefore, did not contribute to the ice accretion.

The situation changed at warmer air temperatures. At $T_a = -4$ °C, the steady model predicted an up-to-35%-greater ice accretion rate. However, the difference was less at lower elevations due to the contribution of water from the upper cells. At $U_{10} = 22$ m s^{-1} and $T_a = -4$ °C, MARICE predicted even greater ice accretion than the steady model at elevations below 17 m (Fig. 13). Therefore, the difference between the total ice accretion rates predicted by the models was reduced to 1%. At $T_a = -2.5$ °C, the local difference was as much as 160%, and the difference was less at lower elevations because of water shed from above, as at −4 °C. Thus, the choice of the water film dynamics is important at temperatures higher than −4 °C.

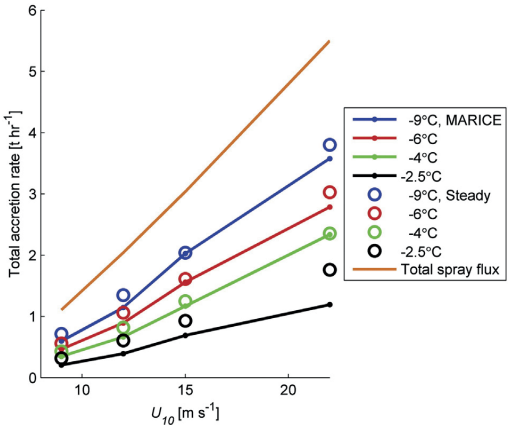

Fig. 12. Total accretion rate on the FPSO in various weather conditions.

3.2.3. Comparison of MARICE with ICEMOD and RIGICE04

The MARICE prediction was different from the predictions of ICEMOD (Brørs et al., 2009) and RIGICE04 (Fig. 14) due to the difference of heat and spray fluxes (Table 1). The water film dynamics had a weak effect on the ice accretion (Section 3.2.2) and, was therefore not included in Table 1.

For the 90-m-diameter cylinder, MARICE predicted a heat transfer coefficient 2–5 times greater than those predicted by ICEMOD and RIGICE04. Data on the heat transfer of the full scale offshore structures do not exist in the literature. However, the heat transfer from buildings is similar (Table 2). MARICE predicts values closer to those measured on buildings compared to ICEMOD and RIGICE04 (Table 2). Even the maximal values predicted by ICEMOD and RIGICE04 are at least 3 times lower than the measurements.

The reason for the underestimation is that RIGICE04 and ICEMOD based their heat transfer calculations on the small-scale wind-tunnel experiments of Achenbach (1977), which were done on a circular cylinder for Re from 2.2 10^4 to 4 10^6. At Re <4 10^6, the boundary layer is partially laminar on the windward side of the cylinder. In contrast, the flow around FPSO corresponds to $Re > 10^7$. At $Re > 10^7$, the laminar boundary layer is unstable and tends to separate and trigger turbulence (Zdravkovich, 1997), and the main part of the boundary layer is turbulent (Achenbach, 1977; Defraeye et al., 2011). Therefore, it is incorrect to use RIGICE04 and ICEMOD for quantitative estimates of icing on such large structures as FPSO because the flow physics and resulting heat transfer are different. The same scaling problem of experiments is known for buildings (Defraeye et al., 2011).

In particular, ICEMOD uses an empirical fit to the experimental data of Achenbach (1977) for the windward side of the cylinder (Horjen, 1990). RIGICE04 uses the model of Makkonen (1985) (Lozowski et al., 2002), which simulates the transition of the boundary layer from the laminar to the turbulent state triggered by surface roughness only. However, in our case, the size of the surface roughness is negligible compared to the 90-m diameter, and the model of Makkonen (1985) does not predict turbulence.

As a result, both RIGICE04 and ICEMOD underestimate the heat transfer by predicting a laminar heat transfer coefficient proportional to $\mathrm{Re}^{0.5} D_{st}^{-1.0}$. Considering that Re ~ $U_{10} D_{st}$, it is clear that underestimation of the heat transfer by ICEMOD and RIGICE04 increases with the structure size. The heat transfer coefficient of the turbulent boundary layer is proportional to $\mathrm{Re}^{0.8} D_{st}^{-1.0}$ (Achenbach, 1975; Defraeye et al., 2011; Lienhard, 2013) and varies less with the structure size. Therefore, similar heat transfer should be expected for large structures ($Re > 10^7$) even though the buildings in Table 2 are smaller than FPSO and have corners. In particular, MARICE predicted a local heat transfer coefficient proportional to $\mathrm{Re}^{0.8} D_{st}^{-1.0}$ that differed by less than 60% from the empirical equation of the heat transfer coefficient of the flat plate in a turbulent flow (Lienhard, 2013).

Thus, even though, there are no measurements of the heat transfer from the cylinders at $Re > 10^7$, we can state that the MARICE predicts heat transfer better for large structures compared with ICEMOD and RIGICE04 based on the general behaviours of the high Reynolds number flows.

As a result, MARICE predicted faster ice growth and melting than ICEMOD. The predictions of MARICE and RIGICE04 are fortuitously similar because RIGICE04 compensated for underestimation of the heat transfer by a spray flux that is greater than the one used in MARICE by a factor of 10–1000. According to MARICE, the ice accretion growth was limited by the heat transfer at elevations below approximately 15 m (depending on H_s), and the ice accretion growth was limited by the spray flux at elevations of 15–30 m (Fig. 13). At elevations of 15–30 m, RIGICE04 predicted more ice than MARICE.

4. Discussions

The two case studies showed that CFD improves the prediction of icing via better prediction of the heat transfer rate. In contrast with other models, MARICE is applicable to structures of any arbitrary geometry and of any size. The accuracy of the heat transfer prediction is

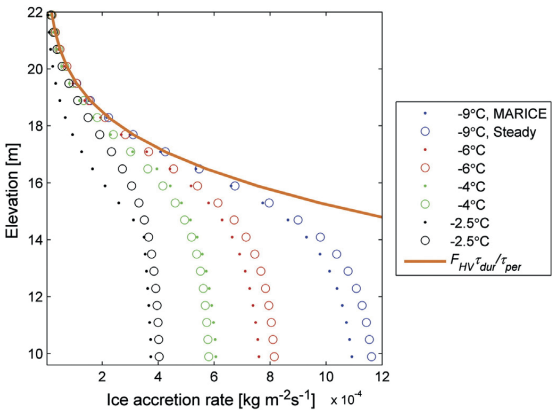

Fig. 13. Ice accretion profiles by different models for $U_{10} = 22$ m s^{-1}.

determined by the choice of the turbulence model and the time available for computations. In the case studies, the airflow was calculated with the RANS k − ω SST model, which is widely used in engineering simulations. To get better resolution of the airflow, more complex models, such as the Reynolds Stress model and Large Eddy Simulation, which are implemented in FLUENT, can be used.

MARICE predicts the spatial distribution of the ice accretion on the structure. This information can be used in the design to either hide or protect the rescue equipment or working areas in the most efficient way from icing. The model of Overland et al. (1986) is widely used to map regions with high icing danger, even though the model was criticised by Makkonen et al. (1991), in particular, for the high sensitivity of the icing rate to the sea temperature. The model is based on the correlation of icing observed on the fishing vessels. The effect of the sea temperature can be different in the case of larger vessels when droplets settling on the upper parts of a superstructure have enough time to cool down and to cause freezing instead of melting. In addition, the definition of the dangerous ice load depends on the vessel size. Therefore, MARICE can be used to calculate icing on the vessel archetypes, and the results can be stored in a database. The data can be further used together with a weather forecast to warn each particular vessel depending on its characteristics.

The model is also applicable to small-scale parts and for ships if used with a different spray-generation function. The DPM can predict the spatial distribution of the spray flux based on the airflow field. However, the model is limited by the uncertainty of the spray generation. Because of the unknown droplet-size distribution, the droplet trajectories and the spray flux on the structure surface could not be predicted for the wave–structure interaction spray with DPM. The direct extrapolation of the measured spray flux to other structures is also incorrect because even droplets with a diameter of 2 mm follow the air stream around a large structure (Kulyakhtin et al., 2012). The structure geometry defines the number of droplets interacting with it. Furthermore, the interactions of waves with different structures create different sprays, and in the case of a multicolumn structure, we expect interference among waves. However, the wave-interaction spray flux of Horjen and Vefsnmo (1985) was measured on the Treasure Scout drilling rig, which has a structure similar to that of West Hercules.

Jones and Andreas (2012) stated that the wind-generated spray caused an ice accretion on the Ocean Bounty semisubmersible drilling rig, which was described by Nauman (1984). MARICE did not predict icing on West Hercules caused by the wind-generated spray due to the low number of droplets interacting with the structure. In our approach, the geometry was simplified, and the surface was smooth. In reality, small parts such as cables, pipes, and surface roughness, can collect wind-generated spray. To model the ice accretion caused by the wind-generated spray on the small parts, a different approach should be implemented in MARICE: either consider the flight of the droplets at a certain threshold distance to the surface as interaction or, better, perform "zoomed in" simulations of the small-scale parts to resolve the geometrical details of the ventilation system, etc. The airflow in the "zoomed in" simulation will require input from the large-scale simulation.

However, the statement of Jones and Andreas (2012) can be incorrect because they assumed that all impinging spray freezes which is not true for saline spray (see Eq. (13)). Spray salinity also increases due to evaporation. At a relative humidity of 80%, the equilibrium diameter of a droplet is half of the diameter at formation, and the salinity of each droplet is therefore 8 times higher than the sea salinity (Andreas, 1990). This spray with a salinity of 280‰ has a freezing temperature below −20 °C, according to Eq. (13), and does not freeze in typical offshore conditions. Nevertheless, for a wind speed of 20 m s^{-1} at a height of 16 m, the MVD is 50 μm. A 100-μm-diameter droplet shrinks to 50 μm

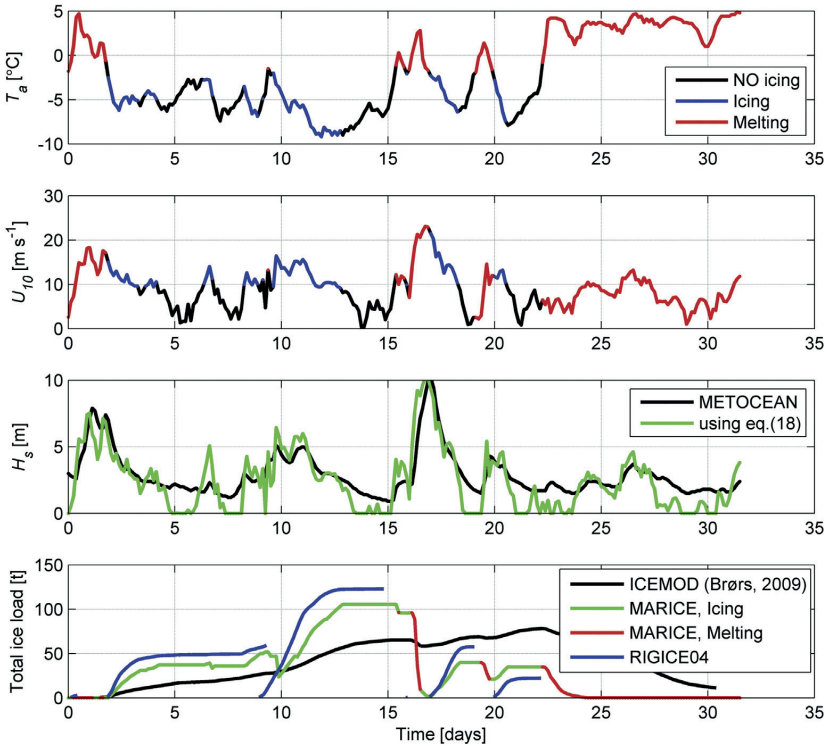

Fig. 14. Time-series of weather conditions and the total ice load predicted by different models.

Table 1
Main parameters of models.

	Spray flux	Heat transfer	Wave run-up	σ	Melting included	References
MARICE	Eq. (1)	~ $Re^{0.86}D_{st}^{-1}$	$H_s \pm 4\%$	0.3	Yes	
ICEMOD	Eq. (1) +10% (on leeside)	~ $Re^{0.5}D_{st}^{-1a}$	$0.5H_s$[a]	0.34	Yes	Horjen (1990), Brørs et al. (2009)
RIGICE04	> Eq. (1) by factor 10–1000[a]	~ $Re^{0.5}D_{st}^{-1a}$	H_s	0–0.4	No	Lozowski et al. (2002), Forest et al. (2005)

[a] Denotes the main sources of difference of each model from MARICE.

in 100 s in the air with a humidity of 80% (Andreas, 1990). Exact salinity is therefore dependent on the time required for the droplet to reach 16 m, which is more than 20 s for the 20-m s^{-1} wind, according to Andreas (1990).

The main deck of the Ocean Bounty is only 16 m above the ocean surface (Jones and Andreas, 2012), which is 19 m lower than the main deck of West Hercules. The wave-structure interaction produces 5 times more spray than the wind at an elevation of 16 m for a wind speed of 33 m s^{-1} (Fig. 6). In addition, the spray flux caused by the wave-interaction is 10–1000 times higher than the one of Horjen and Vefsnmo (1985), according to another source of field data, which is used by RIGICE04 (Forest et al., 2005). Therefore, the wave-interaction spray likely caused the icing on the Ocean Bounty and is in agreement with the prediction of MARICE.

The choice of spray flux functions is essential for icing predictions. The spray flux of Horjen and Vefsnmo (1985) at a wind speed of 33 m s^{-1} created a negligible ice growth rate of less than 0.3 mm h^{-1} on the rescue boats of West Hercules due to their high elevation. However, the spray flux function used in RIGICE04 will cause icing of the rescue boats, i.e., the different functions give opposite conclusions.

The main focus of this paper was the application of CFD. Therefore, certain processes of periodic water freezing were kept unresolved or simplified. The stresses on the water film due to wind and arriving droplets were neglected.

The linear temperature gradient through the water film is correct for $\eta < 3$ mm, according to Myers and Charpin (2004). The spray flux of Horjen and Vefsnmo (1985) above the maximal wave run-up resulted in a water film thickness of less than 0.2 mm. During water shedding along the surface of the structure, the maximum of instant η was less than 1 mm on the vertical walls. The maximum of η was 6 mm and was only on the horizontal shelf of the pontoons of West Hercules in an additional calculation for $T_a = -3$ °C and $U_{10} = 33$ m s^{-1}. The water on the shelf had a salinity of 54.6‰ and did not freeze at −3 °C. Thus, the assumption of a linear temperature gradient through the water film was valid.

As in some models of icing (Lozowski et al., 2000; Makkonen, 1987, 2010) and in contrast to Szilder et al. (1987) and Myers and Charpin (2004), we neglected the heat conduction through the ice. This assumption is true for a thick ice or spongy ice formation (ice with entrapped unfrozen water that is created when the water film temperature is lower than the freezing temperature) caused by continuous spray.

Table 2
Comparison of heat transfer coefficients [W m^{-2} K^{-1}] predicted by models with correlations based on the full scale measurements on buildings collected by Defraeye et al. (2011).

	3 m s^{-1}	9 m s^{-1}
Min and max values across the surface of FPSO (diameter 90 m) predicted by models		
MARICE	4.4–8.9	24–50
ICEMOD	1.4–4.3	4–12
RIGICE04	3.7	9.9
Calculated from correlations for the windward sides of buildings (length × width × height in m)		
Rectangular building with L-shaped ground floor (21 × 9 × 28 m) (Sharples, 1984)	14	31
Tower (20 × 36 × 78 m) (Loveday and Taki, 1996)	15	27

However, the ice thickness in the time-series for the FPSO was less than 20 cm, and the average ice thickness was approximately 5 cm. Brown and Mitten (1988) reported that the icing events on rigs typically produce the ice with a thickness of less than 10 cm. It was therefore incorrect to neglect the heat conduction through the ice in Eq. (12), which is a prevailing heat flux when the ice thickness is less than 2.4 cm under certain conditions (Myers and Charpin, 2004). MARICE also neglects the heat capacities of the water and ice accretion in Eq. (12), which can be estimated as:

$$Q_{Tf} = \left(c_i \rho_i b_{eff} + c_w \rho_w \eta\right) \frac{dT_f}{dt} \tag{23}$$

where c_i and c_w are the specific heat capacities of the saline ice accretion and water film, respectively; b_{eff} is the portion of the accreted ice thickness that affects the growth of new ice. T_f changes when the salinity of the water film changes due to salt rejection between each spray event and after that due to the spray flux in a new spray event. To continue freezing, the water film needs to reach the new freezing temperature. For example, the water film with a thickness of 0.2 mm requires an energy of approximately 800 J m^{-2} to change the temperature by 1 °C. The typical heat flux from the air will require 8 s to change the water temperature by 1 °C, which is 3–10 times less than the spray period. b_{eff} can be even higher than 0.2 mm and, therefore, requires even more energy. Thus, it is incorrect to neglect the heat capacity of the water and ice in the case of periodic spray.

The thermal conductivity and heat capacity can add the heat flux from the ice/water interface and change the spongy growth regime of the ice (Lozowski et al., 2002; Makkonen, 1987, 2010) to the constitutively supercooled (Weeks, 2010). These processes, which were beyond the scope of this paper, will vary the ratio of the entrapped liquid water mass to the mass of ice accretion.

5. Conclusions

The paper presented a useful engineering tool for the prediction of icing, called MARICE. The main advantage of MARICE is the application of CFD to calculate the airflow around a structure in combination with a freezing model. Previous models approximate the structure using a number of simple geometries, i.e., plates and cylinders, and assume that the airflows around them do not interfere. Simple geometries also cannot be used to approximate airflow with separation and reattachment. In contrast with other models, MARICE can predict the heat transfer, the water film flow and freezing on the structures with any arbitrary size and geometry. MARICE calculates spray trajectories in the turbulent airflow, and therefore, improves the prediction of the spray flux to the structure surface. The model was implemented within ANSYS FLUENT and consists of three main modules: airflow, flow of droplets and freezing modelling.

The advantages of the model were evaluated via two case studies, which gave several additional results:

- Both RIGICE04 and ICEMOD underestimate the heat transfer coefficient on the structure surface in the airflow with Reynolds numbers greater than 10^7 because the result of the small-scale experiments cannot be extended to the full scale structures due to the change of the flow regime.

- The wind-generated spray is unlikely to create a significant contribution to icing. The portion of spray that settles on a drilling rig is negligible compared to the spray concentration in the air due to the low inertia of the small droplets (<100 μm), which easily follow the airstreams around the structure. Additionally, the salinity of the wind-generated spray is high, and therefore, the wind-generated spray has a significantly lower freezing temperature than the seawater.
- The water film dynamic has a weak effect on the ice growth. The steady freezing model of Makkonen (1987) predicts an ice growth rate that differs from the ice growth rate predicted by MARICE by less than 13% for air temperatures below −6 °C and instant spray fluxes less than 0.1 kg m^{-2} s^{-1}. Therefore, the model of Makkonen (1987) can be used instead of more complex models under these conditions, and there is no need to resolve the motion of the water film accurately.
- The second case study showed how CFD, which is a computationally expensive tool, can be optimally used to predict the time-series of the ice accretion.

The model emphasised the need to study the spray generation, which is one of the main parameters that affect ice accretion. There is also a lack of measurements of the heat transfer coefficient on the surface of the full scale rig or vessel, which is required to validate the CFD prediction of the heat transfer coefficient. Furthermore, the effect of the heat conduction from the structure surface to the water/ice interface and the heat capacity of the ice and water should be included in the models of icing caused by periodic sea spray.

Acknowledgements

The work presented in this paper is part of MARICE, which is a joint industry project between Det Norske Veritas, Statoil, the Norwegian University of Science and Technology and the Research Council of Norway, and studies marine icing on offshore structures and vessels. The authors thank Dr Andrea Califano for his help in creating the numerical mesh, Dr Tom Forest for sharing RIGICE04, and MSc Sergey Kulyakhtin, MSc Eirik Schrøder Hansen, Dr Lasse Makkonen and Prof Sveinung Løset for fruitful discussions.

References

Achenbach, E., 1975. Total and local heat transfer from a smooth circular cylinder in cross-flow at high Reynolds number. Int. J. Heat Mass Transf. 18 (12), 1387–1396.
Achenbach, E., 1977. The effect of surface roughness on the heat transfer from a circular cylinder to the cross flow of air. Int. J. Heat Mass Transf. 20 (4), 359–369.
Andreas, E.L., 1990. Time constants for the evolution of sea spray droplets. Tellus B 42 (5), 481–497.
ANSYS, 2009. FLUENT 12.0 Theory Guide, Ansys Inc, Cannonsburg p. 5.
ANSYS, 2012. ICEM CFD 13: Geometry and Mesh Generation Preprocessor, Ansys Inc, ANSYS, Cannonsburg.
Brørs, B., Løset, S., Iden, K., Reistad, M., Harstveit, K., Nygård, B., Engedahl, H., 2009. Goliat Environmental/Icing Evaluation Study. 25/08, Norwegian Meteorological Institute.
Brown, R.D., Mitten, P., 1988. Ice Accretion on Drilling Platforms Off the East Coast of Canada. In: Storm, A.H.a.J.F. (Ed.), International Conference on Technology for Polar Areas. Trondheim, Norway. Tapir Publishers, Trondheim, Norway, pp. 409–421.
CD-adapco, 2010. STAR-CCM+ User Manual v5.09, CD-adapco Group, Melville, NY.
Defraeye, T., Blocken, B., Carmeliet, J., 2011. Convective heat transfer coefficients for exterior building surfaces: existing correlations and CFD modelling. Energy Convers. Manag. 52 (1), 512–522.
Finstad, K.J., Lozowski, E.P., Gates, E.M., 1988a. A computational investigation of water droplet trajectories. J. Atmos. Ocean. Technol. 5 (1), 160–170.
Finstad, K.J., Lozowski, E.P., Makkonen, L., 1988b. On the median volume diameter approximation for droplet collision efficiency. J. Atmos. Sci. 45 (24), 4008–4012.
Forest, T., Lozowski, E., Gagnon, R., 2005. Estimating marine icing on offshore structures using RIGICE04. International Workshop on Atmospheric Icing on Structures (IWAIS), Monreal.
Gaches, R., Eik, K., Mathlesen, M., 2013. Skrugard field metocean design basis. PTM MMG MGE RA 58. Statoil, Norway.
Horjen, I., 1990. Numerical Modeling of Time-dependent Marine Icing, Anti-icing and Deicing, Norwegian University of Science and Technology, Trondheim, Norway (175 pp).
Horjen, I., 2013. Numerical modeling of two-dimensional sea spray icing on vessel-mounted cylinders. Cold Reg. Sci. Technol. 93, 20–35.
Horjen, I., Vefsnmo, S., 1985. A Kinematic and Thermodynamic Analysis of Sea Spray (in Norwegian), Offshore Icing — Phase II. STF60 F85014, Norwegian Hydrodynamic Laboratory (NHL), Norway.
Jones, K.F., Andreas, E.L., 2012. Sea spray concentrations and the icing of fixed offshore structures. Q. J. R. Meteorol. Soc. 138 (662), 131–144.
Jørgensen, T.S., 1982. Influence of Ice Accretion on Activity in the Northern Part of the Norwegian Continental Shelf. STF88 F82016, Offshore Testing and Research Group.
Kays, W., Crawford, M., Weigand, B., 2005. Convective Heat and Mass Transfer, McGraw-Hill, New York (546 pp).
Kulyakhtin, A., Løset, S., 2011. Sea spray icing: in-cloud evaporation. Semi-analytical and numerical investigations. The 14th International Workshop on Atmospheric Icing of Structures, Chongqing, China, p. 5.
Kulyakhtin, A., Shipilova, O., Libby, B., Løset, S., 2012. Full-scale 3D CFD simulation of spray impingement on a vessel produced by ship-wave interaction. the 21st IAHR International Symposium on Ice, Dalian, China, pp. 1129–1141.
Kulyakhtin, A., Kulyakhtin, S., Løset, S., 2013. Marine Icing Field Experiment 2012. 2013–1776, Det Norske Veritas.
Kulyakhtin, A., Shipilova, O., Muskulus, M., 2014. Numerical simulation of droplet impingement and flow around a cylinder using RANS and LES. J. Fluids Struct. http://dx.doi.org/10.1016/j.jfluidstructs.2014.03.007.
Lienhard, J.H., 2013. A heat transfer textbook, Courier Dover Publications.
Loveday, D.L., Taki, A.H., 1996. Convective heat transfer coefficients at a plane surface on a full-scale building facade. Int. J. Heat Mass Transf. 39 (8), 1729–1742.
Lozowski, E.P., Szilder, K., Makkonen, L., 2000. Computer simulation of marine ice accretion. Philos. Trans. R. Soc. Lond. Ser. A 358 (1776), 2811–2845.
Lozowski, E.P., Forest, T., Chung, V., Szilder, K., 2002. Study of marine icing. CR-2002-03, National Research Council of Canada, St. John's, NF.
Makkonen, L., 1985. Heat transfer and icing of a rough cylinder. Cold Reg. Sci. Technol. 10 (2), 105–116.
Makkonen, L., 1987. Salinity and growth rate of ice formed by sea spray. Cold Reg. Sci. Technol. 14 (2), 163–171.
Makkonen, L., 2010. Solid fraction in dendritic solidification of a liquid. Appl. Phys. Lett. 96 (9), 091910.
Makkonen, L., Brown, R.D., Mitten, P.T., 1991. Comments on "Prediction of vessel icing for near-freezing sea temperatures". Weather Forecast. 6 (4), 565–567.
Mitten, P., 1994. Measurement and modelling of spray icing on offshore structures. Contract no. 07SE. KM169-8-7439, Final Report to Atmospheric Environment Service of Canada.
Myers, T., 1998. Thin films with high surface tension. Siam Rev. 40 (3), 441–462.
Myers, T.G., 2001. Extension to the Messinger model for aircraft icing. AIAA J. 39 (2), 211–218.
Myers, T.G., Charpin, J.P., 2004. A mathematical model for atmospheric ice accretion and water flow on a cold surface. Int. J. Heat Mass Transf. 47 (25), 5483–5500.
Nakakita, K., Nadarajah, S., Habashi, W., 2010. Toward real-time aero-icing simulation of complete aircraft via FENSAP-ICE. J. Aircr. 47 (1), 96–109.
Nauman, J., 1984. Superstructure icing on the semi-submersible Ocean Bounty in Lower Cook Inlet, Alaska. The 2nd International Workshop on Atmospheric Icing of Structures, Trondheim, Norway, pp. 71–79.
Overland, J., Pease, C., Preisendorfer, R., Comiskey, A., 1986. Prediction of vessel icing. J. Clim. Appl. Meteorol. 25 (12), 1793–1806.
Pope, S.B., 2000. Turbulent Flows, Cambridge University Press, Cambridge.
Ryerson, C., 1995. Superstructure Spray and Ice Accretion on a Large US Coast Guard Cutter. Atmos. Res. 36 (3), 321–337.
Ryerson, C.C., 2008. Assessment of superstructure ice protection as applied to offshore oil operations safety. ERDC/CRREL TR-08-14, U.S. Army Cold Regions Research and Engineering Laboratory, Hanover, NH.
Ryerson, C.C., Gow, A.J., 2000. Ship Superstructure Icing: Crystalline and Physical Properties. ERDC/CRREL TR-00-11, U.S. Army Cold Regions Research and Engineering Laboratory, Hanover, NH.
Sarpkaya, T., Isaacson, M., 1981. Mechanics of Wave Forces on Offshore Structures, 96, Van Nostrand Reinhold Company New York, New York (651 pp).
Schwerdtfeger, P., 1963. The thermal properties of sea ice. J. Glaciol. 4 (36), 789–807.
Sharples, S., 1984. Full-scale measurements of convective energy losses from exterior building surfaces. Build. Environ. 19 (1), 31–39.
Sharqawy, M.H., Lienhard, J.H., Zubair, S.M., 2010. Thermophysical properties of seawater: a review of existing correlations and data. Desalin. Water Treat. 16 (1–3), 354–380.
Szilder, K., Lozowski, E.P., Gates, E., 1987. Modelling ice accretion on non-rotating cylinders—the incorporation of time dependence and internal heat conduction. Cold Reg. Sci. Technol. 13 (2), 177–191.
Szilder, K., Lozowski, E.P., Forest, T.W., 1995. One-dimensional freezing of seawater in a constrained volume. Can. Geotech. J. 32 (1), 122–127.
Thomson, D., Wilson, J., 2013. History of Lagrangian stochastic models for turbulent dispersion. Lagrangian Modeling of the Atmosphere pp. 19–36.
Türk, M., Emeis, S., 2010. The dependence of offshore turbulence intensity on wind speed. J. Wind Eng. Ind. Aerodyn. 98 (8), 466–471.
Weeks, W., 2010. On Sea Ice, University of Alaska Press, Fairbanks, AK (664 pp).
Zakrzewski, W.P., 1986. Icing of fishing vessles part I: splashing a ship with spray. 8th IAHR Symposium on Ice, Iowa City.
Zdravkovich, M., 1997. Flow Around Circular Cylinders, volume 1: Fundamentals, 19, Oxford University Press, Oxford (185 pp).

The role of the ice heat conduction in the ice growth caused by periodic sea spray

Anton Kulyakhtin[a,b,*], Sergey Kulyakhtin[a,b], Sveinung Løset[a,b]

[a]*Department for Civil and Transport Engineering, Norwegian University of Science and Technology (NTNU), Høgskoleringen 7A, 7491, Trondheim, Norway*

[b]*Arctic Technology Department, University Centre in Svalbard (UNIS), P.O. Box 156, 9171, Longyearbyen, Norway*

Abstract

The accurate prediction of the ice accretion on offshore structures or vessels caused by sea spray is important to ensure safe operations in the Arctic. Existing models of marine icing neglect the heat conduction of the accreted ice, which is reasonable only for continuous spray. However, marine spray is periodic, and between spray events accreted ice cools below the freezing temperature of the spray. When a new spray arrives, it freezes primarily due to the heat release into the cold ice accreted before. In this paper, the ice accretion caused by periodic saline spray is studied experimentally and numerically. We present a new model which simulates the heat conduction inside the accreted ice and show that models neglecting the heat conduction in the accreted ice underestimate the ice accumulation by more than 50%.

Keywords: Ice accretion, icing experiments, periodic spray, freezing sea spray, real-time measurements, salt entrapment

Nomenclature

b	ice thickness
b_1, b_2	parts of the fresh ice thickness that do and do not contain unfrozen water, respectively
$\frac{db_M}{dt}$, $\frac{db_{WL}}{dt}$	increments in ice thickness caused by the heat conducted by the ice accretion and caused by air cooling, respectively, see Eq. (14)
c_{cyl}, c_i, c_w	specific heat capacities of the cylinder, pure ice, and water, respectively
D_{cyl}	cylinder diameter
D_{sw}	diffusion coefficient of salt in water

$e(T)$	saturated water pressure
F_d	spray mass flux
g	gravitational constant
H_{ac}, H_w	enthalpies of saline ice accretion and water, respectively, relative to 0 °C
H_{cyl}	energy contribution from the cylinder to the ice growth
h, h_{lee}	average convective heat transfer coefficients of the windward and leeward sides of the cylinder, respectively
k_a, k_{ac}, k_i, k_w	thermal conductivities of air, ice accretion, ice, and water, respectively
L_f	latent heat of fusion
m_{cyl}	mass of cylinder
Nu	Nusselt number
Q_c, Q_d, Q_e, Q_r	heat fluxes at the air-water interface: convection, heat capacity of the impinging spray, evaporation, and radiant heat flux, respectively
Q_{ki}	heat flux absorbed by the previously accreted ice from the formation of new ice, see Eq. (17)
Q_w	energy of supercoiling of the saline water relative to its freezing temperature
Re	Reynolds number of the air flow
r_H	Relative humidity of the air
S_{ac}, S_{sp}, S_w	salinities of the ice accretion, sea spray, and water film, respectively
S_w^{max}	salinity of water film for which the freezing temperature is equal to the air temperature.
T_a, T_d, T_{ac}, T_{cyl}, T_f, T_s, T_w	air temperature, spray temperature, temperature of the ice accretion, temperature of the cylinder, freezing temperature of water, temperature of the structure surface, and temperature of the water film at the air-water interface, respectively
$T_f(S_w)$	freezing temperature of saline water as a function of water salinity
V_w	velocity of the water film run-off
v_{wac}	volume fraction of liquid, saline water inside the ice accretion, see Eq. (11)
x	direction perpendicular to the structure surface
α, α_1	constants equal to -0.0182 °C^{-1} and -0.01 °C^{-1}, respectively
γ	wind direction relative to the positions of the nozzle and cylinder (Fig. 6)
δ	thickness of the diffusion limited boundary layer
η	water film thickness
ν_w	kinematic viscosity of water

ρ_{ac} , ρ_i , ρ_w	densities of the ice accretion, ice, and water, respectively
σ_M , σ_{WL}	coefficients of entrapment of unfrozen water when the freezing is primarily caused by the heat fluxes from the air and from the ice accretion, respectively.
σ_0	constant equal to 0.26

1. Introduction

Marine icing on vessels endangers human activities in the Arctic and may cause operational problems. The ability to predict and prevent icing events is dependent on an understanding of icing phenomena. The process of sea-spray icing caused by ship-wave interactions can be divided into four major stages: 1) the generation of sea spray, 2) the spray flow in the air (i.e., the cloud of water droplets) around the superstructure of the ship, and 3) droplet impingement on the ship structure followed by 4) water run-off and freezing. This paper focuses on the freezing of incoming spray in the fourth stage.

The models of the fourth stage for icing caused by continuous spray (Blackmore et al., 2002; Makkonen, 1987; Makkonen, 2010) are well developed and have been validated based on numerous experimental studies, which are reviewed by Ekeberg (2010) and Kulyakhtin et al. (2013a). However, the spray caused by wave-structure interaction arrives on the structure surface in discrete events that are separated by long periods in which no new water arrives. Most models of the icing caused by periodic saline spray rely on the same assumptions as the continuous models, which are: the ice growth is caused by airflow cooling; and the conductive heat flux in the ice accretion is negligible (Forest et al., 2005; Horjen, 1990; Horjen, 2013; Kulyakhtin and Tsarau, 2014; Lozowski et al., 2000). However, between spray events, the salinity of the water film on the surface of the accreted ice increases because of salt expulsion from freezing water. Therefore, the freezing temperature of the water film decreases and approaches the air temperature. As result, the temperature of the accreted ice also decreases. The next spray event will then dilute the salt in the water film and allow the ice to grow again, and the "cold" stored in the ice and water film will be released to produce new ice. This "stored cold" will also change the mechanism of salt entrapment into ice.

The neglecting of the conductive heat flux contradicts also with Myers and Charpin (2004), who have stated that the conductive heat flux is the prevailing heat flux to the surface of the icing object when the ice is thin, e.g., less than 2.4 cm in the case of continuous fresh water spray. In the field, the "cold" stored in the massive walls of the vessel or offshore rig can produce substantial ice growth which is neglected by the existing models. The total underestimation of the rate of ice growth and the total ice mass may be substantial because observed icing events on offshore rigs typically produce ice with a maximal thickness of less than 10 cm (Brown and Mitten, 1988). In this paper, we answer the question of how great is the contribution of the cold accumulated by the accreted ice between spray events.

The layout of the paper is as follows. Section 2 discusses the differences of the physical phenomena in the icing caused by periodic and continuous spray. Section 3 describes the experimental setup used to observe

the effects induced by the heat capacity of the ice accretion. A new model of icing caused by periodic sea spray that accounts for the heat conduction and heat capacity of the ice accretion is proposed in Section 4 and is experimentally validated in Section 5. The parameterisation of the ice growth, the experimental uncertainties and the effect of the heat capacity for the real-scale structures are discussed in Sections 6 – 9.

2. Continuous versus periodic icing

2.1. Wet (glaze) icing caused by continuous fresh water spray

When the first fresh-water spray reaches the cold surface of a structure, the heat generated by the water freezing is mainly conducted through the ice into the cold structure (Myers and Charpin, 2004; Szilder et al., 1987) (Fig. 1):

$$\rho_i L_f \frac{db}{dt} = -k_i \frac{T_f - T_s}{b} + Q_c + Q_e + Q_d + Q_r \tag{1}$$

where ρ_i is the density of the accreted ice, L_f is the latent heat of fusion, b is the ice thickness in x direction perpendicular to the structure surface, k_i is the thermal conductivity of ice, T_f is the freezing temperature of water and T_s is the temperature of the structure surface. The heat fluxes at the air-water interface are convection, Q_c, evaporation, Q_e, heat capacity of the impinging spray, Q_d, and radiant heat flux, Q_r.

$$Q_c = h\left(T_a - T_w\right) \tag{2}$$

where h is the convective heat transfer, T_a is the air temperature, and T_w is the surface temperature of the water film.

$$Q_e = hE\left(r_H e\left(T_a\right) - e\left(T_w\right)\right) \tag{3}$$

where E is a coefficient, for details see, for example, Lozowski et al. (2000), r_H is the relative humidity of the air, and $e\left(T\right)$ is saturated water pressure, which is a function of temperature, T.

$$Q_d = c_w F_d \left(T_d - T_f\right) \tag{4}$$

where c_w is the specific heat capacity of water, F_d is the spray flux, and T_d is the spray temperature.

Description of Q_r can be found elsewhere (for example. Lozowski et al. (2000)). Q_r consists of long wave radiation described by Stefan-Boltzmann law and sun radiation. Long wave radiation is less than 9% of the

convective heat transfers for typical icing conditions (Jones, 1996; Kulyakhtin et al., 2013a) and sun radiation is omitted here too because experiments considered in this paper were done during the night.

The increase of the ice thickness decreases the temperature gradient in the accreted ice and the rate of the heat flux to the structure caused by the water freezing. Therefore, later the growth regime changes. The heat fluxes at the air-water interface start to be the main contributors to the ice growth. Thus, once an ice dendrite propagated into the water film, the air cooling primarily drives further propagation of the dendrite tip instead of freezing water surrounding the ice dendrite. It happens because ice has higher thermal conductivity than water. As result, the ice entraps liquid water between dendrites, and less cooling is required to produce ice accretion (Blackmore et al., 2002; Makkonen, 2010) (Fig. 2). The ratio of the mass of entrapped liquid water to the mass of the ice accretion is σ_M = 0.3 (Makkonen, 2010).

In the water film out of the freezing front, conduction is the dominant heat transfer mechanism and the temperature gradient is linear when the water film thickness, η, is less than 3 mm (Myers and Charpin, 2004). The heat generated at the freezing interface is conducted through the water film to the air/water interface and is equal to the heat flux to the air. The heat balance at the ice/water interface is therefore:

$$\rho_i L_f \left(1-\sigma_M\right)\frac{db_1}{dt} = -k_w \frac{T_w - T_f}{\eta} = Q_c + Q_e + Q_d + Q_r \tag{5}$$

In this case, the ice accretion does not conduct the heat generated by the freezing of the water layer due to presence of the entrapped, unfrozen water in the ice accretion in layer b_1 (Fig. 2). The heat released by freezing of the water in the layer b_1 near to the edge of layer b_2 is conducted by the completely frozen layer b_2 to the cold structure. Therefore, structure does not affect freezing of the water film.

2.2. Wet icing caused by continuous saline water spray

In the case of icing caused by continuous *saline* spray, the freezing temperature depends on the salinity of the water film, S_w (Schwerdtfeger, 1963):

$$S_w = \begin{cases} \alpha T_f \text{ , if } 0\ ^\circ\text{C} \geq T_f > -8.2\ ^\circ\text{C} \\ 0.149 - \alpha_1\left(T_f + 8.2\ ^\circ\text{C}\right) \text{ , if } -8.2\ ^\circ\text{C} \geq T_f > -23\ ^\circ\text{C} \end{cases} \tag{6}$$

where α = -0.0182 °C^{-1} and α_1 = -0.01 °C^{-1}.

The enthalpy per unit mass of the saline ice accretion referred to 0 °C, H_{ac}, does not experience a stepwise increase at the freezing temperature but rather changes continuously (Fig. 3) (Schwerdtfeger, 1963):

$$H_{ac}\left(T_{ac}, S_{ac}\right) = -\left(L_f - c_i T_{ac}\right)\left(1 - \frac{S_{ac}}{\alpha T_{ac}}\right) - \frac{S_{ac}\left(c_w - c_i\right)}{\alpha} ln\frac{S_{ac}}{\alpha T_{ac}} + \frac{S_{ac}}{\alpha} c_w \text{ , } T_{ac} < \frac{S_{ac}}{\alpha} \tag{7}$$

where T_{ac} and S_{ac} are the temperature and salinity of the ice accretion, respectively; c_i is the specific heat capacities of pure ice (the salt concentration is small, and its heat capacity is neglected); and $S_{ac}\alpha^{-1}$ is the melting temperature of the ice accretion. Schwerdtfeger (1963) has shown that Eq. (7) as well as Eqs. (10) and (12) below provide a reasonably accurate approximation of the properties of saline ice at temperatures below – 8.2 °C.

In contrast to fresh-water icing, there is no sharp boundary between b_1 and b_2 as in Fig. 2; the temperature gradient changes smoothly, and the accreted ice does not act as an insulator. There is a thermal balance between the fraction of entrapped, unfrozen water and its salinity. The entrapped water cannot freeze without a decrease in the ice-accretion temperature. In addition, when the water film with salinity S_w freezes, the ice entraps only a portion of the salt, $S_{ac} = \sigma_M S_w$, and the rest is rejected into the water film (Makkonen, 1987). As a result, S_w is higher than the spray salinity.

During the initial stage of ice growth from saline water, the heat generated by the water freezing is primarily consumed by the structure. In this stage, the entrapment of the saline unfrozen water in the ice, σ_{WL}, is determined by the growth rate of ice dendrites (Weeks, 2010; Weeks and Lofgren, 1967):

$$\sigma_{WL} = \frac{\sigma_0}{\sigma_0 + (1-\sigma_0)\,exp\left(-\delta D_{sw}^{-1}\frac{db}{dt}\right)} \tag{8}$$

where σ_0 = 0.26, δ is the thickness of the diffusion-limited boundary layer, and D_{sw} is the diffusion coefficient of the salt in the water (Weeks, 2010). $\frac{db}{dt}$ is the growth rate of ice dendrites driven by the heat conduction through the ice to the structure. In experiments investigating steady ice growth in semi-infinite water, it has been found that δD_{sw}^{-1} is constant and equal to 724.3 s mm^{-1} for a broad range of ice-growth rates (from $2.0 \cdot 10^{-4}$ mm s^{-1} to $2.8 \cdot 10^{-3}$ mm s^{-1}) (Weeks, 2010).

Note that σ_{WL} may be significantly higher than σ_M, as has been observed in experiments (Smedsrud et al., 2003; Weeks, 2010). Variations in the salt entrapment change the enthalpy of the sea ice and its heat capacity by 50 % (Fig. 3). Additionally, the salinity of ice determines its melting temperature, and therefore, an underprediction of salinity can result in an overestimation of the total ice mass accreted on offshore structure over the winter season.

2.3. Icing caused by periodic saline spray

The existing models of icing caused by *periodic* spray, ICEMOD (Horjen, 1990; Horjen, 2013), RIGICE_N (Lozowski et al., 2000), RIGICE04 (Forest et al., 2005), and MARICE (Kulyakhtin and Tsarau, 2014), all

rely on the same assumption that is valid for steady growth only, namely, no heat conduction from the accreted ice to the freezing interface.

These models consider the change in the water film salinity over time caused by salt expulsion at the interface of freezing. During ice formation, especially after the end of a spray event, the water film salinity increases and causes its freezing temperature to decrease. The ice growth continues until the freezing temperature of the water film decreases until the thermal balance with airflow is reached and there is no heat flux to the air. Therefore, ice formation stops. The system remains in this thermal balance until the next spray event, during which the salinity of the water film is diluted by the new spray and freezing starts again. However, the models assume that the change in the water film temperature does not affect the heat transfer in the ice accretion behind the freezing interface.

The heat capacity of the ice can be neglected in the case of periodic fresh-water icing. The enthalpy of fresh ice changes insignificantly at temperatures below 0 °C (Fig. 3), and therefore, the heat capacity of fresh ice can be neglected. By contrast, saline ice releases a substantial amount of heat from the freezing of the entrapped saline water when it cools down (Fig. 3 and Eq. (7)), and as a result, the heat capacity of the sea ice should be considered.

Let us analyse the process detailed. Imagine that spray arrives in a discrete event on a non-conductive accreted ice and begins to freeze because of heat fluxes from the air (1) (Fig. 4). When the spray ends (2), as described above, the salinity of the water film, S_w, will rise above the initial value of the spray salinity, S_{sp}. For the freezing to continue, the temperature of the film must decrease, and air cooling serves this purpose, i.e., part of the cooling is spent to decrease the internal energy of the water film.

Once the water film has become colder than it was during step (1), freezing continues; however, the temperature of the accretion created during step (2) is lower than the temperature of the ice produced during step (1). This difference creates a temperature gradient in the formed ice. Therefore, the air cooling must serve both to create new ice and to cool the ice accreted during previous step. This process continues until step (3), when the freezing temperature of the water film approaches the air temperature; then, the heat flux from the air mainly serves to freeze the saline, liquid water, brine, inside the ice accretion, not to form new ice.

When a new spray event happens in step (4), the temperature of the ice accretion is lower than the freezing temperature of the spray. “New” ice will form both because of the heat release to the air but mainly to the “old” accretion. This situation contradicts with the initial assumption of no heat conduction from the ice accretion. In addition, the salt entrapment in the new spray event will be σ_{WL} instead of σ_M, and the ice salinity will be higher.

Experiments comparing the ice accretion on small cylinders (4-5 cm in diameter) caused by periodic and continuous spray have been performed in Alberta (Foy, 1988; Lozowski and Zakrewski, 1992) and

Trondheim (Carstens et al., 1984; Horjen and Vefsnmo, 1986). The difference in the total ice masses measured in these experiments under continuous and pulsed spray with the same time-averaged spray flux was less than 50% (Brown et al., 1990). Considering the experimental uncertainties, the difference was considered to be an indication that there is only a small difference between ice accretions caused by periodic and continuous sprays. However, as we showed, the underlying physics of the ice formation and salt entrapment is different in the two cases. In those experiments, the spray period was 20 s and, the spray flux was high (see Kulyakhtin et al. (2013a) for summaries of the experimental setups), and as a result, the temperature of the water film did not substantially change. The heat capacities of the cylinders were small, but their exact masses were not reported, thus making it difficult to compare theoretical models to the experimental results. In addition, the effect of the cylinder heat capacity vanishes over time, when cylinder temperature increases due to the heat generated by freezing, and the heat fluxes to the air-water interface eventually become the main driving force for freezing. However, in real conditions, effect of structure is longer because the heat capacities of offshore structures are substantially greater than those of small cylinders.

To verify the physics mechanism of the periodic ice growth, we performed new experiments in which the spray period was longer (up to 147.8 s), the ice accretion mass was measured continuously during the ice growth process (to measure the percentage of the spray frozen after each spray event, i.e., to investigate the effects of the heat capacities of the cylinder and the ice accretion) and the salinity of the accreted ice was measured to verify salt entrapment.

3. Experiment

The experiment was conducted during the dark season in Spitsbergen (78 12’ 10’’ N, 15° 49’ 41’’ E) to avoid effect of sun radiation. The experimental setup consisted of a spraying rig with an air-atomising nozzle, a compressor, an icing object and a weather station (Fig. 5 and Fig. 6), a detailed description is in Kulyakhtin et al. (2013a) and Kulyakhtin (2013). Only a brief summary is given below.

Seawater (with a salinity of 34 ppt) was stored in a 300-litre water tank in which the temperature was kept constant during each single experiment. The water from the tank was pumped from the tank and sprayed by the nozzle. A system of electronic valves and timers created pulses of spray with a constant duration and a constant interval between them. The water volume discharged by the nozzle per spray event varied by 10%. According to the manufacturer of the nozzle, the median volume diameter of the ejected droplets ranges from 90 to 300 μm for our pressure settings.

One of the major differences between field experiments and wind-tunnel experiments is the unstable wind speed in the field, which complicates comparison between model and experiment. Fig. 7 shows example of weather conditions during Exp. 235 (Kulyakhtin, 2013). The air humidity and temperature were stable throughout the test duration, whereas the wind exhibited both short-term variations related to turbulence and

long-term variations. The wind direction averaged over few minutes varied by 5 – 10°. The spray flew in the direction of the cylinder, partially because of the wind but mainly because of the ejection speed. The diameter of the spray cloud at a location of the cylinder was approximately 1 m and required proper alignment of the spray direction with respect to the cylinder. The wind sensor installed above the nozzle rotated with the target and recorded the wind direction relative to the positions of the nozzle and cylinder, γ (Fig. 6). To maintain the line between the cylinder and nozzle parallel to the wind direction, an automatically controlled trolley with the cylinder moved along a rail to minimize γ. A Campbell CR 1000 data logger was used to register the weather conditions and to steer the target motion. The length of the rail was 5.2 m, and the trolley could move within a 50° angle. A constant distance of 5 m between the nozzle and the cylinder was maintained. The nozzle was placed 2.3 m above the ground to reduce the effects of blowing snow and the turbulence induced by the ground.

Ice accretion was measured on a horizontal aluminium cylinder with a length of 300 mm and a diameter of 100 mm. The cylinder was hollow inside with a wall thickness of approximately 1 mm and a mass of 534 g. The cylinder was thermally insulated from the other parts of the construction. The ends of the cylinder were attached to metal rods with diameters of 10 mm. The ends of the rods were placed on plastic arms (with heat conductivities of less than 0.5 W m^{-1} K^{-1}) to thermally insulate the cylinder from other parts of the rig. Plastic arms were connected to HBM (Hottinger Baldwin Messtechnik) SP4MC3MR/1kg load cells to measure continuously the total mass of the cylinder and the ice and unfrozen water that had accreted on it (Fig. 8). An HBM Amplifier MX440 digitised the data with a 20-Hz frequency and an accuracy of 0.7 g.

A shield concealed the load cells from the spray to prevent icing of them. Only the cylinder and 15 mm of the rods on each side of the cylinder were exposed to the spray. The gap between the cylinder and shield was sufficient to prevent the ice on the cylinder from coming into contact with the shield.

In spite the developed system, the spray flux varied between spray events due to sudden changes of the wind direction (Fig. 7), which were not captured by the system. In certain cases, there was no spray arriving at the cylinder, and sometimes, the total mass of water that arrived during a spray event was up to 20 g. In the spray events when spray was reaching the cylinder, on average, approximately 10 g of water was added to the cylinder per spray event according to the measurements of load cells which are shown in Fig. 8. The mass increase caused by the spray was observed as steps in the measured time-series of the accreted mass (ice mass + water mass on the cylinder surface) (Fig. 10). The stepwise-increase in the accretion mass during spray event was followed by a monotonic decrease corresponding to water runoff. The mass of incoming spray was especially easy to measure by load cells during the first spray events when the run-off was minimal which was also observed visually. However, the signal recorded by the load cells was affected by the impinging spray, the motion of the trolley, and oscillations in the lift force induced by the wind.

4. A model of ice growth caused by periodic sea spray

The numerical model, which was realised in MATLAB R2014a (MathWorks, 2014), is presented below to explain the physical mechanism underlying in the experiment. This new one-dimensional model of the ice growth caused by periodic sea spray is the basis for improving the existing two- and three-dimensional ice accretion models. The model considers a system of three objects transferring heat among each other: a cylinder, an ice accretion and a water film. The ice accretion is spatially discretised into a number of elements, whereas the states of the cylinder and water film are described using average temperatures without spatial discretisation.

The ice accretion is considered to be a mixture of ice, water, and salt, and its overall state is described by the enthalpy, Eq. (7), for temperatures below $S_{ac}\alpha^{-1}$. The heat transfer inside the ice accretion is (Lienhard, 2013):

$$\nabla\left(k_{ac}\nabla T_{ac}\right)=\frac{d\left(\rho_{ac}H_{ac}\right)}{dt} \tag{9}$$

where k_{ac} and ρ_{ac} are the thermal conductivity and density of the ice accretion, respectively. The thermal conductivity of the ice accretion (Schwerdtfeger, 1963):

$$k_{ac}\left(T_{ac},S_{ac}\right)=\mathrm{k}_i\text{-}\left(k_i-k_w\right)v_{wac} \tag{10}$$

where v_{wac} is the volume fraction of liquid, saline water inside the ice accretion:

$$v_{wac}=\frac{S_{ac}\rho_{ac}}{\alpha\rho_w T_{ac}} \tag{11}$$

The density of the ice accretion is (Schwerdtfeger, 1963):

$$\rho_{ac}\left(T_{ac},S_{ac}\right)=\frac{\rho_w\rho_i\alpha T_{ac}}{\alpha T_{ac}\rho_w-S_{ac}\left(\rho_w-\rho_i\right)} \tag{12}$$

where ρ_w is the seawater density. The air content in the ice was 0.5 – 4.5% and its effect on the heat conduction is neglected (Kulyakhtin et al., 2013b); see Section 8 for details.

A linear temperature profile is assumed in the water film, as in Eq. (5), and the change in the temperature of the water film is described as follows:

$$\rho_w\eta\frac{dH_w\left(T_w,S_w\right)}{dt}=Q_c+Q_e+Q_d-k_w\left.\frac{\partial T}{\partial x}\right|_{x=b} \tag{13}$$

where $H_w\left(T_w, S_w\right) = c_w T_w$, the last term defines the heat conduction to the ice, and the radiant heat flux is neglected (Kulyakhtin et al., 2013a).

The freezing process can be described as the movement of the boundary between the ice accretion and the water film. Any water that is added to the ice accretion changes its enthalpy, H_w, to $H_{ac}\left(T_{ac}, S_{ac}\right)$, Eq. (7).

As described above, the ice thickness increases both because of the heat conducted from the ice accretion and because of the cooling from the air:

$$\frac{db}{dt} = \frac{db_{WL}}{dt} + \frac{db_M}{dt} \tag{14}$$

where the growth rate, $\frac{db_{WL}}{dt}$ is nonzero only if the temperature gradient at the ice surface is positive and is determined by the growth rate of the ice dendrites (Weeks and Lofgren, 1967):

$$\frac{db_{WL}}{dt} = \frac{Q_{ki} + Q_w}{L_f \rho_i} \tag{15}$$

where Q_{ki} is the heat flux absorbed by the ice accretion and Q_w is the energy of supercoiling of the saline water relative to its freezing temperature, $T_f = S_w \alpha^{-1}$:

$$Q_w = \frac{db_{WL}}{dt} c_w \rho_w \left(T_w - T_f\right) \tag{16}$$

The growth rate is limited by the rate of heat absorption by the ice accretion, and therefore, it is described in the following way (which is illustrated as the difference between the solid and dashed curves in Fig. 4 (4)):

$$Q_{ki} = \frac{d}{dt}\left(\int_0^b \rho_{ac} H_{ac}\, dx + H_{cyl}\right) \tag{17}$$

where H_{ac} is the enthalpy of the ice accretion per unit mass and H_{cyl} is the energy contribution to the ice growth from the cylinder. The ice accretion contribution is calculated from the heat transfer equation, Eq. (9), in which the conductivity and enthalpy of the accretion are described by Eqs. (10) and (7), respectively.

Equation (9) is solved numerically using the finite volume method assuming that the temperature at the ice-water interface is the freezing temperature for a given salinity of the water film, S_w, $T_{ac}\big|_{x=b} = S_w \alpha^{-1}$. At $x = 0$, the heat flux is transferred to the cylinder.

The change of the cylinder enthalpy was caused by the heat flux from the ice which was released from freezing and by the convective heat flux to the leeward side of the cylinder:

$$\frac{dH_{cyl}}{dt} = \frac{c_{cyl} m_{cyl} \dfrac{dT_{cyl}}{dt}}{0.5\pi D_{cyl} L_{cyl}} = \left[-\left(k_{ac} \frac{dT_{ac}}{dx} \right)\Big|_{x=0} + h_{lee} \left(T_a - T_{cyl} \right) \right] \tag{18}$$

where c_{cyl} is the specific heat capacity of aluminium; m_{cyl} is the mass of the cylinder; T_{cyl} is the average cylinder temperature; D_{cyl} and L_{cyl} are the cylinder diameter and length, respectively; h_{lee} is the convective heat transfer coefficient of the leeward side of the cylinder (discussed later, see Eq. (23)). Equation (18) assumes that (1) all 180° of the cylinder windward side are covered with ice, (2) all 180° of the leeward side is ice free, (3) and the temperature inside the cylinder is uniform because the heat conductivity of aluminium is 100 times higher than that of the ice.

σ_{WL} was calculated using Eq. (8), where δD_{sw}^{-1} was set to a value 20 times lower than 724.3 s mm^{-1} reported by Weeks (2010). This value of δD_{sw}^{-1} gave the best agreement with the experiment and is discussed in Section 6.

The ice growth caused by the convective and evaporative heat fluxes and by the supercooling of the spray from the air-water interface, $\frac{db_M}{dt}$, is described as follows:

$$L_f \left(1 - \sigma_M\right) \rho_{ac} \frac{db_M}{dt} = c_w \rho_w \eta \left(T_f - T_w \right) + Q_c + Q_e \tag{19}$$

The entrapment of saline water, σ_M, is constant and equal to 0.3 (Makkonen, 1987; Makkonen, 2010).

The increment of the accreted ice thickness is described by Eq. (14), and the salinity of the newly formed layer of the ice accretion is:

$$S_{ac} = \frac{\sigma_{WL} \dfrac{db_{WL}}{dt} + \sigma_M \dfrac{db_M}{dt}}{\dfrac{db_{WL}}{dt} + \dfrac{db_M}{dt}} S_w \tag{20}$$

When the new location of the boundary between the water film and the accretion is determined, the heat transfer in the system is calculated to update the temperatures of the water film, ice accretion and cylinder. The temperature was updated with a time step of 0.05 s. This time step was chosen to obtain desired precision. The difference in the total mass and salinity was less than 1% and 2%, respectively, between the results calculated with time step 0.025 and 0.05 s in the case of Exp. 235, see Section 5. The two step calculation process was repeated again in each 0.05 s time step, i.e., the estimation of the new boundary

followed by solving the heat transfer equation. Both the temperature update and the update of the growth rate were done using smaller time step which was automatically defined by the ode15s solver implemented in MATLAB R2014a (MathWorks, 2014) to gain precision of less than 0.1%.

The two-step procedure was used to keep discretisation and computational costs low while achieving good precision. The ice accretion was split into at least 100 elements to solve the heat transfer equation (Eq. (9)) with higher discretisation close to the ice-water interface. When the ice was thicker than 2 mm, the 1 mm of the ice accretion nearest to the water-ice interface was split into another set of 100 elements to determine the location of the boundary between the ice and water. During 0.05 s, the temperature gradient did not penetrate into the ice for more than 1 mm. Thus, the temperature of the ice accretion at a distance of 1 mm from the boundary was held constant during the calculations of new location of boundary and was updated during the temperature update on the coarse mesh.

Using this two-step procedure, the high resolution of the heat transfer near the freezing interface was achieved. In addition, most of the ice grew in bursts with durations less than 20 times smaller than the spray period. Thus, calculations to define location of boundary were skipped after the burst until next spray event and it saved computational time.

To compare the one-dimensional model with experiment, it was necessary to make certain assumptions to approximate the motion of the water film, the heat transfer and the temperature of the incoming spray.

The velocity of the gravity-driven run-off, V_w, of a uniformly distributed water film with thickness η on a vertical wall can be written as (Horjen, 2013; Kulyakhtin and Tsarau, 2014; Myers and Charpin, 2004):

$$V_w = -\frac{\eta^2}{3\nu_w} g \tag{21}$$

where g is the gravitational constant and ν_w is the kinematic viscosity of the water film. Eq. (21) was applied to the cylinder. The amount of water escaping from the cylinder per unit time was assumed to be $V_w L_{cyl} \eta$. The total volume of water on the cylinder is $0.5\pi D_{cyl} \eta L_{cyl}$. The decrease of the thickness of the water film on the cylinder caused by run-off was:

$$\frac{d\eta}{dt} = -\frac{\eta^3 g}{1.5\nu_w \pi D_{cyl}} \tag{22}$$

The approximation of the water motion is discussed in details in Section 8.

The average heat transfer coefficient of the convective and evaporative heat fluxes from the windward side of the cylinder was (Lienhard, 2013):

$$h = \frac{Nuk_a}{D_{cyl}} \tag{23}$$

where k_a is the heat conductivity of air, and Nu is the Nusselt number:

$$Nu = 0.76\, Re^{0.5} \tag{24}$$

where Re is the Reynolds number. Choice of coefficient, such as 0.76 and 0.5, in Eq. (24) depends on the flow regime. In four experiment presented in this paper, Re was in the subcritical range, namely from $3.7 \cdot 10^4$ to $4.8 \cdot 10^4$. Eq. (24) with given coefficients is in a good agreement with numerous experiments available in literature for given range of Re, see Fig. 9. In addition, the difference between heat transfers from smooth and rough cylinders is negligible in this range of Reynolds numbers (Achenbach, 1977). The heat transfer to the air from the ice/water on the windward side of the cylinder primarily occurs through the laminar boundary layer, which acts as insulation and conceals any effects of the surface roughness. Achenbach (1977) has also stated that the heat transfer from the leeward side of a cylinder is approximately the same as that from the windward side for the considered range of Re. Therefore, we used $h_{lee} = h$ in Eq. (18).

The temperature of the droplets was approximated using the theory of spray jets by Abramovich (1963) and the equation of single droplet thermodynamics by Lozowski et al. (2000) (Kulyakhtin, 2014).

In the next section, the model presented here is compared with the experimental results and with the model referred to below as the non-conductive model. As noted in Section 2, the non-conductive ice-growth model is used in all existing marine icing models. The non-conductive model assumes no heat conductivity inside the ice accretion and that the ice growth is caused only by direct cooling from the air, i.e., using Eq. (19).

5. Comparison of numerical and experimental results

To validate the model described above, we chose four representative experiments with different spray periods and air temperatures from the experiments reported in Kulyakhtin (2013) (Table 1). The duration of spray event was 1.1 s in all experiments. It was difficult to obtain exact spray mass in each event due to noise (see Section 3). Therefore, the experimental measurements were compared with results of the model in three simulations with different spray inflow, namely 5, 10 and 20 g per spray event to test all possibilities.

In general, the mass of the ice accretion predicted by conductive model is in an agreement with experiments, which were performed with the long spray period, in contrast to the non-conductive model (Fig. 10 - Fig. 12). The non-conductive model underpredicts the ice accretion rate independently of the assumed spray inflow, except for Exp. 235. The conductive model with a spray inflow per event of 10 g is in a good agreement with Exp. 233 (Fig. 10) and with experiment Exp. 11, but during only the first 3 spray events (Fig. 11). The disagreement increases over time due to the reduced spray inflow to the cylinder caused by the

deflection of the wind direction γ (see Fig. 7Fig. 7) (for example, spray events 4 and 5) and as result the model with a 5 g spray inflow gives better result. The same happened in the Exp. 135 (Fig. 12).

In any way, the conductive model predicts well the initial growth of the ice compared with the non-conductive. All spray that arrived at the cylinder during the first spray event froze, and this observation agrees with the conductive model (Fig. 10 - Fig. 13). The cylinder was stored outside prior to each test, and the cylinder temperature was equal to T_a at the start of the test. The cylinder heat capacity is small and the cylinder temperature was gradually increased by the heat generated during freezing, see Eq. (18). In subsequent spray events, the run–off, which is predicted by the conductive model and experiment, increases until the run-off became approximately constant. At the time of constant run-off, the "cold" stored in the cylinder is exhausted. This run-off change over time was stronger in all tests with a short spray period (Kulyakhtin, 2013; Kulyakhtin et al., 2013a), as in Exp. 235 (Fig. 13).

For Exp. 235 in which the spray period is short, the non-conductive model predicts the total accretion mass similar to the measured mass when the spray flux is set to 20 g per spray event (Fig. 13). This result partially explains why the non-conductive model gave good agreement with previous experiments, which were done with a spray period of 20 s in both Alberta (Foy, 1988; Lozowski and Zakrewski, 1992) and Trondheim (Carstens et al., 1984; Horjen and Vefsnmo, 1986). However, our assumed spray inflow of 20 g per event is overestimation in Exp. 235. Fig. 13 shows that the spray inflow was very low and there was little spray arriving to the cylinder in the events from 15 to 20, The ice + water mass during these 5 sequential spray events increased only by 11 g and it is not due to increased run-off. Later the growth rate was higher and the only reasonable explanation for such measurements is reduced spray inflow. The non-conductive model with 20 g spray inflow underpredicts the ice accretion rate during the first 15 spray events and it "catches up" during event 15-20 the measured mass on the cylinder. That reduced spray inflow also explains why conductive model overpredicts the accretion rate.

In addition, the non-conductive model fails to predict the initial development of the ice accretion and underpredicts the salinity of the ice accretion (Table 2). The non-conductive model predicts ice salinity of 16-18 ‰, which corresponds to approximately 50% of the salinity of the sprayed water and is substantially smaller than the measured value (Fig. 15). By contrast, the conductive model with 10-g-spray fluxes predicted ice salinity which agrees well with all experiments (Table 2).

The underprediction of the ice salinity by the non-conductive model is more significant for the experiments with longer spray periods (Fig. 10 - Fig. 12, Table 2). The reason for the discrepancy is that between spray events, the ice accretion cools and this "cold" is then released to freeze new ice when a new spray event arrives (see Fig. 4(4)). The non-conductive model cannot predict such behaviours. Note also that cooling is transferred to the ice accretion, and therefore, the water temperature decreases slowly (

Fig. 14). The high temperature of the water film keep the convective and evaporative heat transfers from the water film to the air at the high level, as it is proportional to the difference in the temperatures, see Eqs. (2) and (3). This allows conductive ice accretion to store more "cold". However, it is difficult to observe such effects when the spray period is not sufficiently long, as partially in Exp. 235.

The non-conductive model cannot explain the high salinities measured in the experiment because σ_M is smaller than σ_{WL}. σ_M was set to constant in this paper; however, it increases with the supercooling of the spray. σ_M is 0.44 when the spray temperature is 10 °C below the freezing temperature (Makkonen, 2010). However, this is not sufficient to explain the measurements, and the maximal supercooling was less than 6.5 °C in the considered experiments.

Note that the mass of water that freezes after a spray event in the case of the non-conductive model is nearly independent of the spray inflow because it is limited by the heat fluxes which define the freezing rate. In the case of the conductive model, the effect of the spray flux is stronger. The ice accretion accumulates "cold" between spray events and therefore can freeze more spray. In general, the conductive model predicts approximately 2 times more ice accretion then the non-conductive model for Exp. 235. The measured mass for the cases of 76-, 79- and 147.8-s periods, exhibited stepwise increases, which, in most cases, were not followed by any water run-off because of the accumulated "cold" in the ice accretion (Fig. 10 - Fig. 12).

It is important to note that the structure of the ice surface was dependent on the spray period (Fig. 16). The ice accreted on the cylinder because of the 147.8-s-period spray was very smooth and uniform, while there were some nonuniformities in the case of the 79-s-period spray. When the spray period was 31.9 s, the ice was very rough, and it was broken by the incoming spray at the wind-stagnation line exposing bare cylinder surface. The ice was also thicker at the bottom of the cylinder. The impact of the droplets broke a thin layer of newly formed ice into small pieces, which subsequently detached and slid to the bottom of the cylinder. When the spray period was 76 – 147.8 s, the ice had sufficient time between spray events to freeze the salt water entrapped inside and to become stronger. As a result, the ice accretion was smooth and uniformly distributed on the cylinder.

As demonstrated above, the non-conductive model used in existing marine icing models substantially underpredicts the ice accretion rate. Even once the heat capacity of the cylinder is exhausted, the growth rate predicted by the conductive model is higher than the growth rate predicted by the non-conductive model (Fig. 13 - Fig. 12), i.e., the assumption that thick ice diminishes the heat flux from the structure is true, but the heat capacity of the ice nevertheless has a significant effect on the icing growth rate.

6. Growth rate and parameterisation of salt entrapment

As mentioned above, in the model, the coefficient δD_{sw}^{-1} in Eq. (8) was set to 36.2 s mm^{-1}, which is 20 times lower than the value presented by Weeks (2010). δD_{sw}^{-1} = 724.3 s mm^{-1} provided a good fit to the measured

salt entrapment for a steady growth rate in the range of $2.0 \cdot 10^{-4}$ mm s^{-1} to $2.8 \cdot 10^{-3}$ mm s^{-1}. This range of rates is similar to the average accretion rates in the presented icing experiments ($2 \cdot 10^{-3}$ - $5 \cdot 10^{-3}$ mm s^{-1}). However, according to our observations and calculations, the icing process was highly unsteady. After the arrival of a spray, there was a burst of the rapid growth (Fig. 17), and the magnitude of this growth was higher for longer spray periods. 63, 61, 74, and 84% of ice in Exps. 235, 233, 11, and 135, respectively, accretes during spray event and the rest accretes afterwards according to prediction of the conductive model (Fig. 18). Also, the main portion of ice grew due to the heat transfer into the ice accretion (Fig. 18). Then, the growth rate decreased because the cooling was spent to decrease the temperatures of the ice accretion and water to the new freezing temperature of the water film (

Fig. 14). Thus, 90 % of the ice formed during a time interval of less than 8 s after each spray event (see vertical line in Fig. 18). The instant growth rates were 3-100 times higher than the maximum rate in the experiments presented by Weeks (2010).

In addition, Weeks (2010) investigated the ice growth in a "semi-infinite" water solution. In our experiments, the thickness of the water film was small (up to 0.4 mm) and comparable to the thickness of the diffusion-limited boundary layer, δ, which is equal to 0.5 mm (Weeks and Lofgren, 1967). Thus, the rapid change in the growth rate and water salinity justifies the choice of a different value of δD_{sw}^{-1}.

The two-step calculation of the ice accretion process (see Section 4) may potentially affect the calculated growth rate. However, the growth rate was found independent of the time step used in the model; the predictions for the conditions of Exp. 235 calculated using 0.05 s and 0.025 s time steps are compared in Fig. 17. Other tested values are summarised in Table 3 and shows that the ice accretion rate and the salinity in particular are strongly sensitive to the δD_{sw}^{-1} value. We found that the same value of 36.2 s mm^{-1} yielded a good fit for all four experiments.

However, it is desirable to improve precision of the obtained δD_{sw}^{-1} value and validate against a greater number of experiments because of the substantial variation in spray flux in the experiments presented here. There have been 44 and 275 other experiments conducted in Spitsbergen under different weather conditions, which are presented in Kulyakhtin et al. (2013a) and Kulyakhtin (2013), respectively. The model presented here is computationally expensive and therefore, it was validated against only four of these experiments. It is also desirable to validate the model against the wind-tunnel experiments with a long spray period, i.e., longer than 30 s; in this case it is also recommended to perform the experiments using heavier cylinders because the effect of the heat conduction in the ice will be easier to observe, as explained in the next section.

7. Effect of the heat flux from the structure

The heat flux from the vessels or offshore rigs to the ice accretion is difficult to evaluate. Even though the metal structures with thick walls have nearly infinite heat capacity and one may consider it as having

constant temperature, the exact temperature is uncertain. The lower part of the structure is warmed by the sea and some walls of the human-occupied structures are heated, and therefore, temperature of the structure cannot be always considered to be equal to the air temperature. The heat flux from a structure that is conducted by ice to the ice-water interface is the dominant cause of freezing when the thickness of fresh ice is less than 2.4 cm (Myers and Charpin, 2004). Icing events on rigs typically produce ice with a maximal thickness of less than 10 cm (Brown and Mitten, 1988). Thus, the heat flux from the structure is likely negligible only for a maximum of 75 % of the icing event. To estimate the exact ice thickness that isolates the heat flux from the structure and to estimate the error induced by neglecting this effect in the case of marine icing, we have performed additional simulations. The cylinder mass was set to 534 kg instead of 534 g to increase the total heat capacity, the spray inflow was set to 20 g, and the remaining conditions were as in Exp. 235 and 11. In the case of spray with a period of 31.9 s, once the ice thickness reached values of approximately 1.9 cm and 1.2 cm on the 534-kg and 534-g cylinders, respectively, the ice accretion rate was the same within 5 % on the both cylinders. The ice thicknesses were 1.5 cm and 1.1 cm, respectively, in the case of a 76-s-period spray. These thicknesses are comparable to the 2.4-cm thickness estimated by Myers and Charpin (2004). Our calculations indicate that an incorrect estimation of the heat flux from the real structure can result in a relatively small error in the thickness of approximately 0.5 cm at least for the considered spray flux.

8. Model sensitivity, uncertainties and validity of certain assumptions

The icing prediction requires modelling of the heat transfer at the air-water surface, spray temperature, motion of the water film, and heat conduction in the accreted ice. The model used certain assumptions and the experiments presented here contain significant uncertainties, which we discuss in this section.

The air temperature and humidity were rather stable during the experiments, and can therefore be defined precisely (Fig. 7Fig. 7). By contrast, the wind exhibited strong fluctuations, with a standard deviation of up to 20%. The heat transfer in Eq. (24) is proportional to the square root of the wind velocity, and therefore, the wind could produce an error of up to 10%.

The spray temperature, which was calculated approximately (Kulyakhtin, 2014), may have a significant effect on the ice accretion rate. For example, the ice accretion rate presented in Fig. 11, Exp. 11, was calculated for a spray temperature of -3.9 °C, see Section 4. Even though the air temperature is -5 °C, the spray temperature can be as low as –6.1°C due to evaporation. This temperature is possible for low-density spray consisting of small droplets which are unlikely for given settings of the spray nozzle. However, to investigate the effect of the spray temperature, it is logical to use the combination which will give the maximum effect among modelled conditions: the minimal temperature (– 6.1°C), the maximal possible spray inflow (20 g per event) and the non-conductive model (in the case of conductive model, the contribution of the spray temperature relative to the heat flux from the air is lower than for the non-conductive model). The calculated mass of the accreted ice for these settings was higher by less than 23% and salinity lower by 0.4‰

compared to the results obtained with a spray temperature of –3.9 °C. The increment in the accretion mass per spray event increased from 3.33 g to 4.06 g. Therefore, the error in the spray temperature could not qualitatively change the conclusion.

In Eq. (22), the motion of water film is caused by gravity. In reality, the motion of water film is also affected by wind stresses, non-uniformities of the ice-accretion surface (see Fig. 16), surface tension, and changes in the water film viscosity caused by changes in salinity and temperature. All these factors contribute to uncertainties of calculations. To investigate the effect of the uncertainty in the water film motion calculation, we increased the viscosity of the water film in Eq. (21) by a factor of 10. Since the increased viscosity can reflect also the surface roughness and surface tension which slows down the water film motion. The model result for Exp. 11 was that the water film thickness on the ice accretion, immediately prior to the next spray event increased from 20 to 61 μm and from 10 to 33 μm in the cases of the conductive and non-conductive models, respectively. The maximal ice salinity of the water film decreased from 64 to 57‰ and from 112 to 88‰ in the cases of the conductive and non-conductive models, respectively.

A factor of 10 in viscosity is a significant change; however, the ice accretion rate predicted by the conductive model increased by only 6% for Exp. 11. The effect is small because the ice grows during short events followed by the limited growth rate during which the air cooling is spent to cool the ice accretion (see Section 6). This result is extremely convenient, as it shows that it is appropriate to avoid modelling the details of the water film motion, which are uncertain and complicated. The water motion is an effect of the secondary importance compared to the heat capacity of the accreted ice.

By contrast, the effect of increased viscosity on the non-conductive model was significant (Fig. 19). There is no heat flux to the accreted ice and the amount of energy required to cool only the water film is small, therefore, the ice growth is a continuous process and is limited by the water film salinity. The ice accretion predicted by the non-conductive model increased by 70%, and indeed, the predicted accretion rate showed good agreement with experiment. However, the ice salinity predicted by the tuned model was still only 15.3‰ and is lower than the measured value of 24.1‰. This example clearly shows that it is possible to tune the non-conductive model to fit certain experimental results, even without capturing exact underlying physical processes.

The heat conduction in the accreted ice was calculated using Eq. (10) which assumes that the ice accretion is a continuous ice medium containing cylinders of brine oriented along the direction of ice growth (Schwerdtfeger, 1963). However, the structure of the ice formed through icing is better described as a collection of small, randomly-oriented ice grains, approximately 100 – 500 μm or less in diameter, and brine pockets (Kulyakhtin et al., 2013b; Ryerson and Gow, 2000). The lowest possible heat conduction and maximally diverge from Eq. (10) is if the saline water surrounds the ice grains in the accreted ice. The heat conductivity of this bubbled ice structure is described by the following equation:

$$k_{ac}\left(T_{ac},S_{ac}\right)=\frac{2k_w+k_i-2\left(1-v_{wac}\right)\left(k_w-k_i\right)}{2k_w+k_i+\left(1-v_{wac}\right)\left(k_w-k_i\right)}k_w \tag{25}$$

which was adapted to our case from the work of Schwerdtfeger (1963), where it was used to describe the effect of air bubbles entrapped in the ice. Eq. (25) predicts 5 to 25% lower heat conduction than Eq. (10), and the maximal difference occurs at temperatures of 0 – 2 °C below the freezing temperature.

In our experiments, the temperatures were near the freezing point, and therefore, the effect of the heat conductivity was close to maximal, the difference in the ice accretion predicted using Eq. (10) and Eq. (25) was negligible; below 3% in all modelled experiments. The primary difference was apparent during the burst growth of the ice during the arrival of spray. Thus, even computationally-cheaper model of the accretion heat conductivity can give good approximation.

In addition, the conductivity of the ice accretion can be decreased by trapped air. Ryerson and Gow (2000) have reported that the volume of the air trapped in ice accreted on a vessel is typically in the range of 5 to 25 %. However, in our experiments, the air entrapment was in the range of 0.5-4.5 % and was measured with 1.3 % accuracy (Kulyakhtin et al., 2013b). This low air entrapment causes a decrease of heat conductivity of less than 7 %; see Schwerdtfeger (1963) for details.

The effect of the conductivity is weak because the heat capacity of the saline ice accretion is the major phenomena. As explained above, after the burst growth of the ice, immediately following the spray arrival, the cooling from the air acts to cool the ice accretion. The rate of the heat transfer from the air, which is significantly slower than ice or water conduction, is the primary factor that limits the accretion rate.

Thus, none of the considered effects did change the main result of the paper; that the heat capacity of the accreted ice is important and that the non-conductive model describes icing caused by periodic, saline spray incorrectly.

9. Discussion

The heat conduction through the ice is not considered in the existing models of marine icing. However, marine icing is a periodic process, and we have shown that the heat conduction through the ice is an important process that causes the cooling provided by the air to be stored in the accreted ice and then released to produce new ice during a subsequent spray event. The heat transfer to the ice accretion also changes the ice growth regime from the supercooled described by Makkonen (2010) to constitutionally supercooled described by Weeks (2010). Those two regimes differ by the amount of salt entrapped in the ice during growth, which is higher in the case of constitutional supercooling. Specifically the salinity of the accreted ice measured in experiments showed that the non-conductive model does not describe the correct physical mechanism. Higher salt entrapment in the ice accretion leads to higher heat capacity. All that result in a higher accretion growth rate than those predicted by existing icing models.

In addition to increasing the heat capacity, the ice salinity has an important effect on subsequent ice melting. Ice accretion formed at a certain air temperature will melt or at least expel salt, with even a small increase in the air temperature (Cox and Weeks, 1986).

The effect of the heat conduction of the ice on the ice accretion rate was not previously observed because previous experiments with periodic sea spray were done with a shorter spray period of 20 s (Carstens et al., 1984; Foy, 1988; Horjen and Vefsnmo, 1986; Lozowski and Zakrewski, 1992). The effect of the heat capacity of the ice was likely obscured by a massive spray influx (see Exp. 235), the low heat capacity of the cylinders used, or the uncertainties in the measured spray flux and temperature; see Section 8. The effect of the heat capacity was easily observed in experiments for which the spray period was longer than 76 s. In previous experiments, the spray period was determined based on empirical observations. In real conditions, the wave period is typically 5 – 20 s, and splashes occur with every second wave (Horjen, 1990). However, in the case of vessels, the spray period depends on the resonance between the vessel and the waves, and therefore, it may be longer as in the experiments presented in this paper. In addition, the areas of human activities on the offshore rigs are high above the sea level and not every spray event can reach those elevations.

It is also worth mentioning that the conditions used in the experiments presented here were established with the intent to mimic the conditions of a full-scale structure, not small component of the structure. Our experimental setup provided the cooling rates and spray fluxes similar to the conditions encountered by the superstructure of a vessel. First, Ryerson (1995) has measured the spray flux in the range from 0.522 to 18 620 g m^{-2} per event onboard a vessel. The spray flux varied approximately from 1 to 10 000 g $m^{-2}s^{-1}$. In our experiments, the mean spray flux was 300 g m^{-2} s^{-1} (which is within the range of values measured by Ryerson). Second, the heat transfer coefficient for the sides and exposed parts of a vessel is on the order of 30 W $m^{-2}K^{-1}$ (Kulyakhtin and Tsarau, 2014). In our experiments, the wind speed was lower than those in real offshore conditions, but the heat transfer coefficient was approximately 40 W $m^{-2}K^{-1}$ because the heat transfer coefficient decreases with increasing structure size (Kulyakhtin and Tsarau, 2014; Lienhard, 2013).

Another reason why the change in the growth rate over time was not previously observed is that only final ice accretion mass was recorded, which obscured the effect of the cylinder heat capacity. In the presented experiments, we applied a high accuracy system that measured the mass of the ice accretion in real-time. A similar system can be used in the field for similar measurements, thereby, decreasing the number of routine measurements of the ice accretion. The use of such system also provides possibility of simultaneously measuring the spray inflow, accretion mass and water run-off, which would give very valuable data for model validation.

10. Conclusions

The motivation for this study was to obtain a deeper understanding of the icing caused by periodic saline spray. Existing marine icing models, e.g., ICEMOD (Horjen, 1990; Horjen, 2013), RIGICE04 (Forest et al., 2005) and MARICE (Kulyakhtin and Tsarau, 2014), neglect heat conductivity and heat capacity of the accreted ice. These assumptions are reasonable for fresh-water icing or icing created by continuous spray, but they are not valid for ice accretion caused by periodic sea spray. The amount of "cold" stored between spray events is substantial because the heat capacity of a saline ice accretion is substantially higher than that of fresh ice. This "cold" is released during the subsequent spray event after an interval without a spray and is spent to freeze coming water. This phenomenon was studied experimentally and was explained using the presented numerical model.

A model that neglects the heat conduction of an ice accretion – the non-conductive model – cannot explain the high salinities that were measured in the experiments. In addition, the non-conductive model underestimates the ice accretion rate by more than 50%.

We developed and presented a model, which accounts for the heat capacity and conductivity of the ice accretion, and which was in a good agreement with the measurements. The ice salinity and the ice growth rate predicted by the conductive model were in the best agreement with the experimental results when the coefficient δD_{sw}^{-1} was set to 36.2 s mm^{-1}. This value was determined approximately and may require additional study, as it has a substantial effect on the predicted amount of ice accretion and its salinity. The sensitivity study of the conductive model gave the following conclusions:

- The major portion of the ice grew in bursts of 1.5 s in duration, which is similar to the spray duration (1.1 s), and later, the air cooling only decreases the temperature of the accreted ice, and therefore, did not cause substantial ice growth.
- The heat released during water film freezing is rapidly absorbed by the accreted ice. The amount of absorbed heat is defined by the heat flux to the air between spray events and by the heat capacity of the accreted ice. Thus, the exact method of modelling the heat conductivity of the accreted ice is not important.
- Precise modelling of the water film motion is not required also, as the ice growth is mainly determined by the heat fluxes.
- The heat flux from the surface on which the ice accretes affects the ice accretion when the ice thickness is less than approximately 2 cm. Neglecting this heat flux results in an error in the ice thickness of approximately 0.5 cm.

We hope that the ideas presented in this paper will be implemented in future icing models. The model presented in this paper is computationally expensive because it requires the spatial discretisation of the ice accretion. Computational costs may restrict model implementations for solving engineering problems. One

possible method of reducing the computational cost may be to approximate the temperature profile in the ice accretion with a polynomial fit, as described by Myers et al. (2007).

Acknowledgements

The work presented in this paper is part of MARICE, which is a joint industry project between Det Norske Veritas, Statoil, the Norwegian University of Science and Technology and the Research Council of Norway, which studies marine icing on offshore structures and vessels. The authors thank M-Tech, Morten Scharffscher and Petter Scharffscher for building the experimental rig. The authors are grateful to the technical and logistical department of University Centre in Svalbard (UNIS), namely Martin Indreiten, Kåre Johansen, Stefan Claes, and Monica Votvik. The authors also thank Anna Pustogvar, Alexey Prusakov, Jurii Dobrynets, Nikita Onishchenko and Petr Likutov for participating in the experiments, Prof. Alex Klein-Paste and Per Asbjørn Østensen for their advices regarding the development of the electronics components of the experiment, and Dr. Lasse Makkonen for his valuable comments.

References

Abramovich, G.N., 1963. The Theory of Turbulent Jets. MIT Press, Cambridge, MA.

Achenbach, E., 1975. Total and local heat transfer from a smooth circular cylinder in cross-flow at high Reynolds number. International Journal of Heat and Mass Transfer, 18(12): 1387-1396.

Achenbach, E., 1977. The effect of surface roughness on the heat transfer from a circular cylinder to the cross flow of air. International Journal of Heat and Mass Transfer, 20(4): 359-369.

Blackmore, R., Makkonen, L. and Lozowski, E., 2002. A new model of spongy icing from first principles. Journal of Geophysical Research: Atmospheres (1984–2012), 107(D21): AAC 9-1-AAC 9-15.

Brown, R.D. and Mitten, P., 1988. Ice Accretion on Drilling Platforms Off the East Coast of Canada. In: A.H.a.J.F. Storm (Editor), International Conference on Technology for Polar Areas. Trondheim, Norway, Tapir Publishers, Trondheim, Norway, pp. 409–421.

Brown, R.D., Mitten, P.T., Makkonen, L., E.P., L., Zakrzewski, W.P. and Waszkiewicz, M., 1990. Modelling and measurement of spray ice accretion on offshore structures, the 5th International Workshop on Atmospheric Icing of Structures, Tokyo, pp. 1-6.

Carstens, T., Jørgensen, T.S., Karterud, T. and Skaret, O., 1984. The VHL sea spray icing tunnel, The 2nd International Workshop on Atmospheric icing of Structures, Trondheim, Norway.

Cox, G. and Weeks, W., 1986. Changes in the salinity and porosity of sea-ice samples during shipping and storage. Journal of Glaciology, 32(112): 371-375.

Ekeberg, O.-C., 2010. State-of-the-art: on marine icing models and observations, Det Norske Veritas.

Forest, T., Lozowski, E. and Gagnon, R., 2005. Estimating marine icing on offshore structures using RIGICE04, International Workshop on Atmospheric Icing on Structures (IWAIS), Monreal.

Foy, C.E., 1988. The design, instrumentation, and performance of a refrigerated marine icing wind tunnel., University of Alberta, Alberta, Canada.

Horjen, I., 1990. Numerical modeling of time-dependent marine icing, anti-icing and deicing, Norwegian University of Science and Technology, Trondheim, Norway, 175 pp.

Horjen, I., 2013. Numerical modeling of two-dimensional sea spray icing on vessel-mounted cylinders. Cold Regions Science and Technology, 93(0): 20-35.

Horjen, I. and Vefsnmo, S., 1986. Calibration of ICEMOD – extension to a time dependent model, SINTEF.

Jones, K.F., 1996. Ice accretion in freezing rain. 96-2, U.S. Army Cold Regions Research and Engineering Laboratory, Hanover, NH.

Kulyakhtin, A., 2013. Field experiment 2012-2013: sensitivity of icing on spray period and weather conditions. 2013-1778, Det Norske Veritas.

Kulyakhtin, A., 2014. Numerical modelling and experiments on sea spray icing, Norwegian University of Science and Technology, Tapir.

Kulyakhtin, A., Kulyakhtin, S. and Løset, S., 2013a. Marine Icing Field Experiment 2012. 2013-1776, Det Norske Veritas.

Kulyakhtin, A., Kulyakhtin, S. and Løset, S., 2013b. Measurements of Thermodynamic Properties of Ice Created by Frozen Sea Spray, The Twenty-third International Offshore and Polar Engineering Conference. International Society of Offshore and Polar Engineers.

Kulyakhtin, A. and Tsarau, A., 2014. A time-dependent model of marine icing with application of computational fluid dynamics. Cold regions science and technology, 104-105: 33-44.

Lienhard, J.H., 2013. A heat transfer textbook. Courier Dover Publications.

Lozowski, E.P., Szilder, K. and Makkonen, L., 2000. Computer simulation of marine ice accretion. Philosophical Transactions of the Royal Society of London, Series A, 358(1776): 2811-2845.
Lozowski, E.P. and Zakrewski, W.P., 1992. Marine icing laboratory and numerical experiments, Compusult Ltd.
Makkonen, L., 1987. Salinity and growth rate of ice formed by sea spray. Cold Regions Science and Technology, 14(2): 163-171.
Makkonen, L., 2010. Solid fraction in dendritic solidification of a liquid. Applied Physics Letters, 96(9): 091910.
MathWorks, 2014. http://www.mathworks.se/help/matlab/.
Myers, T.G. and Charpin, J.P., 2004. A mathematical model for atmospheric ice accretion and water flow on a cold surface. International Journal of Heat and Mass Transfer, 47(25): 5483-5500.
Myers, T.G., Mitchell, S.L., Muchatibaya, G. and Myers, M.Y., 2007. A cubic heat balance integral method for one-dimensional melting of a finite thickness layer. International Journal of Heat and Mass Transfer, 50(25–26): 5305-5317.
Nakamura, H. and Igarashi, T., 2004. Unsteady heat transfer from a circular cylinder for Reynolds numbers from 3000 to 15,000. International Journal of Heat and Fluid Flow, 25(5): 741-748.
Ryerson, C., 1995. Superstructure spray and ice accretion on a large US Coast Guard cutter. Atmospheric research, 36(3): 321-337.
Ryerson, C.C. and Gow, A.J., 2000. Ship superstructure icing: crystalline and physical properties. ERDC/CRREL TR-00-11, U.S. Army Cold Regions Research and Engineering Laboratory, Hanover, NH.
Scholten, J.W. and Murray, D.B., 1998a. Unsteady heat transfer and velocity of a cylinder in cross flow—I. Low freestream turbulence. International Journal of Heat and Mass Transfer, 41(10): 1139-1148.
Scholten, J.W. and Murray, D.B., 1998b. Unsteady heat transfer and velocity of a cylinder in cross flow—II. High freestream turbulence. International Journal of Heat and Mass Transfer, 41(10): 1149-1156.
Schwerdtfeger, P., 1963. The thermal properties of sea ice. Journal of Glaciology, 4(36): 789-807.
Smedsrud, L., Saloranta, T., Haugan, P. and Kangas, T., 2003. Sea ice formation on a very cold surface. Geophysical research letters, 30(6).
Szilder, K., Lozowski, E.P. and Gates, E., 1987. Modelling ice accretion on non-rotating cylinders—the incorporation of time dependence and internal heat conduction. Cold Regions Science and Technology, 13(2): 177-191.
Weeks, W., 2010. On sea ice. University of Alaska Press, Fairbanks, AK, 664 pp.
Weeks, W. and Lofgren, G., 1967. The effective solute distribution coefficient during the freezing of NaCl solutions. In: H. Oura (Editor), Physics of Snow and Ice. Institute of Low Temperature Science, Hokkaido University, Sapporo, Japan, pp. 579-597.

Table 1. Experimental conditions and average weather parameters used in the computations.

Exp. number	Spray period [s]	Air temperature [°C]	Humidity [%]	Average wind speed [m s^{-1}]	App. spray temperature [°C]
235	31.9	-7.8	75	6.0	-5.6
233	79.0	-8.4	74	4.8	-6.0
11	76.0	-5.0	76	5.5	-3.9
135	147.8	-8.4	67	6.2	-6.1

Table 2. Measured and calculated ice salinity [‰]

	Exp. 235	Exp. 233	Exp. 11	Exp. 135
Measured:	22.9±0.5[a]	28.5±1.0[a]	24.1	29.9
Calculations:				
No conduction, 20 g	16.0	16.8	15.2	17.0
No conduction, 10 g	17.9	18.7	16.2	18.9
20 g	18.45	25.3	20.8	28.3
10 g	22.6	31.4	24.6	32.96
5 g	33.3	33.36	32.9	33.4

[a] Two samples were taken from the cylinder in this case. The results indicated that the uncertainty of the measurments is approximately ±1 ‰.

Table 3. Effect of the value of δD_{sw}^{-1} on the calculated growth rate and salinity of the ice accretion. For brevity, only the ratio of the period-averaged ice growth rate over the coefficient is presented. The average ice growth rate per period becomes constant after the first few spray events because the heat stored in the cylinder is spent in the few first spray events and does not contribute in subsequent events.

δD_{sw}^{-1}	Ratio of accretion rates	Salinity of ice [‰].
1, 724.3 s mm^{-1} (Weeks, 2010)	1.37	31.0
1/10,	1.21	27.8
1/20, 36.2 s mm^{-1}	1	22.6
(Fitted experiments in this paper)		
1/50	0.87	17.3
1/100	0.83	15.8

Figures

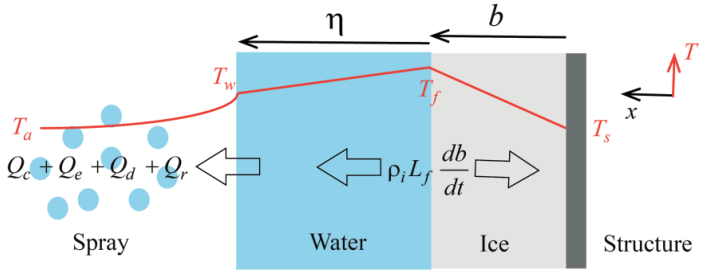

Fig. 1. The initial growth of fresh-water ice.

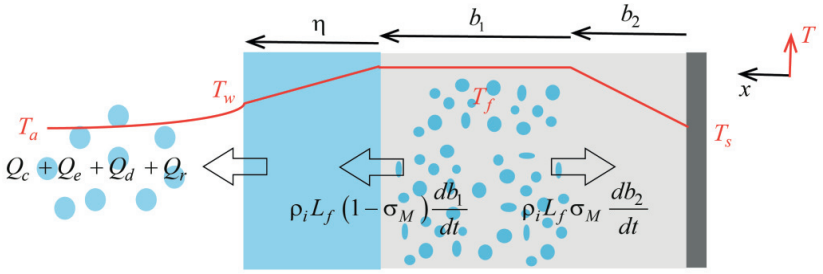

Fig. 2. The growth of fresh-water ice, when the heat conduction through the ice is lower than the heat fluxes from the water film. b_1 is the thickness of the ice portion of the ice that contains unfrozen water, and b_2 is the thickness of the solid ice.

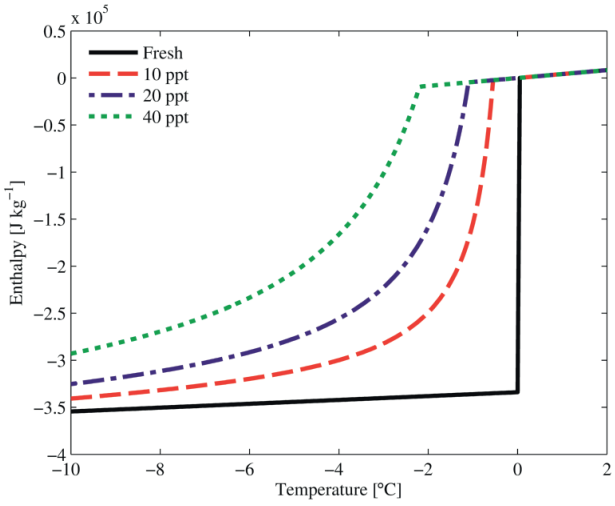

Fig. 3. Enthalpy of fresh and saline water/ice.

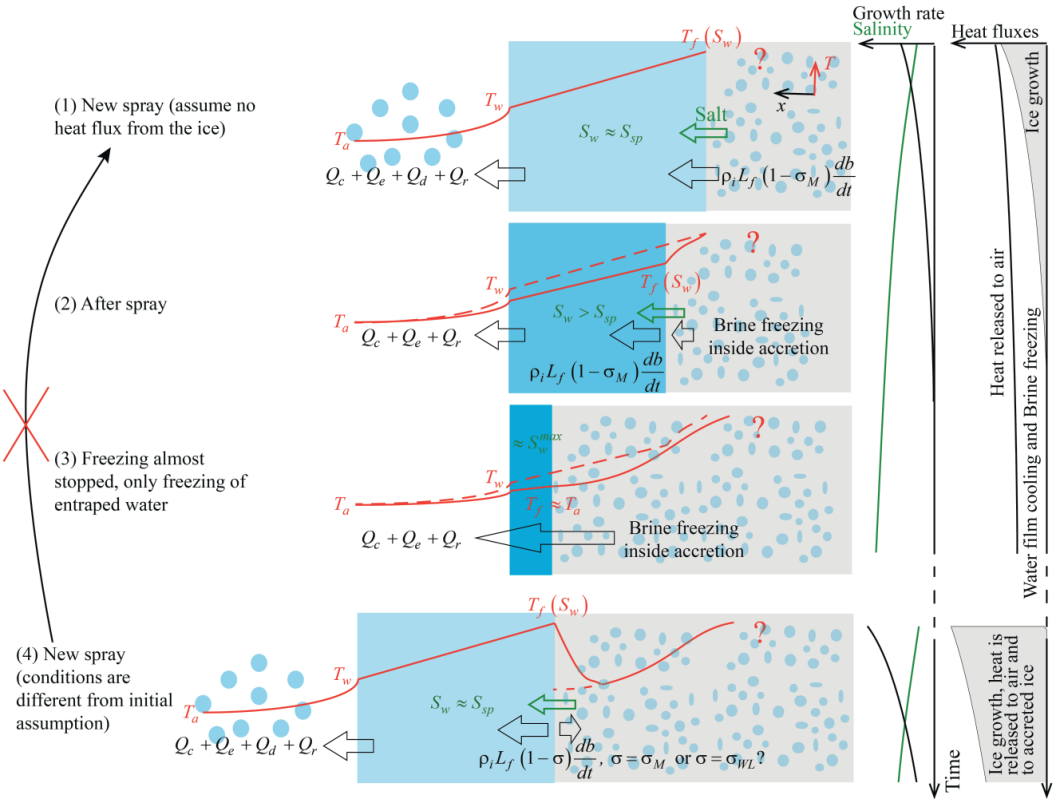

Fig. 4. Scheme of the ice growth caused by periodic sea spray. The black arrows represent the directions of the heat fluxes. The solid red line represents the temperature profile in the water and ice accretion. The dashed red line represents the temperature profile in the previous step.

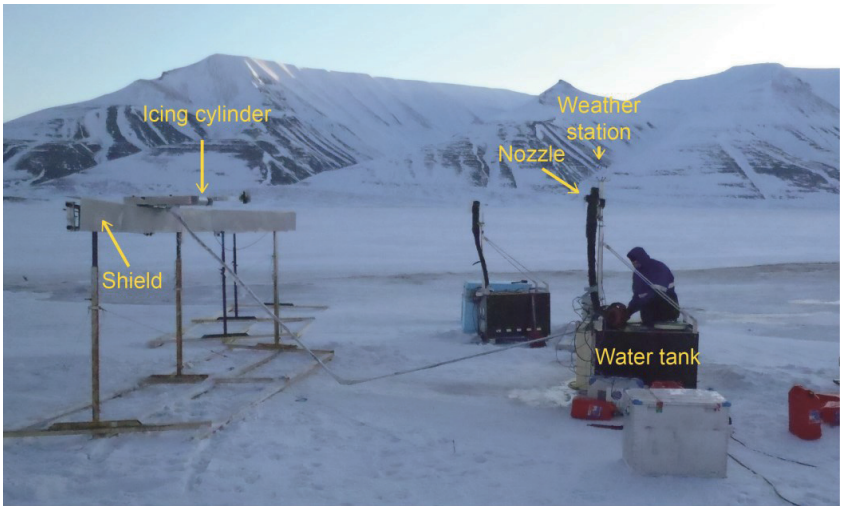

Fig. 5. The experimental setup in Spitsbergen.

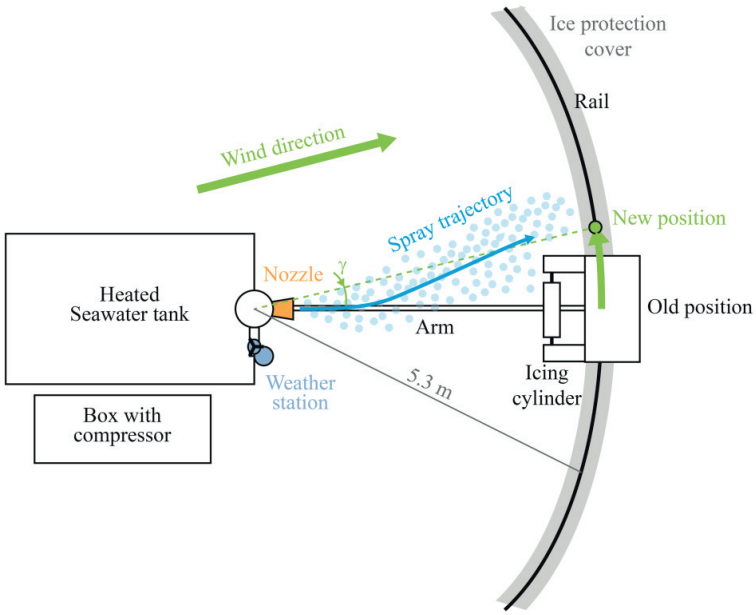

Fig. 6. Scheme of the experimental setup and the control of the position of the icing object (elevated view).

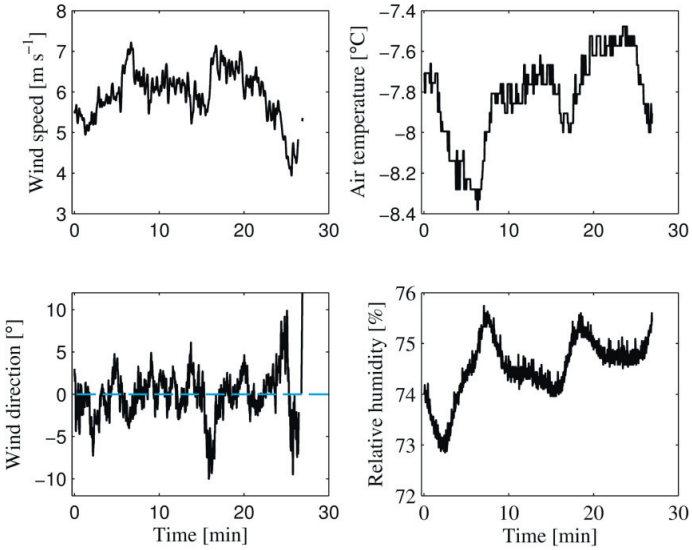

Fig. 7. Weather conditions during Exp. 235. The record of wind speed and direction (relative to the nozzle orientation, γ in Fig. 6) were filtered using Savitzky-Golay filter with the frame size of 10 s and the polynomial function of the 1st and then with the 3rd degree polynomial function sequentially to show long-term changes of the wind.

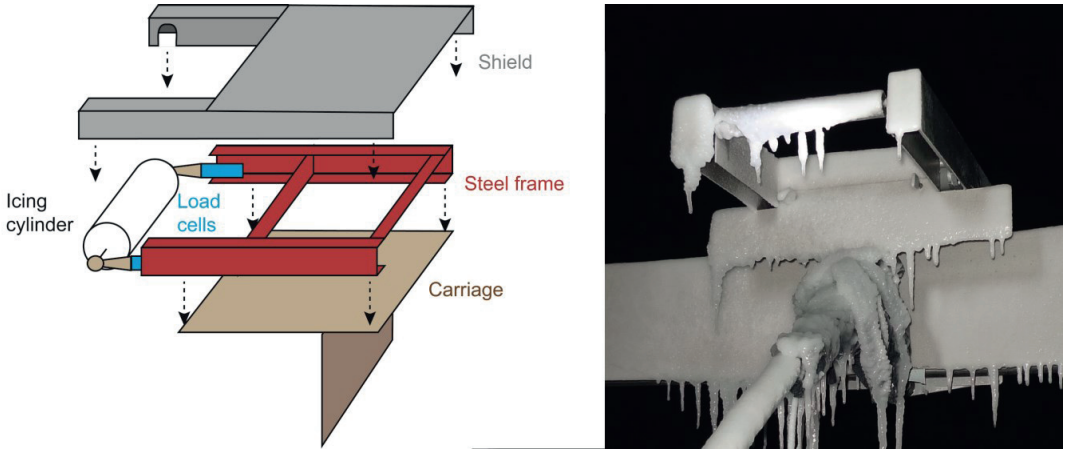

Fig. 8. Sketch of the setup for real-time mass measurements – (left); photo of the ice accretion on a 40-mm-diameter cylinder and system after a test on the 14th of February 2012 – (right).

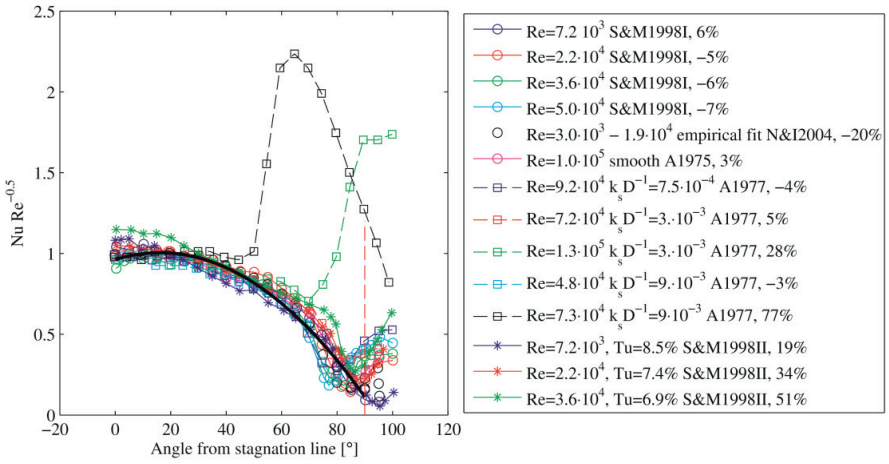

Fig. 9. Collection of experimentally measured heat transfer coefficients over the windward side of the cylinders and the fitting curve. S&M1998I (Scholten and Murray, 1998a); S&M1998II, Tu is turbulence intensity (Scholten and Murray, 1998b); N&I2004 (Nakamura and Igarashi, 2004); A1975 (Achenbach, 1975); A1977, here $k_s D^{-1}$ is the roughness parameter (Achenbach, 1977). A black bold curve is a fitting curve, $Nu(\alpha)\,Re^{-0.5} = -1.64 \cdot 10^{-4}\,\alpha^2 + 5.3 \cdot 10^{-3}\,\alpha + 0.962$, which gives the best match over all experiments. After comma, a relative difference between the mean heat transfer coefficients calculated over angles (α) of 0-90° mean and fitted ($0.76\,Re^{-0.5}$).

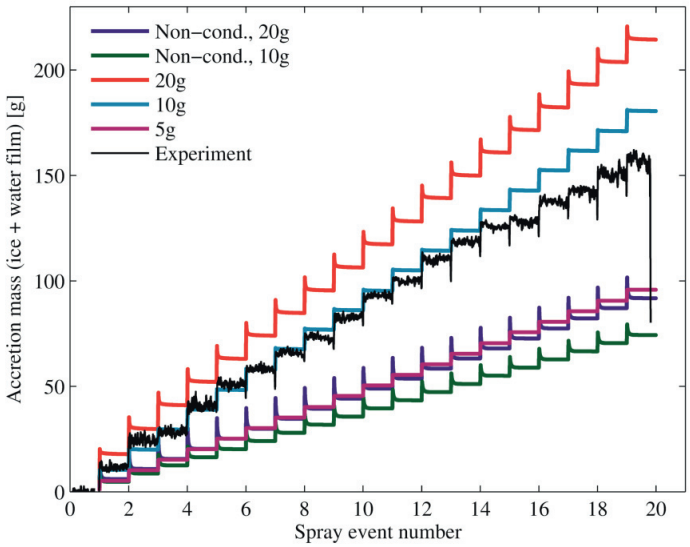

Fig. 10. The ice accretion on the cylinder caused by spray with a period of 79.0 s, Exp. 233.

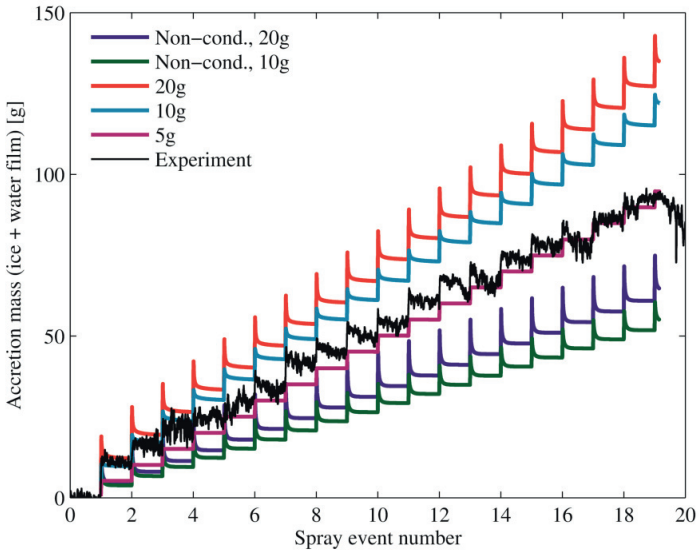

Fig. 11 The ice accretion on the cylinder caused by spray with a period of 76.0 s, Exp. 11.

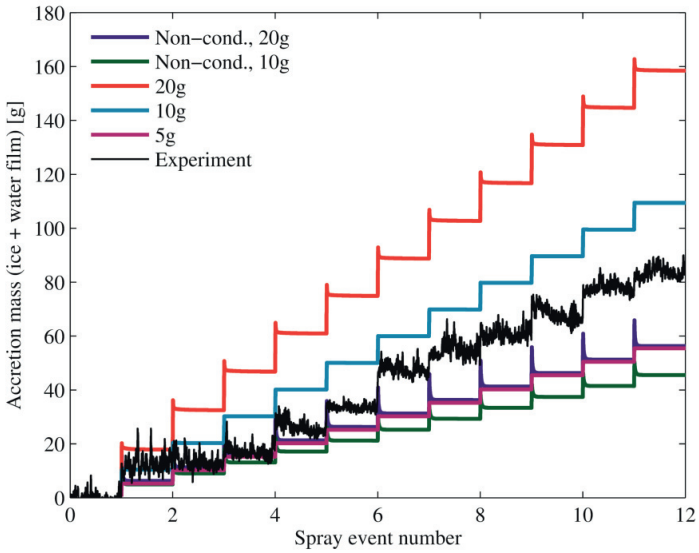

Fig. 12. The ice accretion on the cylinder caused by spray with a period of 147.8 s, Exp. 135. At the second spray event, water did not reach the cylinder.

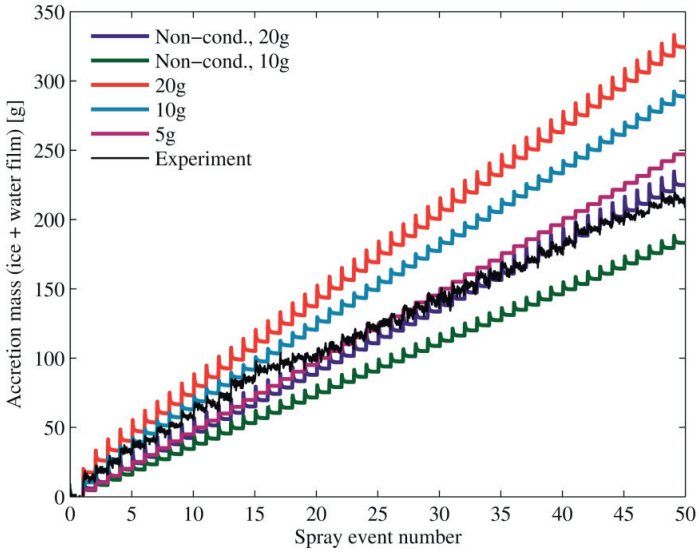

Fig. 13. The ice accretion on the cylinder caused by spray with a period of 31.9 s and different spray influxes per event, Exp. 235.

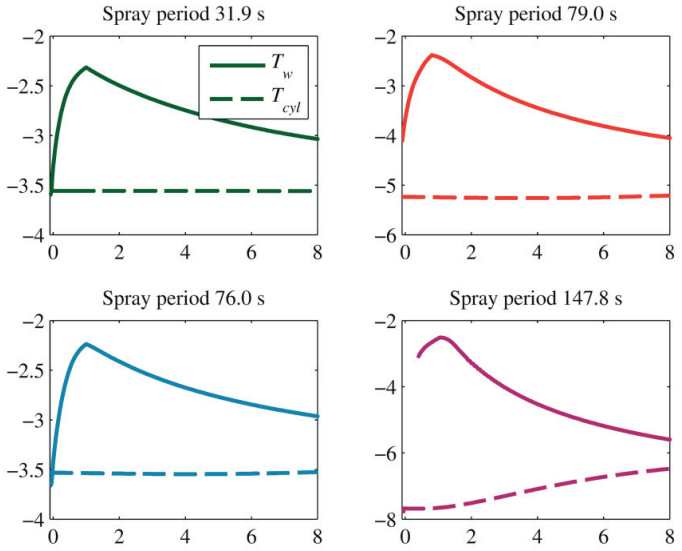

Fig. 14. Water film and cylinder temperatures [°C] over time [s] predicted by the conductive model after spray arrival, approximately 12 min after experiment start, when there is no significant effect from the heat capacity of the cylinder except Exp. 135.

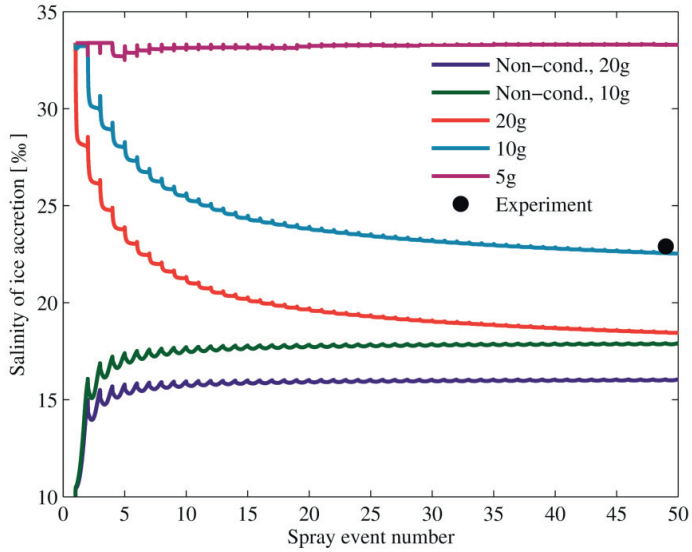

Fig. 15. Evolution of the average ice salinity during growth, Exp. 235. The ice salinity predicted by the non-conductive model increases over time due to increase of the water-film salinity. The ice salinity predicted by the conductive model decreases over time due to increase of the cylinder temperature, and as a result, decrease of σ_{WL} .

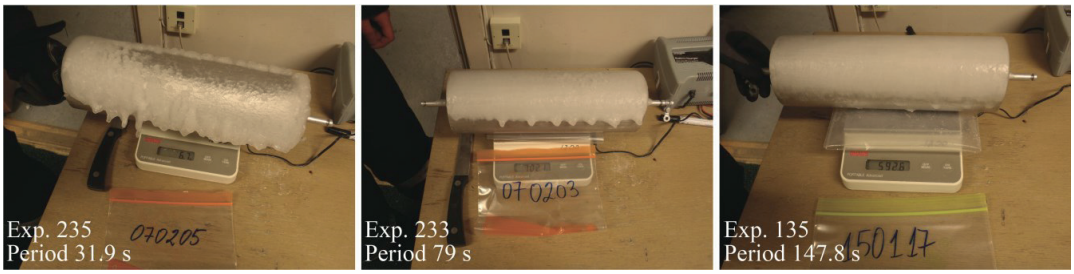

Fig. 16. The surface structure of the accreted ice caused by the spray with different periods.

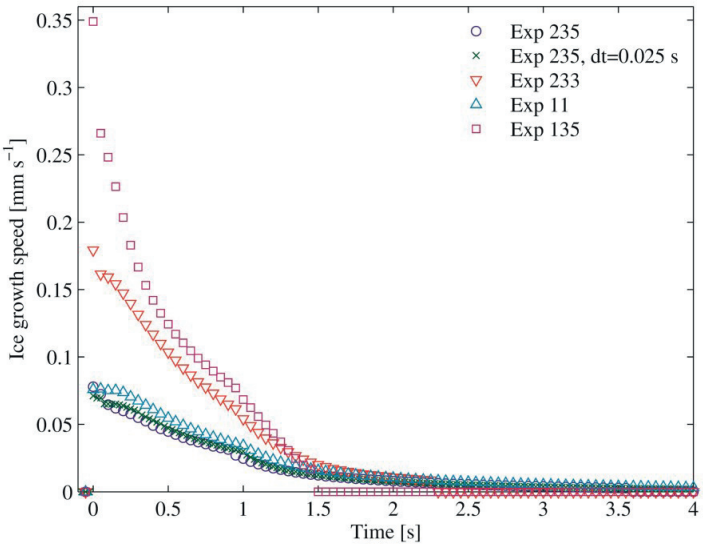

Fig. 17. Ice growth rate predicted by the conductive model after spray arrival, approximately 12 min after experiment start, when there is no significant effect from the heat capacity of the cylinder.

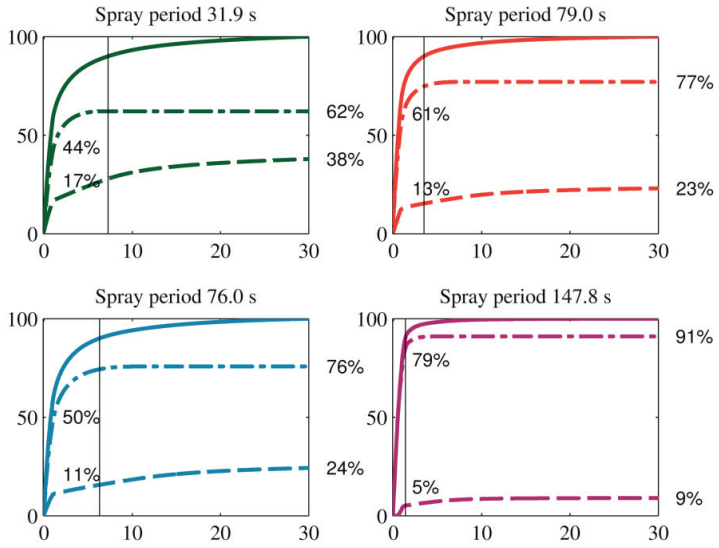

Fig. 18. Ice thickness increase [%] over time [s] relative to the total ice thickness increase predicted by the conductive model after single spray inflow after spray arrival, approximately 12 min after experiment start. Solid line is total thickness, dot-dash line is due to the heat conduction to the ice (Eq. (16)) and dashed line is due to heat release into the air (Eq. (19)).

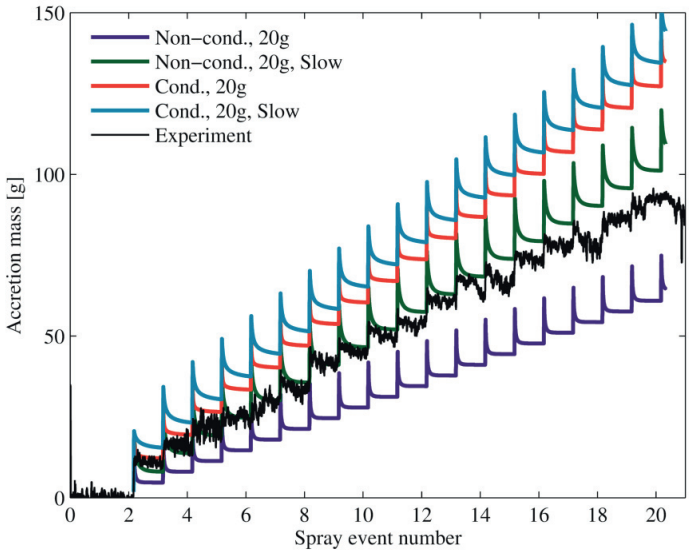

Fig. 19. Effect of the calculation of the rate of water-film motion on the predicted ice accretion rate, conditions of Exp. 11.

Appendix B.Secondary papers

21st IAHR International Symposium on Ice
"Ice Research for a Sustainable Environment"
Dalian, China, June 11 to 15, 2012

Small-Scale Simulation of Seawater Icing in Natural Field Conditions

Anton Kulyakhtin[1,4*], Sveinung Løset[1,3], Laszlo Kollar[2]
1. Norwegian University of Science and Technology (NTNU), Trondheim, Norway
2. University of Quebec at Chicoutimi (UQAC), Chicoutimi, Canada
3. Sustainable Arctic Marine and Coastal Technology (SAMCoT), Centre for Research-based Innovation (CRI), Norwegian University of Science and Technology, Trondheim, Norway
4. The University Centre in Svalbard (UNIS), Longyearbyen, Norway
[*] anton.kulyakhtin@ntnu.no

Sea spray icing can pose a danger to structures and vessels in Arctic waters that are free from level ice. It is important to develop simulation tools that can predict icing and provide the basis for mitigation measures for activities related to oil and gas fields, including associated ship traffic in northern waters, with an emphasis on the waters north of Norway and Russia. To make such tools reliable, it is necessary to improve the physical understanding of the sea spray icing process and to translate this knowledge into numerical models. Field studies of ice accretion were performed in the harbour area of Longyearbyen on Spitsbergen during the winter of 2011. This paper presents the development of a system for measuring ice accretion and the experimental results. This study also shows field conditions and associated complications. The applied spray was periodic and with a high liquid water content (1 - 30 g/m³). Measurements of the ice accretion rate were performed in different weather conditions on stationary and rotating cylinders with diameters of 20, 40 and 104 mm. The study demonstrated the importance of having real-time measurements of the ice accretion mass in the field, where weather conditions may change abruptly. Increased turbulence can decrease the accretion mass a few times for the given experimental setup. The measured turbulence intensity was within the range of 12 to 30 %. It was also found that the amount of accreted ice is lower at higher temperatures, but it is approximately constant at temperatures below -10°C for the periodic spray investigated.

OTC 23762

Mechanism and Dynamics of Marine Ice Accretion on Vessel Archetypes

O. Shipilova[1], A. Kulyakhtin[2], A. Tsarau[2], B. Libby[1], P. O. Moslet[1], S. Løset[2]

[1]Arctic Technology, DNV Research & Innovation, Det Norske Veritas AS
[2]Department of Civil and Transport Engineering, Norwegian University of Science and Technology

This paper was prepared for presentation at the Arctic Technology Conference held in Houston, Texas, USA, 3-5 December 2012.

Abstract

Marine icing (or, 'sea spray icing') is a well-known threat for commercial fishing craft and other relatively small vessels. However, larger vessels, such as supply ships, where localized icing can primarily be a safety or operational hazard, are less well studied. The MARICE project is a multi-year effort by Det Norske Veritas (DNV), the Norwegian University of Science and Technology (NTNU), Statoil and and the Research Council of Norway (NFR) to study this issue. A three-part simulation system has been designed to study the amount of water lifted from different types of ship bows in different weather conditions and estimation of the movement of droplets over, and their impingement with, the superstructure of vessels, neglecting the possibility of droplet break-up or coalescence. It was found that areas where the icing potential might be the greatest are not necessarily intuitive, as the movement of water and air is turbulent. Attempts were made to validate the model for water freezing on a metal unit against land-based spraying measurements conducted on Svalbard in natural weather conditions. The results of this study would be of greatest interest in the design and operation of vessels for cold conditions where sea spray icing might pose a hazard.

Appendix C. Summary of previous icing experiments

The table below is a summary of previous icing experiments and was made to find deficiencies in current knowledge. It shows that the variation in the spray period was investigated least.

Abbreviations: ND – no data in the papers, WT – wind tunnel, CL – closed loop, OE – open end, C – continuous, MVD – median volume diameter, and SMD – Sauter mean diameter. For the LWC and mass rate, a bold font corresponds to the data provided in the paper, and other values were recalculated.[a] 33 and 45 g $m^{-2}s^{-1}$ for an air speed in the tunnel wind tunnel of 20 and 25 m s^{-1}, respectively (Ekeberg, 2010).

Country, City	Canada, Ottawa	Finland, Helsinki	Norway, Trondheim	Japan, Sapporo	Canada, Alberta	Canada, Quebec
Salinity	Fresh	0, 10, 35 ppt	0, 21, 33.5 ppt	33 ppt	0, 20, 34 ppt	Fresh
Duration/period	C	C	2s/20s	C	C and 2 s/20s	C
Approx. LWC [g m^{-3}]	**3.2 (rough estimate)**	**4–5 (1983), 0.8–7.3 (1986)**	1.7	2.2 to 8.9 (for 10 m s^{-1})	**1 (C), 10 (Per.)**	**0.1–10**
Approx. spray flux [g $m^{-2}s^{-1}$][a]	0.14	7-150 (1986)	**33 and 45***	**22, 44, 67, 89**	25 (C), 250 (Per.)	10–60
DSD [μm]	MVD 185, DSD given	MVD 55	MVD 1000	SMD 200, 900, 1600 DSD given	ND in report, approx. 100-700 (Ekeberg, 2010)	MVD ~50, 500 (Veejet)
Method of DSD meas.	Oil slide droplet sampler	Manufacturer data	ND	Oiled slide	OAP probe	Collargol slide, Cloud image probe
Method of LWC meas.	LWC, estimate and hot wire at 50 m/s	Rotating cylinder (carbon dioxide)	Absorption panels	Reference to paper written in Japanese is given	Sponge placed in test section	Rotating cylinder
Air temperature range [°C]	-15 to -5	Ambient air, -15 to 1	Ambient air, -18 to -3	-15, -10, -5	-2, -4, -8, -12	-20 to -5
Water temperature range [°C]	16 to 20	Approx. 0	4	-1.4, 0.2, 4.0	0, -2, 4	~1 to 10
Wind speed [m s^{-1}]	22.4	7.5, 10, 15, 20	20, 25	6, 10, 20	25	10, 20, 30
Experiment orientation	Horizontal	Horizontal	Horizontal	Vertical	Vertical	Horizontal
Object diameter [cm]	3.8, 7.6, 15.2, 30.5, 45.7	5	5	3	4	3.8
Object length [cm]	90	20	17 (100 total)	ND	ND	92
Object orientation	Vertical and horizontal	Vertical	Horizontal non-rotating	Horizontal	Horizontal and 45°, fixed and rotating with a 9 s period	Horizontal (varying angles)
Structure	WT, CL	WT, OE	WT, OE	WT, CL	WT, CL	WT, CL
Duration	1 h	1 to 30 min	1 h	1, 5, 10, 15, 20 min	30 min	15 min
Distance from nozzle	5.18 m	3.5 m (1983), 4.0 m (1986)	7.65 m	1.16 m	Less than 2 m	4.4 m
Humidity	ND	ND	40-80%	ND	ND	75-95%
Spray nozzle	ND	ND	Spray systems, GA3 nozzle	ND	Danfoss: several combinations	Spray systems: 3 air atom., Veejet,
References	Stallabrass and Hearty (1967)	Launiainen et al. (1983); Launiainen and Lyyra (1986)	Horjen and Vefsnmo (1986); Carstens et al. (1984)	Fukusako et al. (1989)	Lozowski and Zakrzewski (1992); Foy (1988)	Karev et al. (2007); Kollar and Farzaneh (2010)

Appendix D. Details of the experimental setup

Here, a more detailed description of the experimental setup is given. Only seasons 2011-2013 are presented when the most useful results were obtained. DNVGL, the Arctic Technology department has the complete data collected in the experiments including real-time measurements, pictures of the ice accretion and measurements of the ice density and salinity. The list of completed experiments is given in Appendix E.

Season 2011-2012

The experiment location was selected based on an analysis of weather conditions. The requirements were stable strong winds along the valleys and concurrent low temperatures which Spitsbergen is known for.

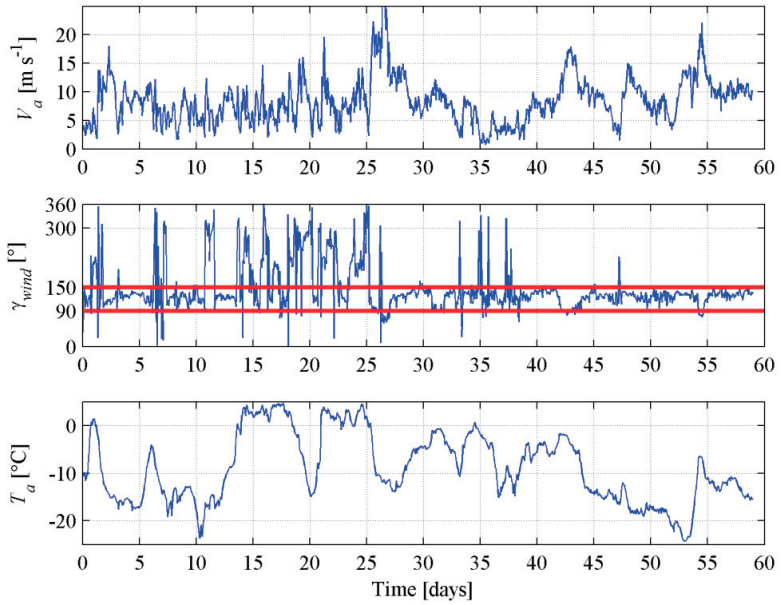

Figure 24. Time series of weather conditions in Adventdalen (Spitsbergen) in January-February 2010.

Figure 24 shows an example of time series of the air temperature, T_a, wind speed, V_a, and direction, γ_{wind}, that were measured near the old Northern Light Station in Adventdalen (78 12' 10'' N, 15° 49' 41'' E). The absence of the sun light during polar night reduces the daily variations in air temperature. Time intervals over a few days exist with approximately constant air temperature and stable wind direction. In

Adventdalen, the wind blows within a 60° sector centred at 120° (a 0° wind is from the north, and the positive direction is clockwise) for 74% of the time and yields excellent conditions for the measurements (Figure 25). The lower panel in Figure 25 shows the distribution of the wind speed and temperature; conditions with concurrent high wind speeds and low air temperatures are non-existent. Conditions under which seawater freezes and is cooled by wind (T_a < - 2°C and V_a > 5 m/s) exists for 44% of the time. When we introduce the additional condition of a wind direction ranging from 90° to 150° (required to use the experimental setup described below), conditions that are suitable for icing measurements exist for 35% of the time, which is a relatively high value.

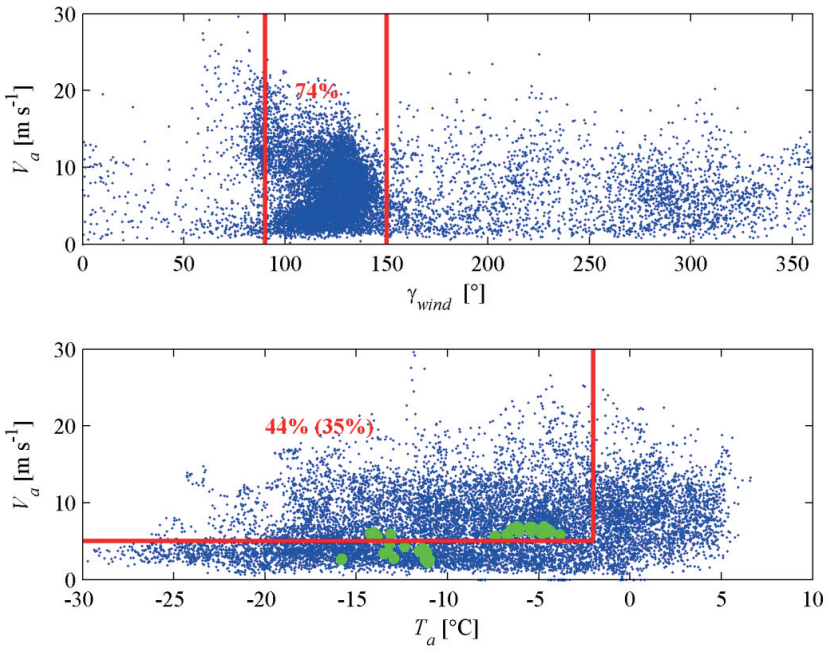

Figure 25. Scatter plots of the weather conditions in Adventdalen (Spitsbergen) from November to April of 2009–2012. Each blue dot corresponds to an average value for 1 h. The air temperatures and wind speeds during experimental tests in the season 2011-2012 are shown as green circles. Red lines outline the parameter space suitable for icing conditions.

The conditions for a following season are difficult to predict because the annual weather conditions vary. Weather conditions in 2012 were mild with approximately 2 to 4 days of harsh weather with T_a < -7°C and V_a > 6 m s^{-1} each month. Generally, from 2 to 12 days of harsh conditions each month were observed in previous years. In

addition, the experiments cannot be performed during snow storms; however, we do not possess any precipitation data to determine the frequency of snowstorms.

The experiments were conducted close to the old Northern Light Station (Figure 26). The experimental setup consisted of a spraying rig, a compressor, an icing object and a weather station. The spraying rig produced periodic spray with fixed durations and intervals without spray for each experiment. The spray flew in the direction of the icing object where it froze due to cold and windy conditions. Wind direction had small variations of 5° – 10° in relatively short intervals of approximately 1 minute. To compensate for these changes the automatically controlled trolley with the icing object moved along the rail, see Figure 26. The direction of movement and distance along the rail were determined according to a wind sensor installed above the nozzle of the rig. In most of the cases it was possible to fit the position of the trolley during spraying in such a way that the line between the trolley and nozzle was parallel to the wind direction. This was impossible only in few cases when the wind changed direction suddenly during the spraying event. Thus, the amount of oncoming spray was more or less constant, yet, with small variations probably caused by air turbulence.

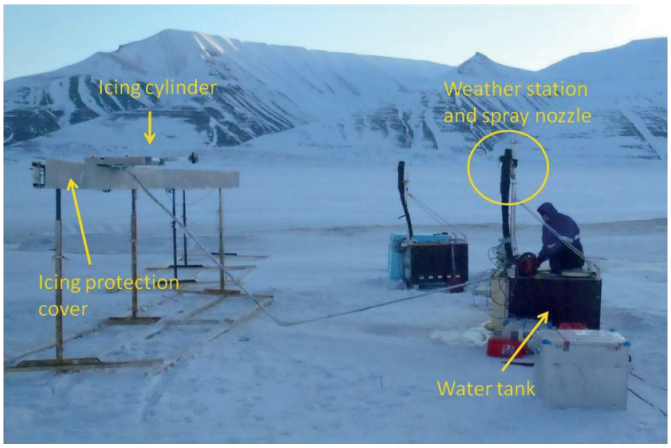

Figure 26. Photo of experimental setup in Adventdalen (Spitsbergen).

The length of the rail was 5.2 m and the trolley could move within 45° - 50°. This range of variation made it possible to adapt the icing object position to the most of the wind directions (Figure 25). However, when the change of wind direction was greater, the whole rail was moved and rotated, and the direction of the spraying rig was changed correspondingly. This was done only between experiments. The distance between rig and rail was kept constant at 5.3 m, giving 5 m distance between cylinder and nozzle. It was difficult to keep the relative height of the nozzle and icing object

constant due to the uneven surface of the snow. And as it will be shown later, it affected the total amount of spray arriving on the icing object and possibly affected the ice accretion rate. The height of the nozzle above the ground was 2.3 meters and the height of the icing object was approximately 15 cm lower than the nozzle but it depended on snow surface height on the particular day. Natural air flow is quite turbulent especially close to the ground. That is the reason why the nozzle and icing object were installed 2 m above ground level.

The air atomising nozzle (1J+SU152 Spraying Systems Co.) created spray. An air compressor (ABAC Air Compressors, mod B 2800B/50 CM 3 V230 OMA) supplied constant pressure of 8 bars. The compressor was installed in a thermally insulated box where the heater was running to avoid freezing of the compressor. The pressure was reduced separately for air and water by a set of reduction valves. The air pressure was set to 3 bar and it was 1.4 bar during spraying. The water pressure was set to 0.8 bar and it reduced to 0.4 bar during spraying. The pressure was measured just after the reduction valves, which are separated from the nozzle by two meters long rubber pipes and thus is different from the pressure in the nozzle inlet.

The total water flow rate was approximately 260 g/s and varied within 10% due to the change of pressure supply from the compressor. Using the measured total spray flow rate and diameter of the spray cloud, one can estimate that the mean spray flow rate per unit area is equal to 880 g/m²s when it arrives on the cylinder surface, see Kulyakhtin et al. (2013a).

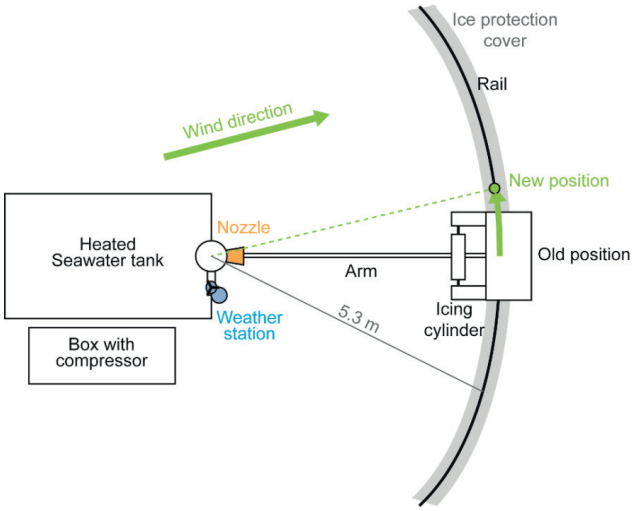

Figure 27. Scheme of experimental setup and control of icing object position.

A system of electronic valves controlled with a set of timers created periodic sprays. The detailed description can be found in Kulyakhtin 2011. Two sets were used:

- duration 1.88±0.02 sec, period 49.8±0.02 sec
- duration 1.94±0.02 sec, period 31.7±0.02 sec

The difference between durations is less than 5% and is neglected.
Seawater (with 34 ppt salinity) was carried to the place of measurements from the University Centre in Svalbard (UNIS) in 20 litres cans. After each working shift the water tank was emptied to avoid freezing of water in the tank in case of power failure. During spray simulations water was stored in the big water tank (approximately 300 litres) from where it was pumped into the nozzle. The temperature in the tank was regulated with a relay. Exact values with errors of 0.5°C were measured continuously every 5 minutes with temperature loggers (NOMAD OM-84-TMP) installed in the bottom of the tank and manually before and after each experiment. Water from the tank was collected several times per day to check its salinity. Variations of the temperature in the water tank occurred mainly when water was refilled in the tank. It would have taken a couple of hours before the temperature reached the value set by the relay, and thus, it was decided to perform tests with varying temperature of water in the tank.

Figure 28 shows the weather monitoring system which was used both to register weather conditions and to control the position of target. Table 2 gives parameters and accuracies of the sensors. The wind sensor rotated with the nozzle and gave wind directions relative to the position of the nozzle and the icing object.

Figure 29 shows the construction used for ice accretion mass measurements. Ice accretion was measured on cylinders with 300 mm length and primarily on cylinders with diameters of 40 and 100 mm, but 2 measurements were done on a 20-mm–diameter cylinder. The ends of cylinder were attached to metal rods with a diameter of 10 mm. The ends of the rods were placed on two load cells, which measured the mass of the cylinder together with that of ice and unfrozen water. Only the cylinders and parts of the rods were exposed to water. The load cells and the rest of the system were protected by a cover. The distance between the edge of the cylinder and the protection against the ice was approximately 15 mm and it was important to keep it big enough. This was done to prevent ice growing on the cylinder from coming into contact with the protection cover, so it would not affect the load cells measurements.

Figure 28. Weather station installed on the top of the spraying rig.

Table 2 Measurements and equipment accompanying the weather station.

Measurements	Equipment	Accuracy	Frequency
Wind velocity and direction	Young 81000 Ultrasonic Anemometer	Wind speed 0.1 m/s wind direction 2°	10 Hz
Air temperature	Campbell HMP155A	around 0.3°C	1 Hz
Relative humidity of air	Campbell HMP155A	1% for experiment conditions	1 Hz
Data storage	Campbell CR1000 Data logger		

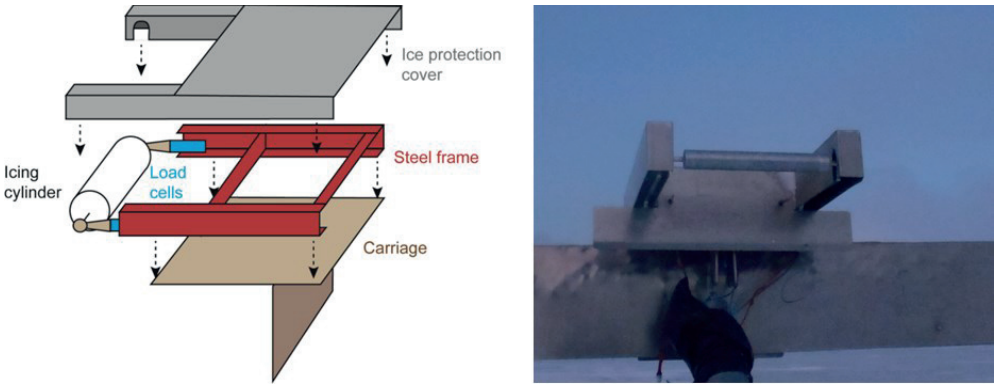

Figure 29. Sketch and the picture of the system for the real time mass measurements.

The HBM (Hottinger Baldwin Messtechnik) SP4MC3MR/1kg load cells used in the experiments had a maximal load of 1 kg and an accuracy of 1 g. Initially it was planned to use a Campbell data logger for data recording. However, it did not give desirable accuracy and thus HBM setup was used. It consisted of an Amplifier MX440 and a data recorder CX22-W. The load was recorded with 20 Hz frequency.

As it was written before, the whole target shown in Figure 29 moved along the rail according to the reading from the wind sensor. Figure 30 shows the construction of the rail and the back side of the target mounted on it. System of relays controlled the work of an electrical motor supplied with 12V by changing polarity. The motor moved the target clinging to a chain stretched along the rail. The use of a chain ensured a good grip of the motor. A multi rotational potentiometer was used to check the target's position because the speed of the motor rotation was not constant.

Figure 30. Pictures of the rail and the carriage from the back. Picture to the right shows the chain and motor which are used to move the target.

Figure 31. Photo of the ice accretion and the system after the test on the 14th of February 2012.

Each single test lasted approximately 20-25 minutes. A few experimental tests were done with a duration of up to 1 hour. Long-time tests had a few problems related to the construction of Real-Time mass Measurements System (RTMS). It was needed to clean the front part of the protection cover every 20 minutes from ice, so that the cylinder would not freeze onto the protection cover. One can see an example of the

described problem in Figure 31 close to the left end of the cylinder. When each test was finished, the mass of the ice sample was measured on the scale. This gave a possibility to verify RTMS measurements, and data on ice accretion mass was available even when the RTMS did not work. After weighing, the ice samples were cut with a knife into pieces, melted, and the salinity of the ice was measured.

Two consecutive tests either with different cylinder diameters or different spray periods were done to obtaining similar weather conditions for two tests with only one varying parameter.

Season 2012-2013

There were still several problems with the experimental setup and several practical problems during Season 2011-2012. As a result, only a small number of experiments were done and only in narrow range of conditions (Figure 25). The experimental setup was improved before the next season. The main changes were as follows:

- A better control of T_w was obtained. The seawater was stored in the water tank before the experiments and the tank was refilled when the working shift was finished. In the previous season the spraying rig was emptied of water after working shift to avoid freezing of water during a potential power failure which can destroy the spraying rig. An alarm system was installed which sent an SMS in the case of a power failure. Thus, the spraying rig was continuously heated through the whole measurement season.
- The measurement data were transferred in real-time to a laptop inside the Northern Light Station. Thus, it was possible to check the quality of data online.
- The length of the rail was extended from 5 m to up to 9 m; therefore there was no need to move the whole system to align it with the wind. This reduced labor work and variation in the spray flux due to change of the vertical position of the target (see Kulyakhtin et al. (2013a) for the problem description).
- The rail was set horizontal ± 1cm using a leveling instrument. As a result, the spray flux to the cylinder surface varied less.
- The electronic control of spray events was rebuilt. Different spray periods and durations were used in these experiments. The spray periods and durations were measured by the analysis of an electronic signal from the valves with a frequency of 100Hz (on 03.02.2012). The duration of spray was 1.085 sec and the periods were: 21.8, 32.08, 48.975, 76.0, 147.8 s. (Starting from Test 115 (12.01.2013 15:57 – 16:24), the spray period changed from 76 sec to 79 sec.

· The water mass sprayed per single spray event was set to 366 g. The spray flux changed due to wind fluctuations and the maximal spray mass reaching the cylinder (0.1 m in diameter and 0.3 m long) in the spray events was 20 g.

Appendix E. List of performed experiments

The Arctic Technology department of DNVGL has received the complete data collected during the experiments including real-time measurements, pictures of the ice accretion and measurements of the ice density and salinity. Here the list of the completed measurements is given. The table below lists data which were collected.

Notation:

- "code" denotes the test and Matlab file name, the first four digits are the date of the experiment and the last two are the sequential experiment number on that day
- D_c is the cylinder diameter [mm]
- "Start" is the time of the experiment start
- t_{per} is the experiment period [s]
- t_{exp} is the experiment duration [min]
- T_a is the average air temperature [°C]
- RH is the average relative humidity [%]
- γ is the average angle of the wind direction deflection from the line connecting nozzle and the cylinder [°]
- V_a is the wind speed [m s^{-1}]
- T_w is the water temperature in the tank [°C]
- M_i is the final mass of the ice accretion
- I_{exp} is the ice accretion rate per unit area [g m^{-2} s^{-1}], which was calculated dividing the total accretion mass by D_c, cylinder length and t_{exp}
- F_{sp} is the average spray inflow per spray event [g]
- R_{off} is the average water run-off per spray event [g]
- S_i is the ice salinity

Season 2011-2012

Table 3. Summary of the conducted tests without real-time measurements of the ice accretion mass; code 40ss denotes a 40-mm-diameter cylinder made of stainless steel, 100al denotes a 100-mm-diameter cylinder made of aluminium, Na indicates that salinity was not measured.

N	Code	Date	Start	t_{exp}	T_a	RH	V_a	γ	T_w	I_{exp}	t_{per}	S_i
1	40ss	26 Mar.	17:05	23.3	-6.5	57	6.6	5.2	4.2	4.96	31.7	25.8
2	40al	26 Mar.	17:40	26.4	-6.1	56	6.8	6.5	3.7	5.34	31.7	26.0
3	40ss	26 Mar.	18:24	25.4	-6.2	57	6.9	7.0	3.5	5.32	31.7	26.8
4	100al	26 Mar.	19:00	23.8	-6.1	57	6.3	4.8	1.2	3.94	31.7	25.8
5	40ss	26 Mar.	19:34	23.3	-5.5	54	5.7	11.4	1.4	4.20	31.7	29.6
7	20ss	26 Mar.	20:56	27.0	-5.4	56	6.3	6.5	2.9	7.42	31.7	24.9
8	40ss	26 Mar.	21:32	19.0	-5.5	58	6.8	7.3	2.6	5.77	31.7	24.9
9	20ss	26 Mar.	22:10	23.3	-6.8	59	5.9	5.4	2.7	8.14	31.7	25.5
10	100al	26 Mar.	22:45	20.6	-6.7	60	5.4	3.8	1.5	3.63	31.7	26.2
11	40ss	26 Mar.	23:51	22.2	-7.4	62	5.7	3.9	3.4	6.02	31.7	27.9
12	100al	27 Mar.	00:24	25.9	-7.4	62	5.5	3.4	3.4	4.21	31.7	23.4
14	40al	28 Mar.	14:49	20.6	-3.8	69	5.9	5.8	5.7	1.94	31.7	22.0
15	40ss	28 Mar.	15:20	20.6	-4.3	69	6.2	5.1	4.8	2.18	31.7	24.8
16	40ss	28 Mar.	15:50	19.0	-4.4	68	6.5	3.7	5.1	2.38	31.7	24.0
17	40ss	28 Mar.	16:32	19.6	-4.9	71	6.4	4.3	2.9	3.05	31.7	26.0
18	40ss	28 Mar.	17:00	21.1	-4.8	72	6.0	5.0	2.6	2.98	31.7	26.1
19	100al	28 Mar.	17:30	19.6	-4.6	71	6.1	5.8	2.6	1.97	31.7	23.3
20	100al	28 Mar.	17:58	18.0	-4.7	71	6.9	4.6	2.8	2.50	31.7	23.7
21*	40ss	28 Mar.	18:29	16.9	-5.4	72	6.8	4.0	4.2	6.58	31.7	Na
23	100al	4 Apr.	17:04	22.2	-12.4	60	4.3	6.4	6.0	6.40	31.7	22.8
25	40ss	4 Apr.	18:02	21.1	-13.3	64	3.6	7.1	2.6	9.56	31.7	28.5
28	40ss	5 Apr.	13:31	22.4	-15.7	63	2.5	8.8	2.0	7.31	49.8	28.0
51	100al	12 Apr.	05:03	23.8	-13.9	63	5.7	4.0	2.5	12.2	31.7	24.1

*Fresh water experiment

Table 4. Summary of the conducted tests with real-time measurements of the ice accretion mass. (1) and (2) denote scenarios used to calculate I_{calc}.

N	Code	Date	Start	t_{exp}	T_a	RH	V_a	γ	T_w	I_{exp}	t_{per}	F_{eff}	R_{off}	S_i
29	40al	5 Apr.	15:57	20.7	-15.8	62	2.7	3.7	4.2	10.0	49.8	300±90	0.93±0.72	25.2
30	40al	5 Apr.	16:27	21.1	-15.9	61	1.6	5.7	4.7	6.84	31.7	170±80	1.43±0.78	21.3
32	40al	6 Apr.	12:23	20.6	-14.5	64	1.9	3.2	6.3	5.98	31.7	150±70	1.39±0.69	16.3
38	40ss	10 Apr.	23:29	21.6	-13.5	64	3.4	1.9	-0.1	11.7	49.8	360±80	1.81±1.29	27.7
40	100al	11 Apr.	00:31	25.9	-12.9	65	3.7	14	0.8	5.91	31.7	120±100	3.17±4.5	29.6
42	100al	11 Apr.	01:52	20.7	-12.9	65	2.8	5.7	1.3	6.39	49.8	210±80	2.64±2.01	21.8
45*	40al	12 Apr.	01:27	24.9	-14.2	68	5.8	2.9	5.3	10.62	49.8	330±60	1.46±1.12	Na
46*	40ss	12 Apr.	01:59	22.4	-14.2	67	6.0	2.2	5.1	10.5	49.8	320±80	1.15±1.02	Na
48	40al	12 Apr.	03:26	24.8	-13.1	63	5.9	2.4	1.4	17.0	31.7	350±90	1.60±1.32	26.4
50	100al	12 Apr.	04:33	21.6	-14.1	64	6.1	1.7	2.6	10.2	49.8	300±40	1.83±2.15	28.0
52	40al	12 Apr.	05:44	20.7	-13.2	61	4.7	3.4	2.4	12.83	49.8	340±80	0.76±0.89	30.6
54*	100al	14 Apr.	20:32	24.1	-11.0	69	2.6	3.0	5.7	5.62	49.8	170±50	0.99±0.64	2.5
55*	100al	14 Apr.	21:06	13.7	-11.2	71	2.9	1.7	6.5	7.50	31.7	150±30	1.91±1.13	0.6
57	40al	14 Apr.	22:14	20.1	-11.1	71	2.2	3.0	1.7	7.25	31.7	200±80	2.24±1.18	21.8
58	40al	14 Apr.	23:02	21.6	-11.2	73	3.6	1.9	2.4	7.35	49.8	250±70	1.10±0.89	28.0
59	100al	14 Apr.	23:33	19.9	-11.6	74	3.8	1.7	2.8	4.46	49.8	120±40	0.83±0.62	28.9
60	100al	15 Apr.	00:03	23.3	-11.5	74	3.8	1.4	3.0	5.06	31.7	120±30	2.32±1.16	26.4
61	40ss	15 Apr.	00:40	20.1	-11.5	75	3.9	1.5	3.2	6.48	31.7	120±30	0.39±0.44	30.0
62	40ss	15 Apr.	01:08	22.4	-11.4	74	4.0	1.5	3.3	6.51	49.8	180±30	0.30±0.3	30.1
63	40al	15 Apr.	01:37	19.9	-11.4	75	3.8	1.9	3.7	7.27	49.8	190±60	0.18±0.26	31.2
64	40al	15 Apr.	02:03	17.4	-11.5	74	3.7	1.5	4.0	6.65	31.7	120±60	0.23±0.34	30.3

*Fresh water experiment

Season 2012-2013

Table 5. The list of performed experiments. All experiments were done on Aluminum cylinders.

* denotes tests with problems, “f” – fresh water experiment, “p” - PSX700 coating, “s” - SHIELD12000 coating, “i” - plastic isolation coating (Kulyakhtin, 2013). After Test 115, the spray period instead of 76 s was 79 s due to problems with electronics.

N	code	D_c	Start	t_{per}	t_{exp}	T_a	RH	γ	V_a	T_w	M_i	I_{exp}	F_{sp}	R_{off}	S_i
1	251101	100	10:11	32.0	25.6	-3.9	75	3.6	13.7	4.4	635	1.80	8.0	5.3	
2*	251102	100	10:47	21.8						4.5	570				
3	251103	100	11:14	49.0	25.3	-3.7	74	3.7	12.2	4.6	626	1.62	6.6	4.9	
4	251104	100	11:46	76.0	25.3	-3.6	73	4.2	11.1	4.7	595	1.16	4.6	1.8	
5*	251105	100	13:54	21.8						4.4	622				23.4
6*	251106	100	14:27	76.0						4.6	570				28.6
7	271101	100	19:30	76.0	24.1	-7.7	69	2.8	6.5	4.8	719	4.13	9.5	0.2	27.9
8	271102	100	20:03	49.0	22.9	-7.2	68	3.8	6.6	4.8	717	4.05	6.2	0.4	28.4
9	271103	100	20:38	32.0	23.5	-6.9	68	3.6	5.1	4.5	638	2.31	3.2	0.7	31.1
10*	271104	100	21:07	21.8						2.3					0.0
11	281101	100	12:01	76.0	22.8	-5.0	76	3.3	5.5	1.6	642	2.23	6.8	1.8	24.1
12	281102	100	12:29	49.0	24.5	-4.9	78	3.0	6.8	1.6	635	2.15	5.6	2.1	23.1
13	281103	100	12:58	32.0	26.1	-4.9	80	3.3	7.4	1.6	648	2.05	4.5	1.2	21.5
14	281104	100	13:29	21.8	26.9	-4.6	78	3.7	6.8	1.7	632	1.90	4.8	2.7	18.0
15	281105	100	14:17	76.0	25.3	-4.4	75	5.4	6.3	1.9	633	1.79	4.6	0.7	24.5
16	281106	100	14:47	49.0	26.1	-4.6	77	2.4	7.0	2.1	645	2.24	6.5	3.3	24.0
17	281107	100	15:17	32.0	25.1	-4.5	77	3.2	6.4	2.1	626	1.67	4.5	2.1	20.5
18	281108	100	15:48	21.8	25.4	-4.3	79	4.2	6.1	2.2	607	1.48	4.7	3.2	20.4
19	281109	100	16:54	76.0	26.6	-4.1	80	5.1	6.6	2.6	621	1.48	4.9	1.6	24.5
20	021201	100	11:47	76.0	26.6	-8.7	74	2.1	4.9	1.0	753	4.23	11.0	0.4	26.7
21	021202	100	12:18	49.0	27.0	-8.7	73	3.1	4.9	1.0	739	4.12			27.0
22*	021203	100	12:50	32.0	25.1	-9.5	76	4.8	3.2	1.1	655	2.31	3.4	0.5	31.1
23*	021204	100	13:20	21.8	26.9	-8.3	74	3.9	4.2	1.2					
24	021205	100	14:50	21.8	23.6	-8.6	74	3.1	3.9	2.0	702	3.57	3.9	1.2	23.4
25	021206	100	15:20	76.0	25.3	-9.7	77	3.0	3.3	2.3	693	3.38	8.2	1.1	29.1
26	021207	100	15:49	49.0	24.5	-9.6	76	2.8	4.4	2.7	744	4.38	7.8	1.1	28.2
27	021208	100	16:19	32.0	25.1	-9.0	76	2.3	4.2	2.8	714	3.86	4.6	0.7	25.1
28*	021209	100	16:49	21.8	25.1	-10.1	78	5.4	2.7	2.7	725	3.87	3.5	0.9	23.8
29	051201	100	10:53	147.8	27.1	-15.2	67	4.3	3.0	1.2	707	3.22	14.6	0.4	29.3
30	051202	100	11:25	76.0	24.1	-16.2	71	2.4	3.3	1.3	777	5.47	12.8	0.1	29.4
31	051203	100	11:59	49.0	27.0	-15.8	69	2.0	3.7	1.4	884	6.88	11.4	1.2	26.6
32*	051204	100	12:31	32.0	25.1	-15.7	70	2.2	3.5	1.5	757	4.81	4.8	0.2	28.6
33	051205	100	13:45	32.0	24.0	-15.5	69	2.7	3.4	1.6	846	6.86	7.4	0.6	25.1
34	051206	100	14:16	32.0	25.1	-16.3	71	5.2	2.2	1.6	788	5.49	6.7	1.1	24.7
35	051207	100	15:02	49.0	31.0	-17.3	73	3.0	3.0	1.8	860	5.55	8.8	0.6	26.3
36	051208	100	15:46	76.0	26.6	-16.4	71	3.4	2.4	2.1	752	4.42	10.5	0.2	29.6
37	051209	100	16:17	147.8	27.1	-16.3	72	1.8	2.9	2.2	680	2.67	11.0	1.8	28.2

38*	051210	100	16:50	76.0						2.2					
39	051211	100	17:20	76.0	25.3	-16.2	72	3.5	3.5	2.2	783	5.09			28.6
40	051212	100	17:57	49.0	25.3	-14.9	71	4.1	4.4	2.2	808	5.86	9.4	0.6	28.4
41	051213	100	18:32	32.0	24.0	-15.2	72	2.7	4.7	2.2	934	8.88	9.1	0.5	25.2
42	051214	100	19:01	147.8	24.6	-14.8	72	3.1	4.6	2.2	639	2.24	9.5	2.1	28.4
43	071201	100	15:38	147.8	27.1	-7.6	77	8.0	2.3	1.2	613	1.50	6.5	1.9	30.5
44	071202	100	16:10	76.0	24.1	-7.7	79	3.1	3.0	1.6	669	2.73	6.5	0.1	27.4
45	071203	100	16:41	49.0	23.7	-6.4	78	2.7	4.3	1.8	641	2.38	5.2	1.6	23.4
46	071204	100	17:12	32.0	25.6	-6.8	80	2.5	4.8	1.8	695	3.14	3.6	0.2	22.5
47	081201	100	14:18	32.0	25.6	-8.2	71	2.7	5.7	1.1	757	4.49	5.3	0.6	24.9
48	081202	100	14:49	49.0	25.3	-8.2	72	3.7	4.8	1.2	721	3.98	6.5	0.4	25.9
49	081203	100	15:18	76.0	25.3	-7.5	70	3.3	5.7	1.3	644	2.05	5.3	0.4	30.4
50	081204	100	16:19	147.8	24.6	-6.2	67	3.9	6.0	1.5	648	2.20	10.3	1.6	31.2
51	081205	100	17:07	147.8	24.6	-5.2	68	3.5	7.3	1.8	620	1.81	7.3	0.5	29.8
52	081206	100	17:37	76.0	24.1	-3.8	70	5.1	5.6	2.0	604	1.23	5.4	2.7	
53*	121201	100	10:37	147.8	24.6	-3.1	72	6.3	3.9	1.1	585	0.78			27.1
54	121202	100	11:05	147.8	24.6	-3.9	73	4.4	4.3	1.4	595	1.25	6.1	0.4	29.1
55	121203	100	11:38	76.0	25.6	-3.5	73	4.2	4.1	1.6	603	1.14	4.2	1.6	21.7
56*	121204	100	12:08	49.0	23.7	-4.0	71	19.6	3.2	1.7	571	0.73	3.5	1.9	30.6
57	121205	100	13:02	32.0	24.0	-5.7	74	19.7	1.6	1.9	617	1.53	2.0	0.2	27.8
58	131201	100	10:25	147.8	24.6	-12.7	74	3.3	3.6	0.9	654	2.57	11.6	0.1	28.3
59	131202	100	10:56	76.0	26.6	-13.6	75	5.7	2.4	1.0	723	3.61	8.4	0.0	28.9
60	131203	100	11:27	49.0	25.3	-12.9	73	4.8	2.7	1.0	729	4.15	6.8	0.7	26.7
61	131204	100	11:57	32.0	25.6	-13.1	75	8.5	2.3	1.1	769	4.74	4.7	0.1	26.1
62*	131205	100	12:45	49.0	58.8	-12.2	74	11.9	2.3	1.2			5.5	0.7	27.7
63*	131206	100	13:59	147.8	27.1	-11.9	75	41.9	1.9	1.2	609	1.20	6.0	2.2	28.7
64	141201	100	11:49	147.8	24.6	-9.6	74	3.4	4.2	1.1	664	2.80			29.6
65	141202	100	12:24	76.0	25.3	-9.8	74	3.2	4.6	1.2	726	3.85	9.1	0.3	28.3
66	141203	100	12:54	49.0	25.3	-10.1	74	4.3	3.9	1.2	751	4.64	7.8	0.8	26.0
67	141204	100	13:29	32.0	17.1	-9.1	71	15.5	3.4	1.2	659	3.53	4.4	0.3	26.6
68	141205	100	14:01	32.0	25.1	-9.8	73	3.7	3.2	1.3	708	3.71	3.8	0.0	24.9
69*	141206	100	15:26	49.0	44.9	-9.3	72	3.4	3.7	1.5			6.7	1.3	
70	171201	100	11:56	32.0	17.1	-17.1	59	4.5	3.2	1.0	877	10.95	5.9	0.6	23.6
71	171202	100	12:25	49.0	15.5	-16.2	58	5.7	3.8	1.1	834	10.12	7.2	0.3	28.1
72	171203	100	12:57	76.0	25.3	-16.9	58	7.0	3.9	1.1	720	3.94			28.5
73	171204	100	14:56	32.0	25.1	-17.0	59	3.5	5.2	1.5	1033	10.68			25.2
74*	171205	100	15:59	147.8						1.3					
75	171206	100	16:10	147.8	27.1	-16.9	58	3.1	5.3	1.3	704	3.12	14.1	0.3	27.9
76	171207	100	19:18	49.0	26.1	-17.7	59	5.6	4.2	1.7	873	6.82	10.0	0.0	28.1
77	171208	100	19:52	76.0	25.3	-17.9	59	4.0	3.8	1.6	780	5.27	12.2	0.1	28.0
78	171209	100	20:24	147.8	24.6	-18.4	62	3.3	3.8	1.4	666	2.57	11.6	0.2	27.6
79	171210	100	21:00	32.0	25.1	-17.4	61	2.9	3.9	1.2	921	8.44	8.2	0.0	25.0
80	171211	100	21:33	49.0	24.5	-16.9	60	3.4	4.5	1.3	866	7.13	10.7	0.3	28.5
81	171212	100	22:25	76.0	26.6	-16.0	59	3.1	5.2	1.3	773	4.86	11.6	0.3	29.0
82	171213	100	22:58	147.8	24.6	-15.7	59	2.5	4.6	1.2	686	3.03	14.1	0.7	28.9
83	171214	100	23:29	32.0	26.7	-15.9	62	3.0	4.2	1.2	930	8.13	8.0	0.0	24.7

84	181201	100	00:19	49.0	25.3	-15.0	64	3.1	5.2	1.2	866	6.91	10.7	0.3	27.1
85	181202	100	00:52	76.0	25.3	-14.8	65	2.2	5.4	1.1	776	5.17	12.0	0.1	29.4
86	181203	100	02:32	32.0	25.1	-13.8	69	2.7	5.2	1.6	947	8.76	8.5	0.0	25.3
87	181204	100	03:02	147.8	24.6	-13.7	72	2.4	5.1	1.5	664	2.79	13.0	0.5	29.1
88	181205	100	03:35	49.0	25.3	-13.2	70	3.3	5.2	1.4	812	5.72	8.7	0.2	28.7
89	181206	100	04:06	76.0	24.1	-12.8	73	2.7	6.0	1.4	759	5.05	11.4	0.0	30.1
90	181207	100	05:08	147.8	24.6	-12.1	77	3.6	6.5	1.9	658	2.40	11.3	2.6	29.7
91	181208	100	05:38	76.0	25.3	-11.4	74	3.5	6.9	1.8	747	4.51	10.4	0.1	29.9
92	181209	100	06:08	49.0	24.5	-10.9	71	5.4	6.6	1.7	795	5.53	9.2	1.2	28.6
93*	181210	100	06:37	32.0	24.5	-10.4	71	5.6	6.6	1.6			6.5	0.8	
94	181211	100	07:10	32.0	25.1	-10.0	74	4.6	7.3	1.6	778	5.02	5.4	0.3	29.5
95*	191201	100	20:09	32.0						1.1					32.5
96*	201201	100	17:04	76.0	26.6	-3.3	90	10.8	8.9	1.1	883	7.14	13.0	0.9	22.2
97	261201	100	14:39	147.8	24.6	-23.6	68	3.8	3.8	1.6	630	1.80	8.3	0.4	30.6
98	261202	100	15:10	76.0	25.3	-24.6	68	3.0	5.2	1.6	707	3.67	9.2	0.3	29.3
99	261203	100	15:40	49.0	25.3	-24.2	68	3.7	5.4	1.5	819	5.89	10.2	1.3	29.9
100	261204	100	16:10	32.0	25.1	-23.9	68	2.4	5.4	1.5	957	9.24	9.0	0.0	26.4
101	261205	100	16:39	147.8	24.6	-24.0	67	2.5	4.8	1.3	653	2.33	10.9	0.2	29.5
102	261206	100	17:10	76.0	22.8	-24.2	66	2.2	5.0	1.4	684	3.52	8.8	0.3	29.7
103	261207	100	17:42	49.0	24.5	-24.4	65	2.7	5.7	1.5	813	5.97	9.9	0.8	28.4
104	261208	100	18:12	32.0	24.5	-24.7	66	2.0	5.9	1.5	1001	10.46	10.0	0.0	26.2
105	261209	100	19:06	147.8	24.6	-23.4	65	1.8	5.8	1.5	649	2.22	10.7	0.5	29.8
106	261210	100	19:38	76.0	24.1	-23.0	65	2.8	5.2	1.5	695	3.59	9.3	0.7	28.4
107	261211	100	20:10	49.0	24.5	-22.0	65	2.1	5.1	1.8	793	5.51	8.6	0.3	28.8
108	261212	100	20:40	32.0	28.3	-21.1	64	2.4	5.1	2.1	966	8.36	8.1	0.0	26.0
109	301201	100	00:04	32.0	20.3	-9.9	66	2.9	7.0	1.8	788	6.80	6.5	0.3	25.8
110	301202	100	00:29	49.0	25.3	-9.7	75	2.4	7.2	2.1	790	5.26	8.3	0.6	28.1
111	301203	100	00:59	76.0	25.3	-9.4	82	2.6	6.7	2.3	708	3.69	9.0	0.5	30.8
112	301204	100	01:29	147.8	27.1	-9.0	83	3.6	6.8	2.3	634	1.72	8.4	0.6	31.6
113	120101	100	14:51	32.0	26.2	-17.0	78	8.9	2.6	1.4	838	6.33	6.6	0.3	25.8
114	120102	100	15:24	49.0	25.3	-17.8	80	5.4	2.8	1.4	820	5.92	9.1	0.2	27.9
115	120103	100	15:57	79.0	26.3	-19.1	78	18.3	2.0	1.4	647	2.27	6.3	0.9	28.6
116	120104	100	16:31	147.8	24.6	-18.9	81	5.4	2.4	1.3	624	1.67	8.0	0.6	29.2
117	120105	100	17:00	32.0	48.1	-18.7	80	12.5	2.1	1.3	1093	6.39	6.9	0.5	
118	120106	100	17:53	79.0	47.4	-18.7	80	14.0	2.0	1.2	713	1.91	5.2	0.6	26.4
119	150101	100	04:56	32.0	25.6	-19.9	71	39.7	1.8	1.4	765	4.66	4.9	0.2	29.6
120	150102	100	05:32	49.0	27.0	-19.8	71	9.6	2.4	1.5	683	2.95	5.9	1.5	29.5
121	150103	100	06:12	79.0	26.3	-16.1	66	7.9	3.6	1.5	702	3.21	8.2	0.3	28.0
122	150104	100	06:45	147.8	24.6	-15.1	65	3.1	5.0	1.6	615	1.71	8.5	0.6	27.9
123	150105	100	07:15	32.0	22.9	-14.1	63	5.8	4.8	1.7	825	6.65	6.3	0.0	26.6
124	150106	100	08:44	49.0	24.5	-13.0	66	3.5	4.1	2.2	732	4.37	6.9	0.3	29.3
125*	150107	100	09:12	79.0	17.1	-13.3	66	2.7	4.4	2.3	611	1.97	5.0	0.2	29.0
126	150108	100	09:40	147.8	24.6	-13.5	66	2.6	4.0	2.3	604	1.45	6.7	0.2	28.6
127	150109	100	13:06	32.0	26.1	-12.3	61	3.0	5.7	1.4	817	5.68	6.5	0.7	27.8
128	150110	100	13:43	49.0	27.0	-12.1	59	3.2	5.1	1.4	711	3.53	6.7	1.2	29.4
129	150111	100	14:15	79.0	26.3	-13.2	63	3.7	6.0	1.5	699	3.15	7.5	0.1	29.3

130	150112	100	14:47	147.8	27.1	-12.1	59	4.0	7.0	1.5	628	1.80	9.7	0.5	28.8
131	150113	100	15:20	79.0	73.7	-12.2	62	3.6	7.0	1.5	975	3.20	9.2	2.7	27.1
132	150114	100	16:45	32.0	25.7	-11.5	60	3.1	6.1	1.6	825	6.18	6.5	0.3	27.3
133	150115	100	18:52	49.0	26.1	-9.9	69	3.5	6.3	1.4	750	4.24	6.3	0.1	29.4
134	150116	100	19:21	79.0	24.1	-9.8	69	4.3	5.2	1.7	667	2.92			29.6
135	150117	100	19:50	147.8	27.1	-8.4	67	5.2	6.1	1.9	630	1.63			29.9
136	150118	100	20:21	32.0	22.9	-8.5	67	4.3	5.1	2.1	712	4.17			26.5
137	150119	100	20:50	49.0	25.3	-8.3	68	4.5	6.4	2.3	724	3.80			29.3
138	150120	100	21:19	79.0	22.8	-7.5	65	4.6	6.3	2.4	625	2.08			30.4
139	150121	100	21:47	147.8	24.6	-7.3	67	5.3	6.9	2.3	623	1.63			30.5
140	150122	100	22:16	32.0	24.5	-6.4	64	5.4	7.3	2.2	741	4.55			25.4
141f	170101	100	15:22	32.0	27.7	-16.7	73	29.6	1.4	2.9	644	1.88			0.8
142f	170102	100	15:53	49.0	24.5	-14.9	76	18.3	2.2	3.2	669	2.92			0.8
143f	170103	100	16:22	79.0	24.1	-11.6	74	10.4	4.2	3.5	627	1.77			0.8
144f	170104	100	16:56	32.0	26.1	-10.4	74	8.6	4.1	3.9	759	4.67			0.6
145f	170105	100	17:40	147.8	27.0	-10.7	76	6.7	5.2	4.7	617	1.37			0.8
146	180101	100	11:24	32.0	24.5	-13.0	73	4.1	5.8	1.6	777	5.36			27.9
147	180102	100	11:54	22.4	25.4	-12.9	71	5.2	5.9	1.7	985	9.52			24.3
148	180103	100	12:23	49.0	27.0	-12.7	68	3.4	6.0	1.8	730	3.92			29.0
149	180104	100	12:55	76.0	25.3	-12.4	67	5.7	6.4	2.1	688	3.01			28.9
150	180105	100	13:28	22.4	28.0	-13.1	67	3.1	5.9	2.4	959	8.32			24.0
151	180106	100	14:02	32.0	28.3	-11.9	62	4.5	4.9	2.5	832	5.53			26.4
152	180107	100	14:37	49.0	26.1	-13.5	62	8.6	3.3	2.5	650	2.35			28.7
153	180108	100	15:09	76.0	25.3	-13.9	61	3.9	4.2	2.7	656	2.31			29.4
154	180109	100	15:43	32.0	120.0	-15.5	63	NaN	3.2	1.9	1626	5.03			21.3
155	190101	100	11:21	22.4	25.0	-10.3	74	3.2	6.0	1.4	817	5.92			25.5
156	190102	100	12:05	49.0	25.3	-10.0	75	4.2	6.2	1.4	732	3.99			30.2
157	190103	100	12:32	32.0	25.6	-9.6	74	4.7	7.2	1.5	823	6.11			26.1
158	190104	100	13:02	76.0	24.1	-9.6	74	6.0	7.4	1.6	675	2.88			30.9
159	210101	100	15:25	22.4	25.4	-16.1	68	4.0	9.6	1.0	1114	12.34			24.9
160	210102	100	15:55	32.0	27.2	-16.4	65	4.2	7.7	0.9	980	8.98			26.5
161	210103	100	16:26	49.0	25.3	-17.0	63	5.6	7.3	1.1	815	5.82			29.8
162	210104	100	16:55	76.0	25.3	-17.4	62	3.6	6.8	1.3	743	4.44			28.8
163	210105	100	17:30	32.0	27.2	-18.2	62	6.1	4.6	1.4	829	5.69			28.3
164	210106	100	18:03	22.4	24.6	-18.5	60	21.2	2.8	1.4	820	6.30			26.1
165	210107	100	18:35	49.0	26.1	-18.6	59	66.0	1.5	1.5	598	1.01			31.0
166	230101	100	11:00	22.4	26.1	-16.2	73	14.0	2.7	1.5	810	5.52			25.1
167	230102	100	11:29	32.0	25.1	-15.8	74	9.3	2.9	1.5	833	6.47			24.7
168	230103	100	12:02	32.0	77.3	-15.6	76	40.6	2.7	1.6	1266	5.14			22.8
169	230104	100	14:46	32.0	52.3	-12.7	68	47.6	2.4	2.2	829	3.06			22.6
170	250101	100	09:48	22.4	24.6	-16.7	67	4.2	5.1	0.8	1013	10.43			22.7
171	250102	100	10:16	32.0	24.5	-17.2	68	3.9	5.5	0.8	942	9.09			26.3
172	250103	100	10:44	49.0	24.5	-17.3	66	4.1	4.9	0.8	783	5.29			28.9
173	250104	100	11:12	76.0	24.1	-17.4	67	4.0	5.9	0.9	751	4.87			29.0
174	250105	100	11:41	22.4	23.1	-17.9	68	4.3	5.5	0.9	1104	13.29			23.1
175	250106	100	12:09	32.0	25.1	-16.9	66	4.3	5.2	0.8	912	8.22			25.6

176	250107	100	12:36	49.0	24.5	-17.0	65	3.7	4.8	0.7	826	6.25	28.4
177	250108	100	13:03	76.0	24.1	-17.4	65	4.7	5.6	0.7	743	4.68	29.4
178	250109	100	13:46	32.0	61.9	-17.8	64	8.1	4.6	0.8	1407	7.70	22.8
179	260101	100	12:05	22.4	27.6	-17.5	67	3.7	6.4	0.6	1101	11.28	22.1
180	260102	100	12:36	32.0	26.1	-17.3	67	3.8	7.1	0.8	1014	9.85	25.2
181	260103	100	13:07	49.0	24.5	-17.0	67	3.6	8.4	0.9	864	7.33	26.3
182	260104	100	13:35	76.0	24.1	-16.8	67	3.5	8.6	1.1	775	5.20	29.0
183	260105	100	14:06	22.4	27.6	-17.2	66	4.5	7.3	1.0	1189	13.03	22.2
184	260106	100	14:36	32.0	25.6	-17.0	66	4.5	7.2	1.0	993	9.60	25.3
185	260107	100	15:06	49.0	24.5	-17.0	64	3.9	7.0	1.0	822	6.39	29.3
186	260108	100	18:00	22.4	55.6	-17.9	63	4.1	6.0	1.4	2007	14.65	21.3
187	260109	100	19:01	76.0	24.1	-18.1	63	3.7	6.0	1.4	759	4.81	29.2
188	260110	100	19:30	49.0	26.1	-18.1	63	4.2	6.8	1.4	887	7.36	28.8
189	260111	100	20:07	32.0	25.6	-18.1	64	3.5	6.6	1.5	980	9.33	25.0
190	260112	100	20:37	22.4	24.6	-18.2	65	3.9	7.1	1.6	1160	13.97	22.7
191	260113	100	21:21	76.0	27.9	-18.1	65	3.7	5.4	1.9	751	4.00	28.9
192	260114	100	21:52	49.0	25.3	-18.1	65	4.0	5.7	2.0	792	5.51	28.8
193	260115	100	22:23	32.0	26.7	-17.8	65	3.3	6.6	1.8	1035	10.11	24.2
194	260116	100	22:52	22.4	25.0	-17.9	65	3.4	6.3	1.8	1101	12.44	22.5
195	280101	100	11:33	22.4	26.9	-18.2	70	3.4	5.8	1.1	1214	13.93	22.3
196	280102	100	12:04	22.4	44.8	-17.6	69	3.3	6.0	0.8	1717	14.47	20.1
197	280103	100	12:53	32.0	43.2	-17.4	70	4.0	6.4	0.7	1260	9.26	24.1
198	280104	100	13:43	49.0	44.9	-17.3	69	3.5	6.4	0.8	1085	6.61	23.4
199	280105	100	14:30	76.0	38.0	-17.1	68	4.0	6.0	1.0	772	3.39	28.2
200	290101	100	12:03	32.0	24.5	-16.7	70	5.0	5.5	0.9	869	7.45	27.7
201	290102	40	12:34	32.0	24.5	-16.2	67	5.2	5.5	1.0	486	9.21	30.3
202	290103	100	13:05	76.0	24.1	-17.1	70	5.4	4.8	1.3	672	3.05	28.5
203	290104	40	13:35	76.0	24.1	-17.3	69	6.5	4.8	1.4	370	2.72	25.0
204	290105	100	14:05	22.4	24.2	-16.9	69	6.4	5.0	1.4	936	9.09	23.7
205	290106	40	14:35	22.4	24.6	-17.4	69	4.9	4.4	1.4	520	11.11	28.8
206	290107	100	15:04	32.0	24.5	-17.1	69	6.7	4.4	1.5	837	6.71	27.9
207	290108	40	15:32	32.0	24.5	-17.0	68	5.2	4.3	1.5	487	9.27	29.9
208	290109	100	16:11	76.0	22.8	-16.5	67	4.1	5.6	1.5	712	4.19	29.1
209	290110	40	16:39	76.0	24.1	-16.6	67	5.5	5.4	1.5	386	3.63	30.8
210	300101	100	14:20	32.0	27.2	-17.6	56	3.8	4.9	1.8	861	6.56	27.6
211	300102	40	14:53	32.0	25.6	-16.5	54	4.4	5.8	1.8	495	9.29	29.7
212	300103	100	15:24	76.0	25.3	-17.6	56	6.0	4.4	1.8	687	3.23	30.8
213	300104	40	15:55	76.0	25.3	-17.5	58	5.9	5.9	1.8	384	3.28	29.7
214	300105	100	16:25	32.0	25.1	-16.6	57	7.7	7.0	1.8	881	7.55	28.6
215	300106	40	16:55	32.0	24.5	-15.7	55	4.1	7.9	1.7	509	10.50	30.0
216	300107	100	17:35	76.0	25.3	-16.5	56	4.7	7.3	1.4	692	3.32	29.6
217	300108	40	18:10	76.0	22.8	-17.0	59	4.2	6.1	1.1	383	3.65	30.1
218	300109	100	18:40	22.4	24.2	-16.4	58	3.9	8.3	1.2	1105	12.98	25.3
219	300110	100	19:17	22.4	25.3	-16.3	63	4.6	8.0	1.3	1081	11.88	24.8
220	310101	100	20:18	22.4	25.7	-10.1	70	4.4	7.7	1.1	1025	10.48	24.3
221	310101	100	20:47	32.0	27.7	-11.4	75	6.4	6.4	1.0	973	8.47	24.9

222	310101	100	21:19	49.0	26.1	-10.5	76	4.5	7.0	1.0	820	5.94	27.7
223	310101	100	21:48	76.0	26.6	-10.4	75	4.6	6.4	1.1	765	4.49	29.8
224	310101	100	22:30	22.4	27.5	-10.2	75	4.6	6.7	1.3	974	8.75	22.6
225	310101	100	23:02	32.0	25.1	-10.3	76	3.9	6.4	1.4	909	7.95	24.9
226	310101	100	23:31	22.4	26.4	-11.1	76	5.9	4.6	1.5	875	7.03	23.7
227	050201	40	14:59	22.4	26.8	-4.4	80	4.2	5.1	1.0	371	2.47	16.04
228	050201	100	15:30	22.4	25.7	-4.1	80	4.9	5.4	1.3	603	1.36	16.46
229	050201	40	15:59	76.0	25.3	-4.3	79	8.4	5.3	1.7	364	2.24	25.2
230	050201	100	16:30	76.0	24.1	-4.6	80	18.9	4.5	2.1	597	1.33	23.4
231	070201	100	17:04	32.0	26.1	-7.5	74	4.1	5.4	0.9	720	3.82	22.9
232	070202	40	17:33	32.0	25.1	-7.6	74	4.6	4.7	1.2	437	6.29	25.3
233	070203	100	18:01	76.0	24.1	-8.4	74	4.0	4.8	1.5	702	3.74	28.5
234	070204	40	18:28	76.0	24.1	-8.1	74	3.6	5.4	1.6	400	4.43	29.0
235	070205	100	18:58	32.0	26.1	-7.8	75	3.8	6.0	1.8	758	4.64	22.9
236	070206	40	19:28	32.0	25.6	-7.3	75	3.8	6.0	2.0	435	6.05	24.2
237	070207	100	19:56	76.0	24.1	-6.7	73	4.2	6.1	2.3	692	3.51	27.1
238	070208	40	20:24	76.0	25.3	-6.7	72	4.6	5.4	2.6	387	3.50	27.0
239*p	150201	100	17:50	32.0	25.1	-16.4	72	59.8	1.2	1.2	600	1.48	29.4
240*s	150202	100	18:24	32.0	30.9	-18.8	74	35.2	1.4	1.5	835	4.95	25.0
241	160201	100	11:16	32.0	24.5	-18.5	67	3.6	4.8	1.6	1062	11.81	22.1
242s	160202	100	11:44	32.0	30.4	-18.2	67	2.9	4.3	1.7	1129	10.41	21.6
243p	160203	100	12:20	32.0	26.7	-17.7	67	3.5	5.6	1.7	1082	11.44	23.5
244	160204	100	12:51	79.0	25.0	-16.7	68	3.1	6.4	1.6	810	6.00	29.9
245s	160205	100	13:20	79.0	25.0	-16.2	67	2.9	6.8	1.6	845	6.35	29.1
246p	160206	100	13:51	79.0	25.0	-15.7	69	3.7	6.6	1.6	804	6.02	29.5
247	160207	100	14:21	22.0	27.1	-14.9	68	3.1	6.8	1.5	1264	14.82	21.1
248s	160208	100	14:51	22.0	22.7	-14.5	69	3.6	7.0	1.7	1163	14.76	23.4
249p	160209	100	15:20	22.0	24.6	-14.3	70	3.6	6.6	1.9	1129	13.48	22.7
250s	160210	100	16:06	32.0	28.3	-14.3	69	4.5	4.4	2.0	995	8.56	23.8
251*p	160211	100	16:41	32.0	25.6	-13.0	66	12.1	2.1	1.7	750	4.72	25.1
252	160212	100	17:09	32.0	24.0	-12.6	66	6.1	4.6	1.7	879	7.85	24.6
253p	160213	100	17:38	32.0	25.6	-13.2	69	3.7	4.6	1.6	893	7.83	24.5
254	170201	100	09:20	32.0	24.5	-8.6	74	14.0	1.5	1.6	623	1.87	
255s	170202	100	09:47	32.0	25.6	-8.7	76	65.2	0.5	2.0	619	1.28	
256p	170203	100	10:15	32.0	24.5	-8.5	75	55.5	1.1	2.4	597	1.45	
257i	180201	100	16:59	32.0	25.1	-10.9	74	4.6	5.2	1.7	712	3.50	25.3
258s	180202	100	17:27	32.0	24.5	-10.9	73	5.0	5.9	1.8	868	6.98	24.9
259i	180203	100	17:55	79.0	25.0	-10.9	74	3.8	5.8	2.0	747	4.29	27.4
260s	180204	100	18:24	79.0	26.3	-10.9	74	4.1	5.6	2.2	758	4.18	28.5
261i	180205	100	19:04	79.0	68.5	-11.0	74	3.8	5.8	2.5	1110	4.51	
262*	200201	100	13:44	22.0	23.1	-15.7	63	28.8	4.9	1.5	909	8.63	
263*	200202	100	14:52	32.0	25.1	-17.0	68	13.0	8.6	1.5	986	9.65	
264i	200203	100	15:26	32.0	28.3	-17.3	66	6.9	8.5	1.3	1149	11.68	
265	200204	100	15:58	49.0	24.5	-17.7	66	7.6	8.2	1.2	834	6.44	
266i	200205	100	16:27	79.0	23.7	-17.9	63	7.7	8.1	1.1	717	3.80	
267	200206	100	16:55	79.0	26.3	-18.7	66	4.7	8.1	1.1	804	5.34	

268	200207	100	17:31	32.0	25.1	-19.0	64	9.3	6.0	1.1	782	5.35
269*	200208	100	19:10	49.0	13.1	-20.5	64	8.1	4.1	2.5		0.00
270s	200209	100	19:27	32.0	27.7	-21.5	64	4.0	4.0	2.5	1016	9.16
271p	200210	100	19:58	32.0	25.1	-21.2	62	3.1	4.9	2.5	991	10.16
272s	200211	100	20:27	79.0	25.0	-21.2	61	2.8	4.7	2.5	771	4.71
273p	200212	100	20:54	79.0	25.0	-21.3	61	2.8	4.5	2.6	726	4.30
274	210201	100	13:45	32.0	25.1	-27.0	58	2.9	3.6	1.6	935	8.75
275	210202	100	14:12	76.0	25.0	-27.0	57	6.4	4.2	1.6	822	6.02

Appendix F. Interaction generated spray, main functions

Here the spray generation equations of Horjen and Vefsnmo (1985) and Forest et al. (2005) are compared. The RIGICE04 equation is taken directly from the code written in Basic in the RIGICE04.xls file. The development of the equation is described in Forest et al. (2005).

Table 6 gives the formulas used in the models. The resulting spray mass inflow to the structure surface per unit area arriving during one hour is shown in Figure 32. The function by Forest et al. (2005) predicts 2-3 orders greater spray flux than Horjen and Vefsnmo (1985). Such an extreme difference likely cannot be caused by the difference of the structures on which these spray fluxes were measured. Thus, it should cause doubts in the reliability of the respective equations.

Table 6. Comparison of the spray generation functions.

Used in model	ICEMOD	RIGICE04
Development is described in	Horjen and Vefsnmo (1985)	Forest et al. (2005)
Spray period	$2\tau_w$	$min\left[\begin{array}{c}\tau_w\, exp\left(2\frac{H_c^2}{H_s^2}\right)\\ 3600\, sec\end{array}\right]$
Spray duration	2 sec	1 sec
Vertical distribution of spray flux	$\frac{M_{HV}U_{10}\tau_{per}}{\tau_{dur}}\frac{1-0.5\frac{(1-10^{-2}U_{10})}{\exp(0.44z_{HV}+0.22)}}{\exp\left(k_{HV}U_{10}^{0.667}z_{HV}^2\right)}$	$\frac{K_3K_1H_s^2}{exp\left(K_2\left(z-H_s\right)\right)}$
Source of measurements	Semisubmersible, 2x3 column structure (centre column diameter 9.75 m and corner columns 10.62 m), Treasure Scout (Jørgensen, 1985)	Artificial island
Spray on the lee side?	10% spray flux on the lee side	No spray, freezing only on upwind side
Wave run-up, no ice accretion below that level	$0.5H_s$	H_s

Notations:

Common for models:

- z [m] is the height above mean sea level
- H_s [m] is significant wave height
- τ_w is the significant wave period.
- For ICEMOD only
- $M_{HV} = 6.28 \times 10^{-4}$ kg m^{-3}
- $k_{HV} = 0.0588$ (s m^{-1})$^{0.667}$
- $z_{HV} = (2z / H_s) - 1$
- U_{10} [m s^{-1}] is the wind speed at z = 10 m.
- τ_{per}, τ_{dur} are the period and duration of spray, respectively

For RIGICE04 only:

- H_c = 3.15 m is the critical wave height, which required to produce spray. If $H_s < H_c$ – no spray.
- K_3 = 2 m s^{-1}. (cloud width is assumed to be 2 m and duration of spray 1 s)
- K_1 = 1.35 kg m^{-5}
- K_2 = 0.53 m^{-1}

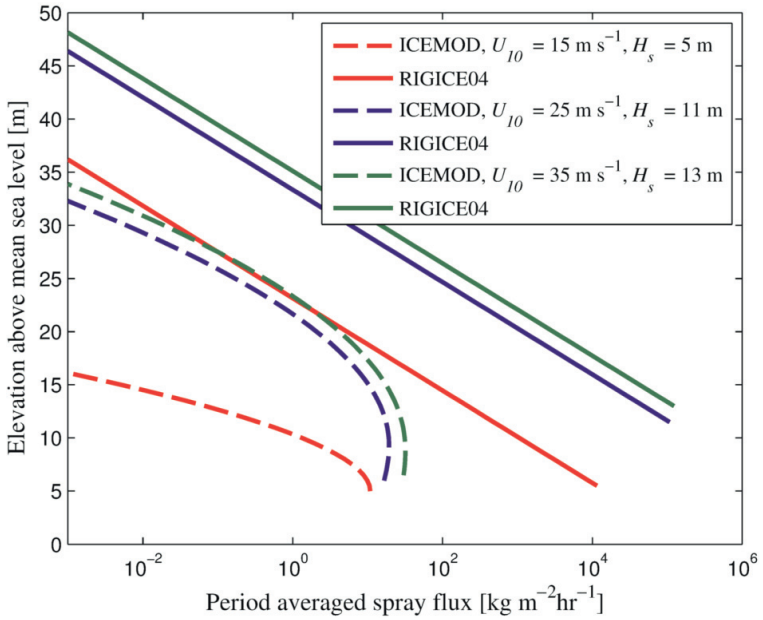

Figure 32. Comparison of spray generation functions by Horjen and Vefsnmo (1985) and Forest et al. (2005).

References:

Forest, T.W., Lozowski, E.P., Gagnon, R.E, 2005. Estimating marine icing on offshore structures using RIGICE04, Conference proceedings IWAIS XI, Montreal, June 2005.

Horjen, I. and Vefsnmo, S., 1985. A kinematic and thermodynamic analysis of sea spray (in Norwegian), Offshore Icing – Phase II, Norwegian Hydrodynamic Laboratory (NHL). Report STF60 F85014, 71 p.

Jørgensen, T.S., 1985. Sea spray characteristics on a semi-submersible drilling rig. NHL-report No STF60 F 85015.